A Technical Guide to MOM4

GFDL Ocean Group Technical Report No. 5

STEPHEN M. GRIFFIES, MATTHEW J. HARRISON,
RONALD C. PACANOWSKI, AND ANTHONY ROSATI

SEPTEMBER 18, 2003

This document is being freely distributed by

S.M. Griffies, M.J. Harrison, R.C. Pacanowski, and A. Rosati
Stephen.Griffies@noaa.gov
Matthew.Harrison@noaa.gov
Ron.Pacanowski@noaa.gov
Tony.Rosati@noaa.gov

It should be referenced as

A TECHNICAL GUIDE TO MOM4
GFDL OCEAN GROUP TECHNICAL REPORT NO. 5
S.M. Griffies, M.J. Harrison, R.C. Pacanowski, and A. Rosati
NOAA/Geophysical Fluid Dynamics Laboratory
Version prepared on September 18, 2003
Available online at www.gfdl.noaa.gov

Information about how to download and run MOM4 can be found at the GFDL Flexible Modeling System (FMS) web site accessible from www.gfdl.noaa.gov.

This document was prepared using LaTeX as described by Lamport (1994) and Goosens et al. (1994).

CONTENTS

LIST OF FIGURES

Part I

Basics of MOM4

BASICS OF MOM4

The purpose of this part of the MOM4 Guide is to familiarize the reader with the basics of MOM4. There are two chapters, with the first providing an overview of MOM4 and its relation to other versions of MOM. The second chapter provides details of the computational aspects of MOM4. This part of the book should satisfy those readers most interested in a quick overview and summary of MOM.

CHAPTER

ONE

An introduction to MOM

Contents

The Modular Ocean Model (MOM) is a numerical representation of the ocean's hydrostatic primitive equations. It is designed primarily as a tool for studying the ocean climate system. The purpose of this chapter is to introduce the Modular Ocean Model (MOM) and to provide an overview of this document. Information about how to download and run MOM4 can be found at
http://nomads.gfdl.noaa.gov/.

1.1 What is MOM?

The Modular Ocean Model (MOM) is a numerical representation of the ocean's hydrostatic primitive equations. It is designed primarily as a tool for studying the ocean climate system. The model is developed and supported by researchers at NOAA's Geophysical Fluid Dynamics Laboratory (GFDL), with contributions also provided by researchers worldwide. The model is freely available via
www.gfdl.noaa.gov/∼fms

MOM evolved from numerical ocean models developed in the 1960's-1980's by Kirk Bryan and Mike Cox at GFDL. Most notably, the first internationally released and supported primitive equation ocean model was developed by Mike Cox (Cox (1984)). It cannot be emphasized enough how revolutionary it was in 1984 to freely release, support, and document code for use in numerical ocean climate modeling. The Cox-code provided scientists with a powerful tool to investigate basic and applied questions about the ocean and its interactions with other components of the climate system. Previously, rational investigations of such questions by most scientists were limited to restrictive idealized models and analytical methods. Quite simply, the Cox-code started what has today become a right-of-passage for every high-end numerical model of dynamical earth systems.

Upon the untimely passing of Mike Cox in 1990, Ron Pacanowski, Keith Dixon, and Tony Rosati rewrote the Cox code with an eye on new ideas of modular programming in Fortran 77. The result was the first version of MOM (Pacanowski et al. (1991)). Version 2 of MOM (Pacanowski (1995)) introduced the memory window idea, which was a generalization of the vertical-longitudinal slab approach used in the Cox-code and MOM1. Both of these methods were driven by the desires of modelers to run large experiments on machines with relatively small memories. The memory window provided enhanced flexibility to incorporate higher order numerics, whereas slabs used in the Cox-code and MOM1 restricted the numerics to second order. MOM3 (Pacanowski and Griffies (1999)) even more fully exploited the memory window with a substantial number of physics and numerics options.

The Cox-code and each version of MOM came with a manual. Besides describing the elements of the code, these manuals aimed to provide transparency to the rationale underlying the model's numerics. Without such, the model could in many ways present itself as a black box, thus greatly hindering its utility to the researcher. This philosophy of documentation saw its most significant realization in the MOM3 Manual, which reaches to 680 pages. The present document is written with this philosophy in mind, yet allows itself to rely somewhat on details provided in the previous manuals as well as theoretical discussions given by Griffies (2004).

The most recent version of MOM is version 4. The origins of MOM4 date back to a transition from vector to parallel computers at GFDL, starting near 1999. Other models successfully made the transition some years earlier (e.g., The Los Alamos Parallel Ocean Program (POP) and the OCCAM model from Southampton, UK). New computer architectures generally allow far more memory than previously available, thus removing many of the reasons for the slabs and memory window approaches used in earlier versions of MOM. Hence, we concluded that the memory window should be jettisoned in favor of a straightforward horizontal 2D domain decomposition. Thus began the project to redesign MOM for use on parallel machines.

1.2 Release of MOM4.0 October 2003

As may be anticipated, when physical scientists aim to rewrite code based on software engineering motivations, more than software issues are addressed. During the writing of MOM4, numerous algorithmic issues were also addressed, with many physical parameterizations, dynamical schemes, diagnostics, etc., being rewritten and/or added. Hence, the naively simple task of rewriting MOM3 into MOM4 has only now matured, after some five years of undertaking.

MOM4 was released twice to the public as a beta-code during the middle of 2002. A third beta release was held September-October, 2004, with only a few experienced users participating. Significant input from users throughout the MOM community has assisted in the development of the code. Such evolution of the code will clearly continue. Nonetheless, the present architecture and overall structure of MOM4 appears robust enough that we are soliciting general usage from the ocean modeling community, without the reservations attendant with a beta-release. That is, we sanction the present code as a full release of MOM4.0.

1.3 MOM4 documentation

The main goal of this document is to provide the ocean climate modeler with a guide to Version 4 of the Modular Ocean Model (MOM4). In particular, we address the needs of the those picking up MOM4 and wishing to use the code and to understand many of the numerical details of the code. There are three other documents written in tandem with the present document:

- The MOM4 Users' Guide. This web-based document is available from the MOM4-link at
  http://nomads.gfdl.noaa.gov/.
  The MOM4 Users' Guide provides details necessary to download the source code and run the model. Here you will also be able to register as a MOM4-user.

- FUNDAMENTALS OF OCEAN CLIMATE MODELS by Griffies (2004) presents a theoretical foundation for ocean climate models, with MOM4 as one example. It is here that a rationalization of the model equations and algorithms are presented. This document will remain available on-line until Sometime during the early part of 2004, at which time it will be published by Princeton University Press.

- THE MOM3 MANUAL of Pacanowski and Griffies (1999) provides a thorough discussion of MOM3, some of which is relevant for MOM4.

1.4 Modeling frameworks

As the field of climate modeling grows, and the realism of numerical models improves, the software engineering issues posed by high-end earth system models increase in complexity. Additionally, the efficient use of rapidly changing computational platforms requires expertise beyond the traditional model developer. Hence,

climate modelers have increased their collaboration with each other and with software engineers and computational scientists. The aim of such collaborations is an improved software infrastructure thus reducing the burden on any particular researcher or group.

1.4.1 The GFDL Flexible Modeling System

To assist with the development of MOM4, we have employed much of the code developed and supported at GFDL for use in all of its numerical models. This Flexible Modeling System (FMS) is the result of many years (starting in force around 1997-1998) of re-thinking, re-structuring, and re-writing the previously disparate research codes at GFDL. FMS is designed with the goal of producing code that is simple to use, simple to understand, simple to modify, well documented, and supported by a sound base of scientists and engineers at GFDL and elsewhere.

In its broadest terms, FMS aims to remove computational barriers (e.g., code structure and language, standards, scripts, units, I/O, etc.) between codes used for the study of dynamical geophysical systems. This goal should not be mistaken as a call to unify or homogenize algorithms. Instead, it provides a common software infrastructure inside of which various algorithms (e.g., different vertical coordinate choices, dynamical cores, and/or physical parameterizations) coexist. FMS also aims to provide a common superstructure (e.g., coupler, run-scripts, post-processing) which allow the various models to communicate with one another, and for the researcher to communicate with the model code and results.

If the broader climate modeling community can realize these rather idealistic, and nontrivial, goals, then the choice to use a particular model code can be based on the physical and numerical attributes of the code, instead of restrictions based on code style or platform issues. The effort spear-headed by NASA's Earth System Modeling Framework (ESMF)
http://www.esmf.ucar.edu)
aims for nothing less.

1.4.2 MOM4 within FMS

Participating within GFDL's FMS allows for MOM4 to use numerous FMS modules. The following represents a sample.

- time manager: keeps time and sets time dependent flags
- coupler and data_override: used to couple MOM4 to other component models and/or datasets.
- I/O: to read and write data
- initial and boundary data: regrids spherical fields to the generally non-spherical ocean model grid
- grid and topography specification: sets model grid spacing and interpolates spherical topography to the model grid
- parallelization tools: for passing messages across parallel processors

- diagnostic manager: to register and send fields to be written to a file for later analysis
- field manager: for organizing multiple tracers for use especially in biogeochemistry studies.

Being part of FMS greatly frees up those interested in developing physical and numerical algorithms to focus on just that, instead of also needing to become experts in computational platforms and various software engineering issues. It also allows for efficient input from computational scientists and engineers since they can more readily focus on computational issues. Finally, it allows us in the ocean modeling community to play a role in establishing common software infrastructures and coding standards, such as the ESMF efforts mentioned previously.

The FMS infrastructure was first released to the public earl 2002, with further releases following on a regular basis. Notably, MOM4 represents the first major model code to be released within FMS. Full documentation of FMS can be found at www.gfdl.noaa.gov.
It is here that the researcher will find information about how to download and run MOM4.

1.4.3 MOM4 on the web

MOM4.0 is released via the GFDL-FMS web site. Originally it was planned that it would be released via the open source site SourceForge. However, as we wish to know more about who actually takes the code, it is necessary that we run a SourceForge-like software locally at GFDL, where all code, documentation, and bulletin boards are maintained. Note that as we aim to nurture the MOM and FMS communities, we strongly encourage users to contact developers via one of the email lists maintained at the FMS web site.

1.5 Some characteristics of MOM4

As with all previous versions of MOM, MOM4 discretizes the ocean's hydrostatic primitive equations on a fixed Eulerian grid, with the Arakawa B-grid defining the horizontal arrangement of model fields. That is, the grid cells live on a lattice fixed in space-time. Given that MOM4 remains a z-coordinate ocean model, it shares much with its predecessors. However, there are some notable characteristics that we highlight in this section.

1.5.1 Streamlining the options

MOM3 arguably contains everything but the proverbial kitchen sink. For example, when building MOM3, we were uncertain what would be the most suitable external mode solver for the needs of z-coordinate ocean climate modeling. Hence, we kept all those ever having been implemented in earlier MOMs. These methods included the traditional rigid lid streamfunction of Bryan (1969), the rigid lid surface pressure of Smith et al. (1992) and Dukowicz et al. (1993), the implicit free surface of Dukowicz and Smith (1994), and the explicit free surface of Killworth

et al. (1991) and Griffies et al. (2001). After investigations leading to the Griffies et al. (2001) paper, it was concluded that the explicit free surface method is most suitable since it allows for efficient use of parallel computers while rendering the model's algorithms physically and numerically sound and simple. Hence, there is only one external mode solver in MOM4, and it is a slight variant of the Griffies et al. method detailed in Griffies (2004).

Other examples abound where numerous options were made available in MOM3 for physical parameterization schemes. Quite simply, MOM3 represented the end of some ten years of research and experience with various approaches used in MOM. Building up to that point required testing of numerous options prior to deciding which ones to jettison. The advantage of this approach is that it allows for ready examination of the many permutations and combinations leading to a well tuned model. The disadvantage is that is leaves the inexperienced modeler with little guidance since there are so many options.

In the development of MOM4, we attempted a balance between including multiple options and hard-line decisions about what would be supported and not supported. We hope that our choices will be suitable for a broad class of ocean climate researchers.

1.5.2 Eliminating *ifdefs*

One of the most noticeable change between MOM3 and MOM4 is that MOM4 has no cpp preprocessor options associated with physical parameterizations, commonly known as *ifdefs*. There remains only a single ifdef associated with code optimization (Section 2.6). The proliferation of physics *ifdefs* in MOM3 presented the user with a complex menagerie of logical structures (e.g., multiple and nested *ifdefs*) to wade through in order to reveal the utilized Fortran code. A rough count of the *ifdefs* available in MOM3.1 came to something between 300 and 400 options, with multiple permutations allowed! Furthermore, cpp pre-processor options cannot be checked at compile time for typos. Locally, we experienced numerous occasions where an *ifdef* was misspelled, yet the model continued to run using an undesired piece of code. We suspect that other researchers have had similar unfortunate experiences.

We have done a few things to replace *ifdefs*. Firstly, as mentioned in the previous subsection, we made decisions to streamline the supported options. Supporting one instead of five external mode solvers helped tremendously. Additionally, we aimed to have the code flexible and simple so that researchers wishing to do something different will find coding their changes to be a trivial task. Hence, we left out many smaller options that MOM3 chose to include. Secondly, we introduced Fortran *if-tests* in many places where *ifdefs* formerly lived. Doing so allows for the Fortran compiler to detect typos, thus enhancing the quality control aspects of the model.

Finally, where large chunks of physical parameterization code could be isolated, we made Fortran modules out of the options. For example, if one wishes to use the KPP vertical mixing scheme, then

`/mom4/ocean_param/mixing/vert/kpp/ocean_vert_mix_coeff.F90`

should be compiled. If instead, one wishes the constant vertical diffusivity approach, then

`/mom4/ocean_param/mixing/vert/const/ocean_vert_mix_coeff.F90`

should be compiled. This approach effectively replaces the selection of major *ifdef* options with a pointer within a shell script to a desired module. The downside to this approach is that some code in the different modules is similar, and so there is a modest increase in code maintenance. The upside is that it cleans up the logic in the separate modules.

1.5.3 Key computational characteristics

We summarize here some of the computational characteristics of MOM4.

1.5.3.1 Computational aspects: overview

- As discussed in Section 1.4, the computational framework (i.e., infrastructure and superstructure) upon which MOM4 is based is that of the GFDL Flexible Modeling System (FMS).
- All code is Fortran 90.
- There is only a single cpp-preprocessor option (i.e., $ifdef$) associated with the static memory option (Section 2.6). Files which use this ifdef must have the extension $.F90$, whereas files with no cpp-preprocessor options have a $.f90$ extension.
- 3D arrays are dimensioned (i, j, k) instead of the slab-like (i, k, j) structure used in earlier MOMs. Consequently, there is no memory window or slabs. It is essentially for these reasons, plus the increased elegance of Fortran 90, that algorithm development and coding is far simpler with MOM4 than earlier MOMs.
- 2D (latitudinal/longitudinal) horizontal domain decomposition is the model standard of use on single or multiple parallel processors.
- Multiple tracers are managed using the FMS *field manager* that organizes tracer names, fluxes, sources, initializations, restarts, advection schemes, etc. This manager was written, in particular, to serve the needs of ocean biogeochemistry research, as well as for use by atmospheric chemists.
- The FMS *diagnostic manager* is used to register and send fields to output for analysis. The diagnostic manager and asociated diagnostic table allows for the trivial addition of a new field to be added to the suite of model diagnostics available for an experiment. This manager has been found to be extremely useful and powerful.
- I/O is generally written in NetCDF. This capability includes files for restarts, boundary forcing, initialization, topography, grids, sponges, etc. Some native format capabilities remain, but with less support by GFDL than NetCDF.

1.5.3.2 Computational aspects: derived types

Motivated by the desire to use MOM4 for a broad range of applications, data flow between the various modules has been streamlined through the use of derived type structures available in F90. The use of derived types, for instance, eases the development of ocean data assimilation systems using mom4, and faciliates generalized managing of biogeochemical tracers. The β1 and *beta*2 releases of mom4 used very few derived types. It is therefore useful to highlight some of their advantages.

- *User-friendliness* - various inputs and outputs to MOM's routines are more clearly defined and protected with the f90 intent attribute.
- *Maintainability* - algorithmic changes requiring additional variables can be easily imbedded within the type structures.
- *Enhanced modularity* - fewer dependencies between the modules. This leads to clarity within the code and easier development.

We provide details of the derived types used in MOM4.0 in Section 2.1.

1.5.4 Key numerical characteristics

Here we summarize some of the numerical aspects of MOM4.

- The model uses generalized orthogonal horizontal coordinates, with spherical curvilinear coordinates a special case. We are supporting the "tripolar" grid of Murray (1996), as discussed in Chapter 4. Other locally orthogonal grids should be readily usable with the MOM4 framework. Because of this added functionality to simulate the Arctic, MOM4 only minimally supports a polar filtering scheme for tracers.
- Bottom topography is represented using the Pacanowski and Gnanadesikan (1998) partial cells. The older "full cell" approach is available via a namelist in the topography generation pre-processing module.
- For the inviscid dynamics, time stepping is with the leap-frog and Robert-Asselin time filter. The Euler forward or Euler backward "mixing" time step used in earlier MOMs has been eliminated. The dissipative dynamics (e.g., friction and diffusion) remains forward, as required for numerical stability.
- As a forward model, MOM4 is compatible with the most recent adjoint compiler of Ralf Giering. To fully exploit this compiler for research requires a license agreement from Giering. See
  http://www.fastopt.de/ralf/
  for more details.
- There are numerous diagnostics for checking code integrity, such as energetic consistency, tracer conservation, solution stability, etc.
- Through FMS, there are a full suite of pre-processing modules available for setting up idealized or realistic grid specification files, initial conditions, and boundary conditions.

1.5.5 Physical aspects

Here we summarize some of the physical aspects of mom4.

- Physical units are MKS.
- MOM4 employs the non-Boussinesq approach of Greatbatch et al. (2001). Hence, the kinematics, dynamics, and physics are based on a mass conserving framework, instead of the traditional volume conserving Boussinesq approach. Notably, the non-Boussinesq simulations yield a more accurate prognostic calculation of the model's sea level, including the steric effects absent in the Boussinesq models. The volume conserving Boussinesq option remains available for comparison via a namelist. Griffies (2004) presents details and rationale. For realistic global simulations where a full physical parameterization suite is used, the non-Boussinesq simulations have been found to be only some 2% to 3% slower.
- The external mode solver is a variant of the Griffies et al. (2001) explicit free surface. Top model grid cells have time dependent volume, thus allowing for conservative fresh water input. Griffies (2004) presents full details and rationale. There is no rigid-lid option in MOM4.
- Neutral tracer diffusion is implemented according to Griffies et al. (1998). Likewise, Gent-McWilliams (Gent and McWilliams (1990); Gent et al. (1995)) stirring is implemented using the skew-diffusion method of Griffies (1998). Flow dependent diffusivities are dependent on the depth integrated Eady growth rate and Rossby radius of deformation, as motivated by the ideas of Held and Larichev (1996) and Visbeck et al. (1997). Griffies (2004) presents full details and rationale.
- Two equations of state are available. The most accurate is that described by McDougall et al. (2003). In particular, the model's density is a function of the local potential temperature, salinity, and pressure. Pressure used for this calculation is the time dependent hydrostatic pressure arising from fluid above the point of interest, including the atmospheric pressure and pressure within the ocean free surface (see Dewar et al. (1998)), and surface pressure is computed using the local surface ocean density, not the constant Boussinesq density ρ_o. The second equation of state is a linearized equation for use in idealized Boussinesq models. Here, density is equated to potential density and is a linear function of potential temperature. Nonlinear and pressure effects are ignored in the linear equation of state. Chapter 20 details the MOM4 implementation.
- Vertical mixing schemes include the time-independent depth profile of Bryan and Lewis (1979), the Richardson number dependent scheme of Pacanowski and Philander (1981), and the KPP scheme of Large et al. (1994).
- Horizontal friction schemes include constant and grid dependent viscosity schemes, as well as the Smagorinsky viscosity scheme implemented according to Griffies and Hallberg (2000). Laplacian and biharmonic operators are

available. The anisotropic scheme of Large et al. (2001) and Smith and McWilliams (2002) has been implemented for both the Laplacian and biharmonic friction operators, as has the associated Laplacian viscosity used in the Large et al. (2001) paper. Griffies (2004) presents full details and rationale. Finally, the methods of Holloway (1992) allow for horizontal friction to be computed as a deviation from an approximate barotropic maximum entropy state (see Chapter 23).

- Tracer advection is available using 2nd, 4th, 6th order centered schemes (Pacanowski and Griffies (1999)), and the quicker scheme documented by Holland et al. (1998) as well as Pacanowski and Griffies (1999). The algorithms for the 4th and 6th order schemes assume constant grid spacing, thus simplifying their code though compromising their accuracy on grids with large anisotropies. MOM4 also provides for two multi-dimensional flux limited schemes ported from the MIT GCM. These schemes are monotonic and quite efficient.

- A sigma diffusion scheme is available, whereby tracers are diffused along topography, with enhanced diffusion when heavy parcels are above lighter parcels. This scheme aims to provide an extra diffusive pathway for dense water to flow off shelves, as well as to add mixing next to the bottom. It is implemented according to the ideas of Beckmann and Döscher (1997) and Döscher and Beckmann (1999). Their sigma advection piece has not been coded, largely due to the recommendations of Döscher and Beckmann (1999) who concluded that the diffusive piece was sufficient for many purposes. Chapter 14 describes the MOM4 implementation.

- The overflow scheme of Campin and Goosse (1999) has been implemented in MOM4. This scheme has similar, yet complementary, characteristics relative to the Beckmann and Döscher (1997) scheme. Chapter 15 describes the MOM4 implementation of Campin and Goosse (1999).

- Tidal forcing from eight lunar and solar constituents has been incorporated into the free surface module of MOM4. Chapter 22 describes the implementation.

- An open boundary condition (OBC) has been implemented into MOM4 to allow the model to be of use for regional studies. Chapter 21 describes the implementation.

1.6 Reproducing older results using MOM4.0

During the development of MOM4.0, there were significant efforts made to verify that results generated with older versions of MOM were consistent with the new code. Numerous bugs were found in such re-engineering exercises. Notably, however, one should not expect to regenerate exactly the same results due to (1) changes in operation order, (2) resolving bugs present in older codes, (3) algorithm changes resulting from increased understanding of the physics, dynamics, and numerics. Nonetheless, for most cases, the overall qualitative behaviour of the solution should

remain identical. Indeed, if such is not the case, then please carefully document the differences and provide input to the developers.

1.7 Planned ocean model development

During the β-testing phase of the MOM4 development (middle 2002 to late 2003), many parts of the code have undergone testing whereby outstanding known and unknown bugs/features have been resolved. As always, even after the β-testing phase, we solicit your critical input to help solidify the model's integrity and functionality. This section outlines plans for future development with mom4 and even longer term plans for mom5.

1.7.1 General requirements for code to be incorporated to mom4

As stated in Section 1.5.1, we aim to maintain a balance between multiple options and hard-line decisions about what is and is not supported. If there are notable omissions or problems that the researcher identifies, then we solicit your input, both in words and code, to expand the utility and integrity of the code.

Given this invitation for contributions, note that we aim to maintain a sound sense of modularity whereby added code minimally interacts with other parts of the code. Notably, any added code must first pass the tests posed by the various MOM4 test cases described in Section 2.9. Finally, patience with your contributions is greatly appreciated, as the authors of this guide, who represent the core MOM developers, are scientists also trying to use MOM4 to address fundamental ocean climate questions.

1.7.2 Algorithm development at GFDL starting from mom4

Differences within models of the same vertical coordinate can be large, depending on details of numerics, physics, and forcing. The climate modeling community needs to clarify these differences and to reduce modeling artefacts based on outdated assumptions and methods. Additionally, it is crucial that future model development reduce computational barriers between different models, so that modelers can easily test different approaches and run different models. That is, it should be trivial for anyone familiar with one model, regardless the vertical coordinate, to run any other model.

Anthough difficult to predict with certainty, it is anticipated that long term MOM development will focus on a generalized vertical coordinate model with a likely move to the Arakawa C-grid. The trend towards generalized vertical coordinates, though motivated theoretically, may be frought with unforeseen practical difficulties tempering the theoretical arguments. Hence, it is necessary to garner the state-of-the-art within each model framework to gauge progress with the more sophisticated generalized models. This mandate motivates our development with the z-coordinate MOM4.

Here, we identify some near-term development paths that are being investigated at GFDL, starting from MOM4. These paths represents steps along the way towards more thorough generalized vertical coordinate capabilities. Much of the near-term development will occur in collaboration with researchers at MIT.

- The leap-frog time stepping scheme has been the traditional approach for time stepping the inviscid dynamics in MOM. Much of the code structure assumes the leap-frog scheme, and such restricts ones ability to investigate the utility of alternative approaches. The main problem with the leap-frog scheme, at least for climate uses, is the inability to construct a discretely exact conservation principle for tracers (e.g., Griffies et al. (2001) and Chapter 7). This scheme can also exhibit substantial time-domain noise, even when using the Robert-Asselin filter. Future development aims to remove the fundamental nature of the three-time level leap-frog scheme in MOM, so to allow testing of alternative methods.

- MOM has always been discretized using a B-grid. With grid resolution increasing, there are arguably some reasons for using the C-grid. In particular, the C-grid provides far more flexibility in representing the complex topography/geometry of an ocean basin since it allows for flow through single tracer grid point channels. Work is planned to allow future GFDL models to use either the B or C grids.

- MOM has always been a z-coordinate model. Recent advances based on the isomorphism between depth and pressure suggest that minimal changes to the dynamical kernal are needed to use sigma, eta, or pressure as the vertical coordinate (e.g., Marshall et al. (2003) and Losch et al. (2003)). Such work is planned for future development.

1.7.3 Concerning a committment to model development

Ocean climate models are not conceived one year, to be then publicly released and supported the next. Instead, they take years of creative passion, with a near infinite amount of obsession to details, from numbers of people. Even to move from MOM3 to MOM4, a move that did not involve fundamental numerical or physical algorithm changes, took roughly four to five years of steady research and development.

It is only through patience and persistence that an ocean model is successfully taken from its initial vision phase, to its prototype phase, and then onto its public release phase. Furthermore, public release in no way represents the final step. Indeed, it is perhaps the most difficult step as it exposes the previously insular model code to the critical eyes of multiple researchers with numerous needs and experiences.

In short, the construction of an ocean model requires a marriage of research with development, with each phase requiring an unpredictable amount of time to debate and explore various avenues. Allowing such time requires dedication and support from funding agencies and managers. In its absence, ocean model development is handicapped and the integrity of the simulations compromised. NOAA and GFDL have provided dedication and support for long-term research and development in the past. Continuance is necessary as we embark upon model development projects into the 21st century thus taking us far beyond MOM4.

CHAPTER

TWO

MOM4 QuickStart Guide

Contents

The purpose of this chapter is to detail some computational aspects of MOM4.0. It is meant to be a quick-start guide for those wishing minimal conceptual details but instead wish to start running the model code as quickly as possible.

2.1 Derived types used in MOM4.0

As discussed in Section 1.5.3.2, MOM4.0 makes use of Fortran90 derived type structures. In particular, the code is organized around several derived types that combine logically related fields. Top-level ocean interfaces accept the following derived types:

- *grid_type* - grid locations, distances, metric terms and coriolis factors
- *domain_type* - local and global indices, mpp_domains flags and domain2d type.

- *time_type* - timestep counter, initial time, current time and time level indices.
- *advective_velocity_type* - horizontal and vertical advective velocities for tracers and momentum.
- *velocity_type* - horizonal velocity and density weighted velocity for non-boussinesq calculations.
- *tracer_prog_type* - tracer concentration, surface and bottom fluxes and tracer metadata including name and units. These are tracers that evolve via the tracer equation.
- *tracer_diag_type* - tracer concentration and tracer metadata including name and units. These are tracers that are diagnosed and so possess only a single time level.
- *external_mode_type* - quantities related to the external mode, including surface height and height tendency and freesurface forcing.
- *density_type* - density quantities, including in-situ pressure and non-boussinesq quantities.
- *ocean_data_type* - Surface quantities for communication with fms coupler.
- *ice_ocean_boundary_type* - surface flux quantities returned from the coupler.

Objects that are not contained in derived types include certain fields not associated with the ocean model as well as certain constants. Time independent objects not contained in a derived type can be accessed by a module via the "use only" statement. Time dependent objects are generally passed through subroutine interfaces. Maintaining this philosophy has reduced the head-aches associated with F90 predessor cycles (i.e., self-referential loops).

2.2 Code organization

We provide here the general flow of mom4.0 where we assume use of the generalaized coupler to drive the model. When using this coupler, the ocean model is run as one of any number of component models, even when the component models are null or dummy models. Using the coupler, even for simplified ocean-only experiments, can be a useful way to familiarize oneself with how to run a coupled model, and so it is recommended that one use the coupler when feasible. However, for those cases with idealized boundary conditions, it may be desirable to focus just on the ocean relevant issues. For this case, the driver ocean_solo.F90 can be used instead. This module is quite similar to the coupler, but omits some of the unnecessary calls. Use of ocean_solo.F90 may also be warranted when one has an alternative coupler to use, such as one arising from the European PRISM effort.

Note that the following list of steps may be a bit out of date due to the introduction of some added physics modules subsequent to the writing of this document. Regardless, the general ideas are relevant and should give the reader an overall sense for the code flow.

```
Coupler_main (driver)

   +initialize fms infrastructure
   +initialize component models (atmos/ice/land/ocean)
   +initialize flux exchange grid
   +begin coupled loop
     + calculate flux from ocean to ice
     + udpate ice surface for atmospheric fast physics
     + time-step atmos/ice/land on ‘‘fast’’ physics timestep
       and perform boundary layer computations
     + update ‘‘slow’’ ice and land processes (dynamics, transport, mass)
     + calculate flux between ice/ocean
     + timestep ocean (update_ocean_model)
         ++derive flux quantities for ocean (ocean_sfc_mod:get_ocean_fluxes)
         ++calculate restoring fluxes or adjustments (ocean_sbc_mod:flux_adjust)
         ++calculate bottom boundary fluxes
           (ocean_bbc_mod:get_ocean_bbc)
         ++calculate ocean density quantities
           (ocean_density_mod:update_ocean_density)
         ++calculate ocean advection fields
           (ocean_advection_velocity_mod:ocean_advection_velocity)
         ++calculate surface height tendency
           (ocean_freesurf_mod:surface_height_tendency)
         ++calculate vertical mixing coefficients
           (ocean_vert_mix_coeff_mod:vertical_mix_coeff)
         ++calculate thickness weighted tracer source from neutral physics
           (ocean_neutral_physics_mod:neutral_physics)
           add update vertical diffusion coefficient
         ++calculate thickness weighted temperature tendency from shortwave
           (ocean_shortwave_pen_mod:sw_source)
         ++calculate tracer tendency due to sponges
           (ocean_sponge_mod:sponge_tracer_source)
         ++calculate thickness weighted tracer tendency from cross-land mixing
           (ocean_xlandmix_mod:xlandmix)
         ++calculate thickness weighted tracer tendency due to river discharge
           (ocean_rivermix_mod:rivermix)
         ++calculate thickness weighted tracer tendency due to sigma diffusion
           (ocean_sigma_diffuse_mod:sigma_diffusion)
         ++update tracer(ocean_tracer_mod:update_ocean_tracer)
         ++calculate polarfiltered version of tracers
           (polar_filter_tracers_mod:polar_filter_tracers)
         ++calculate anomalous density using updated tracer
           (ocean_density_mod:calc_rho_tilde)
         ++calculate density-weighted velocity
           (for non-boussinesq - ocean_velocity_mod:calc_u_rho)
         ++calculate acceleration terms handled explicitly in time
           (ocean_velocity_mod:ocean_explicit_accel)
```

```
        ++calculate acceleration of top layer due to freesurface
          effects(ocean_freesurf_mod:ocean_freesurf_drag)
        ++calculate frictional terms handled implicitly in time
          (ocean_velocity_mod:ocean_implicit_accel)
        ++calculate forcing for freesurface based on baroclinic field
         (ocean_freesurf_mod:ocean_freesurf_forcing)
        ++calculate acceleration terms handled explicitly in time
          (ocean_velocity_mod:ocean_explicit_accel)
        ++calculate Coriolis term handled implicitly in time
          (ocean_velocity_mod:ocean_implicit_coriolis)
        ++update freesurface (replace vertical mean -
          ocean_freesurf_mod:update_ocean_freesurf)
        ++update velocity
         (ocean_velocity_mod:update_ocean_velocity)
        ++compute energetic diagnostics
         (ocean_velocity_mod:energy_analysis)
        ++compute remaining ocean diagnostics
         (ocean_diagnostics_mod:ocean_diagnostics)
        ++apply robert time filter
        ++update top-level thickness
        ++fill boundaries
++perform data assimilation
        ++return ocean surface properties to coupler
         (ocean_sfc_mod:get_ocean_sfc)
 +end coupled loop
```

2.3 How boundary conditions are handled

A major difference in MOM4 compared with previous releases is the availability of a coupler for exchanging fluxes with other component models. Atmosphere, ice and land component models developed at GFDL with interfaces to the coupler are made available publicly. Within the coupling framework, all fluxes to the ocean are routed through the ice component model. The fluxes are made available to mom4.0 via the derived type *ice_ocean_boundary_type*. The boundary field components are as follows:

```
Ice_ocean_boundary%sw_flux : Net downward shortwave flux (Watts/m^2)
Ice_ocean_boundary%lw_flux : Net downward longwave flux (Watts/m^2)
Ice_ocean_boundary%fprec   : frozen precipitation (kg/m^2/sec)
Ice_ocean_boundary%lprec   : liquid precipitation (kg/m^2/sec)
Ice_ocean_boundary%calving : frozen runoff to ocean (kg/m^2/sec)
Ice_ocean_boundary%t_flux  : upward sensible heat flux (Watts/m^2)
Ice_ocean_boundary%q_flux  : upward specific humidity flux (kg/m^2/sec)
Ice_ocean_bounrary%salt_flux : upward salt flux( kg/m^2/sec)
Ice_ocean_boundary%runoff  : liquid runoff to ocean (kg/m^2/sec)
Ice_ocean_boundary%u_flux  : zonal momentum flux to ocean (N/m^2)
Ice_ocean_boundary%v_flux  : meridional momentum flux to ocean (N/m^2)
Ice_ocean_boundary%p       : pressure of overlying ice and atmosphere (N/m^2)
```

In order to use the coupler (coupler/coupler_main.f90), boundaries of the ocean-atmosphere-ice-land grid cells must be supplied. This information is used to define an "exchange grid" for conservative exchange of fluxes. The exchange grid represents the union of the component model grids. Exchange grid information is calculated prior to running the model. This step involves executing the *make_xgrids* command.

At runtime, the atmosphere, ice, land, and/or ocean component models can be disabled through namelist flags *coupler_nml: do_atmos, do_ice, do_land, do_ocean*. The component boundary fields keep their initial values, or may be overridden with data from a specified NetCDF file. This information is provided through the *data_override_table*. For instance, the windstress to the ocean (from the ice model) can be overridden with data from a climatological file with the following table entry:

```
"OCN", "u_flux", "taux" , "INPUT/ssmi_tau.nc",-1,-1,-1.e10,.false.,1
"OCN", "v_flux", "tauy" , "INPUT/ssmi_tau.nc",-1,-1,-1.e10,.false.,1


‘‘OCN’’ - identifies the target component model
‘‘u_flux’’ - corresponds to the name of the boundary field
‘‘taux’’ - is the name of the field as it exists in the NetCDF data file
‘‘INPUT/ssmi_tau.nc’’ - is the name of the file containing the winds
‘‘-1’’ - not used
‘‘-1’’ - not used
‘‘-1.e10’’ - constant value (-1.e10 is a flag to use the data from the file)
‘‘.false.’’ - data is on the target grid (true) or off-grid(false)
‘‘1.0’’ - scale factor
```

Alternatively, the ocean model can be run in stand-alone mode using the stand-alone driver (mom4/drivers/ocean_solo.F90). Boundary fields are inserted into the ice_ocean_boundary field using data_override table entries in an identical fashion to the coupled model. The stand-alone option does not require execution of *make_xgrids* and is appropriate for limited domain ocean configurations or more idealized experiments.

2.4 Grid and topography generation

The *grid_spec.nc* file is fundamental to the running of a model within FMS. This file contains information about the horizontal and vertical grid spacings in the model as well as the land/sea mask. We require this file to subsequently create initial and boundary conditions for the ocean model experiment. When running a coupled model, *grid_spec.nc* also contains information about the exchange grid (as garnered by running *make_xgrids* subsequent to generating the grid for the ocean-alone).

There are various options available for generating the ocean grid specification file. For example, a global grid can be spherical or tripolar, and there are options available for changing the resolution within regions such as the tropics. The topography mask can be generated from an idealized function, or re-mapped from another topography file such as from a dataset. All of these options, and more, are spelled out in the preprocessing directory

```
src/preprocessing/generate_grids/ocean
```

The development of a topography file to be used in a particular ocean model experiment generally requires a great deal of effort. The reason is that it is difficult to provide an objective specification of the topography on an ocean model grid which includes all the essential details about straights and throughflows. The case of Panama is a good example, where an objective specification of a global 4-degree grid often results in a disconnected North and South America, which clearly is unacceptable for a realistic simulation of modern ocean circulation. Hence, some manner of tuning is inevitable.

Topography tuning is as much an art as there comes in ocean modeling, and it typically requires lots of experience and testing. The sensitivity of the solution to topography details is also quite dependent on model subgrid-scale parameters, such as viscosity. One tool that was developed at GFDL for use in organizing hand-edits to the topography file is the *edit_grid* module contained in

```
src/preprocessing/generate_grids/ocean
```

An ASCII file containing index, depth pairs is prepared. *edit_grid* makes the necessary modifications and outputs to a separate grid specification file. Again, refer to the script and code for this module to garner full details for the usage.

edit_grid ASCII file format

```
i_index[:i_index2], j_index[:j_index2], depth
...
```

2.5 Initial conditions and boundary conditions

Initial condition fields can be created in two manners. First, there are various idealized initial conditions (e.g., global constant, zonal averaged Levitus) which can be created for a particular grid specification file. Second, there are more realistic initial conditions which are obtained by regridding an analyzed product, such as that from Levitus (1982), onto the model grid. The first capability is provided by files in

```
src/preprocessing/mom4_prep/idealized_ic
```

The regridding capability is provided by code in

```
src/preprocessing/regrid_3d
```

Notably, the regrid option can take a dataset that is originally gridded on a spherical grid and regrid it to either a spherical ocean model grid, or to a tripolar ocean model grid. Either form of the regridding uses a nearest neighbor approach.

As with initial conditions, it is necessary to setup boundary conditions on the particular model grid (defined by the *grid_spec.nc* file) used to run the experiment. Boundary conditions can be either idealized, with code available in

`src/preprocessing/mom4_prep/idealized_ic`

or taken from some dataset and regridded to the model grid, as done using files in

`src/preprocessing/regrid_2d`

The scripts and code are very similar to those used for the initial conditions, and detailed documentation is provided in the code and scripts.

Note that when running a model using realistic boundary forcing, it is not necessary to perform the *regrid_2d* step. An alternative is to leave the dataset on its native grid and perform the regrid each time step of the model run. This is the procedure for running a coupled model when the atmospheric grid differs from the ocean. When the data has been regridded prior to running the ocean model, as may be appropriate for an ocean-only run, then the "ongrid" flag can be set .true. in the data_override_table, when running with the FMS coupler. Otherwise, the data can reside on an arbitrary spherical grid which covers the ocean domain, in which case "ongrid" is set false in the data_override_table.

Interior tracer restoring (or sponges) are generated exactly the same way as initial conditions, using regrid_3d.pl. An additional NetCDF file containing the damping timescale for the tracers should be generated as well. This can be accomplished with an analysis package such as Ferret.

NOTE: missing values (such as land points) should be removed from the datasets before using the regrid_2d and regrid_3d codes, or data_override. Ferret provides tools for removing missing values.

2.6 Static memory for optimizing on SGI machines

Fundamental to the FMS design philosophy is the desire to maximize flexibility of code. This approach has its benefits in allowing for minimal spin-up time for users to use FMS tools for productive research. Consistent with this philosophy is the use of dynamic memory allocation as the default in mom4.0 and other FMS component models. Dynamic memory allocation means that the model does not know the size of the arrays until specified at runtime via the input of the grid-spec file and the tables setting the number of tracers. Hence, with the same executable, the user can change the processor domain decomposition, model grid, and number of tracers. This flexibility has been found to be quite useful for development purposes, adding tracers at an intermediate point in an experiment, and running ensembles of experiments.

Experience at other research institutions have indicated that dynamic memory allocation can come with the price of relatively poor performance. Experience at GFDL with SGI Origin machines are consistent with this experience. However, it is not fully clear where the problem lives. Preliminary suggestions point to a feature that slows down code employing array syntax, especially array syntax involving derived type fields. However, tests moving from mom4-beta2 to mom4.0 are ambiguous, since mom4-beta2 did not use derived types whereas mom4.0 uses them extensively, and no significant efficiency difference was noted between the two codes. Whether it is a compiler bug or not, SGI is presently investigating this

issue which will hopefully be resolved in the near-future. Furthermore, it is not known whether other machines share this bug.

In the meantime, mom4.0 is provided with a static memory allocation option implemented via the cpp-preprocessor compiler option *STATIC_MEMORY*. Static allocations mean that the memory requirements for the model are specified at compile time. Tests with mom4.0 on the GFDL SGI Origin machines result in an approximately 2x performance enhancement. Use of the *STATIC_MEMORY* cpp-preprocessor option in mom4.0 requires the model domain decomposition and model grid size to be specified at compile time. Furthermore, the resulting processor domain decomposed grid must have an identical number of computational grid points for each processor domain. This constraint restricts ones ability to arbitrarily decompose the grid across processors. It is important to keep this point in mind when developing the grid for an experiment. For example, use of a prime number of grid points severely limits the domain decomposition possibilities available for the experiment.

Although grid information at compile time is needed, we do not need to specify the number of prognostic and diagnostic tracers at compile time. This is due to the treatment of tracers through the FMS *field_manager*, where tracer information is read in via tables.

An example of a compiler option for a model with 180 points in the i-direction, 174 points in the j-direction, 50 vertical levels, and running on 6×6 processors is the following:

```
set cppDefs = ( "-Duse_netCDF -Duse_libMPI -DSTATIC_MEMORY -DNI_=180
 -DNJ_=174 -DNK_=50 -DNI_LOCAL_=30 -DNJ_LOCAL_=29" )
```

2.7 SHMEM versus MPI

MOM4 can be compiled and run using either MPI or SHMEM. For an MPI compilation, we add

```
 -Duse_libMPI
```

the cppDefs as shown above. For SHMEM, we have

```
set cppDefs = ( "-Duse_netCDF -Duse_libSMA -DSTATIC_MEMORY -DNI_=180
 -DNJ_=174 -DNK_=50 -DNI_LOCAL_=30 -DNJ_LOCAL_=29" )
```

On the SGI Origin at GFDL, SHMEM is more efficient than MPI. When running MOM4, the answers obtained with MPI agree at the bit-level to those obtained with SHMEM.

2.8 MOM4 printout

MOM4.0 generates ascii output that is sent to the Fortran units *stdout* and *stdlog*. *stdlog* contains information about the module version being employed as well as the namelist settings for the module. This information is crucial for those wishing to reproduce experimental results at later dates, where code or parameter settings

may have been changed in the interim. All FMS modules write this information to *stdlog*.

For the ocean model, namelist information is also written to *stdout*. In addition, *stdout* contains various quality control statements highlighting what the model is using, as well as warnings to indicate possible conflicts. MOM4.0 has a wide array of options, and it is important that such verbosity be employed to communicate to the user what the model is doing. Correspondingly, it is strongly encouraged that the user frequently read printout files to ensure that the model is running in a physically relevant manner. If users have suggestions for clearer or more complete output statements, please provide such to the MOM4.0 developers.

2.9 Test cases

MOM4 is distributed with test cases. The test cases serve many purposes for both the developers and researchers using the code. Details of the test cases can be found in the runscripts and README files distributed with the code. The first test case is a flat bottom sector model with solid walls. Similar models have been used for idealized studies of thermohaline circulation variability. The second test case is a global model whose grid is based on spherical coordinates. The third test case is a global model whose grid is based on the Murray (1996) tripolar grid described in Chapter 4. No polar filter is used for this test case since the polar singularity has been removed from the ocean. The fourth test case couples the ocean to the GFDL Sea Ice Simulator (SIS) model. The fifth test case is a channel model that tests the open boundary condition.

2.9.1 Purposes of the test cases

Importantly, MOM4 test cases are not sanctioned for physical integrity. Let us be clear on this statement:

MOM4 TESTS ARE NOT SANCTIONED
FOR THEIR PHYSICAL INTEGRITY!

Instead, tests are distributed for the following reasons:

- To illustrate how to set up and run an experiment.
- To verify that the model solution is independent of the number of processors and whether a restart occurred or not.
- To computationally exercise certain parts of the code, such as domain topologies, physical parameterizations, and numerical methods. That is, to provide the researcher with a sense for the baseline numerical/computational behaviour of the code.
- Those wishing to contribute new code to the main branch of mom4 should document how the test cases are affected. If appropriate, a new test case should be constructed exercising the new algorithm.

There has been minimal tuning involved in the construction of test cases. Hence, the researcher should not consider a test case as an "off the shelf model configuration" appropriate for conducting relevant and publishable research. Indeed, there is no guarantee that the test cases will run for an indefinite period of time. Providing full support for "off the shelf" configurations is, unfortunately, beyond the abilities of the MOM team. Given these caveats, the test cases nonetheless can provide a useful starting point for the researcher who wishes to build models addressing particular research questions.

2.9.2 Namelists

A particular experiment is defined by its grid, forcing, physics, and dynamics. Much of the experimental details are specified by namelist settings. Namelists allow one to modify many of the experiment details while using the same executable, and so not requiring a new compilation. This approach, introduced in MOM1, greatly enhances the model flexibility and usability.

A complete listing of the namelist parameters available for a module can be found via the associated html documentation provided with each module. Reading the fortran source code is also, clearly, a way to understand what is available.

2.10 Reproducibility across processors and restarts

Simulations conducted on multiple processors should not be a function of the number of processors. In addition, answers should not depend on whether the model is run with static or dyanamic memory allocation. To verify that answers are identical requires one to simply run the model on various numbers of processor elements (PEs), and the results must be bit-wise exactly the same. Analogously, models running for a time period X on N_a PEs should agree bitwise to models running a time $X/2$ on N_b PEs plus $X/2$ on N_c PEs. The second check is more encompassing since it tests both the integrity of the code used to start and stop the model (i.e., restarts), as well as the internal functioning of the model's algorithms in a parallel computational environment.

2.10.1 Testing for reproducibility

There are two basic ways to test that answers reproduce across PEs. The first is to do a binary comparison of the restarts produced at the end of runs realized on different PEs. A second way is to examine the "ending checksums" printed at the bottom of the MOM4 printout file (the file produced from stdout). This checksum will exhibit differences when there is a bug. The preferred method for checking reproducibility is the checksum approach. The reason is that for some processor counts, we have found that the number "0" within a restart file can be translated into the equivalent "-0". Doing a binary difference of the restart files can then lead to the misconception that there is a significant difference. In these cases, the checksums written to the prinout files will remain identical to the bit. The problem with plus/minus zero in the restart files remains under investigation. Again, it is of no consequence to the ability of the stdout checksums to reproduce.

Bit-wise reproducibility is often a computationally expensive means of computing. Hence, forcing the model to exhibit such reproducibility for all numerical diagnostics may be prohibitively expensive on some platforms. Therefore, some diagnostics (e.g., energetics) printed to stdout will not agree to the bit, and so cannot be used to verify reproducibility across PE counts. Other diagnostics, such as single time step diagnostics for tracers, are bitwise reproducible and can therefore be used to verify the model is properly reproducing.

2.10.2 Reproducibility between static and dynamic allocation

Reproducibility across PEs, across restarts, and between static/dynamic memory allocation are important constraints that generally must be maintained in order for the code's integrity to remain solid. All test cases run on the GFDL SGI Origin machine satisfy these constraints.

However, maintaining a bit-wise agreement between static and dynamic arrays on other machines, such as a Beowulf cluster at GFDL, has been found difficult to achieve. Based on the bit-wise agreement found on the SGI Origin, we believe there is no bug in the code. Instead, we speculate that some compilers may not allow for bit-wise agreement when changing the way memory is allocated. Note that the motivation for using static allocation is far less when running on the Beowulf, since timing differences are much smaller than on the SGI Origin.

In general, we hope to resolve the static and dynamic differences in efficiency found on SGI machines, both by working with compiler writers and modifying certain FMS code algorithms. If we succeed, we plan to remove the static option in the near future.

Part II

Fundamentals of MOM4

FUNDAMENTALS OF MOM4

The purpose of this part of the MOM4 Guide is to provide some grounding in the fundamental physical, mathematical, and numerical aspects of MOM4. There are many topics omitted here, with the book by Griffies (2004) suggested for those wishing to understand fundamentals underlying ocean climate models. Nonetheless, there are many details outlined in this part of the MOM4 Guide that are useful to those wishing to understand certain details of the model's algorithms.

CHAPTER

THREE

Ocean primitive equations

Contents

This chapter presents a summary of the ocean primitive equations. We also describe their ensemble mean form discretized in MOM4. Full details are provided by Griffies (2004).

3.1 Orthogonal coordinates and the Traditional Approximation

The ocean primitive equations are based on taking the *Traditional Approximation* to the Navier-Stokes equations. This approximation represents a statement about the spherical geometry on which fluid parcels move. We summarize here some key mathematical results of use in the following.

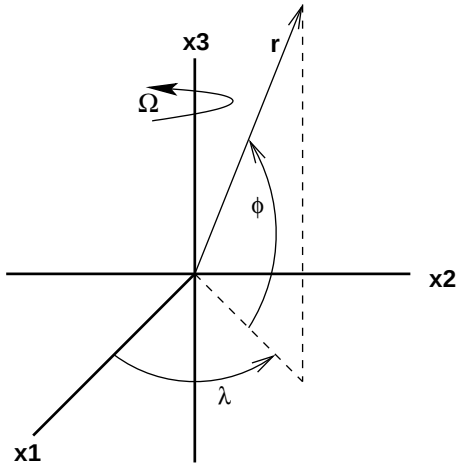

Figure 3.1: A schematic of the coordinates used for describing fluid dynamics on a rotating sphere, where the rotation axis is aligned through the north pole of the sphere. The coordinate $0 \leq \lambda \leq 2\pi$ is the longitude, with positive values measured eastward from Greenwich, England. The coordinate ϕ is the latitude, with values $\phi = 0$ at the equator and $\phi = \pi/2(-\pi/2)$ at the north (south) poles. The radial distance r is measured here with respect to the center of the sphere. The explicit coordinate transformations are $x^1 = r \cos\phi \cos\lambda$, $x^2 = r \cos\phi \sin\lambda$, and $x^3 = r \sin\phi$. Note that for many idealized geophysical fluid studies, *cartesian* coordinates refer to those defined locally to a tangent plane at some point on the surface of the rotating sphere. Such β-plane or f-plane coordinates (e.g., Gill (1982); Pedlosky (1987)) are distinct from the cartesian coordinates defined here.

3.1.1 Spherical and Cartesian coordinates

The World Ocean forms a thin layer of fluid moving on the rotating earth. For purposes of ocean climate modeling, it is sufficient to approximate the earth as a sphere (see Veronis (1973) for a discussion). Such constitutes a fundamental distinction from non-geophysical fluid mechanics formulations of the equations of motion (e.g., Landau and Lifshitz (1987)), where the equations are typically derived in 3D Euclidean space. A rigorous and lucid treatment of fluid motion on arbitrary surfaces is given by Aris (1962).

Figure 3.1 provides a schematic illustrating the relation between spherical and Cartesian coordinates of use for describing fluid dynamics on a rotating sphere. The axis of rotation passes from the southern pole to the northern pole of the sphere. Both sets of coordinates are fixed on the rotating sphere (non-inertial coordinates). In the next subsection, we note that MOM4 generalizes the angular coordinates (λ, ϕ) to allow arbitrary locally orthogonal coordinates to specify angular positions on the sphere.

3.1.2 Elements of horizontal orthogonal coordinates

MOM4 is written in generalized horizontal coordinates, where *horizontal* means coordinates within a locally defined tangent plane on the surface of a spherical

earth (see Figure 3.1). The use of orthogonal curvilinear coordinates (ξ^1, ξ^2) allows for the squared infinitesimal distance between two points in the ocean to be written as

$$(ds)^2 = (h_1\, d\xi^1)^2 + (h_2\, d\xi^2)^2 + dz^2, \tag{3.1}$$

where the metric, or stretching functions, h_1 and h_2 are non-negative. In terms of the dimensionful *physical* horizontal distances

$$dx = h_1\, d\xi^1 \tag{3.2}$$
$$dy = h_2\, d\xi^2, \tag{3.3}$$

the line element takes the compact form

$$(ds)^2 = (dx)^2 + (dy)^2 + (dz)^2, \tag{3.4}$$

the volume of an infinitesimal Eulerian region of the ocean is given by

$$dV = (h_1\, d\xi^1)\,(h_2\, d\xi^2)\, dz = dx\, dy\, dz, \tag{3.5}$$

and the physical components of the horizontal partial derivatives are

$$\partial_x = h_1^{-1}\, \partial_1 \tag{3.6}$$
$$\partial_y = h_2^{-1}\, \partial_2. \tag{3.7}$$

Figure 3.2 illustrates these formulae. Notably, although the introduction of physical displacements brings the metric tensor into a form analogous to that for 3D-Euclidean space, the non-Euclidean nature of the sphere manifests by the non-vanishing commutator

$$\left[\partial_x, \partial_y\right] = \partial_x\, \partial_y - \partial_y\, \partial_x = (\partial_x \ln dy)\, \partial_y - (\partial_y \ln dx)\, \partial_x, \tag{3.8}$$

which vanishes only when the horizontal geometry is flat instead of curved. In particular, the use of spherical coordinates leads to

$$\left[\partial_x, \partial_y\right] = \left(\frac{\tan\phi}{R}\right) \partial_x. \tag{3.9}$$

3.1.3 Geometry of the Traditional Approximation

The Traditional Approximation assumes that the metric functions h_1 and h_2 are dependent *only* on the horizontal coordinates (ξ^1, ξ^2). Radial dependence of the metric functions is reduced to a constant radial factor R, where

$$R = 6.371 \times 10^6\, \mathrm{m} \tag{3.10}$$

is the radius of a sphere with the same volume as the earth. Therefore, the distances used to compute partial derivatives, covariant derivatives, areas, and volumes are determined by a metric tensor whose components are functions only of the horizontal position on the sphere.

This geometric approximation is accurate for many purposes because the ocean forms a thin layer of fluid moving on the outer part of the earth. For example, vertical motions of fluid parcels in stratified regions of the World Ocean occur over distances of only a few centimeters to meters per day, which is far smaller than the earth's radius. For larger deviations, such as those occuring in convective regions, the Traditional Approximation may be less useful (see Marshall et al. (1997) for a discussion).

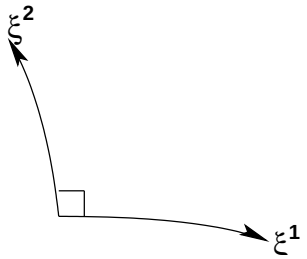

Figure 3.2: Illustrating the generalized horizontal orthogonal coordinates used in MOM4. The coordinate lines intersect at right angles, but generally do not follow lines parallel to constant longitude or latitude on the sphere. An infinitesimal horizontal region has area given by $dA = (h_1\, d\xi^1)\,(h_2\, d\xi^2) = dx\, dy$. For spherical coordinates $(\xi^1, \xi^2) = (\lambda, \phi)$, the infinitesimal horizontal distances are $dx = (r\, \cos\phi)\, d\lambda$ and $dy = r\, d\phi$.

3.2 Ocean primitive equations

The laws of classical physics, including Newtonian mechanics and linear irreversible thermodynamics, form a theoretical basis for a physical description of ocean dynamics. MOM4 also exploits the Traditional Approximation described in Section 3.1. Although previously fundamental to z-coordinate ocean models, MOM4 has eliminated the Boussinesq approximation using the methods of Greatbatch et al. (2001). A full accounting of how MOM4 discretizes a non-Boussinesq is given by Griffies (2004). The purpose of this section is to summarize these equations.

3.2.1 Kinematics, dynamics, and tracers

In fluid mechanics, mass conservation is associated with fluid kinematics, whereas momentum conservation constitutes the fluid dynamics. Mass conservation for a fluid parcel renders a relation between velocity and *in situ* density often known as the *continuity* equation

$$\rho_{,t} + \nabla \cdot (\rho\, \mathbf{v}) = 0. \tag{3.11}$$

Conservation of linear momentum for a fluid parcel leads to the prognostic equation for the velocity field

$$(\rho\, \mathbf{v})_{,t} + \nabla \cdot (\rho\, \mathbf{v}\, \mathbf{v}) = -\rho\, g\, \hat{\mathbf{z}} - (f + \mathcal{M})\, \hat{\mathbf{z}} \wedge \rho\, \mathbf{v} - \nabla p + \rho\, \mathbf{F}^{(\mathbf{v})}. \tag{3.12}$$

In these equations, ρ is the *in situ* density,

$$\mathbf{v} = (\mathbf{u}, w) \tag{3.13}$$

is the three-dimensional velocity field, p is the pressure field, and

$$\mathcal{M} = v\, \partial_x \ln dy - u\, \partial_y \ln dx \tag{3.14}$$

is the *advection metric frequency* arising from the non-Euclidean nature of the sphere. The friction vector $\mathbf{F}^{(\mathbf{v})}$ is associated with momentum transport due to molecular

viscosity.[1] Following the Traditional Approximation, we assume a hydrostatic balance for the vertical momentum equation, thus rendering

$$(\rho \mathbf{u})_{,t} + \nabla \cdot (\rho \mathbf{v} \mathbf{u}) = -(f + \mathcal{M}) \hat{\mathbf{z}} \wedge \rho \mathbf{u} - \nabla p + \rho \mathbf{F}^{(\mathbf{u})} \quad (3.15)$$

$$p_{,z} = -\rho g. \quad (3.16)$$

Coupled to the mass and momentum equations is the equation for conservation of tracers. There are three main ocean tracers: passive tracers, such as certain biological constituents, the active tracers temperature and salinity, and dynamical tracers such as potential vorticity. The terms *passive* and *active* refer to their influence on density, thus influencing dynamics through pressure. MOM4 time steps the equations for passive and active tracers, whose form is generally given by

$$(\rho T)_{,t} + \nabla \cdot (\rho T \mathbf{v}) = -\nabla \cdot (\rho \mathbf{F}) + \rho \mathcal{S}. \quad (3.17)$$

In this equation, T is the tracer mass per mass of water (i.e., the *tracer concentration*), The tracer flux $\mathbf{F}$ is interpreted as that arising from sub-grid-scale (SGS) molecular processes, such as molecular diffusion. It will be reinterpreted in terms of ensemble averages in Section 3.3. $\mathcal{S}$ is an interior tracer source term whose form depends on details of the particular tracer.

3.2.2 Boussinesq equations

The Boussinesq equations are recovered by setting $\rho \to \rho_o$ wherever it appears, except when multiplying gravity

$$\nabla \cdot \mathbf{v} = 0 \quad (3.18)$$

$$\mathbf{u}_{,t} + \nabla \cdot (\mathbf{v} \mathbf{u}) = -(f + \mathcal{M}) \hat{\mathbf{z}} \wedge \mathbf{u} - \nabla (p/\rho_o) + \mathbf{F}^{(\mathbf{u})} \quad (3.19)$$

$$p_{,z} = -\rho g \quad (3.20)$$

$$T_{,t} + \nabla \cdot (T \mathbf{v}) = -\nabla \cdot \mathbf{F} + \mathcal{S}. \quad (3.21)$$

The constraint $\nabla \cdot \mathbf{v} = 0$ means the Boussinesq fluid parcels conserve their volume instead of their mass.

3.2.3 Vertically integrated equations

To time step the dynamical equations, it is most efficient to separate the fast vertically integrated processes from the slower vertically dependent processes. For this purpose, we integrate the continuity equation over the full ocean column of thickness

$$D = H + \eta, \quad (3.22)$$

where $H = H(\xi^1, \xi^2)$ is the time independent ocean depth, and $\eta = \eta(\xi^1, \xi^2, t)$ is the time dependent deviation of the ocean surface from its resting state at $z = 0$. Assuming mass sources/sinks only at the ocean surface leads to the balance of mass per unit area within an ocean column

$$(\overline{\rho}^z D)_{,t} = -\rho_o \nabla \cdot \widetilde{\mathbf{U}} + \rho_w q_w \quad (3.23)$$

[1] Ensemble averaging (Section 3.3) introduces more substantial SGS processes associated with larger-scale turbulence, such as that occuring at the ocean's microscale to mesoscale ranges.

as well as the surface and bottom kinematic boundary conditions

$$\rho \left(\partial_t + \mathbf{u} \cdot \nabla \right) \eta = \rho_w \, q_w + \rho \, w \qquad \text{at } z = \eta \tag{3.24}$$

$$\mathbf{u} \cdot \nabla H + w = 0 \qquad \text{at } z = -H. \tag{3.25}$$

In these expressions,

$$\rho_o \, \widetilde{\mathbf{U}} = \int_{-H}^{\eta} dz \, \rho \, \mathbf{u} \tag{3.26}$$

is the depth integrated horizontal momentum density,

$$\overline{\rho}^z = D^{-1} \int_{-H}^{\eta} dz \, \rho \tag{3.27}$$

is the depth averaged density, ρ_o is a constant density set to

$$\rho_o = 1035 \, \text{kg/m}^3 \tag{3.28}$$

(see page 47 of Gill (1982)), and $\rho_w \, q_w$ is the mass per unit time per unit horizontal area of fresh water crossing the ocean surface.

To consider the time tendency for free surface height η, we expand the columnar mass balance (3.23) to reveal

$$\overline{\rho}^z \, \eta_{,t} = -\rho_o \, \nabla \cdot \widetilde{\mathbf{U}} + \rho_w \, q_w - D \, \partial_t \, \overline{\rho}^z. \tag{3.29}$$

Consequently, the ocean surface height is affected by three processes: convergence of vertically integrated momentum, mass entering through the ocean surface, and dilatations of the water column associated with changes in vertically integated density field (i.e., *steric effects*).

A similar analysis for a Boussinesq column of fluid, assuming volume sources/sinks only at the ocean surface, leads to the balance of volume per unit area within an ocean column

$$\eta_{,t} = -\nabla \cdot \mathbf{U} + q_w \tag{3.30}$$

as well as the surface and bottom kinematic boundary conditions

$$\left(\partial_t + \mathbf{u} \cdot \nabla \right) \eta = q_w + w \qquad \text{at } z = \eta \tag{3.31}$$

$$\mathbf{u} \cdot \nabla H + w = 0 \qquad \text{at } z = -H, \tag{3.32}$$

where

$$\mathbf{U} = \int_{-H}^{\eta} dz \, \mathbf{u} \tag{3.33}$$

is the depth integrated horizontal velocity field, and q_w is the volume per unit time per unit horizontal area of fresh water crossing the ocean surface. Notably, the surface height is affected only by convergence of vertically integrated momentum and surface fluxes of volume; steric effects are absent in Boussinesq fluid kinematics.

3.3 Ensemble averaged ocean primitive equations

The ocean is fundamentally turbulent. Given sensitive dependence on initial conditions, and the limitations of ocean measurements, it is not possible to obtain complete knowledge of the ocean state. Therefore, when formulating the ocean's governing equations, it is necessary to recognize our limited access to information.

3.3.1 Ensemble averages

A common way to account for incomplete information is to consider ensemble averages. As in statistical mechanics, ensemble averages are obtained by formally considering an infinite number of ocean states, each of which is described by the kinematic, dynamic, and tracer balances of Section 3.2. Our interpretation of ensemble averages directly associates the distance in phase space between members of an ensemble with the space-time scales that are not resolved by the "averaged observer." Assuming z-coordinates, we take ensemble averages at a fixed point in space-time (i.e., a single point Eulerian average), and note that they commute with all space-time derivatives and integrals.

Even though we specify averaging at a particular space-time point, there remain ambiguities in details of the averaging method. Different methods reveal different aspects of the averaged or mean dynamics, and deviations from the mean. *Density weighted averaging* plays a central role in our preferred method. Such averaging has recently become more commonplace in the ocean modeling literature (e.g., Smith (1999); McDougall et al. (2002); Lu (2001), yet it has long been part of the compressible fluids literature (e.g., Favre (1965) as noted in the footnote on pages 21-22 of Hinze (1975)).

3.3.2 Averaged kinematics independent of dynamical assumptions

There are two forms of fluid parcel kinematics of importance for ocean modeling: parcels conserving their volume and parcels conserving their mass. In general, parcel kinematic relations provide constraints on the fluid that are maintained regardless the dynamics. Therefore, we believe it to be key to the integrity and usability of the equations describing the ensemble averaged ocean, and consequently the ocean model, that kinematics of the averaged fluid remains independent of dynamical assumptions. In particular, we do not wish to require specification of unknown closure terms, whose form depends on dynamical details, in order to determine kinematic relations satisfied by the averaged ocean or the ocean model. Care in formulating and interpreting the averaged equations is required to maintain this very basic principle.

A key motivation for using density weighted averaging is that it assists in our desire to keep the averaged parcel kinematics independent of dynamical closure assumptions. Providing such a simple mapping between unaveraged and averaged kinematics generally does not require much thought when averaging the Boussinesq equations, since volume conservation $\nabla \cdot \mathbf{v} = 0$ is a linear constraint. Yet for non-Boussinesq equations, mass conservation $\rho_{,t} + \nabla \cdot (\mathbf{v}\, \rho) = 0$ is a nonlinear constraint, thus requiring extra consideration.

Besides the mathematical utility of the density weighed approach for the non-Boussinesq system, McDougall et al. (2002) argued for maintaining this average even when considering the averaged Boussinesq equations. Their reasoning is based on noting that the resulting Boussinesq system is far more accurate than the mean-field equations resulting from non-density weighted averages. In this context, accuracy is based on comparing with the small levels of diapycnal mixing in the ocean interior.

3.3.3 Linear momentum density

For the purpose of ensemble averaging, the linear momentum density (momentum per volume)

$$\rho \, \mathbf{v} = \rho_o \, \widetilde{\mathbf{v}} \tag{3.34}$$

plays a fundamental role. Hence, let us introduce it to the unaveraged balances from Section 3.2 to yield

$$\rho_{,t} + \rho_o \, \nabla \cdot \widetilde{\mathbf{v}} = 0 \tag{3.35}$$

$$\widetilde{\mathbf{v}}_{,t} + \nabla \cdot [(\rho_o/\rho) \, \widetilde{\mathbf{v}} \, \widetilde{\mathbf{v}}] + (\rho_o/\rho) \, \widetilde{\mathcal{M}} \, \hat{\mathbf{z}} \wedge \widetilde{\mathbf{v}} = -(\rho/\rho_o) \, g \, \hat{\mathbf{z}} - f \, \hat{\mathbf{z}} \wedge \widetilde{\mathbf{v}} - \nabla(p/\rho_o) + (\rho/\rho_o) \, \mathbf{F}^{(\mathbf{v})} \tag{3.36}$$

$$(\rho \, T)_{,t} + \rho_o \, \nabla \cdot (T \, \widetilde{\mathbf{v}}) = -\nabla \cdot (\rho \, \mathbf{F}) + \rho \, \mathcal{S}, \tag{3.37}$$

where we wrote the advection metric frequency as

$$\mathcal{M} = v \, \partial_x \ln dy - u \, \partial_y \ln dx = (\rho_o/\rho) \, (\widetilde{v} \, \partial_x \ln dy - \widetilde{u} \, \partial_y \ln dx) = (\rho_o/\rho) \, \widetilde{\mathcal{M}}. \tag{3.38}$$

3.3.4 Summary of the averaged equations

Details of the averaging process require more discussion that warranted here. We refer the reader to McDougall et al. (2002), Greatbatch et al. (2001), and Griffies (2004) for systematic development. For the present purposes, it is sufficient to summarize the results from Griffies (2004).

Using an angular bracket to signify ensemble mean, the averaged non-Boussinesq equations take the following form. First, mass conservation for a fluid parcel and for a vertical column of fluid is given by

$$\langle \rho \rangle_{,t} + \rho_o \, \nabla \cdot \langle \widetilde{\mathbf{v}} \rangle = 0 \tag{3.39}$$

$$\left(D^* \, \overline{\langle \rho \rangle}^z \right)_{,t} = -\rho_o \, \nabla \cdot \langle \widetilde{\mathbf{U}} \rangle + \rho_o \, \tilde{q}^*_w. \tag{3.40}$$

For the Boussinesq fluid, volume conservation for the parcel and column are given by

$$\nabla \cdot \langle \widetilde{\mathbf{v}} \rangle = 0 \tag{3.41}$$

$$\eta^*_{,t} = -\nabla \cdot \langle \widetilde{\mathbf{U}} \rangle + \tilde{q}^*_w. \tag{3.42}$$

In these equations, we introduced density weighted averages via

$$\langle \rho \rangle \langle \Psi \rangle^{\rho} = \langle \rho \, \Psi \rangle, \tag{3.43}$$

and the linear momentum density of fresh water

$$\rho_o \, \tilde{q}_w = \rho_w \, q_w. \tag{3.44}$$

A starred quantity represents a *modified mean field* given by an infinite series of ensemble mean correlations (Griffies (2004)). The precise relation between the starred quantities and the correlations is not important, since the modified mean fields provide the appropriate field to discretize in an ocean model, instead of the corresponding ensemble mean field.

The surface and bottom kinematic boundary conditions for the non-Boussinesq fluid are

$$\langle\rho\rangle\,\eta^*_{,t} + \rho_o\,\langle\widetilde{\mathbf{u}}\rangle\cdot\nabla\eta^* = \rho_o\,\langle\widetilde{w}\rangle + \rho_o\,\tilde{q}^*_w \qquad \text{at } z=\eta^* \tag{3.45}$$

$$\langle\widetilde{\mathbf{u}}\rangle\cdot\nabla H + \langle\widetilde{w}\rangle = 0 \qquad \text{at } z=-H \tag{3.46}$$

and for the Boussinesq fluid we have

$$\eta^*_{,t} + \langle\widetilde{\mathbf{u}}\rangle\cdot\nabla\eta^* = \langle\widetilde{w}\rangle + \tilde{q}^*_w \qquad \text{at } z=\eta^* \tag{3.47}$$

$$\langle\widetilde{\mathbf{u}}\rangle\cdot\nabla H + \langle\widetilde{w}\rangle = 0 \qquad \text{at } z=-H. \tag{3.48}$$

The tracer budget for the non-Boussinesq fluid is

$$(\langle\rho\rangle\,\langle T\rangle^\rho)_{,t} + \rho_o\,\nabla\cdot(\langle\widetilde{\mathbf{v}}\rangle\,\langle T\rangle^\rho) = -\rho_o\,\nabla\cdot\langle\tilde{\mathbf{F}}_{sgs}\rangle + \langle\rho\rangle\langle\mathcal{S}\rangle^\rho \tag{3.49}$$

and for the Boussinesq fluid

$$\partial_t\,\langle T\rangle^\rho + \nabla\cdot(\langle\widetilde{\mathbf{v}}\rangle\langle T\rangle^\rho) = -\nabla\cdot\langle\tilde{\mathbf{F}}_{sgs}\rangle + \langle\mathcal{S}\rangle^\rho. \tag{3.50}$$

Finally, the non-Boussinesq momentum budget is

$$\langle\widetilde{\mathbf{v}}\rangle_{,t} + \nabla\cdot(\langle\mathbf{v}\rangle^\rho\,\langle\widetilde{\mathbf{v}}\rangle) + \langle\widetilde{\mathcal{M}}\rangle\,\hat{\mathbf{z}}\wedge\langle\mathbf{v}\rangle^\rho = \\ -(\langle\rho\rangle/\rho_o)\,g\,\hat{\mathbf{z}} - f\,\hat{\mathbf{z}}\wedge\langle\widetilde{\mathbf{v}}\rangle - \nabla(\langle p\rangle/\rho_o) + \langle\tilde{\mathbf{F}}^{\mathbf{v}}_{sgs}\rangle \tag{3.51}$$

whereas the Boussinesq budget is

$$\langle\widetilde{\mathbf{v}}\rangle_{,t} + \nabla\cdot(\langle\widetilde{\mathbf{v}}\rangle\,\langle\widetilde{\mathbf{v}}\rangle) + \langle\widetilde{\mathcal{M}}\rangle\,\hat{\mathbf{z}}\wedge\langle\widetilde{\mathbf{v}}\rangle = \\ -(\langle\rho\rangle/\rho_o)\,g\,\hat{\mathbf{z}} - f\,\hat{\mathbf{z}}\wedge\langle\widetilde{\mathbf{v}}\rangle - \nabla(\langle p\rangle/\rho_o) + \langle\tilde{\mathbf{F}}^{\mathbf{v}}_{sgs}\rangle. \tag{3.52}$$

Recall that $\langle\widetilde{\mathbf{v}}\rangle = \langle\mathbf{v}\rangle^\rho$ for a Boussinesq fluid, whereas $\rho_o\,\langle\widetilde{\mathbf{v}}\rangle = \langle\rho\rangle\,\langle\mathbf{v}\rangle^\rho$ for the non-Boussinesq case. In the tracer equations, the SGS flux term is given by

$$\rho\,\mathbf{F}_{sgs} = \rho\,T'_\rho\,\mathbf{v}'_\rho \equiv \rho_o\,\tilde{\mathbf{F}}_{sgs}, \tag{3.53}$$

which dominates the contribution from molecular diffusion. The SGS friction vector $\tilde{\mathbf{F}}^{\mathbf{v}}_{sgs}$ likewise incorporates SGS turbulence terms

$$\rho\,\mathbf{F}^{(\mathbf{v})}_{sgs} = \nabla\cdot(\rho\,\mathbf{v}'_\rho\,\mathbf{v}'_\rho) + \hat{\mathbf{z}}\wedge\rho\,\mathcal{M}'_\rho\,\mathbf{v}'_\rho \equiv \rho_o\,\tilde{\mathbf{F}}^{(\mathbf{v})}_{sgs}. \tag{3.54}$$

The averaged equations have the same mathematical form as the unaveraged equations given in Section 3.2. Precisely, the mapping between unaveraged and averaged fields is given by

$$\rho \to \langle\rho\rangle \tag{3.55}$$

$$p \to \langle p\rangle \tag{3.56}$$

$$\mathbf{v} \to \langle\mathbf{v}\rangle^\rho \tag{3.57}$$

$$\widetilde{\mathbf{v}} \to \langle\widetilde{\mathbf{v}}\rangle \tag{3.58}$$

$$T \to \langle T\rangle^\rho \tag{3.59}$$

$$\tilde{\mathbf{F}} \to \langle\tilde{\mathbf{F}}_{sgs}\rangle \tag{3.60}$$

$$\mathcal{S} \to \langle\mathcal{S}\rangle^\rho \tag{3.61}$$

$$\tilde{\mathbf{F}}^{\mathbf{v}} \to \langle\tilde{\mathbf{F}}^{\mathbf{v}}_{sgs}\rangle \tag{3.62}$$

$$\eta \to \eta^* \tag{3.63}$$

$$q_w \to q^*_w. \tag{3.64}$$

$$\tilde{q}_w \to \tilde{q}^*_w. \tag{3.65}$$

This mapping is very useful for purposes of analyzing properties of the two systems, such as their energetic balances discussed in Chapter 6. The fewer equations we need to concern ourselves with, the better!

3.4 Mapping to ocean model variables

Having established a set of self-consistent averaged equations, we are ready to write down the equations to be discretized in the numerical model. The discretization is applied to the appropriate averaged continuous equations, which are written down in this section in a bit more tidy manner than in the previous section.

First, the density variable to be discretized by the ocean model is the Eulerian mean density

$$\langle \rho \rangle \rightarrow \rho_{\text{model}}. \tag{3.66}$$

Again, this is the *in situ* density used for the mass continuity equation. It is generally distinct from potential density. At this point the "model" suffix refers to the continuous ocean model, since no discretization has yet occured. Through the hydrostatic approximation, $\langle \rho \rangle \rightarrow \rho_{\text{model}}$ leads to

$$\langle p \rangle \rightarrow p_{\text{model}}. \tag{3.67}$$

As argued in Section 3.3.2, maintaining a tidy form of the averaged continuity equation motivates our discretizing $\langle \widetilde{\mathbf{v}} \rangle$, instead of the conventional $\langle \mathbf{v} \rangle$. The distinction is nontrivial for both non-Boussinesq and Boussinesq ocean models. Hence, we make the correspondence

$$\langle \widetilde{\mathbf{v}} \rangle \rightarrow \mathbf{v}_{\text{model}}. \tag{3.68}$$

Analogously, we choose to use $\langle T \rangle^{\rho}$ in our model, instead of the conventional $\langle T \rangle$

$$\langle T \rangle^{\rho} \rightarrow T_{\text{model}}. \tag{3.69}$$

Again, the distinction between $\langle T \rangle^{\rho}$ and $\langle T \rangle$ is nontrivial for both non-Boussinesq and Boussinesq ocean models. Finally, the surface height in the ocean model corresponds to the modified mean surface height η^*

$$\eta^* \rightarrow \eta_{\text{model}}, \tag{3.70}$$

as will the modified mean surface fresh water flux

$$\tilde{q}_w^* \rightarrow (q_w)_{\text{model}}. \tag{3.71}$$

These mappings lead to the following equations to be discretized in the non-Boussinesq ocean model (dropping the "model" subscript for brevity)

$$\rho_{,t} + \rho_o \nabla \cdot \mathbf{v} = 0 \tag{3.72}$$

$$(h \overline{\rho}^z)_{,t} = -\rho_o \nabla \cdot \mathbf{U} + \rho_o q_w \tag{3.73}$$

$$\mathbf{v}_{,t} + \nabla \cdot [(\rho_o/\rho) \mathbf{v} \mathbf{v}] + (\rho_o/\rho) \mathcal{M} \hat{\mathbf{z}} \wedge \mathbf{v} = - (\rho/\rho_o) g \hat{\mathbf{z}} - f \hat{\mathbf{z}} \wedge \mathbf{v} - \nabla(p/\rho_o) + (\rho/\rho_o) \mathbf{F}^{(\mathbf{v})} \tag{3.74}$$

$$(\rho T)_{,t} + \rho_o \nabla \cdot (\mathbf{v} T) = -\rho_o \nabla \cdot \mathbf{F} + \rho \mathcal{S}, \tag{3.75}$$

where we also made the correspondence

$$\langle \tilde{\mathbf{F}}_{sgs} \rangle \rightarrow \mathbf{F}_{\text{model}} \tag{3.76}$$
$$\langle \mathcal{S} \rangle^{\rho} \rightarrow \mathcal{S}_{\text{model}} \tag{3.77}$$
$$\langle \tilde{\mathbf{F}}^{\mathbf{v}}_{sgs} \rangle \rightarrow \mathbf{F}^{\mathbf{v}}_{\text{model}}. \tag{3.78}$$

These equations are combined with the surface and bottom kinematic boundary conditions

$$\rho\, \eta_{,t} + \rho_o\, \mathbf{u} \cdot \nabla \eta = \rho_o\, w + \rho_o\, q_w \qquad \text{at } z = \eta \tag{3.79}$$
$$\mathbf{u} \cdot \nabla H + w = 0 \qquad \text{at } z = -H. \tag{3.80}$$

The mapping from unaveraged to averaged fields, and then from averaged to model fields, is summarized in Table 3.1. This table is the key result from this chapter.

The continuous model equations presented above are *identical* in form to the continuous unaveraged non-Boussinesq equations summarized in Section 3.2. Although in the end somewhat trivial (i.e., what a round-about way to get back to the same equations!), the intermediate steps reveal a nontrivial interpretation of the fields discretized in the numerical model. It is hoped that such care in providing a precise physical and mathematical interpretation for the variables adds rigor and clarity to the foundations of MOM.

The Boussinesq model equations arise by setting $\rho_{\text{model}} \rightarrow \rho_o$, except when multiplying gravity. These equations are

$$\nabla \cdot \mathbf{v} = 0 \tag{3.81}$$
$$\eta_{,t} = -\nabla \cdot \mathbf{U} + q_w \tag{3.82}$$
$$\mathbf{v}_{,t} + \nabla \cdot (\mathbf{v}\,\mathbf{v}) + \mathcal{M}\, \hat{\mathbf{z}} \wedge \mathbf{v} = -(\rho/\rho_o)\, g\, \hat{\mathbf{z}} - f\, \hat{\mathbf{z}} \wedge \mathbf{v} - \nabla(p/\rho_o) + \mathbf{F}^{(\mathbf{v})} \tag{3.83}$$
$$T_{,t} + \nabla \cdot (\mathbf{v}\, T) = -\nabla \cdot \mathbf{F} + \mathcal{S} \tag{3.84}$$

along with the surface and bottom kinematic boundary conditions

$$\eta_{,t} + \mathbf{u} \cdot \nabla \eta = w + q_w \qquad \text{at } z = \eta \tag{3.85}$$
$$\mathbf{u} \cdot \nabla H + w = 0 \qquad \text{at } z = -H. \tag{3.86}$$

As emphasized by McDougall et al. (2002) and Greatbatch et al. (2001), upon making the hydrostatic approximation, these equations for the Boussinesq ocean model are identical to those integrated by the Boussinesq version of MOM, with the exception of details that have been absorbed by the turbulence tracer and momentum fluxes $\mathbf{F}$ and $\mathbf{F}^{\mathbf{v}}$. Additionally, McDougall et al. argue that the interpretation of model fields as proposed here allows for the Boussinesq equations to be far more accurate than the alternative interpretation. Hence, for this reason, and for reasons of mathematical elegance, we prefer the interpretation summarized by Table 3.1 for the variables carried by the Boussinesq and non-Boussinesq versions of MOM.

Unaveraged	Averaged	Model	Model Discrete
ρ	$\langle \rho \rangle$	ρ_{model}	ρ
p	$\langle p \rangle$	p_{model}	p
$\tilde{\mathbf{v}}$	$\langle \tilde{\mathbf{v}} \rangle$	$\mathbf{v}_{\text{model}}$	$\mathbf{v}$
$\mathbf{v}$	$\langle \mathbf{v} \rangle^{\rho}$	$\rho_{\text{model}}\, \mathbf{v}^{\rho}_{\text{model}} = \rho_o\, \mathbf{v}_{\text{model}}$	$\rho\, \mathbf{v}^{\rho} = \rho_o\, \mathbf{v}$
η	η^*	η_{model}	η
$\tilde{q}_w$	$\tilde{q}^*_w$	$(q_w)_{\text{model}}$	q_w
T	$\langle T \rangle^{\rho}$	T_{model}	T
$\mathcal{S}$	$\langle \mathcal{S} \rangle^{\rho}$	$\mathcal{S}_{\text{model}}$	$\mathcal{S}$
$\tilde{\mathbf{F}}$	$\langle \tilde{\mathbf{F}}_{sgs} \rangle$	$\mathbf{F}_{\text{model}}$	$\mathbf{F}$
$\tilde{\mathbf{F}}^{(\mathbf{v})}$	$\langle \tilde{\mathbf{F}}^{(\mathbf{v})}_{sgs} \rangle$	$\mathbf{F}^{(\mathbf{v})}_{\text{model}}$	$\mathbf{F}^{(\mathbf{v})}$

Table 3.1: Correspondence between unaveraged continuous fields, ensemble averaged continuous fields, continuous model fields, and discrete model fields.

CHAPTER

FOUR

Grids and halos

Contents

The purpose of this chapter is to detail the horizontal B-grid used in MOM4 as well as the specification of field and grid values in halo regions.

4.1 The B-grid used in MOM4

The continuum partial differential equations of MOM4 are derived and discussed in Griffies (2004). Semi-discrete versions of these equations are also discussed, where the equations are cast on an Arakawa B-grid. As summarized in the review article by Griffies et al. (2000a), the B-grid allows for a reasonably accurate representation of geostrophic currents even when running a coarse grid model. It was this property that motivated Bryan (1969) to choose the B-grid. Future model development,

in which the first baroclinic radius of deformation is assumed to be well resolved, will likely focus on the C-grid. The reasons are that the C-grid typically performs better at fine resolution than course, and it has some advantages over the B-grid when discretizing transport operators. Nonetheless, as pointed out by Webb et al. (1998), there will always be unresolved baroclinic modes, such as in the equatorial region. Hence, the B-grid may continue to have some advantage even at fine resolution.

The purpose of this section is to document the grid used in MOM4. In addition to the usual B-grid conventions, we describe grid factors used to build discrete derivative and integral operators. Chapter 16 of **The MOM3 Manual** Pacanowski and Griffies (1999) provides a complete discussion of the three slices $x - y$, $x - z$, and $y - z$. Although we briefly discuss the vertical grid, our main focus is on the horizontal $x - y$ plane since this is where details of domain decomposition on parallel computers is considered.

4.1.1 Variables on the B-grid

Figure 4.1 illustrates the horizontal arrangement of prognostic model fields used in MOM4's B-grid. The B-grid places both horizontal prognostic velocity components at the same point. MOM's convention is that this point lives at the "northeast corner" of the corresponding tracer cell, where northeast is in a generalized sense when using general orthogonal coordinates. With half-integer notation, the U-point lives at $(i + 1/2, j + 1/2)$ whereas the T-point is at (i, j). As density is a function of temperature, salinity, and pressure, density is naturally defined at the tracer point, as is hydrostatic pressure.

The vertical velocity component is defined according to the requirements of continuity across the tracer and velocity cells. Hence, this component lives at the bottom face of the corresponding cell. Once the horizontal grid placement is defined, the vertical position is specified for both the grid point and the vertical velocity position. Chapter 16 of **The MOM3 Manual** provides further details of the vertical grid.

4.1.2 Describing the horizontal grid

With a generalized horizontal grid, there are many grid distances required to compute discrete derivatives and integrals. When constructing the grid distances in MOM4, we aimed to design a structure useful for both B and C-grids.[1] It is with this goal in mind that the names for the grid distances in the *grid_generator* module are distinct from grid distances used in MOM4's grids module. We note the mapping between the two grid conventions in the following.

4.1.2.1 Four basic grid points and corresponding cells

On both the B and C grids, it is useful to consider the tracer cell as the basic cell, and all other cells in their relation to the tracer cell. Given this convention, there are four basic grid points and corresponding grid cells that can be identified: $T_{i,j}$, $E_{i,j}$, $C_{i,j}$,

[1] Other grids can also be accounted for using the conventions described here. Our focus is on the B and C grids, as these are the two most commonly used grids in ocean modeling.

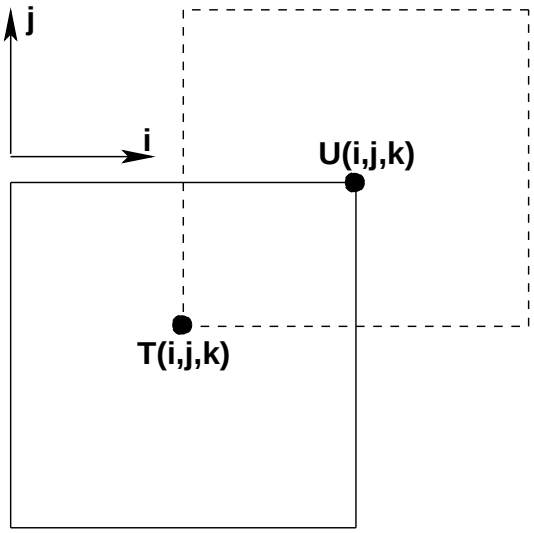

Figure 4.1: Illustration of how fields are placed on the horizontal B-grid used in MOM4. Velocity points $U_{i,j,k}$ are placed to the northeast of tracer points $T_{i,j,k}$. Both horizontal velocity components $u_{i,j,k}$ and $v_{i,j,k}$ are placed at the velocity point $U_{i,j,k}$.

and $N_{i,j}$. Figure 4.2 illustrates these points as oriented according to the tracer cell, with $T_{i,j}$ the usual tracer point. $C_{i,j}$ lives at the northeast corner of the tracer cell, and so represents B-grid velocity point $U_{i,j}$. $N_{i,j}$ lives at the north face of the tracer cell and so represents the C-grid meridional velocity point. $E_{i,k}$ lives at the east face of the tracer cell and so is the C-grid zonal velocity point. The geographical coordinates of these four points is sufficient to place them on the discrete lattice.

4.1.2.2 Computing the grid distances

To support a discretized calculus, we must specify distances between grid points and the grid cells. Knowing the geographical position of the four basic grid points

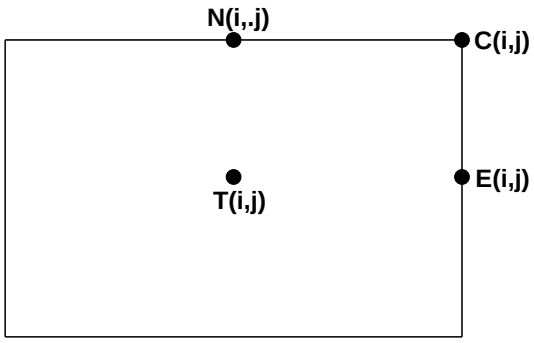

Figure 4.2: The four basic grid points for the B and C grids: $T_{i,j}, C_{i,j}$, $E_{i,j}$, and $N_{i,j}$. $T_{i,j}$ is the usual tracer point, with the corner $C_{i,j}$ and side points $E_{i,j}$, $N_{i,j}$ associated with the tracer point.

as well as the vertices of their corresponding grid cells is not sufficient. In addition, we need information regarding the metric or stretching functions specific to the coordinate system used to tile the sphere.

The traditional approach is to use spherical coordinates for tiling the sphere. In this method, the distance between two points zonally displaced a finite distance from one another is given by the analytic formula

$$\Delta x[a,b] = R\,\cos\phi \int_{\lambda_a}^{\lambda_b} d\lambda = (R\,\cos\phi)\,(\lambda_b - \lambda_a), \tag{4.1}$$

and the distance between two points along a line of constant longitude is given by

$$\Delta y[a,b] = R \int_{\phi_a}^{\phi_b} d\phi = R\,(\phi_b - \phi_a). \tag{4.2}$$

Writing this expression in a general manner leads to the generalized zonal and generalized meridional distance given by

$$\Delta x[a,b] = \int_{\xi_1^{(b)}}^{\xi_1^{(a)}} h_1\,d\xi_1 \tag{4.3}$$

$$\Delta y[a,b] = \int_{\xi_2^{(b)}}^{\xi_2^{(a)}} h_2\,d\xi_2, \tag{4.4}$$

where (ξ_1, ξ_2) represent generalized orthogonal coordinates, and (h_1, h_2) are the stretching functions specific to the coordinate system. They determine the distance between two infinitesimally close points via the line element formula

$$(ds)^2 = (h_1\,d\xi_1)^2 + (h_2\,d\xi_2)^2. \tag{4.5}$$

With $dx = h_1\,d\xi_1$ and $dy = h_2\,d\xi_2$, the line element formula takes the form of the usual Cartesian expression

$$(ds)^2 = (dx)^2 + (dy)^2. \tag{4.6}$$

It is not possible to perform the distance integrals analytically for an arbitrary general orthogonal coordinate system. Therefore, approximations must be made. Indeed, in MOM3 the analytical form for the zonal distance was actually approximated according to

$$\Delta x \approx R\,\cos\overline{\phi} \tag{4.7}$$

where $\overline{\phi} = (\phi_1 + \phi_2)/2$ (see discussion in Section 39.6 of Pacanowski and Griffies (1999)). Assuming information is available only at the grid points and at the cell vertices, MOM4 chooses to compute the distance between two points along a generalized zonal direction ($i-$line) as

$$\Delta x[a,b] = \left|\xi_1^{(a)} - \xi_1^{(b)}\right| \left(h_1^{(a)} + h_1^{(b)}\right)/2. \tag{4.8}$$

Likewise, the distance along a generalized meridional direction ($j-$line) is computed as

$$\Delta y[a,b] = \left|\xi_2^{(a)} - \xi_2^{(b)}\right| \left(h_2^{(a)} + h_2^{(b)}\right)/2. \tag{4.9}$$

4.1.2.3 Grid distances carried by the model

Given coordinates for the grid points and grid vertices, as well as the stretching functions evaluated at these points, we can use the approximate expressions (4.8) and (4.9) to compute distances between the T,U,N, and E points. Figure 4.3 shows the notation for the grid distances that define four quarter-cells splitting up each tracer and velocity cell. Shown is the notation used in the *grid descriptor* module as well as that used in MOM4. The full dimensions of the tracer and velocity cells are shown in Figure 4.4, where again the distances computed in the *grid descriptor* module are translated into the grid distances used in MOM4. Finally, Figure 4.5 shows the distances specifying the separation between adjacent tracer and velocity points.

4.2 The Murray (1996) tripolar grid

The Murray (1996) tripolar grid (see his Figure 7) has been a focus of ocean climate model development with MOM4 during the year 2001-2002. This grid is comprised of the usual spherical coordinate grid southward of a chosen latitude circle, typically taken at $65^\circ N$. This part of the grid has a single pole over Antarctica, which is of no consequence to the numerical ocean climate model. In the Arctic region, the Murray grid places a bipolar region with two poles situated over land, and so these poles are also of no consequence to the numerical ocean model.

Figure 4.6 illustrates the grid lines used to discretize the ocean equations in the Arctic using Murray's grid. The placement of discrete model tracer and velocity points along the bipolar grid lines is schematically represented in Figure 4.7. The arrangement of northern and eastern vector components centered on the tracer cell faces is shown in Figure 4.8. Details for how to transfer information across the bipolar *prime meridion* located along the $j = nj$ line are provided in Section 4.3.

Motivation for choosing the Murray (1996) grid includes the following:

- It removes the spherical coordinate singularity present at the geographical north pole.
- It maintains the usual spherical coordinate grid lines for latitudes southward of the Arctic region, thus simplifying analysis.
- It is locally orthogonal, and so can be used with the MOM4 generalized horizontal coordinates.
- Similar grids have been successfully run by the French OPA modeling group and the Miami MICOM modeling group.

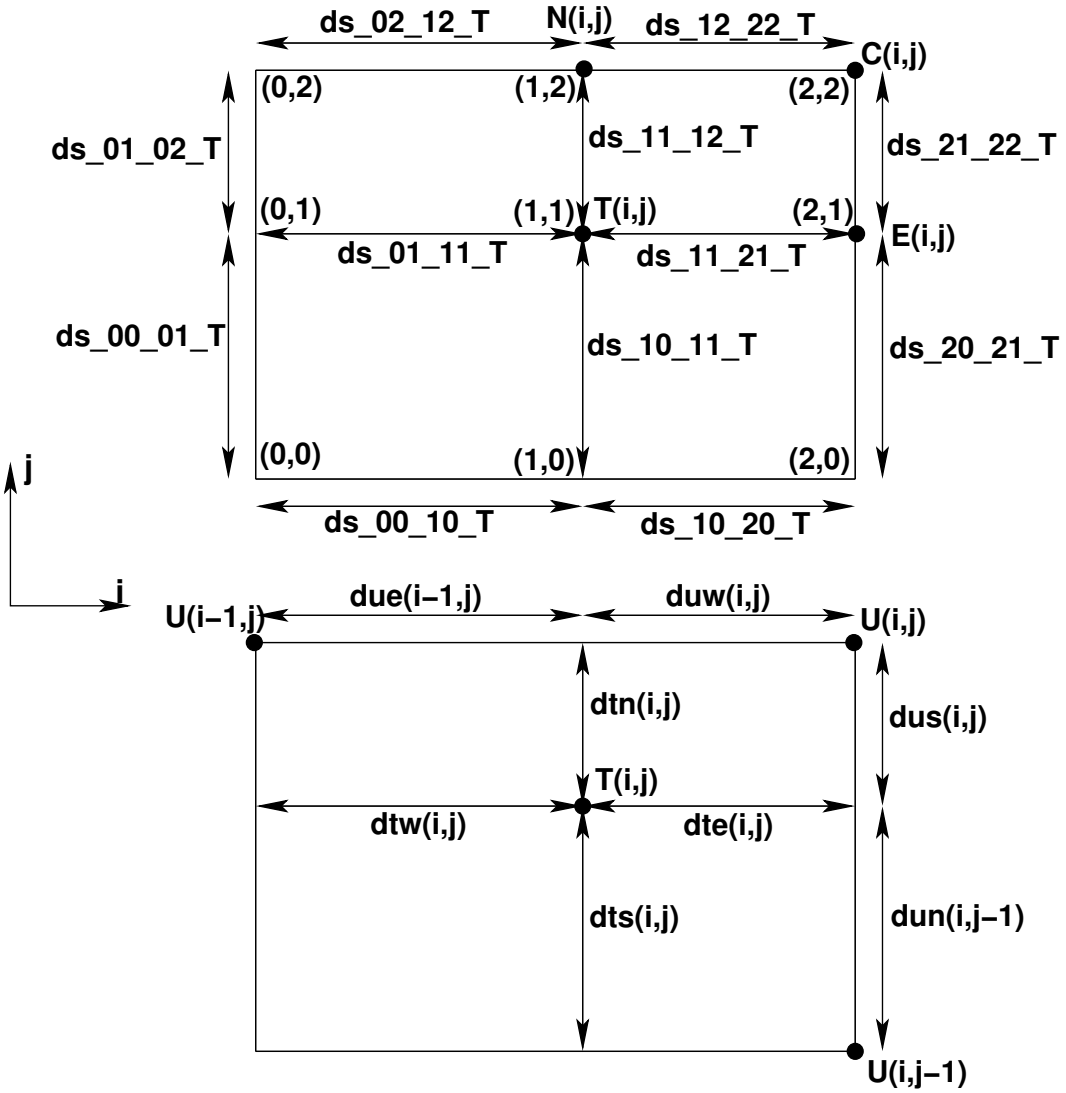

Figure 4.3: Upper panel: Grid distances used to measure the distance between the four fundamental grid points shown in Figure 4.2. These distances are computed in the FMS *grid descriptor* module. The naming convention is based on a Cartesian grid with the origin at the lower left corner of the tracer cell at $(0,0)$, the upper right hand corner is $(2,2)$, the center at $(1,1)$, and all other points set accordingly. The distances are then named as distances between these grid points. Note that each tracer cell has a local Cartesian coordinate set as here, and so there is redundancy in the various grid distances. Lower panel: When read into MOM4, the grid distances set the distance between the tracer and velocity points used in the model (Figure 4.1) and the sides of the corresponding grid cells. A translation of the upper panel distance names to those used in MOM4 is made within MOM4's ocean_grid module.

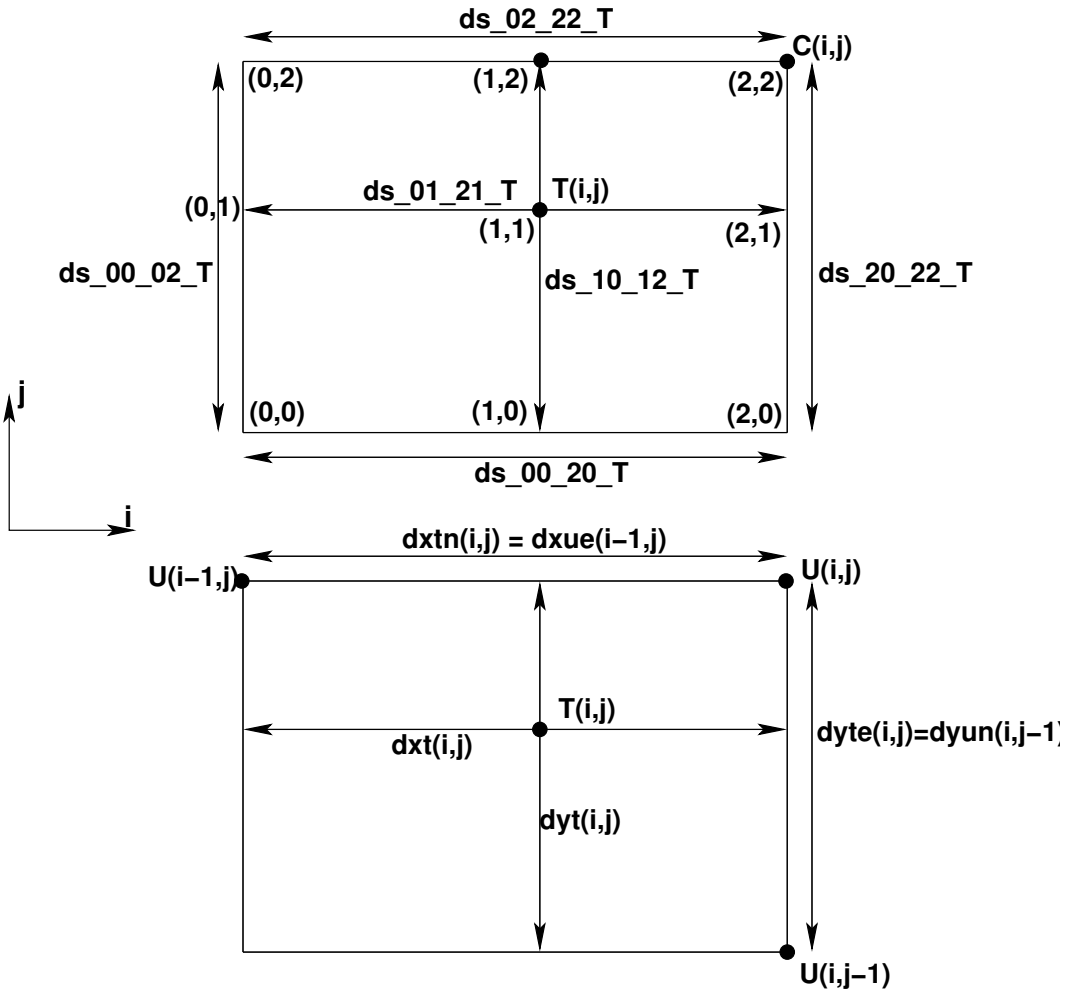

Figure 4.4: Grid cell distances used for computing the area of a grid cell. These dimensions are related to the fundamental quarter-cell dimensions shown in Figure 4.3. Upper panel: distances computed in the FMS *grid descriptor* module. Lower panel: names of the distances used in MOM4.

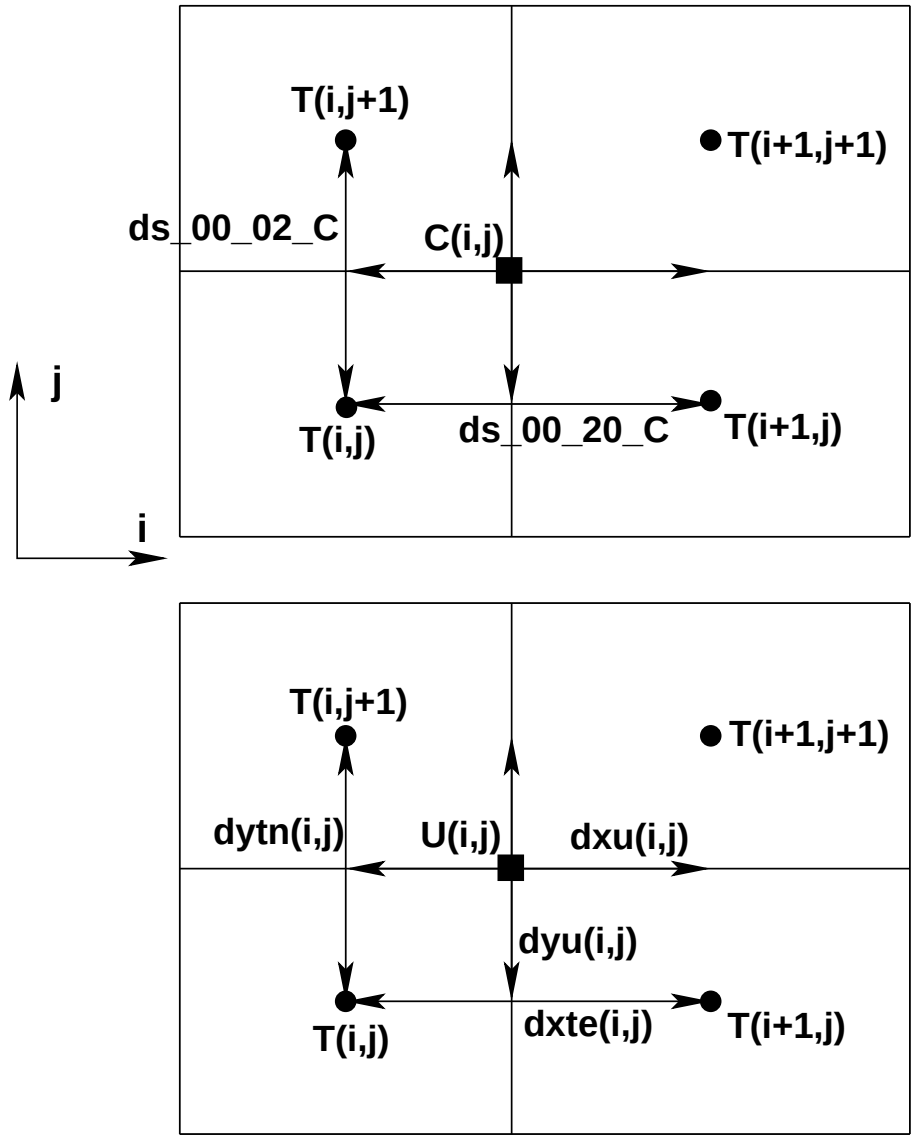

Figure 4.5: Distances between fundamental grid points (upper panel) as computed by the *grid descriptor* module. These distances are taken into MOM4 and used to set the distances between tracer and velocity points (lower panel).

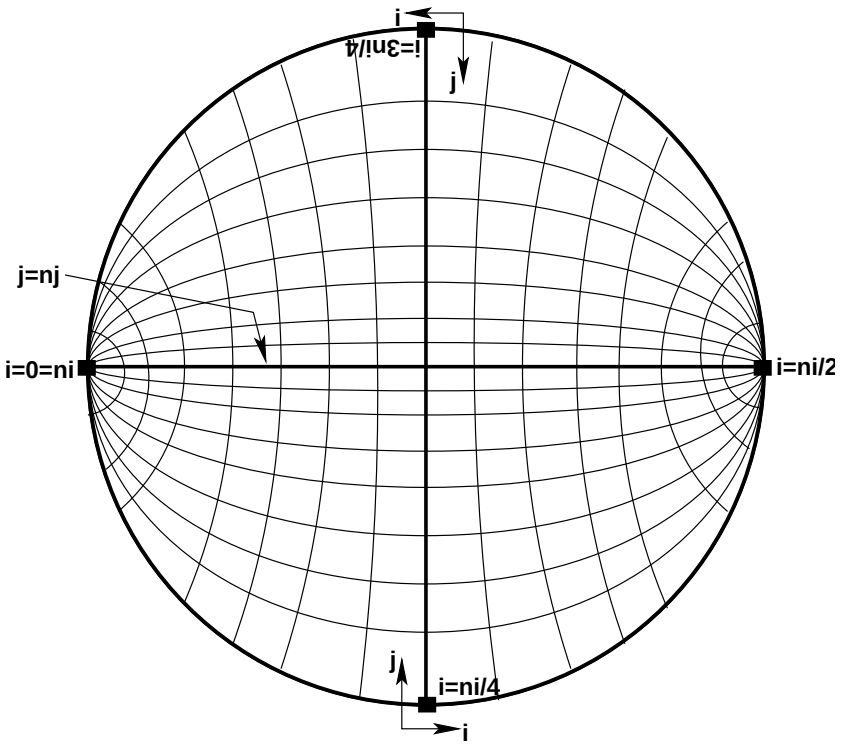

Figure 4.6: Illustration of the grid lines forming the bipolar region in the Arctic. This figure is taken after Figure 7 of Murray (1996). The thick outer boundary is a line of constant latitude in the spherical coordinate grid. This latitude is typically at the latitude nearest to $65^\circ N$. As in the spherical coordinate region, lines of constant i move in a generalized eastward direction. They start from the bipolar south pole at $i = 0$, which is identified with $i = ni$. The bipolar north pole is at $i = ni/2$. As shown in Figure 4.7, the poles are centered at a velocity point. Lines of constant j move in a generalized northward direction. The bipolar prime-meridion is situated along the j-line with $j = nj$. This line defines the *bipolar fold* that bisects the tracer grid. Its fold topology causes the velocity points centered along $j = nj$ to have a two-fold redundancy (see Figure 4.7 for more details).

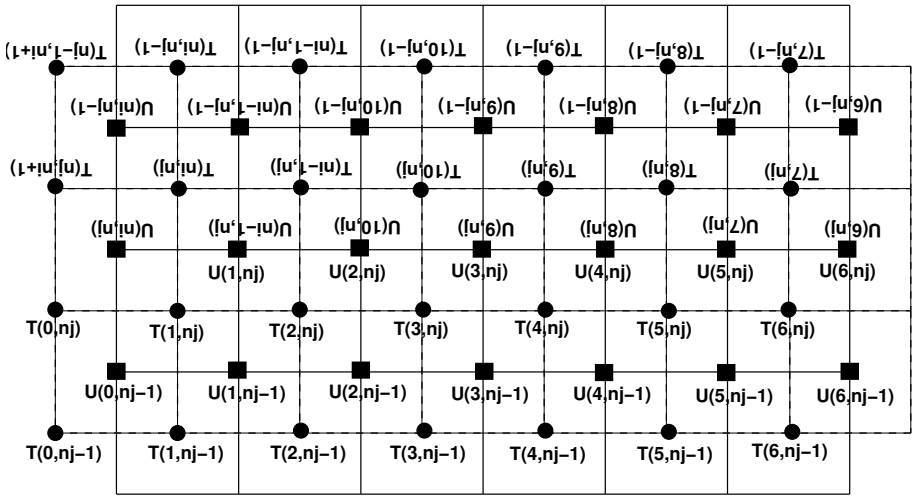

Figure 4.7: Schematic representation of the tracer and velocity cells on the bipolar grid shown in Figure 4.6. The global computational domain consists of $ni = 12$ i-points for this example. The $j = nj$ line bisects the tracer grid, which means there are redundant velocity points along this line. Along an $i-$line of velocity points, velocity cells with $i = ni/2$ live at the bipolar north pole, whereas velocity cells with $i = 0 = ni$ live at the bipolar south pole.

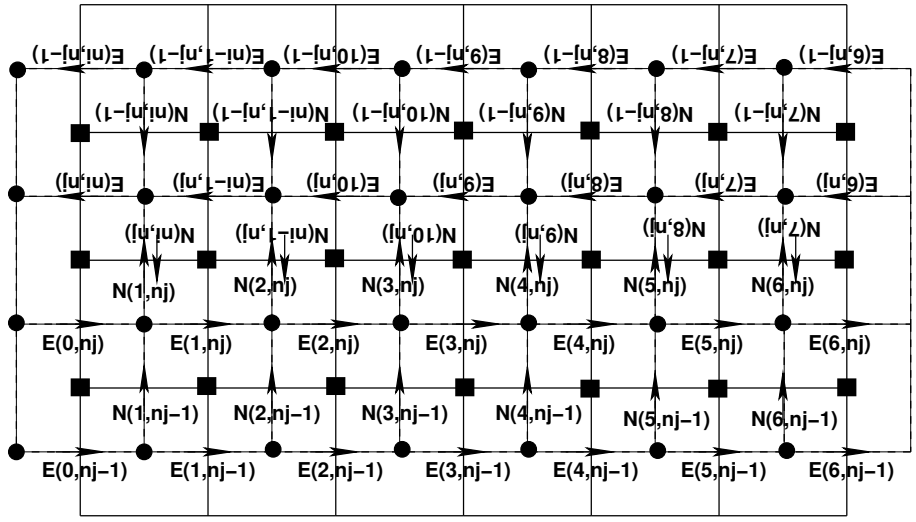

Figure 4.8: Schematic representation of fields living at the north and east faces of the tracer cells as configured using the bipolar grid shown in Figure 4.6. Typical fields of this sort are diffusive and advective tracer flux components, and so they are components to a vector field, hence the vector notation. The global computational domain consists of $ni = 12$ i-points for this example. The $j = nj$ line bisects the tracer grid, which means there are redundant velocity points along this line. Along an $i-$line of velocity points, velocity cells with $i = ni/2$ live at the bipolar north pole, whereas velocity cells with $i = 0 = ni$ live at the bipolar south pole.

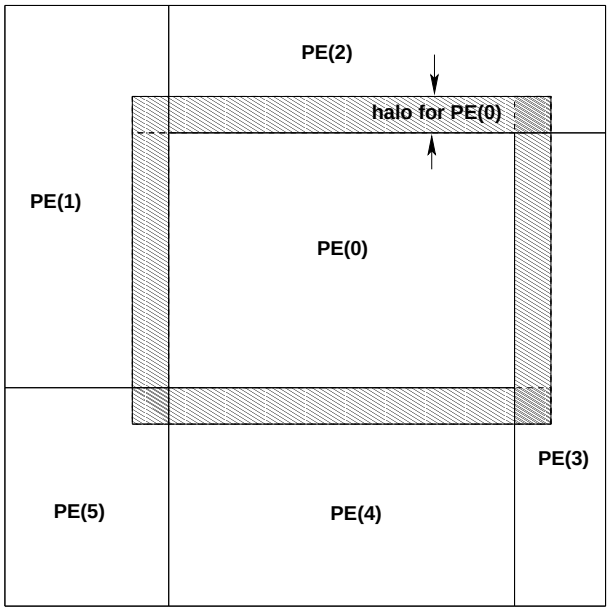

Figure 4.9: Elements of halos needed for computing derivative information on a local domain. The hatched region is comprised of halo points needed in order for the processor labelled PE(0) to time step its equations. The halo values must be transmitted from the surrounding processors since they live outside of PE(0)'s local domain.

4.3 Specifying fields and grid distances within halos

MOM4 has been designed to run on multiple parallel processors. The computation of finite derivative operators requires the passage of information across processor boundaries. In particular, the decomposition of the model's *global* domain into multiple *local* domains requires that fields and grid information from one local domain be mapped to halos of adjacent local domains. For second order numerics, the calculation of derivatives on the boundary of a local domain requires information within one grid row *halo* surrounding the local domain. Higher order numerics require larger halos.

4.3.1 Interior domains

Within the interior of the ocean model, away from global boundaries, the mapping between domains is performed using an FMS utility that fills the halo points for one local domain using information available to another local domain. Figure 4.9 illustrates this basic point. Shown is a central processor, arbitrarily labelled PE(0), and a surrounding hatched region representing halo points. The width of the halo is a function of the numerics used in the model. For second order numerics, a halo width of a single point is sufficient. The values of fields and grid factors within the halo are transmitted from the surrounding processors to PE(0) in order for PE(0) to time step its portion of the ocean equations discretized on its local domain.

4.3.2 Exterior domains

For processors whose boundary touches the global model boundary, it is necessary to specify whether the global boundary is a solid wall as in a sector model, periodic as in a zonal channel, or folded as in the bipolar grid of Murray (1996). That is, we must specify the model's topology. Each of these three topologies requires some special consideration, with the cases built into the MOM4 update boundary condition module. Since these conditions are specific to the experimental design, they are handled by a MOM4 module that sets the boundary conditions. We focus here on the three common topologies supported by MOM4. A fourth case, open boundary conditions, is discussed separately in chapter 21.

4.3.2.1 Solid wall boundary conditions

For a solid wall boundary condition, all fluxes passing across the walls are zeroed out via masks, and fields within the solid wall are either trivial or masked. Hence, no halo updates are necessary for fields and fluxes at solid walls. However, it is important to specify self-consistent grid distances separating points within the solid wall from those within the model's computational domain. The reason is that various remapping operators require grid distances be well defined for all points within the computational domain, including those distances reaching into the halo. See Chapter 5 for details of remapping operators. For this reason, we extend the grid into the solid wall halo so that resolution in this region is given by the resolution between the two nearest interior points.

4.3.2.2 Periodic boundary conditions

Zonally periodic channels (x-cyclic) are commonly run for idealized studies. Meriodionally periodic (y-cyclic) domains may also be of interest for simulations on an $f-$plane or β-plane. For these reasons, we need to specify grid factors within the halo assuming periodicity at the global domain boundary.

We focus here on the needs of the more common zonally periodic boundary conditions, and refer to Figure 4.10. The same considerations hold for y-cyclic conditions. For either case, we envision the grid wrapped onto itself in the appropriate direction. With second order numerics, computation of the prognostic tracer in grid cells $T_{i=1,j}$ requires information regarding $T_{i=0,j}$. Likewise, $T_{i=ni,j}$ requires information about $T_{i=ni+1,j}$. Higher order numerics will need to reach out further.

First consider the eastern boundary of the domain where $i = ni$. For a single grid halo, we need to specify values of fields living at the T, E, N, and C points at $i = ni + 1$ (recall Figures 4.1 and 4.2 where the C point is equivalent to the B-grid U point). Zonal periodicity renders the equalities

$$T_{ni+1,j} = T_{1,j} \tag{4.10}$$
$$E_{ni+1,j} = E_{1,j} \tag{4.11}$$
$$N_{ni+1,j} = N_{1,j} \tag{4.12}$$
$$C_{ni+1,j} = C_{1,j}. \tag{4.13}$$

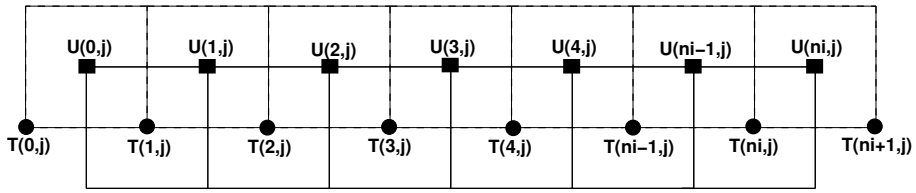

Figure 4.10: A zonally periodic array of tracer and velocity points with a single halo point. In this example there are $ni = 6$ points in the global computational domain, and $halo = 1$ point in the surrounding halo region. The cyclic mapping leads us to specify halo points with values $T_{i=0,j} = T_{i=ni,j}$, $T_{i=ni+1,j} = T_{i=1,j}$, and $U_{i=0,j} = U_{i=ni,j}$.

More generally, halo points with $ni < i \leq ni + halo$ acquire the x-cyclic mapping

$$T_{i,j} = T_{i-ni,j} \tag{4.14}$$
$$E_{i,j} = E_{i-ni,j} \tag{4.15}$$
$$N_{i,j} = N_{i-ni,j} \tag{4.16}$$
$$C_{i,j} = C_{i-ni,j}. \tag{4.17}$$

At the western boundary, similar considerations lead to halo points $1 - halo \leq i < 1$ mapped to interior points according to

$$T_{i,j} = T_{i+ni,j} \tag{4.18}$$
$$E_{i,j} = E_{i+ni,j} \tag{4.19}$$
$$N_{i,j} = N_{i+ni,j} \tag{4.20}$$
$$C_{i,j} = C_{i+ni,j}. \tag{4.21}$$

4.3.3 The bipolar Arctic grid

The ideas considered for the cyclic case are now generalized to the more complex topology of the Murray (1996) bipolar grid shown in Figures 4.6 and 4.7. In particular, Figures 4.7 and 4.8 allow us to deduce the mappings between related points on the grid.

4.3.3.1 Fields defined at points T,U,N, and E

The generalized zonal direction (along a constant i-line) is treated with the x-cyclic conditions shown Figure 4.10. It is the bipolar prime meridion along the $j-$line with $j = nj$ that introduces the most subtle issues. This line bisects the tracer grid. Relating points across the prime meridion requires knowledge of the tensorial nature of the field being considered. In particular, scalar fields map without a change in sign, whereas components of a vector field have a sign change.

The $U-$points contain a two-fold redundancy of points along the $j = nj$ line. For scalars living at these points, such as some grid factors, we have the identity

$$U_{i,nj} = U_{ni-i,nj}. \tag{4.22}$$

Likewise, scalars living at the northern face of a tracer cell contain a two-fold redundancy of points along the $j = nj$ line so that

$$N_{i,nj} = N_{ni-i+1,nj}. \tag{4.23}$$

For vector components living at $U-$points, such as the B-grid horizontal velocity field, we associate transition across the $j = nj$ meridion with a sign change

$$u_{i,nj} = -u_{ni-i,nj} \tag{4.24}$$
$$v_{i,nj} = -v_{ni-i,nj}. \tag{4.25}$$

This sign change takes the right handed orientation into a right handed orientation across the meridion. Likewise, for components of vector fluxes living at the north face of a tracer cell, we have

$$F^n_{N_{i,nj}} = -F^n_{N_{ni-i+1,nj}}. \tag{4.26}$$

Note that numerical roundoff may compromise these equalities in the model. Such compromise will generally make the model energetics appear to be larger than when running with the spherical grid, or with the tripolar grid with the fold closed (*debug_tripolar* = *.true.*).

Moving along a j-line, halo points for scalar fields with $nj < j \leq nj + halo$ are evaluated according to the following rules

$$\left.\begin{array}{l} T_{i,j} = T_{ni-i+1,2nj-j+1} \\ U_{i,j} = U_{ni-i,2nj-j} \\ N_{i,j} = N_{ni-i+1,2nj-j} \\ E_{i,j} = E_{ni-i,2nj-j+1} \end{array}\right\} \text{for} \quad nj < j \leq nj + halo \tag{4.27}$$

Vector components living at these points have the same index mapping along with a sign flip for the field values.

4.3.3.2 Grid distances for horizontal quarter-cells

Grid distances must also be specified in halo points. Some distances also maintain redundancy relations. Since grid distances are taken between T,U,N, or E points, their redudancy relations and halo mappings are determined by those of their endpoints. We start by considering the grid factors defining the dimensions of quarter-cells defined in Figure 4.3. These require the most care. Figure 4.11 illustrates the placement of these factors on the bipolar grid. Immediately we see that the two-fold redundancy in the velocity cells $U_{i,nj}$ leads to the two-fold redundancy in grid cell distances

$$due_{i,nj} = duw_{ni-i,nj} \tag{4.28}$$
$$duw_{i,nj} = due_{ni-i,nj} \tag{4.29}$$
$$dun_{i,nj} = dus_{ni-i,nj} \tag{4.30}$$
$$dus_{i,nj} = dun_{ni-i,nj}. \tag{4.31}$$

Now consider the mappings needed to evaluate distances within halos. First consider the distances associated with the tracer cells. By definition, $dte_{i,j}$ measures

the distance between the tracer point $T_{i,j}$ and its "eastern" neighbor $E_{i,j}$, and $dtw_{i,j}$ is the distance between $T_{i,j}$ with its "western" neighbor $E_{i-1,j}$, where "eastern" and "western" are in a generalized sense. Mathematically, these distances are

$$\begin{aligned} \Delta x(T_{i,j}, E_{i,j}) &= dte_{i,j} && (4.32) \\ \Delta x(T_{i,j}, E_{i-1,j}) &= dtw_{i,j} && (4.33) \end{aligned}$$

where $\Delta x(A, B)$ is the distance between points A and B computed according to the generalized zonal distance in equation (4.8). The question is how to map these distances across the bipolar fold. To do so, we note that if we are in a halo region where $nj < j \leq nj + halo$, then the scalar mappings given by equation (4.27) lead to

$$\begin{aligned} \Delta x(T_{i,j}, E_{i,j}) &= \Delta x(T_{ni-i+1,2nj-j+1}, E_{ni-i,2nj-j+1}) && (4.34) \\ \Delta x(T_{i,j}, E_{i-1,j}) &= \Delta x(T_{ni-i+1,2nj-j+1}, E_{ni-i+1,2nj-j+1}). && (4.35) \end{aligned}$$

Comparison of these equalities with the definitions of dte and dtw then leads to the halo cell relations

$$\left.\begin{aligned} dte_{i,j} &= dtw_{ni-i+1,2nj-j+1} \\ dtw_{i,j} &= dte_{ni-i+1,2nj-j+1} \end{aligned}\right\} \text{for} \quad nj < j \leq nj + halo \tag{4.36}$$

Distances to the northern and southern faces of the tracer cell, dtn and dts, are defined by

$$\begin{aligned} \Delta y(T_{i,j}, N_{i,j}) &= dtn_{i,j} && (4.37) \\ \Delta y(T_{i,j}, N_{i,j-1}) &= dts_{i,j} && (4.38) \end{aligned}$$

where Δy is the generalized meridional distance given by equation (4.9). Equation (4.27) indicate that within the halo region $nj < j \leq nj + halo$,

$$\begin{aligned} \Delta y(T_{i,j}, N_{i,j}) &= \Delta y(T_{ni-i+1,2nj-j+1}, N_{ni-i+1,2nj-j}) && (4.39) \\ \Delta y(T_{i,j}, N_{i,j-1}) &= \Delta y(T_{ni-i+1,2nj-j+1}, N_{ni-i+1,2nj-j+1}). && (4.40) \end{aligned}$$

Comparison of these equalities with the definitions of dtn and dts leads to the halo cell relations

$$\left.\begin{aligned} dtn_{i,j} &= dts_{ni-i+1,2nj-j+1} \\ dts_{i,j} &= dtn_{ni-i+1,2nj-j+1} \end{aligned}\right\} \text{for} \quad nj < j \leq nj + halo \tag{4.41}$$

Velocity cell distances are defined by

$$\begin{aligned} \Delta x(U_{i,j}, N_{i+1,j}) &= due_{i,j} && (4.42) \\ \Delta x(U_{i,j}, N_{i,j}) &= duw_{i,j} && (4.43) \\ \Delta y(U_{i,j}, E_{i,j+1}) &= dun_{i,j} && (4.44) \\ \Delta y(U_{i,j}, E_{i,j}) &= dus_{i,j} && (4.45) \end{aligned}$$

Equation (4.27) indicate that within the halo region $nj < j \leq nj + halo$,

$$\begin{aligned} \Delta x(U_{i,j}, N_{i+1,j}) &= \Delta x(U_{ni-i,2nj-j}, N_{ni-i,2nj-j}) && (4.46) \\ \Delta x(U_{i,j}, N_{i,j}) &= \Delta x(U_{ni-i,2nj-j}, N_{ni-i+1,2nj-j}) && (4.47) \\ \Delta y(U_{i,j}, E_{i,j+1}) &= \Delta x(U_{ni-i,2nj-j}, E_{ni-i,2nj-j}) && (4.48) \\ \Delta y(U_{i,j}, E_{i,j}) &= \Delta x(U_{ni-i,2nj-j}, E_{ni-i,2nj-j+1}), && (4.49) \end{aligned}$$

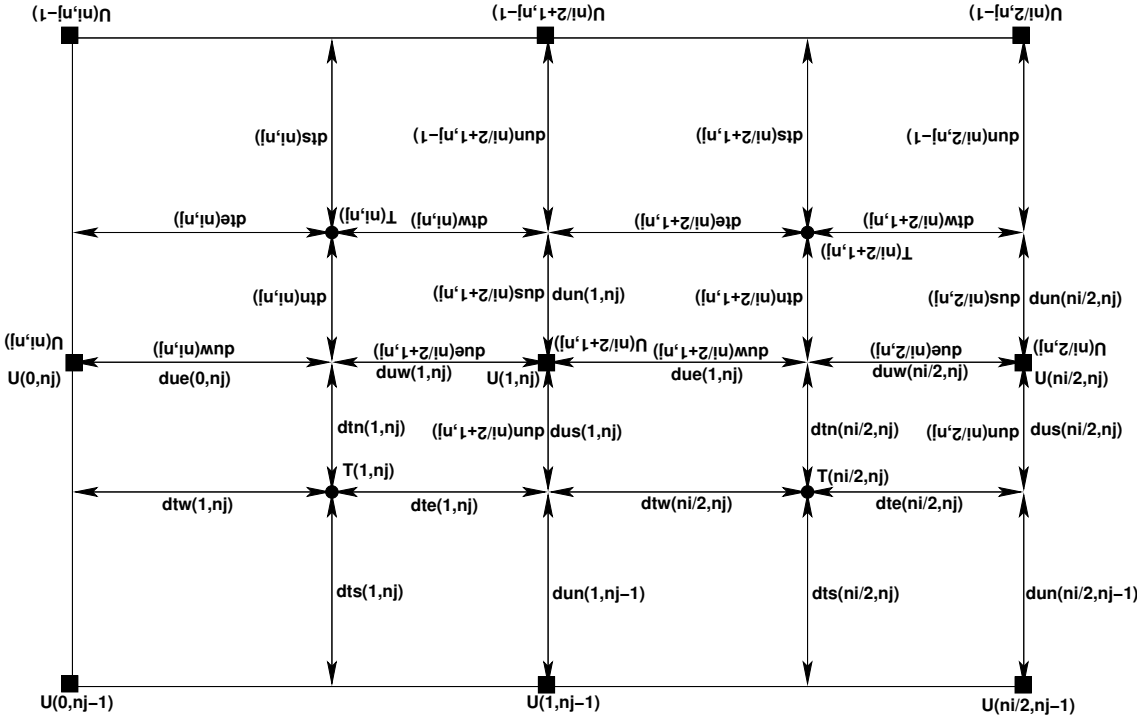

Figure 4.11: Placement of quarter-cells distances at the bipolar fold. For this example, there are $ni = 4$ points in the generalized zonal computational domain. Equivalance of grid factors on the fold leads to the two-fold redundancy for velocity cell distances $due_{i,nj} = duw_{ni-i,nj}$ and $dus_{i,nj} = dun_{ni-i,nj}$.

which then leads to the halo cell relations

$$\left.\begin{array}{l} due_{i,j} = duw_{ni-i,2nj-j} \\ duw_{i,j} = due_{ni-i,2nj-j} \\ dun_{i,j} = dus_{ni-i,2nj-j} \\ dus_{i,j} = dun_{ni-i,2nj-j} \end{array}\right\} \text{for} \quad nj < j \leq nj + halo \tag{4.50}$$

4.3.3.3 Grid distances for horizontal full cells

Inspection of Figures 4.4 and 4.5, with the definitions of grid points shown in Figure 4.2, leads to the definitions of distances for full horizontal cells

$$\Delta x(E_{i-1,j}, E_{i,j}) = dxt_{i,j} \tag{4.51}$$
$$\Delta y(N_{i,j-1}, N_{i,j}) = dyt_{i,j} \tag{4.52}$$
$$\Delta x(U_{i-1,j}, U_{i,j}) = dxtn_{i,j} \tag{4.53}$$
$$\Delta y(U_{i,j}, U_{i,j-1}) = dyte_{i,j} \tag{4.54}$$
$$\Delta x(T_{i,j}, T_{i+1,j}) = dxte_{i,j} \tag{4.55}$$
$$\Delta y(T_{i,j}, T_{i,j+1}) = dytn_{i,j} \tag{4.56}$$
$$\Delta x(N_{i,j}, N_{i+1,j}) = dxu_{i,j} \tag{4.57}$$
$$\Delta y(E_{i,j}, E_{i,j+1}) = dyu_{i,j} \tag{4.58}$$

Figures 4.12, 4.13, and 4.14 show these distances for regions surrounding the bipolar fold. To generate the redudancy conditions and halo mappings, we again use the scalar mappings given by equation (4.27). Using these relations we see that redundancy is satisfied by the distances

$$\begin{aligned} dxtn_{i,nj} &= dxtn_{ni-i+1,nj} && (4.59)\\ dytn_{i,nj} &= dytn_{ni-i+1,nj} && (4.60)\\ dxu_{i,nj} &= dxu_{ni-i,nj} && (4.61)\\ dyu_{i,nj} &= dyu_{ni-i,nj} && (4.62) \end{aligned}$$

Equation (4.27) indicates that within the halo region $nj < j \leq nj + halo$,

$$\begin{aligned} \Delta x(E_{i-1,j}, E_{i,j}) &= \Delta x(E_{ni-i+1,2nj-j+1}, E_{ni-i,2nj-j+1}) && (4.63)\\ \Delta y(N_{i,j-1}, N_{i,j}) &= \Delta y(N_{ni-i+1,2nj-j+1}, N_{ni-i+1,2nj-j}) && (4.64)\\ \Delta x(U_{i-1,j}, U_{i,j}) &= \Delta x(U_{ni-i+1,2nj-j}, U_{ni-i,2nj-j}) && (4.65)\\ \Delta y(U_{i,j}, U_{i,j-1}) &= \Delta y(U_{ni-i,2nj-j}, U_{ni-i,2nj-j+1}) && (4.66)\\ \Delta x(T_{i,j}, T_{i+1,j}) &= \Delta x(T_{ni-i+1,2nj-j+1}, T_{ni-i,2nj-j+1}) && (4.67)\\ \Delta y(T_{i,j}, T_{i,j+1}) &= \Delta y(T_{ni-i+1,2nj-j+1}, T_{ni-i+1,2nj-j}) && (4.68)\\ \Delta x(N_{i,j}, N_{i+1,j}) &= \Delta x(N_{ni-i+1,2nj-j}, N_{ni-i,2nj-j}) && (4.69)\\ \Delta y(E_{i,j}, E_{i,j+1}) &= \Delta y(E_{ni-i,2nj-j+1}, E_{ni-i,2nj-j}) && (4.70) \end{aligned}$$

which then leads to to the halo cell relations

$$\left.\begin{aligned} dxt_{i,j} &= dxt_{ni-i+1,2nj-j+1}\\ dyt_{i,j} &= dyt_{ni-i+1,2nj-j+1}\\ dxtn_{i,j} &= dxtn_{ni-i+1,2nj-j}\\ dyte_{i,j} &= dyte_{ni-i,2nj-j+1}\\ dxte_{i,j} &= dxte_{ni-i,2nj-j+1}\\ dytn_{i,j} &= dytn_{ni-i+1,2nj-j}\\ dxu_{i,j} &= dxu_{ni-i,2nj-j}\\ dyu_{i,j} &= dyu_{ni-i,2nj-j} \end{aligned}\right\} \text{for} \quad nj < j \leq nj + halo \qquad (4.71)$$

4.3.3.4 Summary of redundancies and halo mappings

Table 4.1 summarizes the halo relations and redundancies realized at the bipolar fold. Notice that those distances exhibiting a redundancy have their halo relations reduce to their redundancy relations for $j = nj$. Additionally, the quarter-cell distances all transform from a right handed system to a right handed system. In general, this table should be sufficient to deduce relations for any derived fields, fluxes, etc., computed in the model.

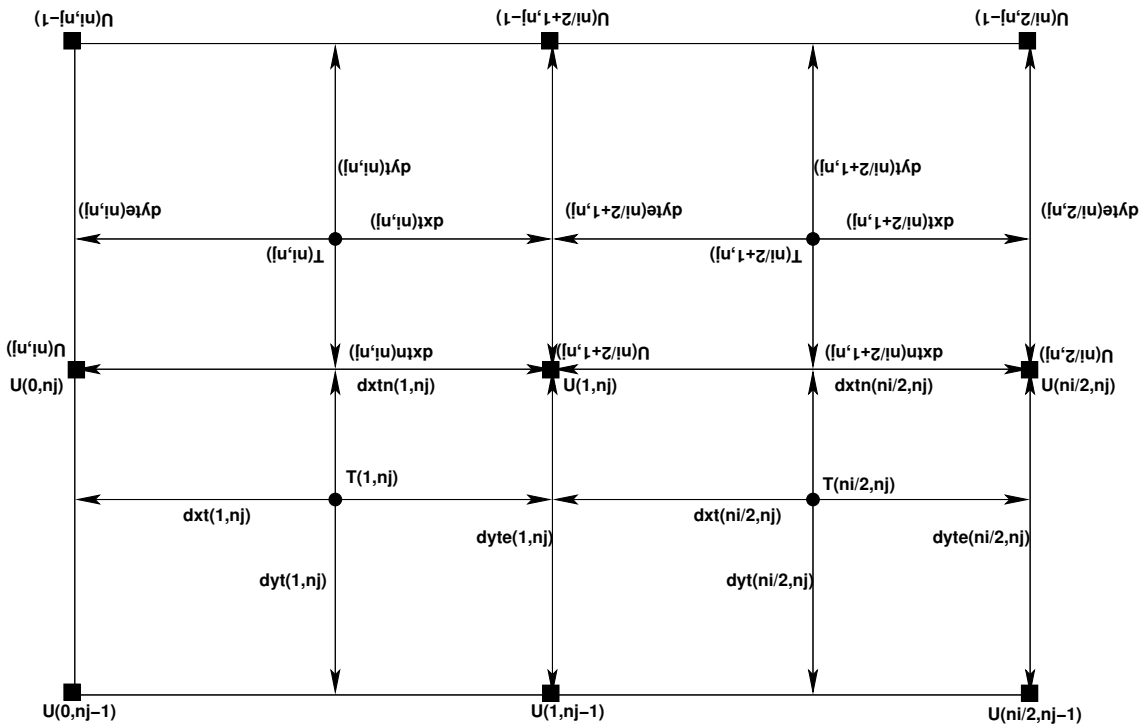

Figure 4.12: Placement of tracer cell dimensions at the bipolar fold. For this example, there are $ni = 4$ points in the generalized zonal computational domain. Equivalance of grid factors on the fold leads to the two-fold redundancy $dxtn_{i,nj} = dxtn_{ni-i+1,nj}$.

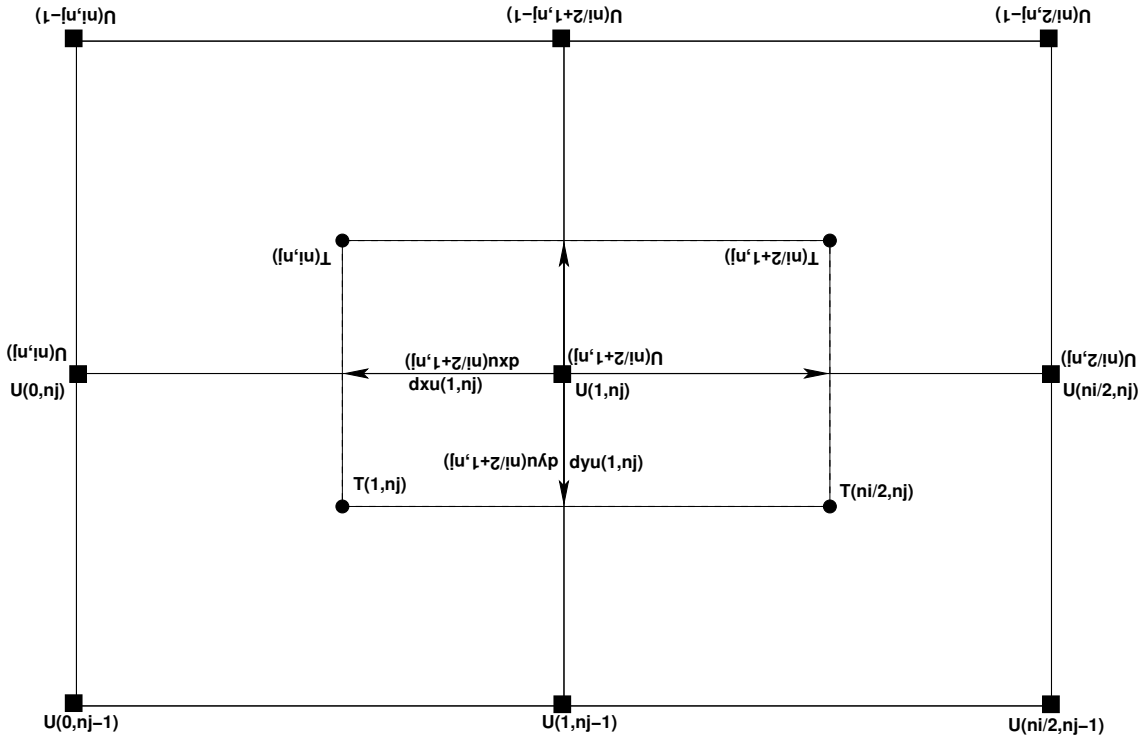

Figure 4.13: Velocity cell distances at the bipolar fold.

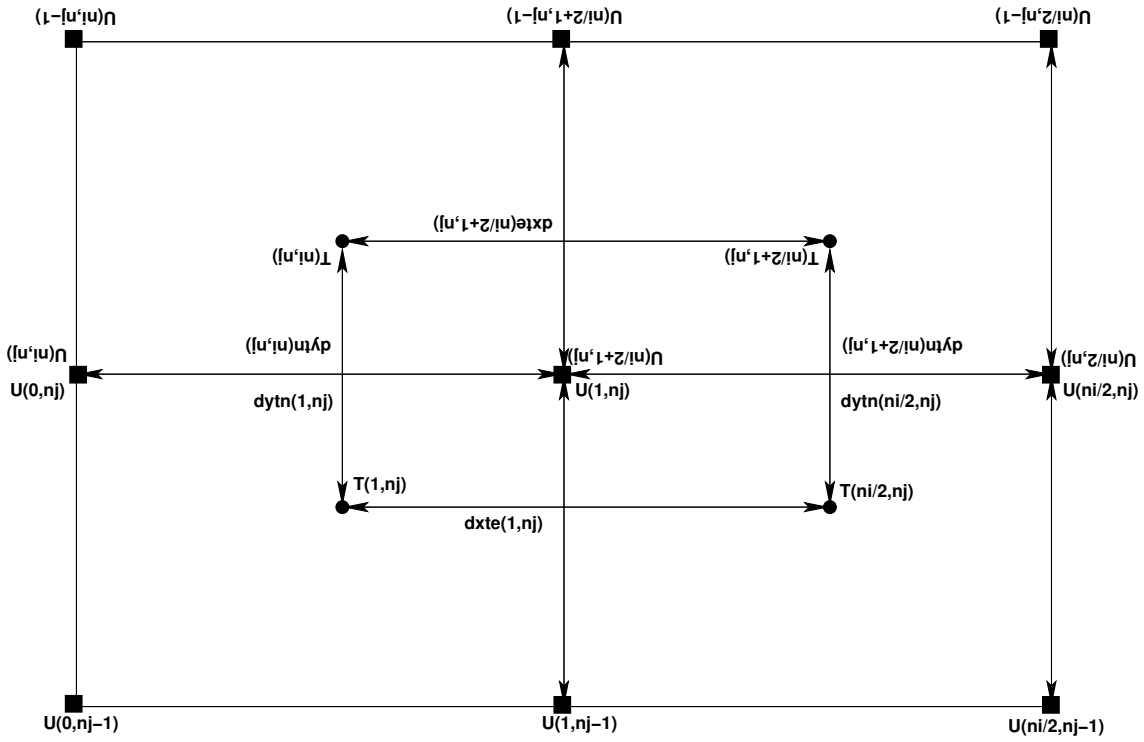

Figure 4.14: Grid distances for tracer points at the bipolar fold.

Halo relations ($nj < j \leq nj + halo$)	**Redundancy relations**
$U_{i,j} = \varepsilon\, U_{ni-i,2nj-j}$	$U_{i,nj} = \varepsilon\, U_{ni-i,nj}$
$T_{i,j} = \varepsilon\, T_{ni-i+1,2nj-j+1}$	
$N_{i,j} = \varepsilon\, N_{ni-i+1,2nj-j}$	$N_{i,nj} = \varepsilon\, N_{ni-i+1,nj}$
$E_{i,j} = \varepsilon\, E_{ni-i,2nj-j+1}$	
$dte_{i,j} = dtw_{ni-i+1,2nj-j+1}$	
$dtw_{i,j} = dte_{ni-i+1,2nj-j+1}$	
$dtn_{i,j} = dts_{ni-i+1,2nj-j+1}$	
$dts_{i,j} = dtn_{ni-i+1,2nj-j+1}$	
$due_{i,j} = duw_{ni-i,2nj-j}$	$due_{i,nj} = duw_{ni-i,nj}$
$duw_{i,j} = due_{ni-i,2nj-j}$	$duw_{i,nj} = due_{ni-i,nj}$
$dun_{i,j} = dus_{ni-i,2nj-j}$	$dun_{i,nj} = dus_{ni-i,nj}$
$dus_{i,j} = dun_{ni-i,2nj-j}$	$dus_{i,nj} = dun_{ni-i,nj}$
$dxt_{i,j} = dxt_{ni-i+1,2nj-j+1}$	
$dyt_{i,j} = dyt_{ni-i+1,2nj-j+1}$	
$dxtn_{i,j} = dxtn_{ni-i+1,2nj-j}$	$dxtn_{i,nj} = dxtn_{ni-i+1,nj}$
$dyte_{i,j} = dyte_{ni-i,2nj-j+1}$	
$dxte_{i,j} = dxte_{ni-i,2nj-j+1}$	
$dytn_{i,j} = dytn_{ni-i+1,2nj-j}$	$dytn_{i,nj} = dytn_{ni-i+1,nj}$
$dxu_{i,j} = dxu_{ni-i,2nj-j}$	$dxu_{i,nj} = dxu_{ni-i,nj}$
$dyu_{i,j} = dyu_{ni-i,2nj-j}$	$dyu_{i,nj} = dyu_{ni-i,nj}$

Table 4.1: Summary of the halo mappings and redundancies realized at the bipolar fold. The symbol ε is 1 for scalar fields, and -1 for horizontal components of vector fields.

CHAPTER

FIVE

Advection velocity components and remapping operators

Contents

The purpose of this chapter is to discuss the computation of advection velocity components in MOM4. We also discuss the linear operators used to interpolate a field from one grid to another. These operators are used to map advection velocity components from the tracer grid to velocity grid, as well as to map selected other fields.

5.1 General considerations

Advective fluxes are fundamental to the Eulerian evolution of tracer and momentum. How these fluxes are discretized represents a basic problem in computational fluid dynamics. Notably, because of the interpretation of model velocity discussed in Griffies (2004), there is no distinction between the advective fluxes for the Boussinesq and non-Boussinesq versions of MOM4: they are computed using the same numerical considerations detailed in this chapter.

5.1.1 Two main issues

There are two considerations required to compute advective fluxes of tracer or momentum. First, there is the question of how to compute the advective velocity. Such is the focus of this chapter. For computing fluxes across cell faces, the three components to the advective velocity must be known on the corresponding face of the tracer and velocity cells. However, on the B-grid, both horizontal prognostic velocity components are placed at the velocity cell point, not at the cell faces. Hence, an averaging operation must be prescribed to diagnose the horizontal advective velocity components from the prognostic B-grid velocity. MOM4 computes the horizontal components of the advection velocity on the faces of T-cells in a manner necessitated by equating pressure work to buoyancy (see Chapter 6). The vertical advective velocity component is then diagnosed at the bottom face of the tracer cell, based on the needs of volume or mass conservation across the tracer cell (see Chapter 6 or Griffies (2004)). Computing the advective velocity on the faces of the velocity cell remains to be determined, and that is the main technical subject of this chapter.

Once the advective velocity is computed on the cell faces, it remains to approximate the tracer and momentum values on these faces for use in constructing the advective tracer and momentum fluxes. There are many different approaches available. As with previous versions of the GFDL ocean model, MOM4 chooses to compute the advective flux of momentum according to the requirements of energetic consistency described in Chapter 6. These constraints necessitate a second order centered approach, as in Bryan (1969). The advective flux of tracer, however, is not so constrained and there are hence many options available, some of which are detailed in **The MOM3 Manual** of Pacanowski and Griffies (1999).

5.1.2 Constraints for discrete vertical velocities

One important constraint for self-consistency of the discretization is that the vertical velocity at the T-cell bottom topography must vanish: $w\_bt_{i,j,k=Nk} = 0$, since the T-cell top and bottom faces are horizontally oriented. A vanising bottom velocity on T-cells is necessitated by the requirements of volume or mass conservation (see Griffies (2004)). Many ocean models choose to set $w\_bt_{i,j,k=Nk} = 0$. However, MOM chooses to start from the ocean surface and integrate the continuity equation downwards. Verification that the computed $w\_bt_{i,j,k=Nk}$ indeed vanishes has been found to be a very useful check on code integrity. Relatedly, for a flat bottomed ocean $w\_bu_{i,j,k=Nk} = 0$. However, with topography, w_bu is generally nonzero at the bottom, since the bottom on velocity cells is not flat. Section 22.3 in **The MOM3 Manual** of Pacanowski and Griffies (1999) details this point.

Furthermore, since the interior of the ocean domain uses constant cell thicknesses, in a Boussinesq model volume should be conserved (the ocean surface conserves volume when also incorporating the possibly nonzero fresh water fluxes). Hence, integrating $w\_bt_{i,j,k}$ across a particular depth $k > 1$ should leave no net volume flux upward or downward: $\sum_{i,j} dxt_{i,j}\, dyt_{i,j}\, w\_bt_{i,j,k} = 0$ for all levels k.

Finally, volume conservation warrants the MOM4 approach for diagnosing surface height on the U-cell, η^u, according to an area weighted average of the surrounding T-cell heights η^T, instead of using the minimum operation used in MOM3

and described in the Griffies et al. (2001) paper. This issue is relevant for the Boussinesq and non-Boussinesq versions of MOM4. We visit this issue in Section 5.3.

5.2 Remapping operators for horizontal fluxes

As stated in Section 5.1, MOM4 computes the horizontal components of the T-cell advection velocity in a manner necessitated by equating pressure work to buoyancy (see Chapter 6). The vertical component is diagnosed based the needs of continuity. Hence, we assume the T-cell advective velocity components are known. We thus need to determine the corresponding advective velocity on the face of velocity cells.

Advective velocities represent fluxes of volume per unit area. There are three remapping operators that take discrete volume fluxes defined at tracer points or sides of tracer cells, to discrete fluxes defined at velocity points or sides of velocity cells. Although MOM4 is generally non-Boussinesq, we use the ideas of volume conservation to generate algorithms for coupling advective velocities on the sides of tracer cells to those on the sides of velocity cells. Here, we describe the linear remapping operator taking horizontal advective velocities centered on the face of a tracer cell to the corresponding face of a velocity cell.

5.2.1 Uniformly distributed volume flux across a face

Reference to Figure 5.1 reveals four eastward fluxes of volume per area leaving a tracer cell that surround the single flux per volume leaving the corresponding velocity cell. The flux leaving a tracer cell is denoted by Et in the figure, which is a shorthand for the model's thickness weighted advective velocity *uh_et*, with the thickness factor dropped since we are concerned here with fluxes at a fixed depth. Eu denotes the corresponding eastward flux leaving the velocity cell, and this flux is to be determined in terms of the surrounding Et and appropriate grid distances.

We assume that along the face of a tracer cell, volume leaves through the face with a uniform distribution. Hence, the volume per unit length per time passing across the meridional face through the velocity point $U_{i,j}$ is given by

$$Et(i,j)\,dus(i,j) + Et(i,j+1)\,dun(i,j), \tag{5.1}$$

where the distances dus and dun are lengths along sides of the four quarter-cells comprising a single velocity cell (Figure 5.2). Likewise, the volume per unit length per time passing across the meridional face through the velocity point $U_{i+1,j}$ is given by

$$Et(i+1,j)\,dus(i+1,j) + Et(i+1,j+1)\,dun(i+1,j), \tag{5.2}$$

and the volume per unit length per time passing across the eastern face of the velocity cell $U_{i,j}$ is given by

$$Eu(i,j)\,dytn(i+1,j), \tag{5.3}$$

where Eu is to be determined in terms of Et, and the grid distance $dytn$ is the meridional distance between tracer points, as defined in Figure 5.3.

5.2.2 Lever-rule and the horizontal remapping operators

We now employ linear interpolation, or a lever-rule average, to construct the volume per time passing across the east face of the $U_{i,j}$ cell, thus leading to

$$\begin{aligned} Eu(i,j)\,dytn(i+1,j)\,dxtn(i+1,j) = [Et(i,j)\,dus(i,j) + Et(i,j+1)\,dun(i,j)]\,duw(i+1,j) \\ [Et(i+1,j)\,dus(i+1,j) + Et(i+1,j+1)\,dun(i+1,j)]\,due(i,j), \end{aligned}$$

where $dxtn$ is the zonal distance along the north face of a tracer cell (Figure 5.4). Solving for Eu leads to the remapping operator

$$\begin{aligned} Eu(i,j) &= REMAP\_ET\_TO\_EU(Et)(i,j) \\ &\equiv [Et(i,j)\,dus(i,j)\,duw(i+1,j) + Et(i,j+1)\,dun(i,j)\,duw(i+1,j) \\ &+ Et(i+1,j)\,dus(i+1,j)\,due(i,j) + Et(i+1,j+1)\,dun(i+1,j)\,due(i,j)] \\ &\quad datnr(i+1,j), \end{aligned} \tag{5.4}$$

where $datnr$ is the reciprocal area at the north face of a T-cell given by

$$datnr(i,j) = \frac{1}{dxtn(i,j)\,dytn(i,j)} \tag{5.5}$$

Analogous considerations lead to the remapping operator that takes a volume flux Nt defined at the north face of T-cells to a flux leaving the north face of U-cells

$$\begin{aligned} Nu(i,j) &= REMAP\_NT\_TO\_NU(Nt)(i,j) \\ &\equiv [Nt(i,j)\,duw(i,j)\,dus(i,j+1) + Nt(i+1,j)\,due(i,j)\,dus(i,j+1) \\ &+ Nt(i,j+1)\,duw(i,j+1)\,dun(i,j) + Nt(i+1,j+1)\,due(i,j+1)\,dun(i,j)] \\ &\quad dater(i,j+1). \end{aligned} \tag{5.6}$$

In this expression, $dater$ is the reciprocal area at the east face of a T-cell given by

$$dater(i,j) = \frac{1}{dxte(i,j)\,dyte(i,j)}, \tag{5.7}$$

$dxte$ is the zonal distance between the T-cell points (Figure 5.3) and $dyte$ is the meridional distance along the east face of the T-cell (Figure 5.4).

5.3 Remapping operator for vertical fluxes

We now consider the remapping taking vertical volume fluxes passing across the bottom face of tracer cells to the bottom face of velocity cells. This operator also maps surface height from T-cells to U-cells. This remapping is distinguished from the horizontal remapping in that there is no analogous lever-rule step. The distinction boils down to noting that the vertical remapping $REMAP\_BT\_TO\_BU$ moves vertical fluxes horizontally, whereas the east and north remapping operators move horizontal fluxes horizontally.

Reference to Figures 5.2 and 5.3, and again assuming fluxes are distributed uniformly across a cell face, indicates that the vertical flux of volume per unit length passing across the southern face of the velocity cell $U_{i,j}$ is given by

$$Bt(i,j)\,dte(i,j) + Bt(i+1,j)\,dtw(i+1,j), \tag{5.8}$$

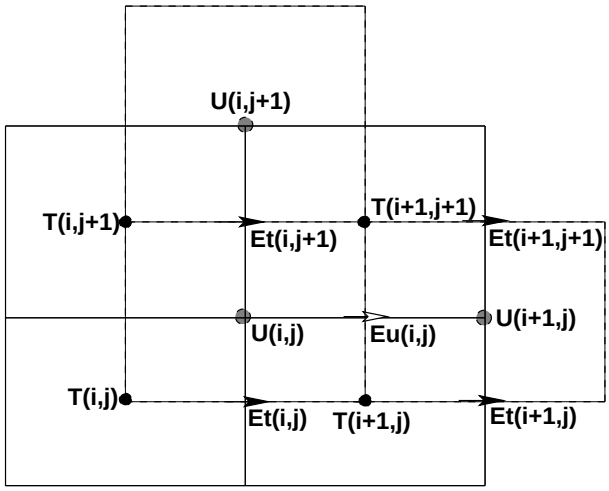

Figure 5.1: Schematic representation of the remapping function $REMAP\_ET\_TO\_EU$ defined by equation (5.4). This function is used to remap a horizontal flux of volume defined at the east face of T-cells (denoted by Et in this figure) onto a horizontal flux of volume defined at the east face of U-cells (denoted by Eu in this figure). The four fluxes $Et(i, j)$, $Et(i+1, j)$, $Et(i, j+1)$, and $Et(i+1, j+1)$ are used to construst the flux $Eu(i, j)$.

the vertical flux of volume per unit length passing across the northern face of the velocity cell $U_{i,j}$ is given by

$$Bt(i, j+1)\, dte(i, j+1) + Bt(i+1, j+1)\, dtw(i+1, j+1), \tag{5.9}$$

and the vertical flux of volume passing through the velocity cell is given by

$$Bu(i, j)\, dxu(i, j)\, dyu(i, j). \tag{5.10}$$

Assuming that the total flux passing through the velocity cell is equivalent to that passing across the northern plus southern parts of the cell leads to

$$\begin{aligned} Bu(i, j)\, dxu(i, j)\, dyu(i, j) = {} & [Bt(i, j)\, dte(i, j) + Bt(i+1, j)\, dtw(i+1, j)]\, dus(i, j) \\ & + [Bt(i, j+1)\, dte(i, j+1) + Bt(i+1, j+1)\, dtw(i+1, j+1)]\, dun(i, j). \end{aligned}$$

Solving for Bu yields the vertical remapping operator

$$\begin{aligned} Bu(i, j) = {} & REMAP\_BT\_TO\_BU(Bt)(i, j) \\ & \equiv [Bt(i, j)\, dte(i, j)\, dus(i, j) + Bt(i+1, j)\, dtw(i+1, j)\, dus(i, j) \\ & + Bt(i, j+1)\, dte(i, j+1)\, dun(i, j) + Bt(i+1, j+1)\, dtw(i+1, j+1)\, dun(i, j)] \\ & daur(i, j) \end{aligned} \tag{5.11}$$

with $daur$ the reciprocal area of the U-cell

$$daur(i, j) = \frac{1}{dxu(i, j)\, dyu(i, j)} \tag{5.12}$$

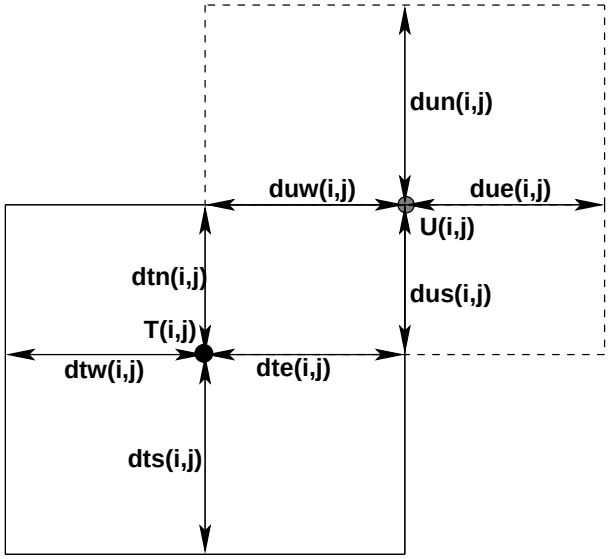

Figure 5.2: Time independent horizontal grid distances (meters) used for the tracer cell $T_{i,j}$ and velocity cell $U_{i,j}$ in MOM4. These "quarter-cell" distances are refined relative to those shown in Figures 5.4 and 5.5, and they are needed for the remapping between T and U cells when computing advection velocities. All distances are functions of both i and j due to the use of generalized orthogonal coordinates. Comparing with Figures 5.4 and 5.5 reveals the identities $dtw(i,j) + dte(i,j) = dxt(i,j)$, $dts(i,j) + dtn(i,j) = dyt(i,j)$, $duw(i,j) + due(i,j) = dxu(i,j)$, and $dus(i,j) + dun(i,j) = dyu(i,j)$.

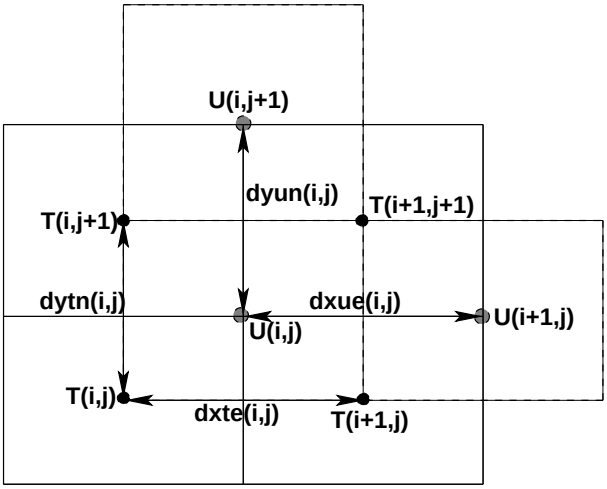

Figure 5.3: Time independent horizontal grid distances (meters) setting the spacing between tracer and velocity points in MOM4. All distances are functions of both i and j due to the use of generalized orthogonal coordinates. When these distances are combined with those in Figures 5.4 and 5.5, and the quarter-cell distances given in Figure 5.2, we then have full information about the discrete horizontal T and U cells on the model grid. Note there is some redundancy with the distances defined in Figures 5.4 and 5.5, where we have $dytn(i,j) = dyue(i-1,j)$, $dxte(i,j) = dxun(i,j-1)$, $dxue(i,j) = dxtn(i+1,j)$, and $dyun(i,j) = dyte(i,j+1)$. Additionally, comparision with Figure 5.2 leads to the identities $dyun(i,j) = dun(i,j) + dus(i,j+1)$, $dxue(i,j) = due(i,j) + duw(i+1,j)$, $dytn(i,j) = dtn(i,j) + dts(i,j+1)$, and $dxte(i,j) = dte(i,j) + dtw(i+1,j)$.

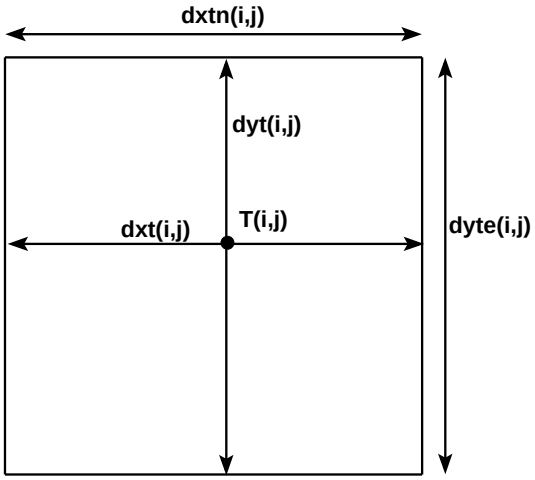

Figure 5.4: Time independent horizontal grid distances (meters) used for the tracer cell $T_{i,j}$ in MOM4. $dxt_{i,j}$ and $dyt_{i,j}$ are the grid distances of the tracer cell in the generalized zonal and meridional directions, and $dat_{i,j} = dxt_{i,j}\, dyt_{i,j}$ is the area of the cell. The grid distance $dxtn_{i,j}$ is the zonal width of the north face of a tracer cell, and $dyte_{i,j}$ is the meridional width of the east face. Note that the tracer point $T_{i,j}$ is not generally at the center of the tracer cell. Distances are functions of both i and j due to the use of generalized orthogonal coordinates.

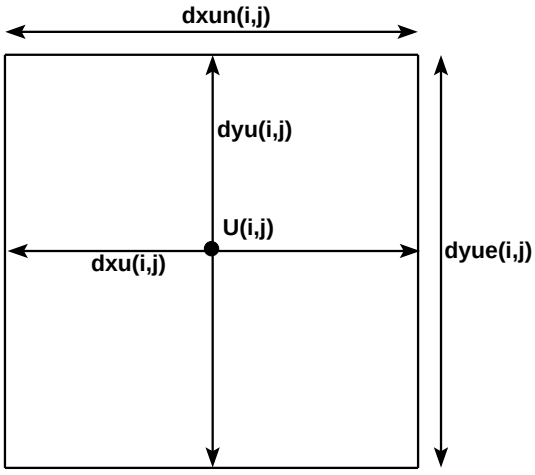

Figure 5.5: Time independent horizontal grid distances (meters) used for the velocity cell $U_{i,j}$ in MOM4. $dxu_{i,j}$ and $dyu_{i,j}$ are the grid distances of the velocity cell in the generalized zonal and meridional directions, and $dau_{i,j} = dxu_{i,j}\, dyu_{i,j}$ is the area of the cell. The grid distance $dxun_{i,j}$ is the zonal width of the north face of a velocity cell, and $dyue_{i,j}$ is the meridional width of the east face. Note that the velocity point $U_{i,j}$ is not generally at the center of the velocity cell. Distances are functions of both i and j due to the use of generalized orthogonal coordinates.

5.4 Remapping error

There are two ways to compute the vertical velocity on the velocity cell. The first method is to compute this velocity according to the requirements of continuity over the velocity cell, using the convergence of the remapped horizontal advective velocities entering the velocity cell. The second method is to use the vertical remap operator *REMAP_BT_TO_BU* to move the vertical velocity on the tracer cells to the velocity cells. The result of these two approaches is identical *when* the tracer and velocity grids are related by a linear average operator, as is the case for a spherical grid. The need to maintain a linear relation between the tracer and velocity grids is based on the use of linear methods to derive the remapping operators.

5.4.1 Linear grids

MOM4 computes a diagnostic that examines the differences between the two approaches for computing vertical advective velocities. It reports the difference as a "remapping error." If the numerical discretization is self-consistent, then the remapping error for a spherical grid will be roundoff, with values on the order of $10^{-20}\mathrm{m\,s^{-1}}$ common. Therefore, with a spherical grid, the remapping error provides a check on the self-consistency of the grid distances and the remapping operators. Effectively, what is done is to check that volume is conserved with the remapping operators. Even when running a non-Boussinesq model, the remapping operators are constructed to respect volume conservation.

5.4.2 Nonlinear grids

For a grid defined via a nonlinear transformation of the spherical grid, such as the bipolar region of the tripolar grid, the grid no longer maintains a linear relation between tracer and velocity cell distances. The result is a nontrivial remapping error. This error can be reduced by defining new remapping operators that account for a generally nonlinear relation between tracer and velocity grid distances. Such remains to be done for MOM4.

One consequence of the nonzero remapping error is that for a flat bottom model in regions where the grid distances are nonlinearly related, $w\_bu_{i,j,k=Nk}$ does not vanish, even though continuity is maintained for all the grid cells. The problem is that $w\_bu_{i,j,k=0}$ is defined by

$$w\_bu_{i,j,k=0} = REMAP\_BT\_TO\_BU(w\_bt_{i,j,k=0}). \tag{5.13}$$

For nonlinear grids, the linear operator *REMAP_BT_TO_BU* results in a slightly different value for $w\_bu_{i,j,k=0}$ than would result from an integration of the continuity equation upwards from the bottom, assuming $w\_bu_{i,j,k=Nk} = 0$. Because the vertical advective flux at the ocean bottom is masked so that no momentum will spuriously leak out the bottom of the ocean, having $w\_bu_{i,j,k=Nk}$ slightly nonzero is of no consequence. Nonetheless, it would be more satisfying to have a general remapping operator to clean-up this issue.

5.5 Subtleties at the southern-most row

Consider the special case of $j = 0$ in Figure 5.1. This row is strictly south of the southern-most latitude comprising the computational domain of the model. However, there is a subtlety related to the treatment of the eastward volume flux leaving the velocity cell $U_{i,j=0}$. That is, since this cell straddles the tracer cells $T_{i,j=0}$ and $T_{i,j=1}$, it contains some portion that is within the computational domain. Thus, the eastward volume flux leaving this cell is nonzero, as it is comprised of weighted average of the four surrounding eastward fluxes leaving the tracer cells. Because the remapping function (5.4) is normalized with the area $datn = dxtn\, dytn$ for $j = 0$, it is necessary to know the grid factors $dxtn_{i,j=0}$ and $dytn_{i,j=0}$. In particular, $dytn_{i,j=0}$ is the distance between the computed tracer point $T_{i,j=1}$ and the tracer point $T_{i,j=0}$ that lives outside the computational domain.

The need to know $dytn_{i,j=0}$ presents a problem with the MOM4 method for computing grid specifications. Grids in MOM4 are computed in two steps. First, there is a preprocessing step whereby grid factors are computed in a generic manner compatible with other models used at GFDL. This step knows nothing about halo regions, so it only computes grid information over the computational domain. The result of this step is a NetCDF grid specification file. The second step is to read the grid specification file into MOM4 and translate the generic grid information into grid arrays used by MOM4. Since there is no halo information contained in the grid specification file, we cannot unambiguously specify values for the grid outside the computational domain. And because we need $dytn_{i,j=0}$ to be known consistently with the values for $dytn_{i,j}$ with $j > 0$, we cannot simply fill $dytn_{i,j=0}$ with an arbitrary placeholder. If we do so, then the remapping function used to compute the eastward flux leaving the velocity cell $U_{i,j=0}$ will be incorrect, thus compromising the vertical velocity leaving $U_{i,j=0}$. The symptom will be most notable in spuriously large values of the vertical velocity on the velocity cell at the computational row $j = 1$, as well as huge remapping errors at $j = 1$.

There are three solutions to this problem. First, we could extend the definition of the grid within the grid specification file to include the extra $j = 0$ row. This solution has been rejected since it adds an extra calculation that is specific to the northeast B-grid used in MOM4. As the grid specification file is designed for use by all grid point models, it is not desirable to corrupt it with special cases. The second solution is to require the southern-most row in MOM4 to be filled with land. This solution is arguably inelegant, and it has indeed prompted some debate with the MOM4 developers. Yet this is the solution used in the GFDL ice model, which is also on a B-grid, and so it has been the most popular solution thus far in MOM4 when aiming to couple MOM4 to other models. The third solution is to extend the grid southward within MOM4 after reading in the grid specification file. This solution is appropriate if we can assume a spherical grid in the southern part of the domain, as true in most cases.

CHAPTER

SIX

Energetics on the B-grid lattice

Contents

The purpose of this chapter is to discuss energetic balances on the discrete B-grid lattice. Most notably, choosing to maintain the integrity of certain balances prescribes the form of the discrete advection velocity components located on the sides of tracer cells. It also necessitates the use of second order finite differenced advective fluxes of momentum. Tracer fluxes can remain arbitrarily discretized. Energy balance diagnostics are important methods of use for checking the integrity of algorithms.

6.1 Introduction

This chapter is concerned with details of how the discrete model respects the conversion between various forms of energy. For example, how does work done by currents against the horizontal pressure gradient get converted into work against gravity and/or compression? How does globally integrated discrete advection of momentum get converted to boundary contributions? How do conversions differ for Boussinesq and non-Boussinesq fluids?

As discussed in Griffies (2004), energy conversions in the continuum largely follow from manipulations using the kinematic and dynamic balances. Analogous manipulations occur on the lattice, yet with more care given to how various terms are discretized. Maintaining exact discrete energic conversions is neither necessary nor sufficient for ensuring a physically realistic solution. However, without analytical solutions to compare with, discrete energy conversions afford the ocean modeler some insurance that the numerical algorithm is performing with a degree of physical integrity.

6.1.1 The utility of discrete energy conversions

Arbitrary discretizations generally fail to satisfy exact energy conversion properties. Hence, maintaining discrete energy conversions is a choice going beyond the usual goal of providing a consistent discretization. Indeed, it can be considered a *guiding-principle*, of which there are others affecting the design of MOM's numerical algorithms. These principles generally reduce many of the arbitrary choices otherwise available when discretizing terms in a continuous partial differential equation. Another analogous principle used in MOM insists that the discrete friction and diffusion operators dissipate the discrete kinetic energy and discrete tracer variance, respectively. Griffies (2004) details these issues.

MOM is predominantly of use for ocean climate modeling, where integrations of many thousands of years are common. Therefore, it is essential that systematic errors in algorithms, however small, be obviated. It is important for the development of algorithms to have well defined energetic balances to test code integrity. Without known analytic solutions, there remain few other methods to track down bugs, short of hoping they manifest in an egregious and obviously unphysical manner.

Unfortunately, it is often found that some physically relevant properties are sacrificed in order to ensure discrete energy conservation. Most notably, the smoothness of the solution is often compromised. Hence, some model developers consider order of accuracy to be the prime consideration for a numerical model. Yet highly accurate operators do not always afford themselves exact discrete conservation laws; only approximate laws.

MOM maintains the traditional use of second order numerics for the momentum equation. Doing so affords satisfaction of the discrete energy conversion properties described in this chapter. Efforts to increase order of accuracy are focused on tracer advection, where various schemes are available beyond the traditional second order scheme of Bryan (1969). Notably, the tracer advection scheme does not affect considerations in this chapter.

6.1.2 Continuous equations for the ocean model

The equations considered in this chapter represent discrete realizations of the continuum model equations presented in Griffies (2004). For completeness, we repeat them here assuming hydrostatic balance. The non-Boussinesq hydrostatic equations are

$$\rho_{,t} + \rho_o \nabla \cdot \mathbf{v} = 0 \tag{6.1}$$

$$(D\,\overline{\rho}^z)_{,t} = -\rho_o \nabla \cdot \mathbf{U} + \rho_w\, q_w \tag{6.2}$$

$$\mathbf{u}_{,t} + \nabla \cdot (\mathbf{v}\,\mathbf{u}^\rho) + \mathcal{M}\,\hat{\mathbf{z}} \wedge \mathbf{v}^\rho = -f\,\hat{\mathbf{z}} \wedge \mathbf{v} - \nabla(p/\rho_o) + (\rho/\rho_o)\,\mathbf{F}^{(\mathbf{u})} \tag{6.3}$$

$$p_{,z} = -\rho\, g \tag{6.4}$$

$$(\rho\, T)_{,t} + \rho_o \nabla \cdot (\mathbf{v}\, T) = -\nabla \cdot (\rho\, \mathbf{F}) + \rho\, \mathcal{S}, \tag{6.5}$$

where

$$\rho\, \mathbf{v}^\rho = \rho_o\, \mathbf{v} \tag{6.6}$$

is the linear momentum density. For finite domains, these equations are combined with the surface and bottom kinematic boundary conditions

$$\rho\, \eta_{,t} + \rho_o\, \mathbf{u} \cdot \nabla \eta = \rho_o\, w + \rho_w\, q_w \qquad \text{at } z = \eta \tag{6.7}$$

$$\mathbf{u} \cdot \nabla H + w = 0 \qquad \text{at } z = -H. \tag{6.8}$$

The Boussinesq hydrostatic equations are recovered by setting $\rho \to \rho_o$, except when multiplying gravity

$$\nabla \cdot \mathbf{v} = 0 \tag{6.9}$$

$$\eta_{,t} = -\nabla \cdot \mathbf{U} + q_w \tag{6.10}$$

$$\mathbf{u}_{,t} + \nabla \cdot (\mathbf{v}\,\mathbf{u}) + \mathcal{M}\,\hat{\mathbf{z}} \wedge \mathbf{v} = -f\,\hat{\mathbf{z}} \wedge \mathbf{v} - \nabla(p/\rho_o) + \mathbf{F}^{(\mathbf{u})} \tag{6.11}$$

$$p_{,z} = -\rho\, g \tag{6.12}$$

$$T_{,t} + \nabla \cdot (\mathbf{v}\, T) = -\nabla \cdot \mathbf{F} + \mathcal{S}. \tag{6.13}$$

The surface and bottom kinematic boundary conditions are

$$\eta_{,t} + \mathbf{u} \cdot \nabla \eta = w + q_w \qquad \text{at } z = \eta \tag{6.14}$$

$$\mathbf{u} \cdot \nabla H + w = 0 \qquad \text{at } z = -H. \tag{6.15}$$

6.1.3 Kinetic energy budget for a continuum ocean model parcel

As discussed in Griffies (2004), the kinetic energy of a fluid parcel is modified by the effects of pressure and friction. It is useful to summarize these results in order to anticipate some of the discrete manipulations made in this chapter. For this purpose, multiply the momentum equation (6.3) by ρ_o to find

$$(\rho\, \mathbf{u}^\rho)_{,t} + \nabla \cdot (\rho\, \mathbf{v}^\rho\, \mathbf{u}^\rho) + \rho\, \mathcal{M}^\rho\, \hat{\mathbf{z}} \wedge \mathbf{v}^\rho = -f\,\hat{\mathbf{z}} \wedge \rho\, \mathbf{v}^\rho - \nabla p + \rho\, \mathbf{F}^{(\mathbf{u})}, \tag{6.16}$$

where we used the relation $\rho\, \mathbf{v}^\rho = \rho_o\, \mathbf{v}$ for the linear momentum density. Now take the inner product of this budget with the horizontal velocity $\mathbf{u}^\rho$ to find

$$\mathbf{u}^\rho \cdot (\rho\, \mathbf{u}^\rho)_{,t} + (\mathbf{u}^\rho)_i\, \partial_j (\rho\, (\mathbf{v}^\rho)_j\, (\mathbf{u}^\rho)_i) = -\mathbf{u}^\rho \cdot \nabla p + \rho\, \mathbf{u}^\rho \cdot \mathbf{F}^{(\mathbf{u})}, \tag{6.17}$$

where tensor labels were exposed where needed for clarity. Use of mass conservation in the form $\rho_{,t} + \nabla \cdot (\rho \, \mathbf{v}^\rho) = 0$ leads to

$$(\rho \, \mathcal{K})_{,t} + \nabla \cdot (\rho \, \mathbf{v}^\rho \, \mathcal{K}) = -\mathbf{u}^\rho \cdot \nabla p + \rho \, \mathbf{u}^\rho \cdot \mathbf{F}^{(\mathbf{u})}, \tag{6.18}$$

where

$$\mathcal{K} = \frac{1}{2} \mathbf{u}^\rho \cdot \mathbf{u}^\rho \tag{6.19}$$

is the kinetic energy per mass of a continuum model fluid parcel. Notably, it is the model's velocity $\mathbf{u}^\rho$, not $\mathbf{u}$, that determines the model's kinetic energy. This distinction is relevant only for the non-Boussinesq fluid, since for the Boussinesq fluid $\mathbf{u} = \mathbf{u}^\rho$.

6.1.4 Semi-discrete momentum budget

A starting point for discretizing the continuum equations is to integrate these equations vertically over the extent of a model grid cell. Vertical integration allows for an explicit treatment of surface and bottom boundary conditions, whose details are crucial for the proper forcing of the ocean model. Griffies (2004) derived such *semi-discrete* budgets, where it was shown that the momentum budget for an interior model grid cell with $k > 1$ is given by

$$\begin{aligned} h_{z_k} \, (\partial_t + f \, \hat{\mathbf{z}} \wedge) \, \mathbf{u}_{z_k} = & -(h \, \mathcal{M} \, \hat{\mathbf{z}} \wedge \mathbf{u}^\rho)_{z_k} - \nabla \cdot (h \, \mathbf{u} \, \mathbf{u}^\rho)_{z_k} - (h \, \nabla p)_{z_k} / \rho_o + (h \, \rho \, \mathbf{F}^{\mathbf{u}}_{horz})_{z_k} \\ & - [(w \, \mathbf{u}^\rho)_{z_{k-1}} - (w \, \mathbf{u}^\rho)_{z_k}] + [(\rho \, \kappa \, \mathbf{u}^\rho_{,z})_{z_{k-1}} - (\rho \, \kappa \, \mathbf{u}^\rho_{,z})_{z_k}] / \rho_o, \end{aligned} \tag{6.20}$$

with h_k the vertical thickness of the cell. The surface cell $k = 1$ has the budget

$$\begin{aligned} h_{z_1} \, (\partial_t + f \, \hat{\mathbf{z}} \wedge) \, \mathbf{u}_{z_1} = & -(h \, \mathcal{M} \, \hat{\mathbf{z}} \wedge \mathbf{u}^\rho)_{z_1} - \nabla \cdot (h \, \mathbf{u} \, \mathbf{u}^\rho)_{z_1} - (h \, \nabla p)_{z_1} / \rho_o + (h \, \rho \, \mathbf{F}^{\mathbf{u}}_{horz})_{z_1} \\ & + \rho_o^{-1} \, [\rho_o \, w \, \mathbf{u}^\rho - \rho \, \kappa \, \mathbf{u}^\rho_{,z}]_{z_1} + \rho_o^{-1} \, [-\mathbf{u}^\rho_{z_1} \, \rho \, \eta_{,t} + \rho_w \, q_w \, \mathbf{u}^\rho_w + \boldsymbol{\tau}]. \end{aligned} \tag{6.21}$$

The budget for a Boussinesq model is recovered by setting densitites to ρ_o and $\mathbf{u} = \mathbf{u}^\rho$. For the surface cell, volume conservation in the form $\eta_{,t} = -\nabla \cdot \mathbf{U} + q_w$ leads to the Boussinesq balance

$$\begin{aligned} h_{z_1} \, (\partial_t + f \, \hat{\mathbf{z}} \wedge) \, \mathbf{u}_{z_1} = & -(h \, \mathcal{M} \, \hat{\mathbf{z}} \wedge \mathbf{u})_{z_1} - \nabla \cdot (h \, \mathbf{u} \, \mathbf{u})_{z_1} - (h \, \nabla p)_{z_1} / \rho_o + (h \, \mathbf{F}^{\mathbf{u}}_{horz})_{z_1} \\ & + (w \, \mathbf{u} - \kappa \, \mathbf{u}_{,z})_{z_1} + [q_w \, (\mathbf{u}_w - \mathbf{u}_{z_1}) + \mathbf{u}_{z_1} \nabla \cdot \mathbf{U} + \boldsymbol{\tau} / \rho_o]. \end{aligned} \tag{6.22}$$

6.1.5 Vertical advective velocities

As discussed in Griffies (2004), the vertical component to the advective velocity is diagnosed by constraining the discrete fluid to satisfy mass continuity over a grid cell. At the base of a grid cell at depth level $k > 1$, the model's vertical advective velocity is given by

$$w_{z_k} = w_{z_{k-1}} + \nabla \cdot (h \, \mathbf{u})_{z_k} + h_{z_k} \, \partial_t \, (\rho / \rho_o)_{z_k}, \tag{6.23}$$

where the time derivative term is dropped for Boussinesq fluids. For surface cells where $k = 1$,

$$\rho_o \, w_{z_1} = (-\rho_w \, q_w + \rho_{z_1} \, \eta_{,t}) + \nabla \cdot (h \, \mathbf{u})_{z_k} + h_{z_k} \, \partial_t \, (\rho / \rho_o)_{z_k}, \tag{6.24}$$

thus prompting us to formally set

$$\rho_o \, w_{z_0} = -\rho_w \, q_w + \rho_{z_1} \, \partial_t \, \eta \tag{6.25}$$

which in the Boussinesq case reduces to

$$w_{z_0} = -\nabla \cdot \mathbf{U}. \tag{6.26}$$

Note that it is important not to confuse the advective velocity w_{z_0}, diagnosed through continuity, with the distinct vertical velocity $w(z = \eta)$ used in the surface kinematic boundary condition.

6.2 Pressure work conversions

We follow here the derivation first given by Semtner (1974) for the rigid lid Boussinesq model. Generalizations are given here for MOM4's bottom partial cells, explicit free surface, and non-Boussinesq formulation. A practical result from this section is the specification of discrete advection velocities used to transport tracers.

6.2.1 Continuum results: Part I

Following the discussion of Section 6.1.3, where we derived the local budget for kinetic energy of a parcel

$$(\rho \, \mathcal{K})_{,t} + \nabla \cdot (\rho \, \mathbf{v}^\rho \, \mathcal{K}) = -\mathbf{u}^\rho \cdot \nabla p + \rho \, \mathbf{u}^\rho \cdot \mathbf{F}^{(\mathbf{u})}, \tag{6.27}$$

we start by noting that the projection of the horizontal velocity $\mathbf{u}^\rho$ onto the horizontal pressure gradient is given by

$$\begin{aligned} \mathbf{u}^\rho \cdot \nabla p &= \mathbf{v}^\rho \cdot \nabla p - w^\rho \, p_{,z} \\ &= \nabla \cdot (\mathbf{v}^\rho \, p) - p \, \nabla \cdot \mathbf{v}^\rho + \rho \, g \, w^\rho \end{aligned} \tag{6.28}$$

where the hydrostatic balance $p_{,z} = \rho \, g$ was used. The divergence $\nabla \cdot \mathbf{v}^\rho$ vanishes for a Boussinesq fluid, yet it represents a nontrivial conversion of kinetic to internal energy for the non-Boussinesq fluid (see Griffies (2004)). Integration over the full ocean domain yields

$$-\int dV \, \mathbf{u}^\rho \cdot \nabla p = \int_{z=\eta} dA \, p \, (\mathbf{u}^\rho \cdot \nabla \eta - w^\rho) + \int dV \, (\, p \, \nabla \cdot \mathbf{v}^\rho - w^\rho \, \rho \, g) \tag{6.29}$$

where use was made of periodic and/or no-normal flow side boundary conditions, as well as the bottom kinematic boundary condition. The surface kinematic boundary

$$\mathbf{u}^\rho \cdot \nabla \eta - w^\rho = \rho_w \, q_w - \rho \, \eta_{,t} \tag{6.30}$$

leads to

$$-\int dV \, \mathbf{u}^\rho \cdot \nabla p = \int_{z=\eta} dA \, p \, [(\rho_w / \rho) \, q_w - \eta_{,t}] + \int dV \, (\, p \, \nabla \cdot \mathbf{v}^\rho - w^\rho \, \rho \, g). \tag{6.31}$$

Note that mass conservation over a fluid column allows us to alternatively write

$$\rho_w \, q_w - \rho \, \eta_{,t} = -\rho_o \, \nabla \cdot \mathbf{U} + \int_{-H}^{\eta} dz \, \rho_{,t} \tag{6.32}$$

with the second term, the so-called *steric contribution*, absent for the volume-conserving Boussinesq fluid (see Griffies (2004) for more discussion of steric effects). Indeed, for the Boussinesq fluid we have (1) $\mathbf{v} = \mathbf{v}^{\rho}$, (2) $\nabla \cdot \mathbf{v} = 0$, (3) the density $\rho(\eta)$ appearing in the surface kinematic boundary condition is set to ρ_o, (4) $\eta_{,t} = -\nabla \cdot \mathbf{U} + q_w$ expressing volume conservation over a fluid column, thus leading to

$$-\int dV \, \mathbf{u} \cdot \nabla p = \int_{z=\eta} dA \, p \, \nabla \cdot \mathbf{U} - \int dV \, w \, \rho \, g. \tag{6.33}$$

It is useful to consider three special cases, the simplest of which is the rigid lid Boussinesq ocean. Most rigid lid models suppress the addition of fresh water[1], in which case $\nabla \cdot \mathbf{U} = 0$ thus rendering

$$\int dV \, \mathbf{u} \cdot \nabla p = \int dV \, w \, \rho \, g. \tag{6.34}$$

That is, for the rigid lid hydrostatic Boussinesq ocean without fresh water forcing, the global effects of work done by the horizontal currents against horizontal pressure gradients are equal to the work by vertical currents against gravity. This equality affords the following interpretation. In a hydrostatic fluid, vertically integrated density directly determines pressure. Hence, work against a horizontal pressure gradient force is associated with a rearrangement of the density field in the vertical, which then involves work against gravity.

A free surface Boussinesq fluid satisfies the more general balance

$$-\int dV \, \mathbf{u} \cdot \nabla p = \int_{z=\eta} dA \, p \, \nabla \cdot \mathbf{U} - \int dV \, w \, \rho \, g. \tag{6.35}$$

The surface term accounts for the possibility of atmospheric pressure to apply work to a dilatating vertical column of fluid.

For a free surface non-Boussinesq fluid, the full identity (6.37) is applicable. The new term $p \, \nabla \cdot \mathbf{v}^{\rho}$ accounts for the ability of pressure forces internal to the fluid to do work on dilatating fluid parcels, and the term $\int_{z=\eta} dA \, (p/\rho) \, (\int_{-H}^{\eta} dz \, \rho_{,t})$ accounts for work done by atmospheric pressure on a column of ocean fluid experiencing expansion and/or contraction due to changes in the depth integrated density–the so-called *steric effects*.

6.2.2 Continuum results: Part II

As noted in Section 6.1.1, one motivation for considering the discrete energy conversions is that they provide guidance on how to discretize objects in the model. In particular, they guide how to discretize advection velocities on the faces of tracer

[1] Huang (1993) noted the possibility of relaxing this restriction, yet we know of no realistic model having implemented this approach.

cells. With the B-grid used in MOM4, it is otherwise not obvious how to compute these velocities. An alternative to the approach in Section 6.2.1 provides insight for this purpose, with the distinction relevant only for the non-Boussinesq case. Instead of $\mathbf{u}^\rho \cdot \nabla p$, we here consider

$$\begin{aligned} \mathbf{u} \cdot \nabla p &= \mathbf{v} \cdot \nabla p - w\, p_{,z} \\ &= \nabla \cdot (\mathbf{v}\, \mathbf{p}) - p\, \nabla \cdot \mathbf{v} + \rho\, g\, w. \end{aligned} \tag{6.36}$$

The divergence term $\nabla \cdot \mathbf{v} = -\rho_{,t}/\rho_o$ vanishes for the Boussinesq fluid. Integrating over the ocean domain and using the surface and bottom kinematic boundary conditions leads to

$$-\rho_o \int dV\, \mathbf{u} \cdot \nabla p = \int_{z=\eta} dA\, p\, (\rho_w\, q_w - \rho\, \eta_{,t}) - \rho_o \int dV\, [\, p\, (\rho_{,t}/\rho_o) + w\, \rho\, g], \tag{6.37}$$

where use was made of periodic and/or no-normal flow side boundary conditions. This result reduces to the same Boussinesq result (6.33) considered in Section 6.2.2. The non-Boussinesq case is distinct.

6.2.3 B-grid results

We now consider manipulations of the globally integrated discrete B-grid representation of $\mathbf{u} \cdot \nabla p$ analogous to those discussed in Section 6.2.2. Note that in this section, discrete grid labels will be exposed when appropriate, with many labels suppressed to reduce clutter.

As stated in Section 6.2.2, we prefer a discrete analysis of $\mathbf{u} \cdot \nabla p$ rather than $\mathbf{u}^\rho \cdot \nabla p$ because of the guidance $\mathbf{u} \cdot \nabla p$ provides for discretizing the tracer advection velocities, as well as the ability to use the resulting discrete balance to check code integrity. However, for the non-Boussinesq case, the direct interpretation of each term according to a work per time is not as straightforward as for the considerations of Section 6.2.1.

The domain integrated scalar product of the horizontal velocity $\mathbf{u}$ and the horizontal pressure gradient $-\nabla p$ is given by

$$\begin{aligned} \mathcal{P} \equiv & -\sum_{i,j,k} dau\, dhu\, [u\, FDX\_NT(FAY(p)) + v\, FDY\_ET(FAX(p))] \\ + & \; g \sum_{i,j,k} dau\, dhu\, [u\, FAY(FAX(\rho)\, \delta_i H)/dxu + v\, FAX(FAY(\rho)\, \delta_j H)/dyu] \end{aligned} \tag{6.38}$$

MOM4 employs the following forward derivative operators

$$FDX\_NT(a) = \frac{a_{i+1} - a_i}{dxu} \tag{6.39}$$

$$FDY\_ET(a) = \frac{a_{j+1} - a_j}{dyu}, \tag{6.40}$$

where the derivatives live on the east and north faces, respectively, of a tracer cell. The operators $\delta_i H$ and $\delta_j H$ compute the forward difference

$$\delta_i H = H_{i+1} - H_i \tag{6.41}$$

$$\delta_j H = H_{y+1} - H_y \tag{6.42}$$

of the bottom topography. The first term in equation (6.38) is the lateral pressure gradient taken between cells living on the same discrete k-level. The second term arises from the use of bottom partial cells, where the depth of a k-level is generally a function of horizontal position. This term is the same that appears in terrain-following *sigma* models. In both cases, the horizontal pressure gradient is given by two terms

$$\nabla_z p = (\nabla_\sigma + \nabla_\sigma H\, \partial_z)\, p = \nabla_\sigma p - \rho\, g\, \nabla_\sigma H, \tag{6.43}$$

where the hydrostatic balance $p_{,z} = -\rho\, g$ was used to reach the second relation. The slope of sigma surfaces can reach $1/100$ next to continental slopes, at which point the "sigma-coordinate correction term" $\rho\, g\, \nabla_\sigma H$ can be on the order of $\nabla_\sigma p$. In this case, the horizontal pressure force becomes the result of two sizable terms, each having separate numerical errors that generally do not cancel. The result can be spurious pressure forces that drive nontrivial unphysical currents. As described by Pacanowski and Gnanadesikan (1998), the sigma correction term introduces only very minor spurious currents in MOM due to (1) MOM's use of z-levels throughout the region above the topography, thus isolating the sigma-correction term to just the bottom-most level, (2) The discrete horizontal pressure gradient is chosen so that if pressure is a linear function of depth, then the discrete gradient vanishes. This discretization choice greatly reduces the magnitude of spurious flows.

6.2.3.1 Defining the horizontal advection velocities

Focus on the zonal piece of the first term

$$\begin{aligned} \mathcal{P}_{1x} &\equiv -\sum_{i,j,k} dau\ dhu\ u\, FDX\_NT(FAY(p)) \\ &= -\frac{1}{2}\sum dyu\ dhu\ u\, \delta_i(p_j + p_{j+1}) \\ &= -\sum BAY(dyu\ dhu\ u)\, \delta_i p_j, \end{aligned} \tag{6.44}$$

where the boundary terms drop out for either periodic or solid wall conditions, and we introduced the backward meridional average operator

$$BAY(a) = \frac{a_j + a_{j-1}}{2}. \tag{6.45}$$

Let us now *define* the zonal thickness weighted advective transport velocity on the eastern face of a tracer cell as

$$uh\_et_{i,j,k} = \frac{BAY(dyu\ dhu\ u)}{dyte_{i,j}}, \tag{6.46}$$

where $dyte_{i,j}$ is the meridional width of the tracer cell's east side (see Figure 6.2 for definitions of grid distances). Doing so leads to

$$\begin{aligned} \mathcal{P}_{1x} &= -\sum \delta_i p\, (dyte\, uh\_et) \\ &= \sum p\, \delta_i\, (dyte\, uh\_et) \\ &= \sum p\, dat\, BDX\_ET(uh\_et), \end{aligned} \tag{6.47}$$

where boundary terms vanish, and

$$BDX\_ET(a) = \frac{a_{i,j}\, dyte_{i,j} - a_{i-1,j}\, dyte_{i-1,j}}{dat_{i,j}} \tag{6.48}$$

is a backwards finite difference operator for fields defined on the east face of tracer cells. Similar manipulations with the meridional term $v\,\partial_y p$ leads to

$$\mathcal{P}_1 = \sum p\ dat\ (BDX\_ET(uh\_et) + BDY\_NT(vh\_nt)), \tag{6.49}$$

with

$$vh\_nt_{i,j,k} = \frac{BAX(dxu\ dhu\ v)}{dxtn_{i,j}} \tag{6.50}$$

the meridional tracer advective velocity on the north face of the tracer cell, and

$$BDY\_NT(a) = \frac{a_{i,j}\, dxtn_{i,j} - a_{i,j-1}\, dxtn_{i,j-1}}{dat_{i,j}} \tag{6.51}$$

is a backwards finite difference operator for fields defined on the north face of tracer cells.

The horizontal advective velocities uh_et and vh_nt are defined at the sides of the tracer cells and at the depth of the tracer point. Hence, their finite differenced derivatives are defined at the tracer point. The corresponding vertical velocity w_bt_k is also defined at the horizontal tracer point, yet at the bottom of the tracer cell, at the "W-point". As discussed in Section 6.1.5, the vertical advective velocity component is diagnosed through continuity. In a discrete form, this velocity component is given by

$$w\_bt_k = w\_bt_{k-1} + BDX\_ET(uh\_et_k) + BDY\_NT(vh\_nt_k) + dht_k\,\partial_t\,(\rho_k/\rho_o). \tag{6.52}$$

In this equation, $dht_{i,j,k}$ is the vertical thickness of the tracer cell, the time derivative term is absent for Boussinesq fluids, and (see Section 6.1.5)

$$\rho_o\, w\_bt_0 = \rho_1\,\partial_t\,\eta - \rho_w\, q_w \tag{6.53}$$

for the non-Boussinesq fluid, and

$$w\_bt_0 = -\nabla\cdot\mathbf{U} \tag{6.54}$$

for the Boussinesq fluid.

6.2.3.2 Completing the manipulations for $\mathcal{P}_1$

Substitution of expression (6.52) for the vertical advective velocity component into equation (6.49) leads to

$$\mathcal{P}_1 = -\sum p_k\ dat\ (w\_bt_{k-1} - w\_bt_k + dht_k\,\partial_t\,(\rho_k/\rho_o)), \tag{6.55}$$

with rearrangement of the sums rendering

$$\mathcal{P}_1 = \sum_{i,j} dat_{i,j}\,(-p_1\, w\_bt_0 + p_{nk+1}\, w\_bt_{nk}) \tag{6.56}$$

$$+ \sum_{i,j,k} dat\ dhwt_k\ w\_bt_k\ \frac{p_k - p_{k+1}}{dhwt_k} - \frac{1}{\rho_o}\sum_{i,j,k} p_k\, dat\, dht_k\,\partial_t\,\rho_k, \tag{6.57}$$

where $dhwt_{i,j,k}$ is the vertical distance between tracer points T_k and T_{k+1}. The $p_{nk+1}\, w\_bt_{nk}$ boundary term vanishes since $w\_bt_{nk} = 0$; however, the surface term $p_1\, w\_bt_0$ is nonzero for a free surface model where $w\_bt_0 \neq 0$ (e.g., equations (6.53) and (6.54)).

The discrete hydrostatic pressure is computed as an estimate of pressure at the depth of the tracer point, rather than as an average pressure over the full tracer cell (Figure 6.1). That is,

$$p_{k+1} = p_k + g\, dhwt_k\, \overline{\rho_k}^z, \tag{6.58}$$

where $\overline{\rho_k}^z = (\rho_k + \rho_{k+1})/2$ is the vertically averaged density over the tracer cell. Using this pressure then leads to

$$\mathcal{P}_1 = -\sum_{i,j} dat_{i,j} \left(p_1\, w\_bt_0 + g \sum_k dhwt_k\, w\_bt_k\, \overline{\rho_k}^z + \frac{1}{\rho_o} \sum_k p_k\, dht_k\, \partial_t\, \rho_k \right). \tag{6.59}$$

6.2.3.3 Correspondence to the continuum results

It is useful to make a correspondence with terms from the continuum given in Section 6.2.2. First, a rigid lid Boussinesq fluid with zero fresh water flux has

$$\mathcal{P}_1 = -\sum_{i,j} dat_{i,j} \left(g \sum_k dhwt_k\, w\_bt_k\, \overline{\rho_k}^z \right), \tag{6.60}$$

where $w\_bt_0 = 0$ and the density time tendency term vanishes. Hence, in this case, work by horizontal currents on the horizontal pressure gradient equals work against gravity. Allowing for a free surface Boussinesq fluid yields

$$\mathcal{P}_1 = -\sum_{i,j} dat_{i,j} \left(-p_1\, \nabla \cdot \mathbf{U} + g \sum_k dhwt_k\, w\_bt_k\, \overline{\rho_k}^z \right), \tag{6.61}$$

where the density time tendency term vanishes and $w\_bt_0 = -\nabla \cdot \mathbf{U}$. The added term accounts for work done by pressure p_1 at the surface tracer point on a dilatating vertical column of fluid. This pressure is given by

$$p_1 = \rho_1\, g\, (dhwt_{k=0} + eta\_t) + p_{atm} \tag{6.62}$$

where eta_t is the surface height on tracer cells, and $dhwt_{k=0}$ is the distance from $z = 0$ to the $k = 1$ tracer point z_1. This pressure has a contribution from the hydrostatic pressure within the fluid layer between $z = eta\_t$ and $z = z_1$, and that from the overlying atmosphere. For a non-Boussinesq fluid, equation (6.53) for w_bt_0 leads to

$$\mathcal{P}_1 = -\sum_{i,j} dat_{i,j} \left((p_1/\rho_o)\, (\rho_1\, \partial_t \eta - \rho_w\, q_w) + g \sum_k dhwt_k\, w\_bt_k\, \overline{\rho_k}^z + \sum_k dht_k\, p_k\, \partial_t\, \rho_k \right), \tag{6.63}$$

which again has a direct correspondence to the continuum results.

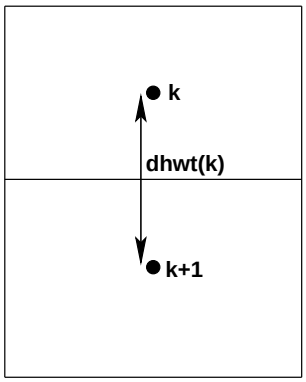

Figure 6.1: Schematic of the vertical grid cell arrangment used for computing the hydrostatic pressure at a depth $k+1$ in terms of the pressure at depth k using the equation $p_{k+1} = p_k + g\, dhwt_k\, \overline{\rho_k}^z$. The vertical average of density is meant to account for the part of density within each of the two adjacent cells. The factor of $1/2$ used in the average operator yields an approximate average when vertical cells are non-uniform. Yet the $1/2$ factor is used for all vertical grid spacing since it renders a simple conversion of discrete pressure work to discrete gravity work.

6.2.3.4 The sigma-correction term $\mathcal{P}_2$

Now consider the zonal piece of the sigma-correction term from equation (6.38)

$$\mathcal{P}_{2x} = g \sum_{i,j,k} dxu\, dyu\, dhu\ u\, FAY(FAX(\rho)\, \delta_i H)/dxu. \tag{6.64}$$

Transferring the forward average FAY to a backward average BAY leads to

$$\mathcal{P}_{2x} = g \sum BAY(dyu\, dhu\ u)\, FAX(\rho)\, \delta_i H, \tag{6.65}$$

where boundary terms vanish. Introducing the zonal thickness weighted advective transport velocity (6.46) yields

$$\mathcal{P}_{2x} = g \sum dyte\, uh\_et\, FAX(\rho)\, \delta_i H. \tag{6.66}$$

Moving the difference operator $\delta_i H = H_{i+1} - H_i$ from the depth H to the remaining terms gives

$$\mathcal{P}_{2x} = -g \sum H\, \delta_i(dyte\, FAX(\rho)\, uh\_et) = -g \sum H\, dat\ BDX\_ET(FAX(\rho)\, uh\_et), \tag{6.67}$$

where boundary terms vanish. Similar manipulations with the meridional piece of $\mathcal{P}_2$ lead to

$$\mathcal{P}_2 = -g \sum H\, dat\ [BDX\_ET(FAX(\rho)\, uh\_et) + BDY\_NT(FAY(\rho)\, vh\_nt)]. \tag{6.68}$$

The $\mathcal{P}_2$ term accounts for alterations in the potential energy due to the use of partial bottom cells.

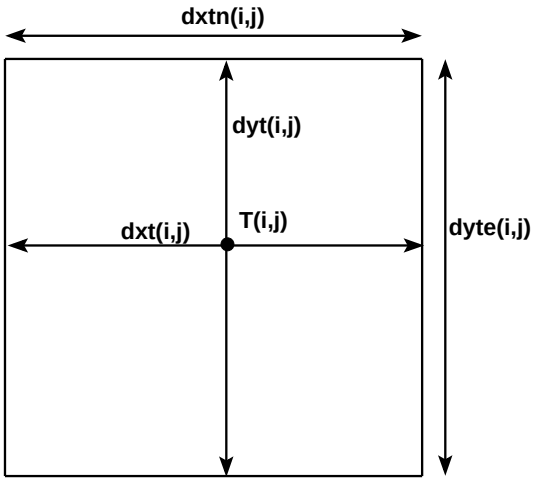

Figure 6.2: Time independent horizontal grid distances (meters) used for the tracer cell $T_{i,j}$ in MOM4. $dxt_{i,j}$ and $dyt_{i,j}$ are the grid distances of the tracer cell in the generalized zonal and meridional directions, and $dat_{i,j} = dxt_{i,j}\, dyt_{i,j}$ is the area of the cell. The grid distance $dxtn_{i,j}$ is the zonal width of the north face of a tracer cell, and $dyte_{i,j}$ is the meridional width of the east face. Note that the tracer point $T_{i,j}$ is not generally at the center of the tracer cell. Distances are functions of both i and j due to the use of generalized orthogonal coordinates.

6.2.3.5 Summary

In summary, the projection of the horizontal velocity onto the downgradient pressure field is given by

$$\begin{aligned}
\mathcal{P} &\equiv -\sum_{i,j,k} dau\, dhu\, [u\, FDX_NT(FAY(p)) + v\, FDY_ET(FAX(p))] \\
&+ g \sum_{i,j,k} dau\, dhu\, [u\, FAY(FAX(\rho)\, \delta_i H)/dxu + v\, FAX(FAY(\rho)\, \delta_j H)/dyu]. \\
&= -\sum_{i,j} dat_{i,j} \left(p_1\, w_bt_0 + g \sum_k dhwt_k\, w_bt_k\, \overline{\rho_k}^z + \frac{1}{\rho_o} \sum_k dht_k\, p\, \partial_t\, \rho_k \right) \\
&- g \sum H\, dat\, [BDX_ET(FAX(\rho)\, uh_et) + BDY_NT(FAY(\rho)\, vh_nt)] \qquad (6.69)
\end{aligned}$$

The MOM4 diagnostic *energy conversion error* has proven to be quite useful for detecting improper discretization of various algorithms. That diagnostic computes the left hand side of equation (6.69) and compares to the right hand side. Differences are due to errors in the code. The reason this diagnostic is so effective is that it involves advective velocities on the tracer cells, both tracer and velocity cell distances, the calculation of pressure, and details of partial cells. Each require precise discretization in order to ensure an energy conversion error at the roundoff level.

6.3 Kinetic energy advection

This section illustrates how second order accurate centered discrete advection conserves globally integrated discrete kinetic energy for a rigid lid Boussinesq model. Notably, such *variance* or *energy* conserving advection schemes are not so useful for tracer transport due to their relatively large dispersion errors (e.g., Griffies et al. (2000b)). Yet second order methods remain the norm for velocity advection in most z-coordinate ocean models based on the original Cox (1984) code, such as MOM. For the more general case with a free surface, the integrated advection term reduces to generally nonzero boundary contributions.

6.3.1 Continuum results

Recall from Section 6.1.3 that the kinetic energy per mass in a hydrostatic fluid is written $\mathcal{K} = \mathbf{u}^\rho \cdot \mathbf{u}^\rho/2$, where $\rho\,\mathbf{u}^\rho = \rho_o\,\mathbf{u}$ is the horizontal component to the linear momentum density (Section 6.1.2). For the Boussinesq fluid, $\mathbf{v}^\rho = \mathbf{v}$, so the distinction between velocities is only relevant for the non-Boussinesq case. Let us now define the volume integral of the scalar product of horizontal velocity $\mathbf{u}^\rho$ and the velocity advection terms in equation (6.3) as

$$\mathcal{A} \equiv -\int dV\, \mathbf{u}^\rho \cdot [\nabla \cdot (\mathbf{v}\,\mathbf{u}^\rho) + \mathcal{M}\,(\hat{\mathbf{z}} \wedge \rho\,\mathbf{v}^\rho)]. \tag{6.70}$$

The advection metric term drops out trivially. For clarity, we selectively expose tensor labels on the horizontal velocity components to rewrite the divergence term as

$$\begin{aligned} u^\rho_m\, \nabla \cdot (\mathbf{v}\, u^\rho_m) &= \nabla \cdot (\mathbf{v}\,\mathbf{u}^\rho \cdot \mathbf{u}^\rho) - (\mathbf{v}\, u^\rho_m) \cdot \nabla\, u^\rho_m \\ &= 2\,\nabla \cdot (\mathbf{v}\,\mathcal{K}) - \mathbf{v} \cdot \nabla \mathcal{K} \\ &= \nabla \cdot (\mathbf{v}\,\mathcal{K}) + \mathcal{K}\,\nabla \cdot \mathbf{v} \\ &= \nabla \cdot (\mathbf{v}\,\mathcal{K}) - \mathcal{K}\,(\rho_{,t}/\rho_o), \end{aligned}$$

where the continuity equation $\rho_{,t} = -\rho_o\,\nabla \cdot \mathbf{v}$ was used in the last step. For a Boussinesq fluid, similar manipulations lead to

$$u_m\, \nabla \cdot (\mathbf{v}\, u_m) = \nabla \cdot (\mathbf{v}\,\mathcal{K}), \tag{6.71}$$

where use was made of the non-divergence condition $\nabla \cdot \mathbf{v} = 0$. Integration over the ocean domain and use of the surface and bottom kinematic boundary conditions leads to the non-Boussinesq result

$$\begin{aligned} \rho_o\, \mathcal{A}_{nB} &= \int dV\, \mathcal{K}\, \rho_{,t} - \rho_o \int_{z=\eta} dA\, \mathcal{K}\,(w - \mathbf{u} \cdot \nabla \eta) \\ &= \int dV\, \mathcal{K}\, \rho_{,t} + \int_{z=\eta} dA\, \mathcal{K}\,(\rho_w\, q_w - \rho\, \eta_{,t}) \end{aligned} \tag{6.72}$$

and to the Boussinesq result

$$\mathcal{A}_B = \int_{z=\eta} dA\, \mathcal{K}\, \nabla \cdot \mathbf{U}. \tag{6.73}$$

For a rigid lid Boussinesq model with zero fresh water forcing, $\mathcal{A}_B = 0$. More general models have nonzero $\mathcal{A}$ due either to boundary contributions and/or dilatations of fluid parcels/columns.

6.3.2 B-grid results

We first verify that the scalar product of horizontal velocity and the advection metric term trivially vanishes at each grid point. Similar manipulations are appropriate for the Coriolis term. Written as in the numerical model, keeping only grid labels of relevance, we have

$$\mathbf{u}^\rho \cdot \mathcal{M}\,(\hat{\mathbf{z}} \wedge \mathbf{u}^\rho) \rightarrow \sum_{n=1}^{2} u_n^\rho\, u_{3-n}^\rho\, (u_1^\rho\, dh1dy - u_2^\rho\, dh2dx) = 0. \tag{6.74}$$

In this equation,

$$dh1dy = \partial_y \ln dx \tag{6.75}$$
$$dh2dx = \partial_x \ln dy \tag{6.76}$$

are the model arrays carrying information about the partial derivatives of the grid spacing in the two orthogonal directions. The sum in equation (6.74) vanishes trivially at each grid point upon writing out the two terms.

We next consider the scalar product of the horizontal convergence term with the horizontal velocity $\mathbf{u}^\rho$, and integrate over the full ocean

$$-\mathcal{A}_{horz} = \sum_{i,j,k} dau\; dhu\; \mathbf{u}^\rho \cdot \Big[BDX\_EU(uh\_eu * FAX(\mathbf{u}^\rho)) + BDY\_NU(vh\_nu * FAY(\mathbf{u}^\rho)) \Big] / dhu. \tag{6.77}$$

MOM4 uses the following forward averaging operators

$$FAX(a) = (a_{i+1} + a_i)/2 \tag{6.78}$$
$$FAY(a) = (a_{j+1} + a_j)/2. \tag{6.79}$$

These operators are the unweighted averages used to estimate velocity on the velocity cell faces. They are used to define the centered difference advective fluxes of velocity. MOM4 also uses the backward derivative operators

$$BDX\_EU(a) = \frac{dyue_{i,j}\, a_i - dyue_{i-1,j}\, a_{i-1}}{dau_{i,j}} \tag{6.80}$$
$$BDY\_NU(a) = \frac{dxun_{i,j}\, a_j - dxun_{i,j-1}\, a_{j-1}}{dau_{i,j}}. \tag{6.81}$$

These backward derivative operators act on fields defined at the east and north face of velocity cells, respectively (see Figure 6.3 for definitions of grid distances).

As detailed in Chapter 5, thickness weighted horizontal advective velocities *uh_eu* and *vh_nu* are defined in MOM4 by remapping the horizontal advective velocities *uh_et* and *vh_nt*, defined in Section 6.2.3.1, onto the velocity cell faces. They

satisfy continuity for each velocity cell

$$w\_bu_k = w\_bu_{k-1} + BDX\_EU(uh\_eu_k) + BDY\_NU(vh\_nu_k) + dhu_k\,\partial_t\,(\rho_k/\rho_o). \tag{6.82}$$

In this equation, w_bu is vertical advective velocity component defined at the bottom face of the velocity cells. It is defined as a remapped version[2] of the analogous advective velocity on the bottom of tracer cells (equations (6.52)-(6.54)). The thickness dhu is the thickness of the velocity cell, and ρ_k is the density in this cell. Both quantities are defined as remapped versions of the tracer cell thickness and densities, respectively, using the MOM4 horizontal remap function $REMAP\_BT\_TO\_BU$.

We now perform the discrete analog of integration by parts. For this purpose, expand the backwards derivative and average operators on the zonal flux terms, dropping the j,k labels for brevity

$$\begin{aligned}
&2\sum_i dau\,\mathbf{u}^\rho_i \cdot BDX_EU(uh_eu * FAX(\mathbf{u}^\rho)) = \\
&\sum \mathbf{u}^\rho_i \cdot \left[dyue_i\,uh_eu_i\,\mathbf{u}^\rho_{i+1} + dyue_i\,uh_eu_i\,\mathbf{u}^\rho_i - dyue_{i-1}\,uh_eu_{i-1}\,\mathbf{u}^\rho_i - dyue_{i-1}\,uh_eu_{i-1}\,\mathbf{u}^\rho_{i-1}\right] \\
&= \sum \mathbf{u}^\rho_i \cdot \mathbf{u}^\rho_i\,(dyue_i\,uh_eu_i - dyue_{i-1}\,uh_eu_{i-1}) \\
&+ \sum \mathbf{u}^\rho_i \cdot (dyue_i\,uh_eu_i\,\mathbf{u}^\rho_{i+1} - dyue_{i-1}\,uh_eu_{i-1}\,\mathbf{u}^\rho_{i-1}).
\end{aligned} \tag{6.83}$$

Focus now on the second group of terms, where shifting sum labels leads to

$$\begin{aligned}
&\sum_{i=1}^{nx} \mathbf{u}^\rho_i \cdot \mathbf{u}^\rho_{i+1}\,dyue_i\,uh_eu_i - \sum_{i=1}^{nx} \mathbf{u}^\rho_i \cdot \mathbf{u}^\rho_{i-1}\,dyue_{i-1}\,uh_eu_{i-1} = \\
&\sum_{i=2}^{nx+1} \mathbf{u}^\rho_{i-1} \cdot \mathbf{u}^\rho_i\,dyue_{i-1}\,uh_eu_{i-1} - \sum_{i=1}^{nx} \mathbf{u}^\rho_i \cdot \mathbf{u}^\rho_{i-1}\,dyue_{i-1}\,uh_eu_{i-1} \\
&= \mathbf{u}^\rho_{nx} \cdot \mathbf{u}^\rho_{nx+1}\,dyue_{nx}\,uh_eu_{nx} - \mathbf{u}^\rho_1 \cdot \mathbf{u}^\rho_0\,dyue_0\,uh_eu_0.
\end{aligned} \tag{6.84}$$

This result vanishes for either solid wall or periodic boundary conditions. Similar manipulations apply for the meridional term $\sum \mathbf{u}^\rho \cdot dau\,dhu * BDY\_NU(vh\_nu * FAY(\mathbf{u}^\rho))$, thus leading to

$$\begin{aligned}
\mathcal{A}_{horz} &= -\sum \mathcal{K}\,(dyue_i\,uh_eu_i - dyue_{i-1}\,uh_eu_{i-1} + dxun_j\,vh_nu_j - dxun_{j-1}\,vh_nu_{j-1}) \\
&= -\sum dau\,dhu\,\mathcal{K}\,\left[BDX_EU(uh_eu) + BDY_NU(vh_nu)\right]/dhu,
\end{aligned} \tag{6.85}$$

where

$$\mathcal{K}_{i,j,k} = \frac{1}{2}\,\mathbf{u}^\rho_{i,j,k} \cdot \mathbf{u}^\rho_{i,j,k} \tag{6.86}$$

is the discrete kinetic energy per mass.

Now focus on the vertical advection term. We choose to handle the surface cell $k = 1$ separately from the interior cells with $k > 1$. For the interior cells,

$$\begin{aligned}
-2\,\mathcal{A}^{interior}_{vert} &= \sum_{k=2}^{N_k} dau\,\mathbf{u}^\rho_k \cdot \left[w_bu_{k-1}\,(\mathbf{u}^\rho_{k-1} + \mathbf{u}^\rho_k) - w_bu_k\,(\mathbf{u}^\rho_k + \mathbf{u}^\rho_{k+1})\right] \\
&= \sum dau\,w_bu_1\,(\mathbf{u}^\rho_2 \cdot \mathbf{u}^\rho_1) - \sum dau\,w_bu_{Nk}\,(\mathbf{u}^\rho_{Nk} \cdot \mathbf{u}^\rho_{Nk+1}) \\
&+ 2\sum_{k=2}^{Nk} dau\,\mathcal{K}_k\,(w_bu_{k-1} - w_bu_k).
\end{aligned}$$

[2] Using the MOM4 mapping function $REMAP\_BT\_TO\_BU$.

It is appropriate to set

$$\mathbf{u}_{Nk+1} = 0 \tag{6.87}$$

since $k = Nk + 1$ is interpreted as part of the solid earth, thus leading to

$$-2\,\mathcal{A}_{vert}^{interior} = \sum dau\, w\_bu_1\, (\mathbf{u}_2^\rho \cdot \mathbf{u}_1^\rho) + 2 \sum_{k=2}^{Nk} dau\, \mathcal{K}_k\, (w\_bu_{k-1} - w\_bu_k).$$

For the surface cell, reference to the semi-discrete momentum budget (6.21) leads to

$$-2\,\mathcal{A}_{vert}^{k=1} = -\sum dau\, w\_bu_1\, \mathbf{u}_1^\rho \cdot (\mathbf{u}_1^\rho + \mathbf{u}_2^\rho) - \rho_o^{-1} \sum dau\, \mathbf{u}_1^\rho \cdot (-\mathbf{u}_{z_1}^\rho\, \rho_1\, \eta_{,t} + \rho_w\, q_w\, \mathbf{u}_w^\rho) \tag{6.88}$$

which when added to $\mathcal{A}_{vert}^{interior}$ yields

$$\begin{aligned} \mathcal{A}_{vert} = &\sum_{k=2}^{Nk} dau\, \mathcal{K}_k\, (w\_bu_k - w\_bu_{k-1}) + \sum dau\, \mathcal{K}_1\, w\_bu_1 \\ &+ (2\,\rho_o)^{-1} \sum dau\, \mathbf{u}_1^\rho \cdot (-\mathbf{u}_1^\rho\, \rho_1\, \eta_{,t} + \rho_w\, q_w\, \mathbf{u}_w^\rho). \end{aligned} \tag{6.89}$$

To bring this expression more in line with the continuum results of Section 6.3.1, let us write

$$\mathbf{u}_w^\rho = (\mathbf{u}_w^\rho - \mathbf{u}_1^\rho) + \mathbf{u}_1^\rho \tag{6.90}$$

to yield

$$\begin{aligned} \mathcal{A}_{vert} &= \sum_{k=2}^{Nk} dau\, \mathcal{K}_k\, (w\_bu_k - w\_bu_{k-1}) + \sum dau\, \mathcal{K}_1\, w\_bu_1 \\ &\quad + \rho_o^{-1} \sum dau\, \mathcal{K}_1 (-\rho_1\, \eta_{,t} + \rho_w\, q_w) + (2\,\rho_o)^{-1} \sum dau\, \mathbf{u}_1^\rho \cdot (\mathbf{u}_w^\rho - \mathbf{u}_1^\rho)\, \rho_w\, q_w \\ &= \sum_{k=1}^{Nk} dau\, \mathcal{K}_k\, (w\_bu_k - w\_bu_{k-1}) + (2\,\rho_o)^{-1} \sum dau\, \mathbf{u}_1^\rho \cdot (\mathbf{u}_w^\rho - \mathbf{u}_1^\rho)\, \rho_w\, q_w \end{aligned} \tag{6.91}$$

where we used equation (6.25) to write $\rho_o\, w\_bu_{k=0} = \rho_1\, \eta_{,t} - \rho_w\, q_w$. The second term in equation (6.91) vanishes for the special case of fresh water velocity equal to the ocean surface velocity. This is the case typically used in ocean climate models.

Combining the results for $\mathcal{A}_{horz}$ and $\mathcal{A}_{vert}$ renders

$$\begin{aligned} \mathcal{A}_{horz} + \mathcal{A}_{vert} &= -\sum_{k=1}^{Nk} dau\, \mathcal{K}\, [BDX\_EU(uh\_eu) + BDY\_NU(vh\_nu) + (w\_bu_{k-1} - w\_bu_k)] \\ &\quad + (2\,\rho_o)^{-1} \sum dau\, \mathbf{u}_1^\rho \cdot (\mathbf{u}_w^\rho - \mathbf{u}_1^\rho)\, \rho_w\, q_w \\ &= \sum_{k=1}^{Nk} dau\, dhu\, \mathcal{K}_k\, \partial_t\, (\rho_k/\rho_o) + (2\,\rho_o)^{-1} \sum dau\, \mathbf{u}_1^\rho \cdot (\mathbf{u}_w^\rho - \mathbf{u}_1^\rho)\, \rho_w\, q_w \end{aligned} \tag{6.92}$$

where the continuity equation (6.82) was used to reach the second equality. For the Boussinesq model with zero fresh water forcing, or with $\mathbf{u}_w^\rho - \mathbf{u}_1^\rho = 0$, then $\mathcal{A}_{horz} + \mathcal{A}_{vert} = 0$, whereas the more general case is nonzero due to the compressibility of seawater and/or fresh water forcing.

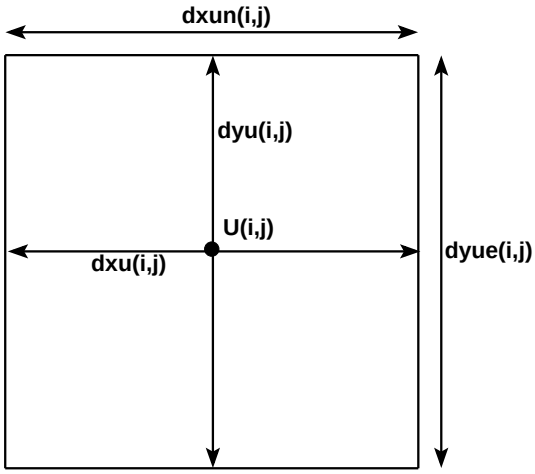

Figure 6.3: Time independent horizontal grid distances (meters) used for the velocity cell $U_{i,j}$ in MOM4. $dxu_{i,j}$ and $dyu_{i,j}$ are the grid distances of the velocity cell in the generalized zonal and meridional directions, and $dau_{i,j} = dxu_{i,j}\, dyu_{i,j}$ is the area of the cell. The grid distance $dxun_{i,j}$ is the zonal width of the north face of a velocity cell, and $dyue_{i,j}$ is the meridional width of the east face. Note that the velocity point $U_{i,j}$ is not generally at the center of the velocity cell. Distances are functions of both i and j due to the use of generalized orthogonal coordinates.

6.4 Kinetic energy in the external and internal modes

We note here a feature of global balances of kinetic energy related to the splitting of the velocity field into a vertically averaged (external mode) and a deviation from that average (internal mode). This decomposition prompts an analysis of the global kinetic energy budget taking the split into account, where we introduce a depth averaging operator

$$\overline{\psi}^z \equiv \frac{1}{H+\eta} \int_{-H}^{\eta} dz\, \psi, \tag{6.93}$$

and deviations from the depth average

$$\widehat{\psi} = \psi - \overline{\psi}^z. \tag{6.94}$$

Using this notation, the horizontal velocity is split into its external and internal modes

$$\mathbf{u} = \overline{\mathbf{u}}^z + \widehat{\mathbf{u}}. \tag{6.95}$$

Substituting these velocities into the kinetic energy per unit mass yields

$$\mathcal{K} = \frac{1}{2}(\overline{\mathbf{u}}^z \cdot \overline{\mathbf{u}}^z + \widehat{\mathbf{u}} \cdot \widehat{\mathbf{u}} + 2\, \overline{\mathbf{u}}^z \cdot \widehat{\mathbf{u}}). \tag{6.96}$$

The depth averaged kinetic energy per mass is given by

$$\overline{\mathcal{K}}^z = \frac{1}{2}(\overline{\mathbf{u}}^z \cdot \overline{\mathbf{u}}^z + \overline{\widehat{\mathbf{u}} \cdot \widehat{\mathbf{u}}}^z). \tag{6.97}$$

Note the decoupling of the external and internal modes when vertically integrating. Hence, the depth averaged kinetic energy per mass can be thought of as the sum of a contribution from the external mode kinetic energy per mass

$$\mathcal{K}_{ext} = \frac{1}{2}\,\overline{\mathbf{u}}^{z} \cdot \overline{\mathbf{u}}^{z}, \tag{6.98}$$

and the depth averaged internal mode kinetic energy per mass

$$\overline{\mathcal{K}}^{z}_{int} = \frac{1}{2}\overline{\widehat{\mathbf{u}} \cdot \widehat{\mathbf{u}}}^{z}. \tag{6.99}$$

In particular, this means that when computing the terms contributing to the evolution of global kinetic energy, it is sufficient to take the scalar product of the terms in the equation of motion with the internal and external mode velocities, respectively, and then volume average. Notably, surface pressure gradients contribute only to the external mode energy.

6.5 A caveat regarding the tripolar grid

When running MOM4 with spherical coordinates, the diagnosed energetic balances discussed in Sections 6.2 and 6.3 are maintained to an accuracy far exceeding the largest nontrivial term in the equations of motion. Hence, as stated in Section 6.1.1, energetic balances provide a useful means for diagnosing problems with the discretization of new algorithms.

The implementation of the tripolar grid leads to a problem with the diagnosed energetic balances. The problem is solely diagnostic, and so does not represent a fundamental problem with the prognostic equations. The issue is related to the need to specify exact agreement between terms computed along the bipolar fold (see Sections 4.2 and 4.3). Redundancies are handled for the prognostic equations thus ensuring model stability and self-consistency. However, for the energetic diagnostics in MOM4, we have not added the additional calls to the domain updates necessary to maintain the energetic diagnostics. A debugging tool useful for checking that the energetic balances are maintained in the nonlinear bipolar region is to simply set land at the $j = nj$ row. Setting *debug_tripolar_topog* = *.true.* inside the namelist *ocean_topog_nml* will perform this step, thus leading to improved energetics. As this step sets land across the Arctic, it is of relevance only for debugging.

CHAPTER

SEVEN

Total ocean tracer content

Contents

The purpose of this chapter is to interpret the evolution of total ocean tracer content. It is noted that a fundamental problem of time filtered leap-frog time stepping schemes is the inability to exactly conserve total tracer content.

7.1 Introduction

Time evolution of the total ocean tracer is determined by its input through the ocean boundaries and source/sink terms within the interior. Upon time discretization, the definition of total ocean tracer becomes dependent on details of the time stepping scheme. Furthermore, the introduction of explicit time filters, such as the Robert-Asselin filter used with the leap-frog scheme or time averaging used in the MOM4 explicit free surface method, alters the evolution of total tracer in a non-conservative manner. The goal of this section is to precisely define what we mean by total ocean tracer content in light of time discretization details.

7.2 Continuum model budget

Before discussing the discrete issues, let us review the continuum results. The total ocean tracer mass is given by

$$M_T = \int (\rho \, dV) \, T. \tag{7.1}$$

Note that for a Bouissinesq fluid, tracer concentration remains a scalar if it is interpreted as the tracer mass per volume of a water parcel, since volume is a scalar for Boussinesq fluids. In this case, the total tracer mass for a Bouissinesq fluid is given by $M_T = \rho_o \int dV\, T$.

Time evolution of the total tracer mass is determined by sources and sinks of tracer within the fluid and at the oceanic boundaries. Using the mass and tracer budgets given in Chapter 3 leads to

$$\begin{aligned}
\partial_t M_T &= \partial_t \left(\int (\rho\, dV)\, T \right) \\
&= \int dA \left((\rho\, T)_{z=\eta}\, \eta_{,t} + \int_{-H}^{\eta} dz\, (\rho\, T)_{,t} \right) \\
&= \int_{z=\eta} dA \left(T\, (\rho\, \eta_{,t} - \rho_o\, \widehat{\mathbf{N}} \cdot \mathbf{v}) - \widehat{\mathbf{N}} \cdot \rho\, \mathbf{F} \right) + \int (\rho\, dV)\, \mathcal{S} \\
&= \int_{z=\eta} dA \left(T\, \rho_w\, q_w - \widehat{\mathbf{N}} \cdot \rho\, \mathbf{F} \right) + \int (\rho\, dV)\, \mathcal{S} \\
&= \int_{z=\eta} dA \left(T\, \rho_w\, q_w - \widehat{\mathbf{N}} \cdot \rho\, \mathbf{F} \right) + \int (\rho\, dV)\, \mathcal{S} \\
&= - \int_{z=\eta} dA\, \rho\, Q_T + \int (\rho\, dV)\, \mathcal{S},
\end{aligned} \tag{7.2}$$

where we used the surface kinematic boundary condition, assumed zero flux through the solid boundaries and/or periodic lateral boundary conditions, and set the surface tracer flux equal to that coming in from boundary layer model.

7.3 Discrete Boussinesq rigid lid budget

We start our considerations of the discrete budget by focusing on the simplest case, that being the rigid lid Boussinesq ocean with no surface fresh water fluxes. In this case, the volume of all model grid cells is constant in time. We also drop interior source/sink terms and set $\widehat{\mathbf{N}} = \hat{\mathbf{z}}$, both for purposes of brevity.

The thickness weighted tendency for tracer concentration at a depth k is given by (see Griffies (2004) for a derivation)

$$\partial_t\, (h\, T)_{z_k} = -\nabla \cdot (h\, \mathbf{u}\, T + h\, \mathbf{F}^h)_{z_k} - [(w\, T + F^z)_{z_{k-1}} - (w\, T + F^z)_{z_k}], \tag{7.3}$$

where $w_{z_0} = 0$ for the rigid lid. Integrating over the total model volume cancels the horizontal fluxes so long as there are no tracer sources, such as geothermal heating, at the solid boundaries. The volume integrated vertical flux convergence reduces to an area integral of the surface tracer flux. Hence, exposing some model grid fields and discrete indices leads to the time tendency

$$\partial_t \left(\sum_{i,j,k} dat\, dht\, T \right) = - \sum_{i,j} dat\, Q_T = - \sum_{i,j} dat\, Q_T^{turb} \tag{7.4}$$

where $dht_{i,j,k}$ is the tracer cell thickness, $dat_{i,j} = dxt_{i,j}\, dyt_{i,j}$ is the horizontal area of a tracer cell, and indices are exposed only when needed. Multiplying both sides by the constant density ρ_o renders the budget for total tracer mass in the rigid lid Boussinesq fluid.

The balance (7.4) takes on various forms depending on how time is discretized. Following the approach in MOM, we introduce a leap-frog time stepping scheme for the tendency of tracer concentration

$$\sum_{i,j,k} dat\ dht\ T(\tau + \Delta\tau) = \sum_{i,j,k} dat\ dht\ T^R(\tau - \Delta\tau) - 2\,\Delta\tau \sum_{i,j} dat\ Q_T, \tag{7.5}$$

where

$$T^R(\tau - \Delta\tau) = T(\tau - \Delta\tau) + (\alpha/2)\,[T(\tau) - 2\,T(\tau - \Delta\tau) + T^R(\tau - 2\Delta\tau)] \tag{7.6}$$

is a Robert-Asselin time filtered version of the lagged tracer concentration (e.g., Haltiner and Williams (1980)). A weak form of such filtering, with $\alpha \approx 0.01 - 0.05$, has been found sufficient to suppress splitting between the two leap-frog branches in MOM4. However, it is notable that the use of a time filter compromises the conservation properties of the model. Namely, it alters the tracer content at each grid point, yet is not associated with a physical source/sink of tracer. We now discuss this point further.

To reduce clutter, introduce the following expression for domain integrated tracer mass

$$\mathcal{T}(\tau) \equiv \rho_o \sum_{i,j,k} dat\ dht\ T(\tau), \tag{7.7}$$

and area integrated surface tracer flux

$$\mathcal{F}(\tau) \equiv -\rho_o \sum_{i,j} dat\ Q_T, \tag{7.8}$$

with positive $\mathcal{F}$ indicating tracer added to the ocean domain. $\mathcal{T}$ represents the total mass of tracer if T represents mass per volume, or the total ocean heat divided by C_p if T is the potential temperature θ. The budget for total tracer mass now takes the more tidy form

$$\mathcal{T}(\tau + \Delta\tau) = \mathcal{T}^R(\tau - \Delta\tau) + 2\,\Delta\tau\,\mathcal{F}(\tau). \tag{7.9}$$

Because of the Robert time filter, tracer mass at $\tau + \Delta\tau$ does not equal that at $\tau - \Delta\tau$ plus that input through the ocean surface. That is, time filtering compromises the discrete balance of total ocean tracer mass. It is as if the flux input via the surface term $\mathcal{F}(\tau)$ were modified, with the magnitude of the modification depending on the amount of time filtering applied. This is not a satisfying situation. Yet it is a necessary consequence of using the time filtered leap-frog scheme. Such will also be the case with the free surface, where there is a time filter applied to both the tracer and surface height, thus further compromising the integrity of the conservation properties. Two-time level schemes, such as predictor-corrector, avoid these problems via the use of implicit time dissipation, and so are preferable from the present perspective. Yet we will have more to say on two-time level schemes in Section 7.5.

To pursue this point a bit further, consider the special case of zero surface tracer flux for all time, for which case

$$\mathcal{T}(\tau + \Delta\tau) = \mathcal{T}^R(\tau - \Delta\tau). \tag{7.10}$$

Hence, there is an apparent time evolution of total tracer content even when there are no surface fluxes. However, upon assuming $\mathcal{T}$ constant for all earlier time steps, one can show inductively that $\mathcal{T}$ remains constant for all future time steps. As shown in the next section, the nonlinear product of the time dependent surface thickness and time dependent tracer concentration, in the presence of separately applied time filters, leads this conservation statement to be compromised with a free surface.

7.4 Discrete non-Boussinesq free surface budget

To garner a budget for total tracer mass in the discrete non-Boussinesq free surface model, we first integrate the tracer budget over the ocean domain and drop boundary terms at solid walls, and use the surface cell budget derived in Griffies (2004). The result is

$$\partial_t \left(\sum_{i,j,k} dat\, dht\, \rho\, T \right) = \mathcal{F}(\tau), \tag{7.11}$$

where the area integrated surface tracer flux is given by the sum of the turbulent and fresh water terms

$$\mathcal{F}(\tau) = -\sum_{i,j} dat\, \rho\, Q_T = -\sum_{i,j} dat\, (\rho\, Q_T^{turb} - \rho_w\, q_w\, T_w). \tag{7.12}$$

The density weighting, fresh water term, and time dependent surface cell thickness each provide added features relative to the rigid lid Boussinesq case.

Performing a leap-frog time step on the thickness weighted tracer concentration leads to the conservation statement

$$\mathcal{T}(\tau + \Delta\tau) = \mathcal{T}(\tau - \Delta\tau) + 2\Delta\tau\, \mathcal{F}(\tau), \tag{7.13}$$

where

$$\mathcal{T}(\tau) \equiv \sum_{i,j,k} dat\; dht(\tau)\; \rho(\tau)\, T(\tau) \tag{7.14}$$

is the domain integrated tracer mass, and time filtering is briefly ignored. This conservation statement has the same form as that for the rigid lid. In both cases, the use of time filters compromises our familiar interpretation of the discrete time budget for total tracer. Additionally, because thickness must be time stepped separately from the thickness weighted tracer, time filtering is also applied separately. Hence, upon introducing time filtering, the nonlinear product of thickness times tracer concentration further compromises the integrity of the conservation statement. No such issue arises with density, and hence total ocean mass, since its time stepping is diagnosed by the extrapolation method described in Greatbatch et al. (2001) and Griffies (2004).

7.4.1 Separate time stepping for tracer, density, and thickness

We dissect this result a bit further by separately considering the leap-frog time stepping of density, tracer concentration, and thickness

$$\sum_{i,j,k} dat \Big(dht(\tau)\,[\rho(\tau+\Delta\tau)\,T(\tau+\Delta\tau) - \rho(\tau-\Delta\tau)\,T(\tau-\Delta\tau)] + \rho(\tau)\,T(\tau)\,[dht(\tau+\Delta\tau) - dht(\tau-\Delta\tau)]\Big) = 2\Delta\tau\,\mathcal{F}(\tau). \quad (7.15)$$

This time discretization has the same accuracy as when discretizing the product $h\,\rho\,T$ as a single object. However, the conservation statement is a bit more complicated in the present approach, as seen in the following. Note that $dht(\tau+\Delta\tau) - dht(\tau-\Delta\tau)$ is nonzero only for the surface grid cell. However, for purposes of symmetry, it is useful to keep it around for all depths.

To proceed, rearrange the previous result and indicate where the time filtered fields are used in the model's time stepping.

$$\sum_{i,j,k} dat \Big([dht(\tau)\,\rho(\tau+\Delta\tau)\,T(\tau+\Delta\tau) + dht(\tau+\Delta\tau)\,\rho(\tau)\,T(\tau)] - [dht^F(\tau-\Delta\tau)\,\rho(\tau)\,T(\tau) + dht(\tau)\,\rho(\tau-\Delta\tau)\,T^R(\tau-\Delta\tau)]\Big) = 2\,\Delta\tau\,\mathcal{F}(\tau), \quad (7.16)$$

where there is no time filtering applied to the density field since it is updated via an extrapolation method. Furthermore, as detailed in Griffies (2004), the time filtered ocean surface height takes the form of a time average over the barotropic cycle

$$\eta^F(\tau) = \overline{\eta^{(b)}}(\tau) = \frac{1}{N+1}\sum_{n=0}^{N} \eta^{(b)}(\tau-\Delta\tau, t_n). \quad (7.17)$$

To isolate the effects of time filtering on the tracer content, we find it convenient to write

$$\begin{aligned}\sum_{i,j,k} dat\,[dht(\tau)\,\rho(\tau+\Delta\tau)\,T(\tau+\Delta\tau) + dht(\tau+\Delta\tau)\,\rho(\tau)\,T(\tau)] \\ - \sum_{i,j,k} dat\,[dht(\tau-\Delta\tau)\,\rho(\tau)\,T(\tau) + dht(\tau)\,\rho(\tau-\Delta\tau)\,T(\tau-\Delta\tau)] \\ + \sum_{i,j,k} dat\,dht(\tau)\,\rho(\tau-\Delta\tau)\,[T(\tau-\Delta\tau) - T^R(\tau-\Delta\tau)] \\ + \sum_{i,j,k} dat\,\rho(\tau)\,T(\tau)\,[dht(\tau-\Delta\tau) - dht^F(\tau-\Delta\tau)] \\ = 2\,\Delta\tau\,\mathcal{F}(\tau). \quad (7.18)\end{aligned}$$

To bring this equation into a more tidy form, define the two-time level tracer mass

$$2\,\mathcal{T}(\tau,\tau+\Delta\tau) = \sum_{i,j,k} dat\,[dht(\tau)\,\rho(\tau+\Delta\tau)\,T(\tau+\Delta\tau) + dht(\tau+\Delta\tau)\,\rho(\tau)\,T(\tau)] \quad (7.19)$$

and the time filtered form of this mass

$$2\,\mathcal{T}^F(\tau,\tau+\Delta\tau) = \sum_{i,j,k} dat\,[dht^F(\tau)\,\rho(\tau+\Delta\tau)\,T(\tau+\Delta\tau) + dht(\tau+\Delta\tau)\,\rho(\tau)\,T^R(\tau)], \quad (7.20)$$

thus bringing the conservation statement (7.18) to the form

$$\mathcal{T}(\tau,\tau+\Delta\tau) = \mathcal{T}(\tau-\Delta\tau,\tau) + \Delta\tau\,\mathcal{F}(\tau) + [\mathcal{T}^F(\tau-\Delta\tau,\tau) - \mathcal{T}(\tau-\Delta\tau,\tau)]. \quad (7.21)$$

This result leads to the following interpretation: consider $\mathcal{T}(\tau,\tau+\Delta\tau)$ as centered at $\tau+\Delta\tau/2$ and $\mathcal{T}(\tau-\Delta\tau,\tau)$ centered at $\tau-\Delta\tau/2$. Equation (7.21) then says that a leap-frog time step $\Delta\tau$ links the two half-time step total tracer mass; Figure 7.1 provides an illustration. The difference $\mathcal{T}^F(\tau-\Delta\tau,\tau) - \mathcal{T}(\tau-\Delta\tau,\tau)$ acts as a source/sink in addition to the physical source/sink $\Delta\tau\,\mathcal{F}(\tau)$. The size of this time filtering source can be nontrivial in some situations.

7.4.2 Concerning the tracer and baroclinic time steps

As discussed in Griffies (2004), the free surface height is time stepped using a "big-leap-frog" at the end of the small barotropic sub-cycle. Consequently, it is natural to update the free surface using the baroclinic time step. However, the rearrangement used to reach equation (7.16) assumed the same time steps were used to update tracer and volume. Without equating the two time steps, we cannot identify a total ocean tracer content. This result is to be expected for the following reason. The undulating surface height (and undulating volume) closely couples the tracer and mass/volume budgets in the surface grid cells, necessitating the use of equal time steps to maintain a self-consistent time stepping so that tracer mass can be conserved.

In Pacanowski and Griffies (1999) and Griffies et al. (2001), it was assumed that the surface height would always be updated using the baroclinic time step. However, tests in MOM4 indicate that the time stepping scheme for the surface height is stable enough to allow η to be updated using the tracer time step. Hence, even for those coarse resolution models where tracer time steps are typically much larger than baroclinic time steps, it is possible to maintain compatibility between the volume and tracer budgets. The usual *tricks* for quickly spinning-up coarse resolution ocean models (Bryan (1984); Killworth et al. (1984); Danabasoglu et al. (1996)) are therefore still available with the MOM4 free surface, all while maintaining volume and tracer compatibility. Conservation, however, is still compromised due to the time filtering.

7.4.3 MOM4 diagnostics for tracer mass

Equation (7.16) represents a simple rearrangement of the discrete equations as they are implemented in the ocean model. Hence, the two sides should be equal even if they are evaluated separately. However, in the development of various algorithms, it has proven extremely useful to separately diagnose the two sides of this equation and verify that they are indeed equal, to within some value determined by roundoff errors. Notably, if the tracer and volume budgets are updated using a different time

step, this diagnostic reveals the extent of the associated tracer non-conservation. Such is part of the tracer-change diagnostic in MOM4.

In addition to checking the left and right hand sides of equation (7.16) over a single time step, it is important to check how well the ocean inputs the tracer fluxed through its surface over a period of time. That is, does the tracer content at some given time equal to that at an earlier time plus the total tracer input through the surface during the intermediate times? We already answered this question in the negative for the rigid lid, in which case the mis-match arises from the use of time filters. The negative answer applies also for the free surface, again because of time filters as seen by equation (7.21). We now consider details in order to formulate the MOM4 diagnostic which determines the magnitude of the mis-match.

For this purpose, integrate equation (7.21) over a finite time $N\,\Delta\tau$ to obtain

$$\mathcal{T}(\tau + N\Delta\tau, \tau + (N+1)\Delta\tau) = \mathcal{T}(\tau, \tau + \Delta\tau) + \Delta\tau \sum_{n=1}^{N} \mathcal{F}(\tau + n\Delta\tau)$$
$$+ \sum_{n=1}^{N} [\mathcal{T}^F(\tau + (n-1)\,\Delta\tau, \tau + n\,\Delta\tau) - \mathcal{T}(\tau + (n-1)\,\Delta\tau, \tau + n\,\Delta\tau)]. \quad (7.22)$$

A useful means to define an error due to time filtering is to convert to a flux. We do this in two ways. First, compute an effective flux due to the filter

$$\text{error}_{(1)} = \left(\frac{1}{N\,\Delta\tau\,A}\right) \times$$
$$\sum_{n=1}^{N} [\mathcal{T}^F(\tau + (n-1)\,\Delta\tau, \tau + n\,\Delta\tau) - \mathcal{T}(\tau + (n-1)\,\Delta\tau, \tau + n\,\Delta\tau)] \quad (7.23)$$

where $A = \sum dat$ is the total tracer cell area at the ocean surface. Second, compute an effective flux

$$\text{error}_{(2)} = \left(\frac{1}{N\,\Delta\tau\,A}\right) \times$$
$$[\mathcal{T}(\tau + N\Delta\tau, \tau + (N+1)\Delta\tau) - \mathcal{T}(\tau, \tau + \Delta\tau) - \Delta\tau \sum_{n=1}^{N} \mathcal{F}(\tau + n\Delta\tau)] \quad (7.24)$$

where ideally we have

$$\text{error}_{(1)} = \text{error}_{(2)}. \quad (7.25)$$

Differences can be interepreted as due to numerical roundoff. Note that for potential temperature, multplying by C_p yields an error with units Watts per meter squared. For other tracers, the error is in units of kilograms per second per meter squared. The magnitude of these errors is dependent on the model configuration, the frequency at which surface forcing is altered, the level of time filtering, and the time interval over which the diagnostic is computed.

Figure 7.1 illustrates the time steps involved in integrating tracer concentration and the implied integration of total tracer mass. Total tracer mass is centered on the half-time steps and is moved forward $\Delta\tau$ upon each $2\Delta\tau$ leap-frog update of the tracer concentration. Assuming knowledge of the tracer, density, and thickness fields at times τ and $\tau + \Delta\tau$, we can diagnose the total tracer mass

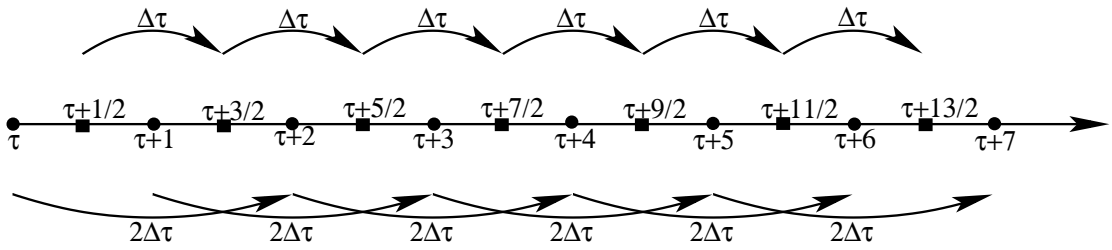

Figure 7.1: Schematic of time stepping for tracer concentration and total tracer mass in the case where $N = 6$. The lower branch shows the N over-lapping $2\Delta\tau$ leap-frog steps used for updating the tracer field. The upper branch shows the N time steps of length $\Delta\tau$ moving the total tracer mass over the half-integer τ levels. Note that the increments for τ are in units of $\Delta\tau$.

$\mathcal{T}(\tau, \tau + \Delta\tau) = \mathcal{T}(\tau + \Delta\tau/2)$. The $N = 6$ time steps used to move from $\mathcal{T}(\tau, \tau + \Delta\tau)$ to $\mathcal{T}(\tau + 6\Delta\tau, \tau + 7\Delta\tau)$ require the surface tracer flux over the six time steps $\mathcal{F}(\tau + n\Delta\tau)_{n=1,6}$.

7.5 Comments on three-time level schemes

As pointed out in this chapter, a fundamental problem of the three time level leap-frog scheme is the inability to exactly conserve discrete total tracer mass in the ocean model, either using a free surface or a rigid lid model. Again, the problem arises when applying some form of time filtering, either the Robert-Asselin filter to the tracer concentration (7.6) or the barotropic time average applied to the free surface (see Griffies (2004)). This result prompts some comments regarding the utility of two time level schemes, many of which are common in ocean models (see Griffies et al. (2000a) for a summary). These comments should be considered speculative, since we have not under-taken a systematic investigation of the issues. Nonetheless, they are presented in hopes that they highlight certain relevant points.

Let us first summarize the issues arising with the leap-frog. Because tracer is time stepped via a leap-frog, it is necessary to also update surface height with a leap-frog using the same time step. Otherwise, the discrete volume and tracer budgets would be incompatible and there would be no way to form a discrete analog of total ocean tracer content which undergoes a physically relevant time evolution, even in the absence of time filtering. When the volume and tracer budgets are compatible, non-conservation of total tracer content still arises when applying a time filter to both the tracer and the surface height, with tests indicating that both contribute roughly an equal amount to the non-conservation. Additionally, due to the tendency for the surface height to generate noise when time stepping the split equations on the B-grid, it has proven essential to compute the filtered surface height contribution using the time averaged surface height from the previous and future time steps. Note that this computational mode is absent on the C-grid, thus motivating its use for discretizing gravity waves. However, C-grid models suffer from a computational mode associated with the Coriolis force, and such is nontrivial to damp in a conservative manner. See Adcroft et al. (1999) for a review with

suggestions.

The two-time level predictor-corrector schemes contain time damping applied in a semi-implicit manner. Hence, there is no need to employ a Robert filter. Careful discretization in the C-grid Hallberg Isopycnal Model Hallberg (1997) allows for an exact conservation of total tracer if the predictor-corrector is applied to the tracer fields as well as within the barotropic sub-cycle. The surface height that is used to maintain conservation is driven by the barotropically time averaged vertically integrated transport.

In an attempt to see whether a two-time level scheme is warranted for MOM, we implemented a predictor-corrector approach for the barotropic system (similar to Hallberg's), yet maintained the leap-frog for the tracer and baroclinic velocity. Unfortunately, the model was very unstable, likely due to the B-grid computational mode, unless a time averaged surface height was incorporated at some stage in the barotropic algorithm (see Griffies et al. (2001) for comments on such instabilities). Yet the use of time averaging no longer allows for exact tracer conservation, even if the tracer equation is changed to a predictor-corrector. Hence, we have found little motivation in modifying the leap-frog scheme in the B-grid MOM. Conversion to a C-grid may lead to more positive results, so long as the Coriolis null mode does not then become pernicious (Adcroft et al. (1999)).

Even with the rigid lid, a leap-frog compromises the total tracer conservation. Short of a fully two-time level scheme, it has been common to remove the leap-frog splitting mode by periodically applying a two-time level Euler step instead of using a time filter. Extensive experience with this approach has prompted modelers to abandon the use of such special-time step "tricks", largely due to subtleties related to vertical adjustment processes (see Griffies et al. (2000a) for a review and references). A predictor-corrector for a rigid lid B-grid model thus makes more sense, because the issues of stabilizing the free surface are no longer relevant and all time steps are treated the same. Because the rigid lid is not suitable for other reasons (e.g., Griffies (2004)), there has been no attempt to see how useful a two-time level B-grid MOM would be.

Part III

Vertical physics and transport

NUMERICS OF VERTICAL PHYSICS

Vertical physics is relatively simple to implement in a z-coordinate ocean model. Nonetheless, we find it useful to discuss some issues relevant to the implementation of vertical processes in MOM4, and so present salient issues in this part of the MOM4 Guide.

CHAPTER

EIGHT

Shortwave heating

Contents

The purpose of this chapter is to discuss the numerical implementation of shortwave heating. Sensitivity of the ocean solution to the penetration of shortwave radiation into the ocean column can be quite large. Penetrative shortwave heating is implemented in MOM4 via the tracer source array.

This chapter, especially Section 8.3, benefitted from contributions by Colm Sweeney (cos@gfdl.noaa.gov).

8.1 General considerations and model implementation

Solar penetration brings solar shortwave heating downward in the ocean column, thus providing a heating at depth. The parameterization of the oceanic absorption of downward solar radiation is generally written as

$$I(x, y, z) = I_{0^-}(x, y)\, \mathcal{F}(z), \tag{8.1}$$

where I_{0^-}, in units of W m^{-2}, is the total shortwave downwelling radiative heating per unit area incident at the earth surface, and $\mathcal{F}(z)$ is a dimensionless attenuation function. Note that the total downwelling radiation I_{0^-} is to be distinguished from the total shortwave heating I_0, where $I_{0^-} = (1 - \alpha)\, I_0$, with $\alpha \approx 0.06$ the sea surface albedo.

Shortwave heating affects the heat budget locally according to

$$(\rho\, T)_{,t} = -(\rho_o / c_p)\, \partial_z\, (c_p\, F^z - I). \tag{8.2}$$

In this equation, F^z accounts for vertical processes such as advection and diffusion, c_p is the heat capacity of seawater, ρ is the *in-situ* density which for a Boussinesq fluid is set to the Boussinesq reference density ρ_o.

Shortwave heating leads to the following net heat flux over a column of ocean fluid

$$(\rho_o/c_p) \int_{-H}^{\eta} dz\, \partial_z I = (\rho_o/c_p)\, [I(\eta) - I(-H)]. \tag{8.3}$$

where $I(\eta)$ is often approximated as $I(0)$. We assume there is no shortwave heating of the solid rock underneath the ocean fluid, so $I(z = -H) = 0$ is appropriate, with this boundary condition set via masks in MOM4. Although the expression (8.5) suggests the upper boundary condition $I(0) = I_{0^-}$, we must be careful to not double-count the shortwave source in MOM4 since it is typically also carried as part of the surface temperature flux array stf. We now present the two approaches available in MOM4.

The vertical convergence of penetrative shortwave radiation, $(\rho_o/c_p)\partial_z I$, is incorporated into MOM4's potential temperature equation via a source term. Additionally, it is typical to include the total downwelling shortwave heating I_{0^-} within the surface flux array stf, where other forms of heating such as those from latent and long-wave affects are also incorporated. Hence, for proper accounting of the shortwave heating, the upper boundary condition for the irradiance function must be specified as

$$I(\eta) = \begin{cases} 0 & \text{if } I_{0^-} \text{ is already included in } stf \\ I_{0^-}(x,y) & \text{if } I_{0^-} \text{ is NOT already included in } stf. \end{cases} \tag{8.4}$$

The typical practice at GFDL is to set $I(\eta) = 0$ since I_{0^-} is already included in stf. Care should be exercised by those using the opposite convention.

8.2 The Paulson and Simpson (1977) irradiance function

Jerlov (1968) classified water into five types according to its optical properties, which determines the extent that solar radiation penetrates into a vertical fluid column. For example, clear water allows for deeper penetration, whereas mirky water, as occurs in the presence of active biology, more rapidly attenuates the radiation. Studies by Paulson and Simpson (1977) then suggest a form for the attenuation function $\mathcal{F}(z)$ based on the optical properties of water.

The parameterization of solar shortwave absorption of downwelling solar radiation used by Rosati and Miyakoda (1988) is given by the Paulson and Simpson (1977) form

$$I(x,y,z) = I_{0^-}(x,y)\, [R\, e^{z/\zeta_1} + (1-R)\, e^{z/\zeta_2}], \tag{8.5}$$

where I_{0^-} is the total shortwave downwelling radiative heating per unit area incident at the earth surface, ζ_1 and ζ_2 are attentuation lengths and R is an empirical constant dependent on the optical properties of the water. In the Rosati and Miyakoda (1988) study, they chose $R = 0.58$, $\zeta_1 = 0.35$m, and $\zeta_2 = 23$m, corresponding to Jerlov Type I water (clear water). This is the form of shortwave penetration originally implemented in MOM. However, MOM4 now implements the scheme discussed in Section 8.3.

8.3 Shortwave penetration based on chlorophyll-a

This Section was contributed by Colm Sweeney (cos@gfdl.noaa.gov).

Recent investigations with solar penetration have indicated a strong sensitivity of ocean simulations to how light penetrates into the ocean and warms the upper few tens of meters. This section describes recent work at GFDL whereby the use of a spatially and temporally dependent penetration depth is specified according to climatological chlorophyll data. Although this data is taken from a climatology, its use is believed to be preferable, even for climate change simulations, to the use of a space-time independent optical type. Research into bio-optical influences on ocean climate remains an active area, and the methods presented here remain under investigation by various groups.

8.3.1 Solar penetration in the ocean

Observations and models describing the distribution of solar radiation with depth in seawater have demonstrated that nearly all (99.9%) of the downwelling infrared radiation (wavelengths of 750nm-2500nm) is absorbed in the upper 2 meters of the ocean. While variability in the penetration depth of long wave radiation has large implications for skin temperature and surface layer heat fluxes, this IR radiation has little effect below the surface over the depths (roughly 10 m) used in present day ocean models (Morel and Antoine (1994), Ohlmann and Siegel (2000)).

In contrast, attenuation of shortwave solar radiation (wavelengths < 750nm) is both spatially and temporally variable at scales important to ocean climate models. In waters with high particulate and dissolved organic matter concentrations, the 1% light penetration depth can be less than 10 meters while in the clear, biologically unproductive waters of the subtropical gyres, solar radiation can directly contribute to the heat content at depths greater than 100 meters.

Previously, ocean climate models have parameterized the penetration of light into the ocean by identifying six water types distinguished by the "clarity" of the water (Paulson and Simpson (1977)). This method is described in Section 8.2. More recently, the correlation between chlorophyll pigment concentrations and short wave penetration depths has enabled us to parameterize shortwave penetration of solar radiation with satellite observations of ocean color (Morel (1988), Morel and Antoine (1994), Ohlmann and Siegel (2000)). By assimilating satellite observations of ocean color (e.g., SeaWiFS, OCTS, MODIS), it is possible to more accurately simulate the spatial and temporal variability of penetrating radiation.

8.3.2 Morel and Antoine (1994) shortwave penetration model

Present modeling work at GFDL (Spring 2003) makes use of a parameterization developed by Morel and Antoine (1994). This scheme was explicitly developed for large-scale ocean models with coarse depth resolution (i.e., grids with $\Delta z > 5$m). Morel and Antoine (1994) expand the exponential function used by Denman (1973) into three exponentials to describe solar penetration into the water column.

The first exponential is for wavelengths > 750nm (i.e., I_{IR}) and assumes a single attenuation of 0.267meter with a solar zenith angle $\theta = 0$. At present we assume that the solar zenith angle stays constant throughout the daily integration of the

model. Thus, the resulting equation for the infared portion of the downwelling radiation is:

$$I_{IR}(x,y,z) = I_{IR^-}(x,y)\, e^{-z/(0.267\cos\theta)} \tag{8.6}$$

where again $\theta = 0$. This relationship assumes z is the depth in meters and that $I_{IR^-}(x,y)$ is a fraction, of the total downwelling radiation, I_{0^-} such that

$$I_{IR^-}(x,y) = F_{IR}\, I_{0^-} \tag{8.7}$$

and

$$F_{IR} + F_{VIS} = 1 \tag{8.8}$$

where F_{IR} and F_{VIS} are the fractions of infared (750nm to 2500nm) and visible (300nm to 750nm) radiation downwelling from the surface ocean. Although Morel and Antoine (1994) note that water vapor, zenith angle, and aerosol content each can effect the fraction of incoming radiation that is represented by infared and visible light, in the present implementation we have chosen to keep these fractions constant such that $F_{IR} = 0.46$.

The second and third exponentials represent a parameterization of the attenuation function for downwelling radiation in the visible range (300nm -750nm) in the following form:

$$I_{VIS}(x,y,z) = I_{VIS^-}(x,y)\,(V_1\, e^{z/\zeta_1} + V_2\, e^{z/\zeta_2}). \tag{8.9}$$

This form further partitions the visible radiation into long (V_1) and short (V_2) wavelengths assuming

$$V_1 + V_2 \equiv 1. \tag{8.10}$$

V_1, V_2, ζ_1 and ζ_2 are calculated from an empirical relationship as a function of chlorophyll-a concentration using methods from Morel and Antoine (1994). Throughout most of the ocean $V_1 < 0.5$ and $V_2 > 0.5$. The e-folding length scales ζ_1 and ζ_2 are the e-folding depths of the long (ζ_1) and short visible and ultra violet (ζ_2) wavelengths. Based on the chlorophyll-a climatology used in the GFDL models, ζ_1 should not exceed 3m while ζ_2 will vary between 30m in oligotrophic waters and 4m in coastal regions. All of these constants are based on satellite estimates of chlorophyll-a plus Pheaophytin-a, as well as parameterizations which have "nonuniform pigment profiles" (Morel and Antoine (1994)). The "nonuniform pigment profiles" have been proposed to account for deep chlorophyll maxima that are often observed in highly stratified oligotrophic waters (Morel and Berthon (1989)).

8.3.3 SeaWiFS based chlorophyll-a climatology

A "non- El Niño" chlorophyll-a climatology was produced from estimates of the Sea-viewing Wide Field-of-view Sensor (SeaWiFS). The "non - El-Niño" climatology is based on 8-day composites of SeaWiFS images taken from 1999 to the end of 2001. The climatology calculates the weighted average chlorophyll-a concentration on the 15th day of each month considering all data 16 days before, and after the 15th day of each month. Each 8-day composite is assigned a gaussian (alpha = 2.5) weight based on its proximity to the 15th day of each month. This data set is available from the GFDL NOMADS server where MOM4 datasets are distributed.

CHAPTER

NINE

Vertical adjustment schemes

Contents

The purpose of this chapter is to present the vertical adjustment schemes available in MOM4.

9.1 Introduction

The hydrostatic approximation necessitates the use of a parameterization of vertical overturning processes. The original parameterization used by Bryan in the 1960's was motivated largely from ideas then used for modeling convection in stars (Bryan (1969)). Work by Marshall and collaborators (Klinger et al. (1996), Marshall et al.

(1997)) have largely indicated that the basic ideas of vertical adjustment are useful for purposes of large-scale ocean circulation.

The Cox (1984) implementation of convective adjustment (the "NCON" scheme) may leave columns unstable after completing the code's adjustment loop. Various full convective schemes have come on-line, with that from Rahmstorf (1993) implemented in MOM4. An alternative to the traditional form of convective adjustment is to increase the vertical mixing coefficient to some large value (say $\geq 10 \mathrm{m}^2\,\mathrm{s}^{-1}$) in order to quickly diffuse vertically unstable water columns. Indeed, it is this form recommended from the study of Klinger et al. (1996), and it is the approach commonly used in mixed layer schemes such as Pacanowski and Philander (1981) and Large et al. (1994).

9.2 Summary of the vertical adjustment options

The handling of gravitationally unstable water columns in MOM4 can happen in one of two basic ways.

- Implicit vertical mixing: By setting the namelist parameter $aidif = 1.0$, all vertical diffusion is handled implicitly. There are two approaches depending on the vertical mixing scheme used.

  1. When using the constant vertical mixing module, the vertical diffusivity is set to a maximum value determined by a namelist $diff\_cbt\_limit$ upon reaching a gravitationally unstable situation. $diff\_cbt\_limit = 10.0$ (MKS) is a typical value.
  2. When using the Pacanowski and Philander or KPP vertical mixing scheme, both the vertical diffusivity and vertical viscosity are set to the namelist settings $diff\_cbt\_limit$ and $visc\_cbu\_limit$ upon reaching a gravitationally unstable situation. $diff\_cbt\_limit = visc\_cbu\_limit = 10.0$ (MKS) are typical values.

- Convective adjustment: There are two convective adjustment schemes in MOM4. Both schemes act only on tracers when mixing. The default is the *full convect* scheme of Rahmstorf (1993). The alternative scheme is the older one from Cox (1984) and is known colloquially as the "NCON scheme". The NCON scheme has been implemented in mom4.0 for legacy purposes and is not recommended for new models.

9.3 Concerning a double application of vertical adjustment

Whether solving the vertical diffusion equation implicitly ($aidif = 1.0$) or explicitly ($aidif = 0.0$), it is possible to use convective adjustment. To avoid a double application of vertical adjustment, one should keep in mind the following points.

When using neutral diffusion, it is necessary to have $aidif = 1.0$ for numerical stability. Hence, vertical diffusion will be computed implicitly in time. For those wishing to have vertical adjustment applied just via the convective adjustment scheme, then it will be necessary to set $diff\_cbt\_limit = kappa\_h$ and $visc\_cbu\_limit =$

kappa_m. If wishing to adjust via large vertical diffusivities, then set $diff\_cbt\_limit$ to a large value as described above, and set the namelist $convective\_adjust = .false.$.

9.4 Boussinesq and non-Boussinesq cases

The treatment of vertical adjustment schemes differs somewhat between Boussinesq and non-Boussinesq formulations in MOM4. We highlight these differences in this section.

9.4.1 Vertical momentum friction

As mentioned in Chapters 3 and 6 in this document, and more fully discussed in Greatbatch et al. (2001) and Griffies (2004), friction is computed in the non-Boussinesq formulations using the model velocity $\mathbf{u}^\rho$ rather than $\mathbf{u}$, where the linear momentum per volume in the ocean model is given by

$$\rho_o \, \mathbf{u} = \rho \, \mathbf{u}^\rho. \tag{9.1}$$

Hence, for the non-Boussinesq model, it is $\mathbf{u}^\rho$ that is mixed implicitly in time when using the implicit mixing scheme. There is no distinction between $\mathbf{u}^\rho$ and $\mathbf{u}$ for the Boussinesq model.

9.4.2 Vertical tracer diffusion

As also treated in Greatbatch et al. (2001) and Griffies (2004), the vertical tracer diffusion equation takes the form

$$(\rho \, T)_{,t} = -\rho_o \, \partial_z F^z \tag{9.2}$$

where

$$F^z = -\kappa \, T_{,z} \tag{9.3}$$

is the downgradient vertical tracer flux. In MOM4, we prefer to separate the density and tracer concentration prior to temporal discretization, thus to isolate the time tendency of the tracer concentration

$$T_{,t} = -(T/\rho) \, \rho_{,t} - (\rho_o/\rho) \, \partial_z F^z \tag{9.4}$$

The density time tendency term vanishes for the Boussinesq case, and the factor ρ_o/ρ is set to unity. For the non-Boussinesq case, the term $-(T/\rho) \, \rho_{,t}$ provides an added forcing to the tracer concentration, and the ρ_o/ρ factor modifies the vertical diffusion operator. The modification to the vertical diffusion operator is considered in the following sections where we discuss the implicit treatment of this equation via either implicit vertical diffusion or convective adjustment.

9.5 Implicit vertical mixing

When the namelist *aidif* is set to unity, vertical mixing of momentum and tracers is time stepped implicitly. When $aidif = 0.0$, vertical mixing is time stepped explicitly. Intermediate values give a semi-implicit treatment, although at present MOM4

does not support semi-implicit treatments. An implicit treatment of vertical mixing allows unrestrained values of the vertical mixing coefficients. An explicit treatment, especially with fine vertical grid resolution, places an unreasonable limitation on the size of the time step. The use of fine vertical resolution with sophisticated mixed layer and/or neutral physics schemes has prompted the near universal implicit treatment of vertical mixing in ocean climate models.

We now detail the implicit treatment of one dimensional vertical mixing in MOM4. As discussed in Section 9.4, the tracer equation presents the most generality through the added ρ_o/ρ factor seen in equation (9.4), and so we consider the tracer equation here. For vertical tracer diffusion in the Boussinesq system, and for the Bousinesq or non-Boussinesq vertical velocity equation, the ρ_o/ρ factor is set to unity.

9.5.1 General form of discrete vertical diffusion

We can write the vertical diffusion equation in the discrete form

$$\phi_k(\tau+1) = \phi^*_k(\tau+1) - \Gamma_k(\tau)\,(F^z_{k-1} - F^z_k). \tag{9.5}$$

where we introduced the inverse velocity

$$\Gamma_k(\tau) = \frac{aidif\,2\,\Delta\tau}{(\rho_k(\tau)/\rho_o)\,dht_k(\tau)} \tag{9.6}$$

which appears quite frequently in the following discussion. The profile $\phi^*_k(\tau+1)$ represents the tracer at the updated model time $\tau+1$ arising from all processes treated explicitly in time. The leap-frog time step $2\,\Delta\tau$ is generally larger than that allowed by CFL stability given the value of the vertical diffusivity, hence the need to solve the equation implicitly in time. The implicit vertical mixing parameter $aidif$ is set to unity for the fully implicit method. The field dht_k is the vertical thickness of the tracer cells at time τ. For vertical mixing of velocity, dht becomes the velocity cell thickness dhu.

The influence of the non-Boussinesq formulation can be thought of as modifying the vertical thickness dht_k of the tracer cells to $(\rho_k(\tau)/\rho_o)\,dht_k(\tau)$ (e.g., see equation (9.6)). Notably, this modification holds whether we are considering vertical diffusion or vertical convective adjustment, since it is independent of vertical diffusivity.[1]

9.5.2 Discretization of vertical fluxes

The vertical flux F^z_k is located at the bottom of the k^{th} tracer or velocity cell. A positive value for F^z_k leads to an increase in $\phi_k(\tau+1)$. Away from surface and bottom boundaries, this flux takes the downgradient form

$$F^z_k = -\kappa_k \left(\frac{\phi_k(\tau+1) - \phi_{k+1}(\tau+1)}{dhwt_k} \right). \tag{9.7}$$

[1] For these purposes, vertical convective adjustment can be thought of as vertical diffusion with an infinite diffusivity.

The factors of ϕ are evaluated at time $\tau + 1$ because of the implicit treatement. The vertical mixing coefficient κ_k has a general space-time dependence set by a vertical mixing scheme. As for the flux itself, the diffusivity κ_k is situated at the bottom of the tracer or velocity cell, depending on whether ϕ is a tracer field or velocity component. The array $dhwt_k$ represents the vertical distance between tracer points at time τ. For vertical mixing of velocity, $dhwt$ becomes the distance between velocity points $dhwu$.

At the ocean surface, the vertical flux is given by the surface boundary condition $sflux$ placed on the velocity or tracer. For a tracer,

$$F^z_{k=0} = -stf, \tag{9.8}$$

with stf MOM4's surface tracer flux array with units of velocity times tracer concentration. The minus sign arises from the MOM4 convention that associates a positive stf with an increase in tracer within the $k = 1$ cell. In contrast, the present discussion assumes a convention for the flux F^z whereby a positive $F^z_{k=0}$ is associated with a decrease in tracer within the $k = 1$ cell. For velocity,

$$F^z_{k=0} = -smf, \tag{9.9}$$

with smf the surface momentum flux with units of squared velocity. At the ocean bottom, a similar condition leads to

$$F^z_{k=kmt} = -btf \tag{9.10}$$

for bottom tracer fluxes, and

$$F^z_{k=kmt} = -bmf \tag{9.11}$$

for bottom momentum fluxes. The minus signs again represent a difference in convention between MOM4 and the present discussion. In MOM4, a negative btf represents the passage of tracer from solid rock into the ocean domain, as in geothermal heating. For velocity, a positive bmf represents a drag on the ocean momentum field.

9.5.3 Manipulating into a generic form

To develop the solution algorithm, it is necessary to put the vertical diffusion equation into a generic form. For this purpose, let us consider in sequence the equation for surface cells $k = 1$, interior cells with $k > 1$, and bottom cells with $k = kmt$.

9.5.3.1 Surface cells

For surface cells with $k = 1$ we have

$$\begin{aligned}
\phi^*_k(\tau+1) &= \phi_k(\tau+1) + \Gamma_k(\tau)\,(F^z_{k-1} - F^z_k) \\
&= \phi_k(\tau+1) - \Gamma_k(\tau)\,(stf + F^z_k) \\
&= \phi_k(\tau+1) - \Gamma_k(\tau)\,stf + \Gamma_k(\tau)\,\kappa_k \left(\frac{\phi_k(\tau+1) - \phi_{k+1}(\tau+1)}{dhwt_k} \right),
\end{aligned} \tag{9.12}$$

which leads to

$$\phi_k^*(\tau+1) + \Gamma_k(\tau)\, stf = \phi_k(\tau+1)\,\left(1 + \frac{\Gamma_k(\tau)\,\kappa_k}{dhwt_k}\right) - \phi_{k+1}(\tau+1)\,\left(\frac{\Gamma_k(\tau)\,\kappa_k}{dhwt_k}\right). \tag{9.13}$$

For velocity mixing, stf becomes smf, and $dhwt$ becomes $dhwu$.

9.5.3.2 Interior cells

For interior cells,

$$\begin{aligned}\phi_k^*(\tau+1) &= \phi_k(\tau+1) + \Gamma_k(\tau)\,(F_{k-1}^z - F_k^z) \\ &= \phi_k(\tau+1) - \Gamma_k(\tau)\,\kappa_{k-1}\left(\frac{\phi_{k-1}(\tau+1) - \phi_k(\tau+1)}{dhwt_{k-1}}\right) \\ &\quad + \Gamma_k(\tau)\,\kappa_k\left(\frac{\phi_k(\tau+1) - \phi_{k+1}(\tau+1)}{dhwt_k}\right)\end{aligned} \tag{9.14}$$

which leads to

$$\begin{aligned}\phi_k^*(\tau+1) = \phi_k(\tau+1)\,&\left(1 + \frac{\Gamma_k(\tau)\,\kappa_{k-1}}{dhwt_{k-1}} + \frac{\Gamma_k(\tau)\,\kappa_k}{dhwt_k}\right) \\ &- \phi_{k-1}(\tau+1)\,\left(\frac{\Gamma_k(\tau)\,\kappa_{k-1}}{dhwt_{k-1}}\right) - \phi_{k+1}(\tau+1)\,\left(\frac{\Gamma_k(\tau)\,\kappa_k}{dhwt_k}\right).\end{aligned} \tag{9.15}$$

9.5.3.3 Bottom cells

Bottom cells with $k = kmt(i,j)$ have

$$\begin{aligned}\phi_k^*(\tau+1) &= \phi_k(\tau+1) + \Gamma_k(\tau)\,(F_{k-1}^z - F_k^z) \\ &= \phi_k(\tau+1) + \Gamma_k(\tau)\,(F_{k-1}^z + btf) \\ &= \phi_k(\tau+1) + \Gamma_k(\tau)\,btf - \Gamma_k(\tau)\,\kappa_{k-1}\left(\frac{\phi_{k-1}(\tau+1) - \phi_k(\tau+1)}{dhwt_{k-1}}\right),\end{aligned} \tag{9.16}$$

which leads to

$$\phi_k^*(\tau+1) - \Gamma_k(\tau)\,btf = \phi_k(\tau+1)\,\left(1 + \frac{\Gamma_k(\tau)\,\kappa_{k-1}}{dhwt_{k-1}}\right) - \phi_{k+1}(\tau+1)\,\left(\frac{\Gamma_k(\tau)\,\kappa_{k-1}}{dhwt_{k-1}}\right). \tag{9.17}$$

9.5.3.4 A generic form

Introducing the notation

$$A_k = \begin{cases} -\Gamma_k(\tau)\,\kappa_{k-1}/dhwt_{k-1} & \text{if } k > 1 \\ 0 & \text{if } k = 1 \end{cases} \tag{9.18}$$

$$C_k = \begin{cases} -\Gamma_k(\tau)\,\kappa_k/dhwt_k & \text{if } k < kmt \\ 0 & \text{if } k = kmt \end{cases} \tag{9.19}$$

$$B_k = 1 - A_k - C_k \tag{9.20}$$

$$\Phi_k^* = \begin{cases} \phi_k^*(\tau+1) + \Gamma_k(\tau)\, stf & \text{if } k = 1 \\ \phi_k^*(\tau+1) & \text{if } 1 < k < kmt \\ \phi_k^*(\tau+1) - \Gamma_k(\tau)\, btf & \text{if } k = kmt \end{cases} \tag{9.21}$$

renders

$$\Phi_k^* = A_k\,\phi_{k-1}(\tau+1) + B_k\,\phi_k(\tau+1) + C_k\,\phi_{k+1}(\tau+1). \tag{9.22}$$

9.5.3.5 Solution method

The solution is arrived at by performing a decomposition and forward substitution. The details are taken from pages 42 and 43 of Press et al. (1992).

9.6 Convective adjustment

This section provides a description of the NCON and full convective adjustment schemes.

9.6.1 Comments on the convective adjustment schemes

As detailed in Rahmstorf (1993) and Pacanowski and Griffies (1999), the NCON convection scheme takes multiple passes through the water column, alternately looking for instability on odd and even model levels. When an instability is found, tracers are mixed, with their means (weighted by cell thickness) preserved. This process may induce further instability and therefore more than one pass through the water column may be needed to remove all instability. The number of passes through the water column is controlled by the parameter *ncon*, hence the name of the scheme.

The NCON convection scheme has come under a lot of scrutiny. The discussion in Rahmstorf (1993), Killworth (1989) and Marotzke (1991), provide some elaboration and motivation to *not* employ the NCON scheme. Its presence in MOM4.0 is solely for legacy purposes so that modelers can attempt to reproduce older results using the new code.

The question inevitably arises of whether to mix or not mix momentum during a vertical adjustment process. When momentum is not mixed, it is thought that it is simply carried along through the effects on the density field. Killworth (1989) supports this idea, so long as the purpose is large-scale ocean modeling. Basically, through geostrophy, adjusting density appears sufficient. Also, the vertical thermal wind shears in simulated convection regions were found by Killworth to not be too strong. Hence, mixing momentum along with density did little to affect the overall solution. These ideas, however, appear less sound for equatorial oceanography, and so the mixing of both momentum and tracers might be more important in there.

9.6.2 Coding of full convection by M. Eby

In June 2000, Michael Eby (eby@uvic.ca) ported a new coding of the Rahmstorf scheme to MOM3.1. His code is a bit more efficient and modern. In particular, there are no more "goto" statements. This code was incorporated into MOM3.1 and MOM4. Tests reveal that the results from the Eby code and the original Rahmstorf code are nearly identical. The researcher can uncomment/comment out two lines highlighted in the code to get the exact same results if one so desires.

CHAPTER

TEN

Vertical advection

Contents

Vertical advection has been found to constrain the model time step for certain global model configurations moreso than other of transport processes. The purpose of this chapter is to present two methods to relax the vertical CFL constraint. The first method time steps second order centered advection implicitly in time. The second method is based on ideas presented by Lin and Rood (1996).

MATERIAL IN THIS CHAPTER HAS YET TO BE IMPLEMENTED IN MOM4

10.1 Vertical transport equation

The vertical tracer transport equation in MOM4 takes the form

$$(\rho\, T)_{,t} = -\rho_o\, \partial_z F^z, \tag{10.1}$$

where we focus on tracer concentration for the moment, with trivial generalization available for treating vertical velocity transport. For diffusive transport, as treated in Chapter 9,

$$F^z = -\kappa\, T_{,z} \tag{10.2}$$

is the downgradient vertical tracer flux. For advection, as treated in this chapter,

$$F^z = w\, T \tag{10.3}$$

is the vertical advective flux. In MOM4, we prefer to separate the density and tracer concentration prior to temporal discretization, thus to isolate the time tendency of the tracer concentration

$$T_{,t} = -(T/\rho)\,\rho_{,t} - (\rho_o/\rho)\,\partial_z F^z. \tag{10.4}$$

The density time tendency term vanishes for the Boussinesq case, and the factor ρ_o/ρ is set to unity. For the non-Boussinesq case, the term $-(T/\rho)\,\rho_{,t}$ provides an added forcing to the tracer concentration, and the ρ_o/ρ factor modifies the vertical transport operator. The modification to the vertical transport operator is considered in the following sections where we discuss the implicit treatment of this equation.

10.2 Vertical CFL violations

Consider the leap-frog time stepped vertical transport equation for an arbitrary tracer field T

$$T_k(\tau + \Delta\tau) = T_k(\tau - \Delta\tau) + \left(\frac{2\,\rho_o\,\Delta\tau}{\rho_k(\tau)\,dht_k}\right)(F^z_k - F^z_{k-1}) \tag{10.5}$$

where F^z_k is the vertical flux of T entering the k^{th} tracer cell through its bottom face (see Figure 10.1). The thickness of the k^{th} tracer cell is written dht_k to correspond to the numerical model's notation. Note that all considerations in this chapter focus on a single vertical column, so the horizontal grid labels i, j are dropped for brevity.

There are many occasions where large vertical diffusive transport engenders large vertical diffusive CFL numbers, especially in mixed layer regions. In this case, it is computationally advantageous to move to a time implicit solution of the vertical diffusion equation. Otherwise, the model's time step would need to be quite low in order to maintain numerical stability. Such is the common means for time stepping vertical mixing in ocean climate models, and the details are presented in Section 9.5.

We can also have problems with onerous time step constraints in model configurations with large vertical velocities and refined vertical resolution. As for the diffusive case, "large" is defined via the vertical CFL number, with the CFL number increasing when we refine the vertical resolution, enhance the current strengths, and increase the strength and frequency of the surface forcing. Indeed, the time step used in many ocean climate models (circa 2003) are constrained by vertical advection. Hence, ways to reduce the tightness of this constraint, if only by a few tens of percents, greatly enhance model efficiency. As with any methods used for computational expediency, they must be tested against conventional approaches to see whether the solution's physical integrity is unacceptably compromised.

10.3 Implicit second order vertical advection

Second order centered advection is the means used in mom4 to vertically advect velocity. It is becoming less common, however, for advecting tracer. Nonetheless, we detail how to implement time implicit second order vertical advection. Doing so removes the vertical advection CFL constraint. Much here follows from the discussion of vertical mixing in Section 9.5.

10.3.1 Discrete implicit advection

As in the discussion of Section 9.5, we start by focusing on vertical tracer transport given by equation (10.5). Second order centered advection leads to the discrete vertical flux

$$F_k^z = \alpha\, w\_bt_k/2\,[T_k(\tau+\Delta\tau) + T_{k+1}(\tau+\Delta\tau)] + (1-\alpha)\, w\_bt_k/2\,[T_k(\tau) + T_{k+1}(\tau)]. \quad (10.6)$$

In this equation, $0 \le \alpha \le 1$ sets the level by which the advective flux is evaluated implicitly, with $\alpha = 1$ fully implicit, and $\alpha = 0$ fully explicit. A similar factor, known in the model as $aidif$, is used for vertical diffusion in Section 9.5. We focus now on the implicit piece of vertical advection.

In equation (10.6), w_bt_k is the vertical component to the tracer advection velocity. It is centered at the bottom face of the k^{th} tracer cell (see Figure 10.1). For the α part of this equation, tracer concentration is evaluated at the new time step $\tau+\Delta\tau$, representing an implicit discretization of the flux. The vertical velocity is computed at the present time step τ regardless whether we consider implicit or explicit advection. If we instead tried to use velocity at the new time $\tau+\Delta\tau$; i.e., implicitly, then the implicit method would become nonlinear and impractical. Note that a similar approach is taken when implementing implicit vertical mixing schemes. In these cases, although we may time step the tracer concentration implicitly, the flow dependent diffusivity is computed at time τ instead of $\tau+\Delta\tau$. Again, to do otherwise would entail an impractical nonlinear implicit algorithm for vertical mixing. Because we always evaluate velocity at τ, we do not expose its time dependence.

In mom4, we time step the explicit terms first to compute a partially updated tracer $T_k^*(\tau+\Delta\tau)$. Then, we time step the implicit portion, which for tracers includes vertical diffusion and, if using the present scheme, second order vertical advection. For velocity, we may also choose to compute the Coriolis force implicitly in time, as discussed in Chapter 24. The implicit vertical advection piece leads to

$$T_k(\tau+\Delta\tau) = T_k^*(\tau+\Delta\tau) + \left(\frac{\alpha\,\rho_o\,\Delta\tau}{\rho_k(\tau)\,dht_k}\right) [w\_bt_k\,(T_k(\tau+\Delta\tau) + T_{k+1}(\tau+\Delta\tau)) - w\_bt_{k-1}\,(T_{k-1}(\tau+\Delta\tau) + T_k(\tau+\Delta\tau))]. \quad (10.7)$$

Following the discussion of vertical diffusion in Section 9.5.1, we introduce the shorthand

$$\Gamma_k^{(adv)}(\tau) = \frac{2\,\alpha\,\Delta\tau}{(\rho_k(\tau)/\rho_o)\,dht_k(\tau)}. \quad (10.8)$$

The density ratio is set to unity when employing the Boussinesq approximation. Note that the parameter α used for vertical advection need not be equal to the $aidif$ parameter used for vertical diffusion. Hence, it is useful to introduce the adv label on Γ, thus bringing equation (10.7) to the form

$$T_k(\tau+\Delta\tau) = T_k^*(\tau+\Delta\tau) + (\Gamma_k^{(adv)}/2)\,[w\_bt_k\,(T_k(\tau+\Delta\tau) + T_{k+1}(\tau+\Delta\tau)) - w\_bt_{k-1}\,(T_{k-1}(\tau+\Delta\tau) + T_k(\tau+\Delta\tau))]. \quad (10.9)$$

We can put these results into a standard form via manipulations similar to those used for vertical diffusion in Section 9.5.3. For this purpose, some rearrangement brings equation (10.7) into the form

$$T^*_k(\tau+\Delta\tau) = T_k(\tau+\Delta\tau)\,\left(1-(\Gamma^{(adv)}_k/2)\,w\_bt_k+(\Gamma^{(adv)}_k/2)\,w\_bt_{k-1}\right) + T_{k-1}(\tau+\Delta\tau)\,(\Gamma^{(adv)}_k/2)\,w\_bt_{k-1} - T_{k+1}(\tau+\Delta\tau)\,(\Gamma^{(adv)}_k/2)\,w\_bt_k. \quad (10.10)$$

This equation holds for all grid points in the vertical, starting from $k=1$. However, it is useful to distinguish the treatment at the top and bottom boundaries. For $k=1$, the $w\_bt_{k=0}$ contribution is handled via a separate portion of the update process associated with surface height time tendencies. So this term does not contribute here, thus leading to

$$T_{k=1}(\tau+\Delta\tau) = T^*_{k=1}(\tau+\Delta\tau) + (\Gamma^{(adv)}_{k=1}/2)\,[w\_bt_{k=1}\,(T_{k=1}(\tau+\Delta\tau)+T_{k=2}(\tau+\Delta\tau))-0], \quad (10.11)$$

or in the rearranged form

$$T^*_{k=1}(\tau+\Delta\tau) = T_{k=1}(\tau+\Delta\tau)\,\left(1-(\Gamma^{(adv)}_{k=1}/2)\,w\_bt_{k=1}+0\right) + 0 - T_{k=2}(\tau+\Delta\tau)\,(\Gamma^{(adv)}_{k=1}/2)\,w\_bt_{k=1}. \quad (10.12)$$

A similar equation results for vertical advection of velocity at the $k=1$ velocity cell. At the bottom of a tracer column, $w\_bt_{k=kmt}$ generally vanishes due to volume/mass conservation, thus leading to

$$T_{k=kmt}(\tau+\Delta\tau) = T^*_{k=kmt}(\tau+\Delta\tau) + (\Gamma^{(adv)}_{k=kmt}/2)\,[0-w\_bt_{k=kmt-1}\,(T_{k=kmt-1}(\tau+\Delta\tau)+T_{k=kmt}(\tau+\Delta\tau))], \quad (10.13)$$

or in the rearranged form

$$T^*_{k=kmt}(\tau+\Delta\tau) = T_{k=kmt}(\tau+\Delta\tau)\,\left(1-0+(\Gamma^{(adv)}_{k=kmt}/2)\,w\_bt_{k=kmt-1}\right) + T_{k=kmt-1}(\tau+\Delta\tau)\,(\Gamma^{(adv)}_{k=kmt}/2)\,w\_bt_{k=kmt-1}-0. \quad (10.14)$$

At the bottom of a column of velocity points, $w\_bu_{k=kmu}$ generally does not vanish, since this velocity does not sit at the ocean bottom when there is nontrivial topographic slope. Hence, both advective fluxes are present for the velocity equation at $k=kmu$. The issue of vertical velocities at the ocean bottom is discussed in Section 22.3.3 of Pacanowski and Griffies (1999).

Following the diffusion discussion in Section 9.5.3, we introduce

$$2\,A_k = \begin{cases} \Gamma^{(adv)}_k(\tau)\,w\_bt_{k-1} & \text{if } k>1 \\ 0 & \text{if } k=1 \end{cases} \quad (10.15)$$

$$B_k = 1+A_k+C_k \quad (10.16)$$

$$2\,C_k = -\Gamma^{(adv)}_k(\tau)\,w\_bt_k \quad (10.17)$$

to render

$$T_k^*(\tau+\Delta\tau) = A_k\, T_{k-1}(\tau+\Delta\tau) + B_k\, T_k(\tau+\Delta\tau) + C_k\, T_{k+1}(\tau+\Delta\tau). \quad (10.18)$$

Note that higher order advection schemes lead to larger stencils. So, if time stepped implicitly, these schemes require a more expensive matrix inversion.

10.3.2 Comparing to implicit vertical diffusion

There are two differences in details between implicit vertical mixing and implicit vertical advection: (1) advection and mixing generally use different $aidif$ factors, (2) the sign for A_k for advection, defined above equation (10.18), is opposite that for mixing (see Section 9.5.3.4), (3) B_k for diffusion is defined as $1 - A_k - C_k$ whereas for advection it is $1 - A_k - C_k$. These differences must be kept in mind when inverting the system.

10.4 Implicit first order upwind advection

Second order advection suffers from the well known null-mode. One may wish to employ, instead, a first order upwind scheme which is made more stable via its large levels of implicit diffusion. If the implicit upwind is applied only at select places, then the cost in solution integrity of added diffusion may be worth the advantage of running with longer time steps.

10.5 Integer and non-integer advection

THIS MATERIAL IS UNFINISHED

Lin and Rood (1996) present a means to relax the CFL constraint on 3-dimensional advection. Because vertical advection constrains the time step for some global models, we limit our considerations just to the one-dimensional implementation of their scheme.

The numerically realized vertical advective flux of T is a discretization of the advective flux $w\,T$. Motivated by Lin and Rood (1996), consider the special case in which the vertical advective velocity component at the bottom face of the k^{th} tracer cell, w_bt_k, has the positive value $w\_bt_k = dht_k/(2\,\Delta\tau)$. That is, the vertical "upwind" Courant number for the k^{th} cell is unity

$$C_k = w\_bt_k\,(2\Delta\tau)/dht_k = 1. \quad (10.19)$$

If we assume that the tracer concentration for a grid cell represents the value for a uniformly distributed concentration within the cell, then the first order upwind advective flux

$$F^z_{k+1} = w\_bt_k\, T_{k+1} = (dht_k/2\,\Delta\tau)\, T_{k+1} \quad (10.20)$$

is an exact discretization of the continuum advective flux passing through the bottom face of the k^{th} tracer cell.

If the vertical velocity is larger, say with a Courant number $C_k = 2$, then

$$F^z_{k+1} = w\_bt_k\,(T_{k+1} + T_{k+2}) \quad (10.21)$$

$$= (dht_k/2\,\Delta\tau)\,(T_{k+1} + T_{k+2}). \quad (10.22)$$

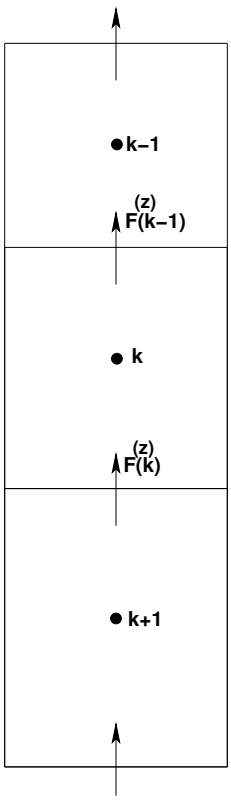

Figure 10.1: Schematic illustrating the vertical advective transport passing across the faces of a model grid cell.

Part IV

Some coupled modeling issues

SOME COUPLED MODELING ISSUES

MOM has traditionally been used as a component within a coupled climate modeling system. Moving to a free surface has introduced some new issues that must be addressed when coupling MOM4 to sea ice and river models. These issues are outlined in this part of the MOM4 Guide.

CHAPTER

ELEVEN

Considerations for ice-ocean modeling

Contents

This chapter presents some considerations relevant for coupling a z-coordinate free surface ocean model to a dynamical ice model. We focus on the issues within the context of a Boussinesq model, although the points are generic to any free surface z-coordinate model.

11.1 Introduction

There are regions where ice-sheets have yet to form, yet ice is present in the liquid water. This slurry of water-ice is commonly known as *frazil*. The liquid water portion of frazil has a temperature given by the freezing temperature, which is a function of the salinity and pressure.

During the formation of frazil, latent heat and salt is released to the liquid seawater. To get a rational representation of the salt added to the ocean model requires that it be coupled to a sea ice model. For the present purposes, we describe a simple means to represent the heating effect. Note that when implementing a "frazil"

option in MOM4 without sea ice, we are led to the unphysical circumstance of having sea ice formation stabilize the ocean water column. Hence, one should be quite careful not to over interpret solutions where frazil heating occurs without the corresponding salinification.

11.2 Ocean heating due to frazil formation

To represent the heating due to frazil formation, we assume a linear empirical relation can be used to express the temperature at which sea ice starts to form (ignoring pressure and nonlinear salinity effects)

$$T(^\circ\mathrm{C}) = -0.054\, s(\mathrm{psu}). \tag{11.1}$$

Water with higher salinity freezes at lower temperatures than water with lower salinity. If the model's prognostic temperature equation (i.e., advection, diffusion, surface cooling) predict that $T(^\circ\mathrm{C}) < -0.054\ s(\mathrm{psu})$, two effects occur. First, heat is input to the liquid ocean water as it is extracted from the freezing ocean water. The amount of heat given to the liquid is

$$Q_{frazil}(\mathrm{Joule}) = |0.054\, s(\mathrm{psu}) + T(^\circ C)|\, dV\, \rho\, C_p \tag{11.2}$$

where

$$dV = dx\, dy\, (\Delta z + \eta) \tag{11.3}$$

is the surface grid cell volume, ρ is the *in situ* ocean density, and C_p is the heat capacity of seawater with

$$\rho_o\, C_p = 1035\,\mathrm{kg\,m^{-3}} \times 3985\,\mathrm{Joule\,^\circ C^{-1}\,kg^{-1}} = 4.125 \times 10^6\,\mathrm{Joule\,m^{-3}\,C^{-1}}. \tag{11.4}$$

As defined, Q_{frazil} is the heat sufficient to raise the sea surface temperature to $T(^\circ\mathrm{C}) = -0.054\, s(\mathrm{psu})$. Note that as the frazil heat is given to the liquid ocean over the course of a tracer leap-frog time step, the rate of heating of the liquid due to frazil formation is given by

$$\mathrm{d}Q_{frazil}/\mathrm{d}t = (2\, dtts)^{-1}\, |0.054\, s(\mathrm{psu}) + T(^\circ C)|\, dV\, \rho_o\, C_p. \tag{11.5}$$

Written as in a prognostic leap-frog time step, we have

$$T(\tau + dtts) = T^*(\tau + dtts) + 2\, dtts\, \mathrm{d}Q_{frazil}/\mathrm{d}t, \tag{11.6}$$

with $T^*(\tau + dtts)$ the potential temperature updated to the new time step due to the effects of processes other than frazil formation.

We determine the frazil heat $Q_{frazil}(\mathrm{Joule})$ within the ocean model. This heat is applied to the ocean over a single leap-frog time step of length $2\, dtts$. For heat conservation within the coupled ocean and sea ice system, this same amount of heat must be extracted from the sea ice model. Importantly, if the sea ice model uses a different time stepping scheme than MOM4's leap-frog, then the frazil heat Q_{frazil} extracted from the sea ice model must be adjusted accordingly. For example, the GFDL sea ice model (Sea Ice Simulator) uses a single-time step scheme rather than a leap-frog. So the frazil heat Q_{frazil} extracted from the sea ice model over a

single $dtts$ time step within the ice model will be given by one-half that input to the ocean model over a single ocean leap-frog time step $2\,dtts$

$$|Q^{MOM4}_{frazil}(\text{Joule})| = 2\,|Q^{SIS}_{frazil}(\text{Joule})|. \tag{11.7}$$

An example helps to illustrate the magnitude of this heating. Consider the cooling of a surface grid cell with salinity 35psu, and let the cooling be such that the model's prognostic temperature equation predicts an updated surface cell temperature of $-2\,^\circ$C. Since $-2 < -0.054 \times 35 = 1.89$, frazil will form. The latent heat given to the liquid ocean associated with the frazil formation is

$$Q_{frazil}(\text{Joule}) = |1.89 - 2|\, dV\, \rho_o\, C_p, \tag{11.8}$$

where we made the Boussinesq approximation and so set the *in situ* density to the reference density ρ_o. For a surface grid cell of volume $10^5\,\text{m} \times 10^5\,\text{m} \times 10\,\text{m}$, the formation of frazil leads to a local heat given to the ocean of

$$Q_{frazil} = 4.5 \times 10^{16}\,\text{Joule}. \tag{11.9}$$

If this heating occurs over the course of a day (i.e., $2\,dtts = 1$ day), then the rate of heating is given by

$$\mathrm{d}Q_{frazil}/\mathrm{d}t = 4.25 \times 10^{11}\,\text{Watt}. \tag{11.10}$$

If the surface area $\mathrm{d}A$ of the grid cell is $10^5\,\text{m} \times 10^5\,\text{m}$, this heating by frazil contributes

$$(\mathrm{d}Q_{frazil}/\mathrm{d}t)/\mathrm{d}A = 42.5\,\text{Watt m}^{-2}. \tag{11.11}$$

11.3 Ice with a free surface in a z-model

The remainder of the chapter is concerned with the issues of how sea-ice on the ocean surface affects the surface height and thus the ocean currents. To introduce the issues, recall that a column of Boussinesq ocean expands and contracts according to

$$\eta_{,t} = -\nabla \cdot \mathbf{U} + q_w. \tag{11.12}$$

This equation represents a volume budget over a column of fluid, and it is derived in Griffies (2004). In this equation, η is the deviation of the ocean surface from its resting position at $\eta = 0$. The first term on the right hand side is the convergence of the vertically integrated velocity. For non-tidal motions, this term accounts for some one-two meters of surface height deviation. The second term is the fresh water forcing. Rain, rivers, evaporation, and non-tidal dynamics typically lead to $|\eta| \leq 3m$. Our concern in this chapter is the additional effect associated with ice formation. Figure 11.1 illustrates this balance.

11.4 Steady state mass budget

We consider here the steady state mass budget for a single ocean model grid cell before and after the formation of ice, as shown in Figure 11.2. Without ice, the mass of fluid in the grid cell is given by

$$dM_{ocean} = \rho_{ocean}\, dV = (\Delta z + \eta_{initial})\, \rho_{ocean}\, dx\, dy, \tag{11.13}$$

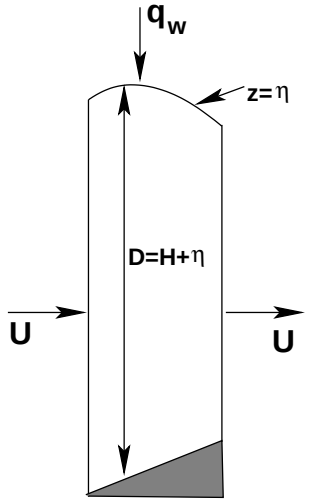

Figure 11.1: The balance of volume within a column of Boussinesq fluid extending from the free surface to the ocean bottom is represented by $\eta_{,t} = -\nabla \cdot \mathbf{U} + q_w$, where η is the time dependent deviation of the surface height from its resting state at $z = 0$. Time dependent fluctuations ($\eta_{,t}$) are driven by (1) the convergence of volume fluxes associated with the vertically integrated horizontal currents, and (2) the flux of volume across the ocean surface from fresh water.

where ρ_{ocean} is the *in situ* density of ocean fluid, and

$$\Delta z + \eta_{initial} = h^{ocean}_{initial} \tag{11.14}$$

is the initial thickness of ocean liquid in the grid cell. For the purposes of deriving the ice-ocean mass balance, we are not concerned with the *in situ* density of ocean fluid, but the *in situ* density of fresh water in the surface grid cell. That is, we are concerned with the mass of fresh water in the cell

$$dM_{fresh} = \rho_{fresh}\, dV = (\Delta z + \eta_{initial})\, \rho_{fresh}\, dx\, dy. \tag{11.15}$$

As determined by the dynamical ice model, some fraction of this fresh water freezes into sea ice with density ρ_{ice}, thus forming ice of mass

$$dM_{ice} = h_{ice}\, \rho_{ice}\, dx\, dy, \tag{11.16}$$

where h_{ice} is the ice thickness. Assuming all the fresh water mass used to form ice comes locally from an ocean model grid cell, ice formation reduces the thickness of liquid ocean in this grid cell. At equilibrium, the thickness of ocean fluid is therefore given by

$$(\Delta z + \eta_{final}) = (\Delta z + \eta_{initial}) - h_{ice}\, (\rho_{ice}/\rho_{fresh}). \tag{11.17}$$

11.5 Dynamical budgets

We now consider an oceanic perspective on the volume and momentum budgets associated with ice formation and thawing.

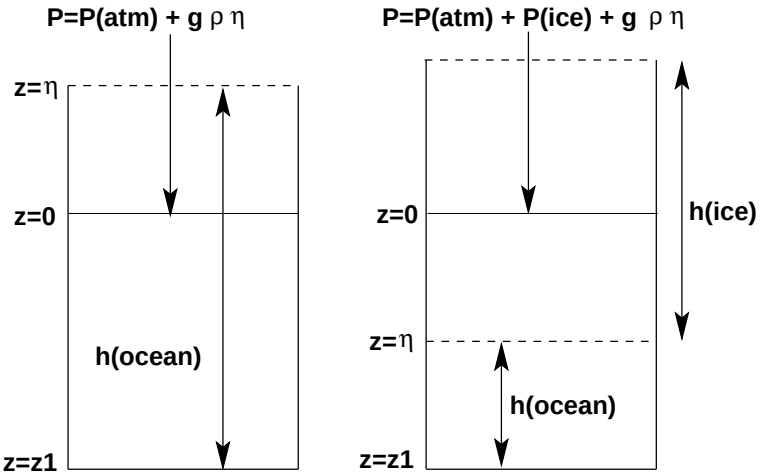

Figure 11.2: Freezing of liquid ocean to form sea ice. Shown here is a single surface model grid cell with vertical thickness $\Delta z + \eta$, where $\Delta z = |z_1|$. The left panel shows a cell filled with liquid ocean of some thickness h_{ocean}. The right panel shows a cell with ice floating on liquid ocean in an equilibrium state after the transfer of fresh water from ocean to ice has occured.

For the volume budget, the ice model provides the ocean model with a rate at which fresh water is transferred between the sea ice and ocean. That is, the ice model determines the ice contribution to the fresh water flux q_w to be applied to the surface height equation (11.12).

For the momentum budget, we consider the pressure applied at $z = 0$. This pressure drives the vertically integrated momentum field in the model. Without ice, Figure 11.2 shows that $p_{z=0}$ is set by the atmospheric pressure as well as the hydrostatic pressure arising from the layer of fluid between $z = 0$ and $z = \eta$

$$p_{z=0} = p_{atm} + \rho_{ocean}\, g\, \eta, \tag{11.18}$$

where again ρ_{ocean} is the *in situ* ocean fluid density. In the presence of ice, pressure at $z = 0$ has a contribution due to the mass of ice floating on the ocean. This pressure is given by the weight per area of ice, thus leading to

$$p_{z=0} = p_{atm} + \rho_{ocean}\, g\, \eta + \rho_{ice}\, g\, h_{ice}. \tag{11.19}$$

The overall dynamical effect of ice on the ocean is small since the density of ice is close to that of fresh water. Hence, the pressure $p_{z=0}$ is nearly the same whether there is ice or liquid ocean in the grid cell.

11.6 The problem for z-coordinate ocean models

Sea ice in parts of the high latitudes can reach thicknesses on the order of ten meters or more. Hence, the ocean surface height can be depressed by a large amount, which in many cases is larger than the thickness of the ocean model's surface grid cell. This situation is unfortunate for MOM4 since the model does not allow for the

vanishing of grid cells. Additionally, for purposes of simulating the surface mixed layer, modelers refine the vertical resolution near the surface, and so the depression of the surface by ice could easily cause the surface grid cell to vanish.

This limitation of z-coordinate models is fundamental. It warrants the consideration of other vertical coordinates. One which has been proposed is $p - p_{atmosphere}$. This coordinate will always vanish at the ocean surface, no matter how low the surface height is. It is presently a research topic to see whether this coordinate is indeed useful for global ocean climate modeling.

11.7 The alternatives

We discuss here some choices available to the z-coordinate ocean modeler.

11.7.1 Coarse vertical resolution

One option for ocean-sea ice coupling is to use coarse vertical resolution so that Δz of the ocean surface grid cell is larger than the anticipated sea ice thickness. When considering this as an option, be sure to recognize the following points. Low vertical resolution will compromise the integrity of surface ocean mixed layer simulations. Empirically, we have found resolutions in the upper ocean on the order of 10m or finer is required within the mixed layer. Intermediate resolutions, such as 20m-40m, traditionally have been avoided since they neither provide the necessary resolution for a mixed layer scheme, nor enough volume to form a simple bulk mixed layer. For this reason, climate modelers running without a surface mixed layer scheme typically set their top box to some 50m thick.

11.7.2 Limit the ice thickness

If we insist on have refined vertical resolution for a mixed layer, then coupling a sea ice model to a free surface z-coordinate ocean model requires one of two alternatives. First, we can run the ocean model with real fresh water forcing, yet limit the ice thickness. From an ocean perspective, this choice is preferable. However, artificially limiting the ice thickness may in turn affect ice extent. As one key role of ice in the climate system is how it affects the earth's albedo, artificially affecting the ice extent is not desirable.

11.7.3 Zero fresh water fluxes and nonzero virtual salt fluxes

Another alternative is to let the ice thickness be unlimited, yet to remove the direct effects of fresh water forcing from the ocean. That is, we solve the free surface equation as

$$\eta_{,t} = -\nabla \cdot \mathbf{U}, \tag{11.20}$$

instead of the budget (11.12). In turn, there is no pressure applied to the ocean from the overlying ice. It is as if the ice has a zero mass and it exchanges zero mass of liquid with the ocean. Since the non-tidal dynamical effects yield a surface height deviation on the order of a few meters, this choice ensures that the ocean model

will not loose surface grid cells, so long at Δz is something larger than some few meters (e.g., $\Delta z = 5$m should be sufficient).

By removing fresh water from the volume budget, we reduce the Boussinesq ocean to an ocean with constant total volume. There is no longer a transfer of volume across the ocean surface. As the volume transfer between sea ice and ocean is the problem, one may wish to remove just this transfer, but still allow the ocean to feel the effects of fresh water from rivers, precipitation, and evaporation. However, doing so will compromise the conservation of fresh water in the fully coupled system. The reason is that ice grows via precipitation (snow). If we allow precipitation to fall into the ocean as rain, but do not allow fresh water melt from sea ice to enter the ocean, we have an open loop and so cannot conserve.

Removing fresh water transfers between the ocean and the rest of the climate system is not the full story for the ocean. The reason is that freshening changes the ocean salinity, which in turn changes the ocean density. This effect is crucial for driving ocean currents, and so must be parameterized. As in the rigid lid models, a means for incorporating this effect into the constant volume ocean model is to introduce a salt flux across the model surface whenever there is a transfer of fresh water in the real system.

To motivate the form of the salt flux, let us first consider the case of an ocean model consisting of a single free surface grid cell affected only by surface water fluxes. Due to the large hydration energy of salts, there is no salt flux across the ocean surface, thus leading to the salt budget

$$\partial_t [dx\, dy\, (\Delta z + \eta)\, s] = 0. \tag{11.21}$$

That is, total salt is constant in time. Solving for the salinity tendency leads to

$$s_{,t} = -\left(\frac{s\, q_w}{\Delta z + \eta} \right), \tag{11.22}$$

where $\eta_{,t} = q_w$ was used since we are considering the whole ocean to be one grid cell, and so the $\nabla \cdot \mathbf{U}$ term is absent. This budget says that as water is added to the ocean ($q_w > 0$) it drives salinity to smaller values ($s_{,t} < 0$).

We now consider the case where there is no transfer of volume across the ocean surface, and so the total ocean volume is constant. For the present example of a single grid cell ocean, we therefore have η constant in time. To allow for the freshening effect, fresh water transported into the ocean is replaced by a *virtual salt flux* out of the ocean. In order to provide the same salinity tendency as in the case of fresh water transfer, we are motivated to define our virtual salt flux as

$$F^{exact} = -s\, q_w. \tag{11.23}$$

However, this flux, which is the product of the local time dependent value of salinity and the local fresh water flux, will not allow for conservation of total salt, even if fresh water is globally constant. That is, $\int dx\, dy F^{propose}$ is not constant, even if $\int dx\, dy\, q_w$ is constant. Instead, to conserve total salt we must take the virtual salt flux as

$$F^{virtual} = -s_o\, q_w, \tag{11.24}$$

where s_o is a constant. In this case, the salinity equation becomes

$$s_{,t} = -\left(\frac{s_o\, q_w}{\Delta z + \eta}\right). \tag{11.25}$$

Comparison with the salinity tendency for the case of real fresh water fluxes reveals that a virtual salt flux yields an accurate salinity tendency only when the constant salinity s_o is close to the local salinity s. Errors scale as s_o/s. With global salinity running on average near 35psu, it is typical to set $s_o = 35$psu. With this value, however, river mouths introduce problems with this approach, especially with higher resolution ocean models where the local salinity can become quite small. In this case, as the river introduces fresh water to the ocean, the virtual salt flux is too large in magnitude, thus causing the salinity tendency to be too large. Such large jumps in salinity can introduce numerical problems on top of the physical problems associated with spuriously large haline forcing in the model.

11.7.4 Pressure coordinate ocean models

If we redefine our vertical coordinate to be $s = p(z) - p_{atm} - p_{ice}$, then the surface of the ocean is always at $s = 0$. Discretizing the vertical according to s-levels allows for arbitrary deviations of the ice thickness, since ice always lives at $s = 0$. Investigation of this vertical coordinate has not been thorough, and there may be nontrivial issues to deal with, especially at the ocean bottom. Such remains a topic for future studies.

11.8 Heat budget in coupled models

The change in energy at the solid/liquid phase transition is hundreds of times larger than changes associated with raising the temperature of liquid water by a degree celcius. Hence, global atmospheric models traditionally do not carry temperature for water. River and land models similarly do not carry a temperature for its fresh water. Sea ice models do carry a temperature of sea ice by default, since the water temperature is always at the freezing point. Ocean models, of course, do carry temperature, as this determines ocean density which in turn affects its circulation. This different treatment of water in the coupled system leads to a global non-conservation of heat when fresh water is allowed to be transferred across the ocean interface.

To garner a sense for the magnitude of the imbalance, consider an ocean of two grid boxes. Fresh water evaporating from a warm box and then condensing into a cool box will lead to an ocean heat transport per unit area given by

$$\Delta H/A = \rho_{fresh}\, C_p\, q_w\, (T_{warm} - T_{cold}). \tag{11.26}$$

This result assumes that fresh water transferred across the ocean-atmosphere interface, either as precipitation or evaporation, has the same temperature as the sea surface temperature carried by the ocean model. With $\rho_{fresh}\, C_p \approx 4 \times 10^6 \mathrm{J}/(\mathrm{m}^3\, K^\circ)$, q_w on the order of a meter per year, and $T_{warm} - T_{cold} \approx 10K^\circ$, we have $\Delta H/A \approx$

$1\,\mathrm{W\,m^{-2}}$. With atmospheric models not carrying temperature, there is no corresponding atmospheric heat transport. The coupled system thus has an open loop and so conservation is lost.

Fluxes crossing the ocean surface are on the order of tens to hundreds of $\mathrm{W\,m^{-2}}$, and so this imbalance is small from an ocean-only perspective. Yet the imbalance is systematic since evaporation tends to occur over certain regions, and precipation in other regions. Furthermore, this heat flux imbalance is on the order of that associated with global warming forcing. Hence, for climate simulations, it may be unacceptable and "corrections" or "adjustments" may be necessary to maintain proper balances. Notably, this conclusion is independent of the limitations of z-coordinate models discussed in the previous sections.

CHAPTER

TWELV

River discharge into the ocean model

Contents

This chapter presents a method to distribute river runoff throughout a vertical column comprised of more than a single ocean model grid cell. This issue is most important for ocean models with fine vertical grid resolution. Care is taken to account for the needs to conserve properties using the constraints of a z-model where only the top cell is allowed to change its volume. The algorithm presented here is based on discussions with Mike Winton (mw@gfdl.noaa.gov).

We formulate the river mixing process in terms of sources added to the tracer concentration equations. Changes in the free surface height are handled just as for other forms of fresh water, such as precipitation and evaporation.

12.1 Introduction

Coupling rivers to an ocean model is necessary when building fully coupled climate models. For z-models, river discharge is typically given fully to the top model grid cell. Depending on the model resolution, dumping all the river properties to the top grid cell can cause problems. Notably, without enhanced mixing, a strong halocline can arise, with associated problems appearing due to noise from vertical advection across the strong front. This problem is enhanced in models with relatively fine vertical resolution, such as the 10m now common for the top grid cell in ocean climate models.

In the real world, there are two reasons that the halocline at river mouths is somewhat weaker than can occur in ocean climate models. First, river water does not generally fill only a single layer of some 10m depth. Instead, rivers discharge into the ocean over a vertical column whose depth can be deeper than 10m. Second, and more generally, river properties are mixed through a vertical column due to waves and tides near the coasts.

Two methods to relieve numerical problems can be considered. First, we can enhance vertical mixing of tracers in the region next to river mouths. This approach is straightforward and is available in MOM4. In detail, the enhanced mixing is strongest near the surface and tapers to zero at a specified depth. Such is the only method available to rigid lid ocean models for handling enhanced mixing at river mouths. Another method is to distribute the river water, along with its tracer content, over a pre-defined vertical column. Since the top model grid cell in the z-coordinate MOM4 is the only one capable of changing its volume through changes in the surface height, distributing river water into deeper cells must be done carefully. In the remainder of this chapter, we detail such a method.

Note that we typically do not alter the transfer of momentum from the river to the ocean. Instead, we assume that river horizontal momentum is the same as the corresponding ocean cell, thus leading to no change in the ocean momentum associated with river discharge. This assumption may require modifications for careful studies of coastal processes, but it should be sufficient for ocean climate modeling.

12.2 General considerations

Consider a column of discrete ocean with kr cells in the vertical over which we aim to discharge river water:

$$kr = \#\text{ of vertical ocean cells into which river water is discharged.} \tag{12.1}$$

Allow the river to be discharging at a volume per area per time given by R, which has units of a velocity:

$$R = \text{volume per area per time of river water discharge.} \tag{12.2}$$

The river water flux R is distinguished in MOM4 from fresh water associated with evaporation and precipitation.

The tracer concentration within the river water is given by C_{river}:

$$C_{river} = \text{tracer concentration within river water.} \tag{12.3}$$

C_{river} is distinguished in MOM4 from the tracer concentration associated with evaporation and precipitation. What tracer concentration should be taken for the river water? Typically, we think of rivers at their discharge point as having tracers of uniform concentration. More information about tracer profiles requires a river model, and even so we may wish to summarize the river information prior to passing it into the ocean. Assuming a single uniform value for the river tracer concentrations, and absent a river model, it is typical to assume the following river tracer concentration

$$\theta_{river} = \theta^{k=1}_{ocean} \tag{12.4}$$

$$s_{river} = 0 \tag{12.5}$$

$$T_{river} = T^{k=1}_{ocean} \tag{12.6}$$

where $k = 1$ is the top cell of the ocean column into which the river water is discharged, θ is the potential temperature, which equals the *in situ* temperature at the ocean surface, s_{river} is the zero salinity of the fresh water river, and T_{river} is the concentration of a passive tracer in the river. By assuming $\theta_{river} = \theta^{k=1}_{ocean}$, vertically distributing river water acts to warm the ocean column in regions where the ocean surface is warmer than depth. In contrast, rivers with zero salinity do not alter the ocean salt content, yet they do reduce the salinity.

Over a leap-frog tracer time step $2\,dtts$, a thickness $H_{river} = R * 2\,dtts$ of river water is to be distributed throughout the vertical ocean column:

$$H_{river} = R * 2\,dtts = \text{river water thickness discharged per tracer leap-frog.} \quad (12.7)$$

Along with this distribution of river water into the ocean column, we distribute the tracer content of the river into the ocean column:

$$C_{river}\,H_{river} = \text{river tracer content discharged per tracer leap-frog.} \quad (12.8)$$

12.3 Steps in the algorithm

We derive the algorithm by considering the conservation equations for tracer in a vertical column of ocean model grid cells. To isolate effects from river discharge, we ignore all horizontal processes. Without distributing river runoff with depth, tracer conservation is given by

$$\begin{aligned} \partial_t\,(V\,\rho\,C)_{k=1} &= \rho_o\,A\,R\,C_{river} \\ \partial_t\,(V\,\rho\,C)_{k>1} &= 0 \end{aligned} \quad (12.9)$$

where $V = A\,h$ is the volume of a grid cell, C is the tracer concentration, ρ is the *in situ* density, R is the river discharge rate, and C_{river} is the concentration of tracer in the river. As the horizontal area A is constant, it can be dropped from the discussion. Conservation of total tracer in the four-box system is manifest by

$$\partial_t \sum_{k=1}^{kr} (h\,\rho\,C) = \rho_o\,R\,C_{river}. \quad (12.10)$$

Whatever is done to redistribute river runoff with depth, this conservation law must be preserved.[1]

To derive the algorithm, we refer to Figure 12.1. Here, we prescribe that a fraction of the river water and its tracer content is inserted into each of the cells within the column, where the fractions sum to unity

$$\sum_{k=1}^{kr} \delta_k = 1. \quad (12.11)$$

We choose the fractions according to the grid cell thickness

$$\delta_k = \frac{h_k}{\sum_{k=1}^{kr} h_k} \quad (12.12)$$

[1]The appearance of ρ_o on the right hand side, rather than ρ_{river}, is described in Chapter 3 as well as Griffies (2004).

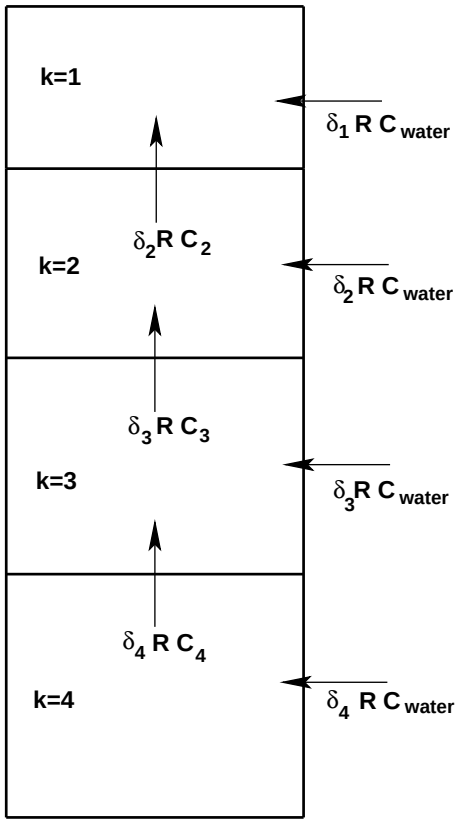

Figure 12.1: Schematic of river discharge algorithm for the case with $kr = 4$. We insert a fraction of the river water into grid cells throughout the column, with a corresponding amount leaving each cell bubbling upwards in order to conserve water mass/volume.

where h_k is the tracer cell thickness, and is known as dht_k in the MOM4 code.

Because the interior cell volumes remain constant in MOM4, the same amount of water that entered the cell via the river water must then leave. We assume that it leaves with the tracer concentration of the cell prior to the insertion of the river water. That is, by inserting some of the river water into the cell at tracer concentration C_{river}, we then displace the same amount of water but at concentration C_k. This displaced water is bubbled upwards towards the surface cell. Conservation equations for this algorithm take the form

$$\begin{aligned} \partial_t (h\,\rho\,C)_1 &= R\,[(\delta\,\rho\,C)_2 + \delta_1\,\rho_o\,C_{river}] \\ \partial_t (h\,\rho\,C)_k &= R\,[(\delta\,\rho\,C)_{k+1} - (\delta\,\rho\,C)_k + \delta_k\,\rho_o\,C_{river}] \\ \partial_t (h\,\rho\,C)_{kr} &= R\,[-(\delta\,\rho\,C)_{kr} + \delta_{kr}\,\rho_o\,C_{river}] \end{aligned} \tag{12.13}$$

where the first equation is for $k = 1$, the second for $1 < k < kr$, and the third for $k = kr$. The algorithm has the appearance of upwind advection throughout the column. Hence, conservation of total tracer for the column is trivially verified.

Formulation as a thickness-weighted tracer source leads to

$$\begin{aligned}
\rho_o \,\mathrm{dht} \cdot \text{tracer-source}_1 &= R\left[(\delta\,\rho\,C)_2 + \delta_1\,\rho_o\,C_{river}\right] \\
\rho_o \,\mathrm{dht} \cdot \text{tracer-source}_k &= R\left[(\delta\,\rho\,C)_{k+1} - (\delta\,\rho\,C)_k + \delta_k\,\rho_o\,C_{river}\right] \\
\rho_o \,\mathrm{dht} \cdot \text{tracer-source}_{kr} &= R\left[-(\delta\,\rho\,C)_{kr} + \delta_{kr}\,\rho_o\,C_{river}\right]
\end{aligned} \tag{12.14}$$

For $kr = 1$, the method reduces to the default discharge of river into the top cell.

Part V

Quasi-physical Parameterizations

QUASI-PHYSICAL PARAMETERIZATIONS

In the construction of a realistic ocean climate model, there are issues that arise warranting a quasi-physical, or engineering, approach rather than a first principles approach. Tracer transport between regions of the ocean disconnected due to lack of model resolution (e.g., Mediteranean and Atlantic), and tracer transport across overflows within coarse models, each provide cases where engineering approaches have been used. We describe approaches taken in MOM4 to address these aspects of the simulation.

CHAPTER

THIRTEEN

Cross-land mixing

Contents

The purpose of this chapter is to present the method used in MOM4 for mixing tracers and mass/volume across land separated points, such as across an unresolved Strait of Gibraltar.

13.1 Introduction

In climate modeling, it is often necessary to allow water masses that are separated by land to exchange properties. This situation arises in models when the grid mesh is too coarse to resolve narrow passageways that in reality provide crucial connections between water masses. For example, coarse grid spacing typically closes off

the Mediterranean from the Atlantic at the Straits of Gibraltar. In this case, it is important for climate models to include the effects of salty water entering the Atlantic from the Mediterranean. Likewise, it is important for the Mediterranean to replenish its supply of water from the Atlantic to balance the net evaporation occurring over the Mediterranean region.

We describe here a method used in MOM4 to establish communication between bodies of water separated by land. The communication consists of mixing tracers and mass/volume between non-adjacent water columns. Momentum is not mixed. The scheme conserves total tracer content, total mass or volume (depending on whether using the non-Boussinesq or Boussinesq versions of MOM4), and maintains compatibility between the tracer and mass/volume budgets. It's only restriction is that no mixing occur between cells if their time independent thicknesses differ. This constraint is of little practical consequence.

13.2 Tracer and mass/volume compatibility

Consider two boxes with fluid masses $M^{(1)} = \rho^{(1)} V^{(1)}$ and $M^{(2)} = \rho^{(2)} V^{(2)}$ and tracer concentrations (tracer mass per mass of fluid) $T^{(1)}$ and $T^{(2)}$ (for a Boussinesq fluid, the density is set to the constant Boussinesq density ρ_o). A mixing process that conserves total tracer mass and total fluid mass must satisfy

$$\partial_t (T^{(1)} \rho^{(1)} V^{(1)} + T^{(2)} \rho^{(2)} V^{(2)}) = 0 \tag{13.1}$$

$$\partial_t (\rho^{(1)} V^{(1)} + \rho^{(2)} V^{(2)}) = 0. \tag{13.2}$$

Notably, mass conservation can be considered a special case of total tracer conservation when the tracer concentration is uniform and constant: $T \equiv 1$. This result provides an important *compatibility* constraint between the discrete tracer and mass/volume budgets. For constant volume boxes with a Boussinesq fluid, such as considered in rigid lid models, compatibility is trivial. For boxes which change in time, such as the top cells in MOM4's free surface, and/or for non-Boussinesq formulation where total mass is conserved, then compatibility provides an important constraint on the methods used to discretize the budgets for mass/volume and tracer. The remainder of this chapter incorporates these ideas into the proposed cross-land mixing scheme.

13.3 Tracer mixing in a Boussinesq fluid with fixed boxes

To start in our formulation of cross-land mixing, let us consider mixing of two volumes of Boussinesq fluid, where the separate volumes remain constant in time

$$\partial_t V^{(1)} = \partial_t V^{(2)} = 0. \tag{13.3}$$

An example is the mixing between two constant volume grid cells. If the mixing takes place instantaneously and between the full contents of both boxes, as in convective adjustment, then the final tracer concentration in both boxes is given by

$$T_{final} = \frac{T^{(1)} V^{(1)} + T^{(2)} V^{(2)}}{V^{(1)} + V^{(2)}}. \tag{13.4}$$

It is assumed in convective mixing that the volumes of the two boxes remains unchanged. The picture is of an equal volume of water rapidly mixing from one box to the other, without any net transport between the boxes.

Instead of instantaneous and complete convective mixing, consider mixing of the two boxes at a volume rate U. That is, U represents an equal volume per time of water mixing between the boxes, with no net transport. As shown in Figure 13.1, U is chosen based on the observed amount of water exchanged through the passageway. Just as for convective adjustment, the volumes of the two boxes remains fixed. But the tracer concentrations now have a time tendency. One form for this tendency relevant for constant volume cells is given by

$$\partial_t (V^{(1)}\, T^{(1)}) = U\, (T^{(2)} - T^{(1)}) \tag{13.5}$$

$$\partial_t (V^{(2)}\, T^{(2)}) = U\, (T^{(1)} - T^{(2)}). \tag{13.6}$$

Since the volumes are constant, we can write these budgets in the form

$$\partial_t T^{(1)} = \frac{U}{V^{(1)}}\, (T^{(2)} - T^{(1)}) \tag{13.7}$$

$$\partial_t T^{(2)} = \frac{U}{V^{(2)}}\, (T^{(1)} - T^{(2)}), \tag{13.8}$$

This is the form of cross-land tracer mixing used in the rigid lid full cell MOM1.

In the real world, transport is often comprised of stacked flows where deep water flows one way and shallow water oppositely (e.g., see Figure 13.1). Hence, a more refined form of cross-land mixing may consist of upwind advective fluxes acting between non-local points in the model, where the advective velocity is specified based on observations. Such sophistication, however, is not implemented in MOM4. Indeed, it is arguable that one may not wish to have more details than provided by the simpler form above, since more details also further constrain the solution.

13.4 Mixing of mass/volume

In a model with a coarse mesh, the Mediterranean is typically land-locked. Hence, the net evaporation experienced over the Mediterranean region will cause an ocean model's free surface height to decrease without bound. In a model resolving the Straits of Gibraltar, there is a transfer of mass across the Strait from the Atlantic. This mass transfer creates a change in the height of the free surface.

Our goal is to have a parameterized mass transfer associated just with a difference in the free surface height. That is, if the densities are different yet the free surface heights are equal, then there is no mixing. By transferring masses of water, we must also recognize that the water contains tracer. Hence, mass and tracer mixing must maintain the compatibility mentioned in Section 13.2. In this section, however, we only introduce a basic form for mass transfer. Full compatibility with tracer transfer is achieved in Section 13.5

13.4.1 Instantaneous and complete mixing

To start by considering what form for mixing is appropriate, consider a convective analog whereby a complete mixing of masses $\rho^{(1)}\, A^{(1)}\, h^{(1)}$ and $\rho^{(2)}\, A^{(2)}\, h^{(2)}$ leaves

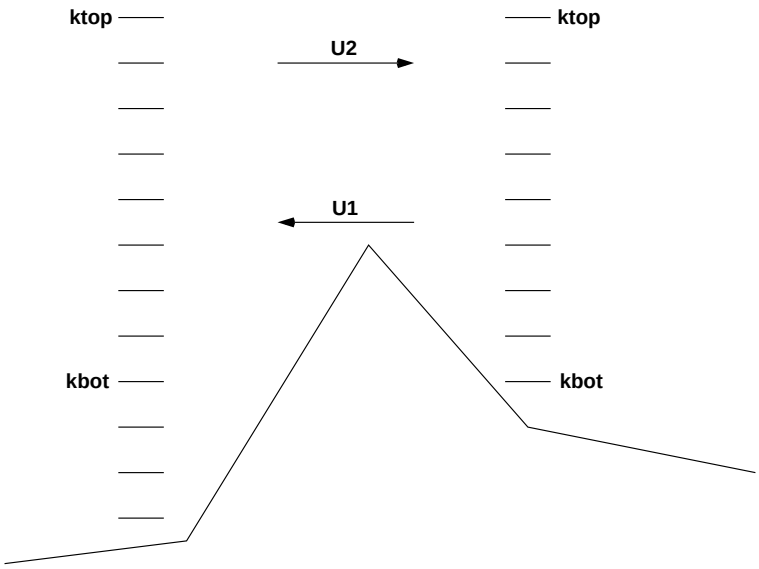

Figure 13.1: Schematic of cross-land mixing. The model's grid mesh is assumed too coarse to explicitly represent the lateral exchange of water masses. For this schematic, we consider an observed sub-grid scale transport U_1 moving in one direction, and U_2 in another. To represent the mixing effects on tracers by these transports, we suggest taking the exchange rate U in MOM4's cross-land mixing to be the average of the transports $U = (U_1 + U_2)/2$. Cross-land mixing occurs between the user-specified depth levels $k = k_{top}$ and $k = k_{bot}$. If $k_{top} = 1$, then cross-land mixing of volume in the top cell must be considered, in addition to tracer transport, in order to maintain compatibility between volume and tracer budgets.

the final mass per area in both cells given by

$$(\rho\, h)_{final} = \frac{\rho^{(1)}\, A^{(1)}\, h^{(1)} + \rho^{(2)}\, A^{(2)}\, h^{(2)}}{A^{(1)} + A^{(2)}}, \tag{13.9}$$

where $A^{(1)}$ and $A^{(2)}$ are the temporally constant horizontal areas of the two grid cells and $h^{(1)}$ and $h^{(2)}$ are their generally time dependent thicknesses. There are two problems with this mixing. First, it is too rapid and too complete. Second, it changes the mass within a grid cell in cases where the initial masses per area are equal yet the constant horizontal areas of the cells differ.

13.4.2 A finite time incomplete mixing

A finite time and incomplete mixing is analogous to that taken for the tracers in Section 13.3. Here, we consider the time tendencies for the mass per area within a cell

$$\partial_t(\rho^{(1)}\, h^{(1)}) = \gamma^{(1)}\, (\rho^{(2)}\, h^{(2)} - \rho^{(1)}\, h^{(1)}) \tag{13.10}$$

$$\partial_t(\rho^{(2)}\, h^{(2)}) = \gamma^{(2)}\, (\rho^{(1)}\, h^{(1)} - \rho^{(2)}\, h^{(2)}), \tag{13.11}$$

where $\gamma^{(1)}$ and $\gamma^{(2)}$ are inverse damping times. This proposed mixing results in a transfer of mass only when the mass per area within the two boxes differs. The

total mass of the two-box system is conserved if the following constraint is satisfied

$$\partial_t[(\rho\, h\, A)^{(1)} + (\rho\, h\, A)^{(2)}] = (A^{(1)}\, \gamma^{(1)} - A^{(2)}\, \gamma^{(2)})\, (\rho^{(2)}\, h^{(2)} - \rho^{(1)}\, h^{(1)}) = 0. \quad (13.12)$$

This relation places a constraint on the inverse damping times $\gamma^{(1)}$ and $\gamma^{(2)}$

$$A^{(1)}\, \gamma^{(1)} = A^{(2)}\, \gamma^{(2)} \quad (13.13)$$

which is easily satisfied.

The problem with the mixing prescribed by equations (13.10) and (13.11) is that mixing will ensue in the following two undesirable cases. First, if the densities of the two cells are initially the same $\rho^{(1)} = \rho^{(2)} = \rho$, yet we have time independent cells with different thicknesses (e.g., partial bottom cells), then we have a density change driven solely by the difference in cell thicknesses

$$h^{(1)}\, \partial_t \rho^{(1)} = \rho\, \gamma^{(1)}\, (h^{(2)} - h^{(1)}) \quad (13.14)$$

$$h^{(2)}\, \partial_t \rho^{(2)} = \rho\, \gamma^{(2)}\, (h^{(1)} - h^{(2)}). \quad (13.15)$$

This situation prompts us to restrict our application of cross-land mixing to between grid cells with either the same time independent thicknesses, of between two surface grid cells.

Another problem with the mixing prescribed by equations (13.10) and (13.11) is seen by considering the situation whereby two top model grid cells have initially equal thicknesses $h^{(1)} = h^{(2)} = h$ yet different densities. The model grid cell thickness will evolve because of the difference in densities

$$\rho^{(1)}\, \partial_t\, h^{(1)} = h\, \gamma^{(1)}\, (\rho^{(2)} - \rho^{(1)}) \quad (13.16)$$

$$\rho^{(2)}\, \partial_t\, h^{(2)} = h\, \gamma^{(2)}\, (\rho^{(1)} - \rho^{(2)}). \quad (13.17)$$

However, as stated at the beginning of this section, we aim to prescribe a mixing process that occurs only when the tracer concentration and/or free surface heights differ. Therefore, we must consider an alternative to equations (13.10) and (13.11)

13.4.3 A finite time incomplete mixing only when surface heights differ

The following prescription satisfies our desires to mix only when the surface heights differ

$$\partial_t(\rho^{(1)}\, h^{(1)}) = \gamma^{(1)}\, \overline{\rho}\, (h^{(2)} - h^{(1)}) \quad (13.18)$$

$$\partial_t(\rho^{(2)}\, h^{(2)}) = \gamma^{(2)}\, \overline{\rho}\, (h^{(1)} - h^{(2)}). \quad (13.19)$$

When considered over interior time independent model grid cells, then we restrict its application to grid cells of equal thicknesses. Restricted as such, the right hand side vanishes for the time independent interior cells, thus leading to no density mixing. The density factor $\overline{\rho}$ can be given by anything convenient, such as

$$\overline{\rho} = \frac{\rho^{(1)} + \rho^{(2)}}{2}, \quad (13.20)$$

or the even simpler prescription (used in MOM4)

$$2\overline{\rho} = \rho_o. \quad (13.21)$$

13.5 Tracer and mass mixing

The general case of mixing tracers and mass is now considered. There are four constraints desired in the formulation.

- Total fluid mass in the two boxes is conserved.
- Total tracer mass in the two boxes is conserved.
- In the rigid lid Boussinesq full cell case, the tracer tendency reduces to equations (13.7) and (13.8) used in MOM1.
- If the tracer concentration in the two boxes is the same yet the mass differs, then mixing of mass will leave the tracer concentrations unchanged.

The last constraint is satisfied if the tracer and mass budgets are compatible, as described in Section 13.2.

Mixing that satisfies these constraints is given by

$$\partial_t(\rho^{(1)}\, h^{(1)}\, T^{(1)}) = \left(\frac{2\, U\, \overline{\rho}}{A^{(1)}\, (h^{(1)} + h^{(2)})}\right) (h^{(2)}\, T^{(2)} - h^{(1)}\, T^{(1)}) \tag{13.22}$$

$$\partial_t(\rho^{(2)}\, h^{(2)}\, T^{(2)}) = \left(\frac{2\, U\, \overline{\rho}}{A^{(2)}\, (h^{(1)} + h^{(2)})}\right) (h^{(1)}\, T^{(1)} - h^{(2)}\, T^{(2)}) \tag{13.23}$$

$$\partial_t(\rho^{(1)}\, h^{(1)}) = \left(\frac{2\, U\, \overline{\rho}}{A^{(1)}\, (h^{(1)} + h^{(2)})}\right) (h^{(2)} - h^{(1)}) \tag{13.24}$$

$$\partial_t(\rho^{(2)}\, h^{(2)}) = \left(\frac{2\, U\, \overline{\rho}}{A^{(2)}\, (h^{(1)} + h^{(2)})}\right) (h^{(1)} - h^{(2)}) \tag{13.25}$$

In these equations, h is the vertical thickness of a tracer cell. For the top cell, thickness takes the form

$$h = \Delta z + \eta \tag{13.26}$$

where Δz is the time independent thickness of the fixed volume rigid lid case, and η is the surface height. The mass per area equations (13.24) and (13.25) result from the tracer equations (13.22) and (13.23) upon setting the tracer concentrations to a constant, as required for compatible budgets. When the cell thicknesses are time independent, such as the ocean model interior with $k > 1$, then we restrict our applications to cases where $h^{(1)} = h^{(2)}$, for reasons articulated in Section 13.4.2.

13.6 Formulation with multiple depths

We now consider the case where there are multiple boxes in the vertical, with the top box generally possessing space-time dependence yet interior cells static. We restrict attention to situations where mixing occurs between boxes at the same vertical level, as shown in Figure 13.1, and where the time independent boxes have the same vertical thicknesses.

13.6.1 MOM1 formulation of cross-land tracer mixing

In MOM1, the vertical cells all have time independent thicknesses (i.e., no free surface), and the fluid is Boussinesq. It is useful to start with this case prior to considering MOM4's more general case.

In the full cell rigid lid case, we follow the approach given by equations (13.7) and (13.8), where the relevant volume now becomes that for the respective column. The volumes for the two columns $lx = 1, 2$ are given by

$$V^{(lx)} = A^{(lx)} \sum_{k=kbot}^{ktop} dz_k = A^{(lx)}\, H^{(lx)}, \tag{13.27}$$

where

$$A^{(lx)} = dxt_{i,j}^{(lx)}\, dyt_{i,j}^{(lx)} \tag{13.28}$$

are the generally different horizontal cross-sectional areas of the tracer cells in the two columns, and $H^{(1)} = H^{(2)}$ is the vertical thickness of the two columns. The top and bottom k-levels for the columns are set by $k = ktop$ and $k = kbot$. As mentioned earlier, the formulation here allows for mixing only between boxes that live on the same k-level, so $k = ktop$ and $k = kbot$ are the same for both columns $lx = 1, 2$.

Use of these volumes in equations (13.7) and (13.8) leads to the tracer time tendencies for a particular k-level

$$\partial_t T_k^{(1)} = B^{(1)}\, (T_k^{(2)} - T_k^{(1)}) \tag{13.29}$$

$$\partial_t T_k^{(2)} = B^{(2)}\, (T_k^{(1)} - T_k^{(2)}), \tag{13.30}$$

where

$$B^{(lx)} = \frac{U}{V^{(lx)}} \tag{13.31}$$

represents the rate ($B^{(lx)}$ has units of inverse time) at which the two columns participate in the mixing. Conservation of total tracer is maintained between two horizontally adjacent boxes within the two columns. We see such conservation via multiplying the above tendencies by the respective time independent volumes of the two cells, and adding

$$\partial_t (V_k^{(1)}\, T_k^{(1)} + V_k^{(2)}\, T_k^{(2)}) = (T_k^{(2)} - T_k^{(1)})\, (A^{(1)}\, B^{(1)}\, h_k^{(1)} - A^{(2)}\, B^{(2)}\, h_k^{(2)}) = 0, \tag{13.32}$$

where $A^{(1)}\, B^{(1)}\, h_k^{(1)} = U\, (h_k^{(1)}/H^{(1)}) = U\, (h_k^{(2)}/H^{(2)}) = A^{(2)}\, B^{(2)}\, h_k^{(2)}$ was used.

13.6.2 Generalizing to free surface and non-Boussinesq

We now generalize to the case of time varying top model grid cells with a non-Boussinesq fluid. Based on the considerations of Section 13.5 and the form used in MOM1, we write for the general case

$$\partial_t (\rho_k^{(1)}\, h_k^{(1)}\, T_k^{(1)}) = \left(\frac{2\, U\, \overline{\rho}_k}{A^{(1)}\, (H^{(1)} + H^{(2)})} \right) (h_k^{(2)}\, T_k^{(2)} - h_k^{(1)}\, T_k^{(1)}) \tag{13.33}$$

$$\partial_t (\rho_k^{(2)}\, h_k^{(2)}\, T_k^{(2)}) = \left(\frac{2\, U\, \overline{\rho}_k}{A^{(2)}\, (H^{(1)} + H^{(2)})} \right) (h_k^{(1)}\, T_k^{(1)} - h_k^{(2)}\, T_k^{(2)}), \tag{13.34}$$

where $H^{(1)}$ and $H^{(2)}$ are the generally different depths of the two columns. By inspection, for each k-level this formulation conserves total tracer mass and total fluid mass (recall Section 13.4). Also, when the mass per area (ρh) is constant in time, as in a rigid lid Boussinesq fluid, and when $H^{(1)} = H^{(2)}$, as in a full cell model, then these budgets reduce to equations (13.29) and (13.30) used in MOM1. Furthermore, setting the tracers to uniform constants leads to the transfer of mass per area between two cells living at the same k-level

$$\partial_t(\rho_k^{(1)}\, h_k^{(1)}) = \left(\frac{2\,U\,\overline{\rho}_k}{A^{(1)}\,(H^{(1)}+H^{(2)})}\right)(h_k^{(2)} - h_k^{(1)}) \tag{13.35}$$

$$\partial_t(\rho_k^{(2)}\, h_k^{(2)}) = \left(\frac{2\,U\,\overline{\rho}_k}{A^{(2)}\,(H^{(1)}+H^{(2)})}\right)(h_k^{(1)} - h_k^{(2)}). \tag{13.36}$$

Again, for time independent cells with $k > 1$, we restrict our applications to those cells with $h^{(1)} = h^{(2)}$, which means there is no added density mixing. This restriction is minimal as it only precludes our using cross-land mixing within a partial cell bottom.

Both of these budgets can be written in a form familiar from other damping processes

$$\partial_t(\rho^{(1)}\, h^{(1)}\, T^{(1)}) = \gamma^{(1)}\,\overline{\rho}\,(h^{(2)}\, T^{(2)} - h^{(1)}\, T^{(1)}) \tag{13.37}$$

$$\partial_t(\rho^{(2)}\, h^{(2)}\, T^{(2)}) = \gamma^{(2)}\,\overline{\rho}\,(h^{(1)}\, T^{(1)} - h^{(2)}\, T^{(2)}) \tag{13.38}$$

$$\partial_t(\rho^{(1)}\, h^{(1)}) = \gamma^{(1)}\,\overline{\rho}\,(h^{(2)} - h^{(1)}) \tag{13.39}$$

$$\partial_t(\rho^{(2)}\, h^{(2)}) = \gamma^{(2)}\,\overline{\rho}\,(h^{(1)} - h^{(2)}) \tag{13.40}$$

where the depth label k was omitted for brevity, and

$$\gamma^{(1)} = \frac{2\,U}{A^{(1)}\,(H^{(1)}+H^{(2)})} \tag{13.41}$$

$$\gamma^{(2)} = \frac{2\,U}{A^{(2)}\,(H^{(1)}+H^{(2)})} \tag{13.42}$$

defines the damping coefficients. Note that the damping coefficients are generally time dependent for cases with mixing in the top cell and where the free surface height is included when computing the column thicknesses $H^{(1)}$ and $H^{(2)}$. One may alternatively be motivated to keep the damping coefficients constant in time by setting $H^{(1)}$ and $H^{(2)}$ to be the time independent depth of the respective columns. This choice is appropriate when using cross-land mixing between columns in shallow regions where the free surface height is some nontrivial fraction of the full column depth. MOM4 generally sets the thicknesses to their time independent depths.

To get a sense for the strength of the mixing, consider the case of a one-degree horizontal grid mesh where the upper thousand meters of the water column is mixed across Gibraltar with $U = 1.75 \times 10^6\,\mathrm{m}^3\,\mathrm{s}^{-1}$, which is a reasonable value. With $H^{(1)} = H^{(2)} \approx 1000m$ we have

$$V^{(1)} \approx V^{(2)} \approx 1.2 \times 10^{13}\mathrm{m}^3, \tag{13.43}$$

and to the damping coefficient

$$\gamma^{(1)} \approx \gamma^{(2)} = \frac{U}{V} \approx 1.5 \times 10^{-7}\mathrm{s}^{-1} \approx 77\ \mathrm{days}^{-1}. \tag{13.44}$$

Just as for any other form of mixing, if the damping coefficients are too large, then it is possible for there to be numerical instabilities. MOM4 provides a check so that no more than one-half of a particular grid cell is mixed per model time step.

13.7 Implementation in MOM4

In MOM4, both the tracer and surface height budgets are affected by processes in addition to the cross-land mixing effects discussed in this chapter. Cross-land mixing effects are introduced to these budgets via source terms as described in this section.

13.7.1 Semi-discrete mass and tracer budgets

Prior to our incorporating cross-land mixing into the budgets, consider the forms by which mass and tracer are budgeted absent cross-land mixing. For this purpose, we note that Griffies (2004) derives the following semi-discrete budget for mass within a discrete column of ocean fluid

$$\partial_t \left(\sum_{k=1}^{Nk} \rho_k \, h_k \right) = -\rho_o \, \nabla \cdot \mathbf{U} + \rho_w \, q_w. \tag{13.45}$$

In this equation, $\rho_k \, h_k$ is the mass per unit area within a tracer grid cell with vertical label k, $-\rho_o \, \nabla \cdot \mathbf{U}$ is the convergence of the vertically integrated horizontal velocity with $\mathbf{U} = \sum_{k=1}^{Nk} h_k \, \mathbf{u}_k$, and $\rho_w \, q_w$ is the mass per horizontal area per time of fresh water entering the ocean surface. In words, this budget says that the mass per horizontal area contained in a column of fluid changes in time according to the convergence of the vertically integrated horizontal mass per area, plus any mass per area entering the ocean through its surface. Since only the top model grid cell has a time-dependent thickness

$$h_1(x, y, t) = \eta(x, y, t) + \Delta z, \tag{13.46}$$

we can use the mass balance over a column to derive a prognostic equation for surface height

$$\rho_1 \, \eta_{,t} = -\rho_o \, \nabla \cdot \mathbf{U} + \rho_w \, q_w - \sum_{k=1}^{Nk} h_k \, \partial_t \rho_k. \tag{13.47}$$

The density time derivative term accounts for the so-called steric effects which arise from time changes in the vertically integrated density. This term vanishes for a Boussinesq fluid.

The semi-discrete budget for tracer within a discrete grid cell is given by

$$\partial_t (\rho \, h \, T) = -\rho_o \, \nabla \cdot (h \, \mathbf{F}) - \rho_o \, h \, \partial_z \, F^z, \tag{13.48}$$

where $\mathbf{F}$ represents the advective and sub-grid-scale tracer fluxes. Compatibility (see Section 13.2) between the mass and tracer budgets manifests when the tracer budget reduces to the mass budget upon setting tracer concentration to a uniform value throughout the ocean, at which point the mass of tracer is equal the mass of fluid.

13.7.2 Semi-discrete budgets with cross-land mixing sources

If we now add a source to the mass and tracer budgets corresponding to the cross-land mixing effects, the semi-discrete budgets become

$$\partial_t \left(\sum_{k=1}^{Nk} \rho_k \, h_k \right) = -\rho_o \, \nabla \cdot \mathbf{U} + \rho_w \, q_w + \rho_o \, \gamma^{(1)} \, (h^{(2)} - h^{(1)}) \, \delta_{k1}$$

$$\partial_t (\rho \, h \, T) = -\rho_o \, \nabla \cdot (h \, \mathbf{F}) - \rho_o \, h \, \partial_z \, F^z + \rho_o \, \gamma^{(1)} \, (h^{(2)} \, T^{(2)} - h^{(1)} \, T^{(1)}), \quad (13.49)$$

where the equations are written for the point (1) and δ_{k1} is unity for $k = 1$ and vanishes elsewhere. Again, the added mass source is present only for the surface cell since we restrict application to those cases where the time independent interior cells have $h^{(2)} = h^{(1)}$.

Given these results, we identify the density weighted source for surface height

$$\rho^{(1)} \, \text{eta-source}^{(1)} = \rho_o \, \gamma^{(1)} \, (h^{(2)} - h^{(1)}) \, \delta_{k1} \quad (13.50)$$

$$\rho^{(2)} \, \text{eta-source}^{(2)} = \rho_o \, \gamma^{(2)} \, (h^{(1)} - h^{(2)}) \, \delta_{k1}. \quad (13.51)$$

All terms on the left hand side are evaluated in time at the present time step τ. Those terms on the right hand side are evaluated at the lagged time $\tau - 1$, as is required for linear numerical stability. The density and thickness weighted tracer concentration source takes the form

$$\rho^{(1)} \, h^{(1)} \, \text{tracer-source}^{(1)} = \rho_o \, \gamma^{(1)} \, (h^{(2)} \, T^{(2)} - h^{(1)} \, T^{(1)}) \quad (13.52)$$

$$\rho^{(2)} \, h^{(2)} \, \text{tracer-source}^{(2)} = \rho_o \, \gamma^{(2)} \, (h^{(1)} \, T^{(1)} - h^{(2)} \, T^{(2)}), \quad (13.53)$$

where again terms on the left hand side are evaluated at time τ whereas those on the right are at time $\tau - 1$.

In practice, the tracer equation is time stepped for tracer concentration, with the time tendencies $h_{,t}$ and $\rho_{,t}$ forcing tracer concentration tendencies. In this case, we consider

$$\begin{aligned} \rho \, h \, T_{,t} = & -\rho_o \, \nabla \cdot (h \, \mathbf{F}) - \rho_o \, h \, \partial_z \, F^z - T \, h \, \rho_{,t} - T \, \rho \, h_{,t} \\ & + \rho_o \, \gamma^{(1)} \, (h^{(2)} \, T^{(2)} - h^{(1)} \, T^{(1)}), \end{aligned} \quad (13.54)$$

where $h_{,t}$ vanishes for interior cells with $k > 1$. Care should be taken to include the contributions to $h_{,t}$ arising from all processes, including cross-land mixing. For example, if cell (1) is in the surface $k = 1$, then the tracer concentration budget for this cell takes the form

$$\begin{aligned} \rho \, h \, T_{,t} = & -\rho_o \, \nabla \cdot (h \, \mathbf{F}) - \rho_o \, h \, \partial_z \, F^z - T \, h \, \rho_{,t} - T \, [\rho \, h_{,t}^{no-xland} + \rho_o \, \gamma^{(1)} \, (h^{(2)} - h^{(1)})] \\ & + \rho_o \, \gamma^{(1)} \, (h^{(2)} \, T^{(2)} - h^{(1)} \, T^{(1)}) \end{aligned} \quad (13.55)$$

where

$$\rho_1 \, h_{,t}^{no-xland} = -\rho_o \, \nabla \cdot \mathbf{U} + \rho_w \, q_w - \sum_{k=1}^{Nk} h_k \, \partial_t \rho_k \quad (13.56)$$

is the time tendency for the surface height, sans the cross-land mixing effects (see the mass conservation equation (13.45)). Time indices on the cross-land terms are given by

$$T\,(h^{(2)} - h^{(1)}) = T(\tau)\,[(h^{(2)}(\tau - 1) - h^{(1)}(\tau - 1)] \tag{13.57}$$

$$h^{(2)}\,T^{(2)} - h^{(1)}\,T^{(1)} = h^{(2)}(\tau - 1)\,T^{(2)}(\tau - 1) - h^{(1)}(\tau - 1)\,T^{(1)}(\tau - 1). \tag{13.58}$$

13.7.3 Comment on MOM3 implementation

MOM3 provided a form of cross-land mixing of volume and tracer for a Boussinesq fluid. However, the implementation failed to provide for compatibility between the volume and tracer budgets and so was flawed.

13.8 Suppression of B-grid null mode

When mixing the free surface height across an unresolved strait, it has been found essential to mix between two pairs of adjacent columns in order to suppress the checkerboard null mode present on the B-grid (see Chapter 25). For the Mediterranean example, this means choosing any two adjacent points on each side of Gibraltar and setting the volume transport for each column to $U = (1/2)\,1.75 \times 10^6 \mathrm{m}^3\,\mathrm{s}^{-1}$.

CHAPTER

FOURTEEN

Sigma tracer diffusion

Contents

The purpose of this chapter is to detail the method for diffusing tracers along the bottom topography within the bottom-most model grid cells.

14.1 Motivation for the scheme

As described by Winton et al. (1998), coarse resolution z-coordinate models generally have a difficult time moving dense water from shallow to deep regions. This problem has prompted modelers to formulate ways to embed sigma-coordinate-like bottom-layer transport into z-coordinate models. The papers by Beckmann and Döscher (1997) and Döscher and Beckmann (1999) present one of the simplest approaches. They prescribe changes only to the tracer equation, in which there is advection and diffusion within a bottom sigma-layer instead of in the usual horizontal/vertical orientation. More complete and physically based approaches, in which the momentum equations are also affected, tend to have problems with spurious horizontal pressure gradients within the sigma-layer, much as found with sigma-models (see Griffies et al. (2000a)). These approaches remain a topic of ongoing research.

Advection and neutral transport schemes often have a difficult time maintaining positive-definite tracer values next to rough topography. Without either a large amount of implicit mixing via the advection scheme, or some added diffusion such as through sigma-diffusion, the tracer field can soon move outside its physically realistic range. Sigma diffusion in the model thus works where there is indeed enhanced mixing in the real ocean, and where the numerical ocean requires such.

14.2 Diffusivities

When applying sigma-diffusion, the diffusive flux between two adjacent cells living at the ocean bottom is given by

$$\mathbf{F}_\sigma = -A \, \nabla_\sigma T, \tag{14.1}$$

with ∇_σ the horizontal gradient operator taken between cells in the bottom sigma-layer. We follow the approach of Döscher and Beckmann (1999) in which sigma-diffusion dominates when favorable according to densities of the participating cells. That is, the following diffusivity is used

$$A = \begin{cases} A_{\text{max}} & \text{if } \nabla_\sigma \rho \cdot \nabla H < 0 \\ A_{\text{min}} & \text{if } \nabla_\sigma \rho \cdot \nabla H \geq 0, \end{cases} \tag{14.2}$$

where $z = -H(x,y)$ is the bottom depth. Note that in practice, this constraint is applied separately in the two horizontal directions. That is, the zonal diffusivity is large if $\rho_{,x} \, H_{,x} < 0$ and the meridional diffusivity is large if $\rho_{,y} \, H_{,y} < 0$. A ratio of the two diffusivities $A_{\text{max}}/A_{\text{min}}$ has been taken as $\approx 10^6$, as suggested by Döscher and Beckmann.

An additional velocity dependent diffusion was also found by Döscher and Beckmann to be of use. In this case, an added sigma-diffusive flux in the zonal direction is computed using the diffusivity

$$A = \begin{cases} |u| \, \Delta x & \text{if } \rho_{,x} \, H_{,x} < 0 \text{ and } u \, H_{,x} > 0 \\ A_{\text{min}} & \text{otherwise.} \end{cases} \tag{14.3}$$

In this expression, $|u|$ is the magnitude of the zonal velocity component and Δx is the zonal grid spacing. An analogous meridional flux is computed as well.

14.3 Implementation

The bottom sigma-layer in MOM3 was appended to the very bottom of the model and effectively lived beneath the deepest rock. This approach has its advantages. However, it makes for awkward analyses; it precludes direct comparison between models run with and without sigma-physics since the grid used by the respective models is different; and it makes it difficult to consider convergence when refining the grid mesh. For these reasons, the bottom sigma-layer in MOM4 is included along with the rest of the model domain. This is the approach used by Beckmann and Döscher (1997) (e.g., see their Figures 1 and 2). The disadvantage is that the sigma-layer thickness *bbl_thickness* in MOM4 has a generally non-constant thickness determined by the thickness of the model grid cell next to topography.

To address the limitation of having *bbl_thickness* constrained by the bottom partial cell thickness *dht*, we suggest two approaches. For the simple case where *dht* is thick, then we set

$$bbl\_thickness = \min(dht, sigma\_thickness\_max), \tag{14.4}$$

where *sigma_thickness_max* is a namelist parameter. Values on the order of 50m are suggested.

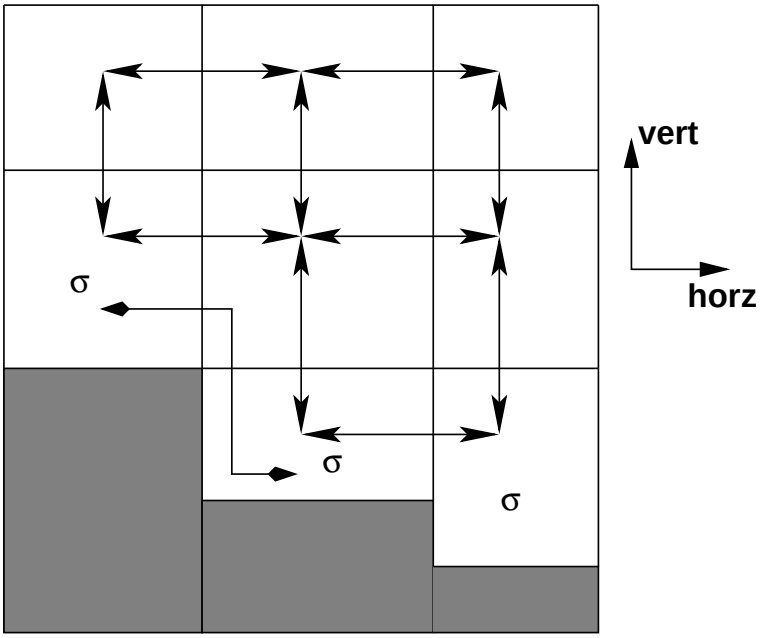

Figure 14.1: Schematic of the extra along-topography pathway for diffusive transport afforded by the sigma-diffusion scheme applied to the bottom-most model cells. Darkened regions denote land cells. Tracers in the z-level cells communicate with their horizontal and vertical neighbors via the usual advection, diffusion, and convective processes. Tracers in the bottom "sigma-layer" can also communicate with their sigma-neighbors via sigma-diffusion.

For the more complicated case where *dht* is thin, then we have no work-around since doing so involves allowing the sigma-diffusion process to take place between arbitrary numbers of grid cells laterally adjacent within the sigma layer. The only option at present is to limit the partial cell thicknesses *dht* to be no smaller than ones desired minimum *bbl_thickness*. This approach reduces the fidelity of the bottom topography representation, but perhaps by gaining a better transport by sigma diffusion. Such issues remain an ongoing research topic at GFDL.

Consistent with Beckmann and Döscher, the sigma-layer momentum equations remain the same as interior z-level cells. We now just allow tracers in the bottom-most cell to be affected by diffusion with their "sigma-neighbors" in addition to their horizontal and vertical neighbors. If desired, communication with horizontal and vertical neighbors can be removed for the sigma cells. Figure 14.1 provides a schematic of the extra sigma-pathway available with sigma tracer diffusion.

CHAPTER

FIFTEEN

Discharging overflow waters into the deep

Contents

This chapter documents the MOM4 implementation of the Campin and Goosse (1999) scheme that discharges dense overflow waters into the deep. The goal of the scheme is similar to that of the sigma-diffusion scheme of Beckmann and Döscher (1997), as described in Chapter 14. We discuss differences between the two methods in Section 15.4.

15.1 The ubiquitous cliffs in coarse z-models

We start this chapter by mentioning some of the limitations inherent in the respresentation of steeply sloping topography in coarse z-models. Consider the case in Figure 15.1, which shows a typical situation where a steeply sloping topographic feature is represented in a coarse z-model via a vertical cliff, with many vertical cells sitting next to the wall. To better resolve such finite, yet steep, topography requires greatly enhanced horizontal resolution. As discussed by Winton et al. (1998), "resolving" the topography requires a grid spacing that satisfies

$$\Delta z / \Delta s \geq |\nabla H|, \tag{15.1}$$

with Δz the vertical grid spacing, Δs the horizontal grid spacing, and $|\nabla H|$ the magnitude of the bottom topography slope. Resolving a slope of $1/100$ with vertical resolution of $\Delta z = 20$m thus requires $\Delta s \approx 2$km, which is some 50-100 times smaller

than the typical resolution of the 1-2 degree ocean climate models commonly used today. Note that refined vertical resolution, desired for resolving/parameterizating vertical physical processes, requires one to further refine the horizontal resolution required to resolve the slope. Notably, there is little difference between the representation of steeply sloping features via either full or partial cells in z-models. Hence, such cliff features remain ubiquitous in the typical ocean climate z-model.

It due to our inability to fully resolve such steeply sloping topographic features that we require enhanced bottom mixing/transport whose aim is to allow dense water to move into the deep, rather than sitting on top of the shelf.

15.2 The Campin and Goosse (1999) algorithm

Consider a heavy water parcel sitting on top of a shelf/cliff that is horizontally adjacent to a lighter parcel sitting over a deeper water column. We may expect that the dense parcel will move off the shelf, down the slope, and into the deep. Along the way, entrainment will occur, with many important processes determining the details of the final water mass. This is indeed a cartoon of an important oceanic process forming much of the deep and intermediate waters in the ocean. Unfortunately, without some extra "engineering" help, Winton et al. (1998) show that coarse resolution z-models are incapable of providing the proper dynamical pathways for this transfer of dense shelf water into the deep. Beckmann and Döscher (1997) suggest one means to enhance the representation of this process in z-models (see Chapter 14). Campin and Goosse (1999) propose yet another, which we detail in this chapter. Both schemes only affect the tracer equation. Killworth and Edwards (1999) discuss a more physically complete, yet numerically difficult, scheme that alters both the momentum and tracer equations.

15.2.1 Finding the depth of neutral buoyancy

Figure 15.1 illustrates a typical situation in a horizontal-vertical plane. Here, we see a heavy parcel of *in situ* density $\rho^{so}(k = kup)$ sitting horizontally adjacent to a lighter parcel of *in situ* density $\rho^{do}(k = kup)$. The superscript "so" refers to water in the "shallow ocean" column, whereas "do" refers to water in the "deep ocean" column.

If the heavy parcel is allowed to adiabatically move off the shelf and then vertically within the deep column, it will equilibrate at its depth of neutral buoyancy. To compute the depth of neutral buoyancy, we evaluate the *in situ* density for the parcel taken at the local value for the *in situ* pressure of the environment where it may potentially equilibrate. For the example shown in Figure 15.1, with (i, j) setting the horizontal position of the shelf parcel and $(i + 1, j)$ setting the horizontal position of the deep column, we have

$$\rho^{so}(kup, kup) = \rho(s_{i,j,kup}, \theta_{i,j,kup}, p_{i,j,kup}) \tag{15.2}$$

$$\rho^{so}(kup, kdw - 1) = \rho(s_{i,j,kup}, \theta_{i,j,kup}, p_{i+1,j,kdw-1}) \tag{15.3}$$

$$\rho^{so}(kup, kdw) = \rho(s_{i,j,kup}, \theta_{i,j,kup}, p_{i+1,j,kdw}) \tag{15.4}$$

$$\rho^{so}(kup, kdw + 1) = \rho(s_{i,j,kup}, \theta_{i,j,kup}, p_{i+1,j,kdw+1}). \tag{15.5}$$

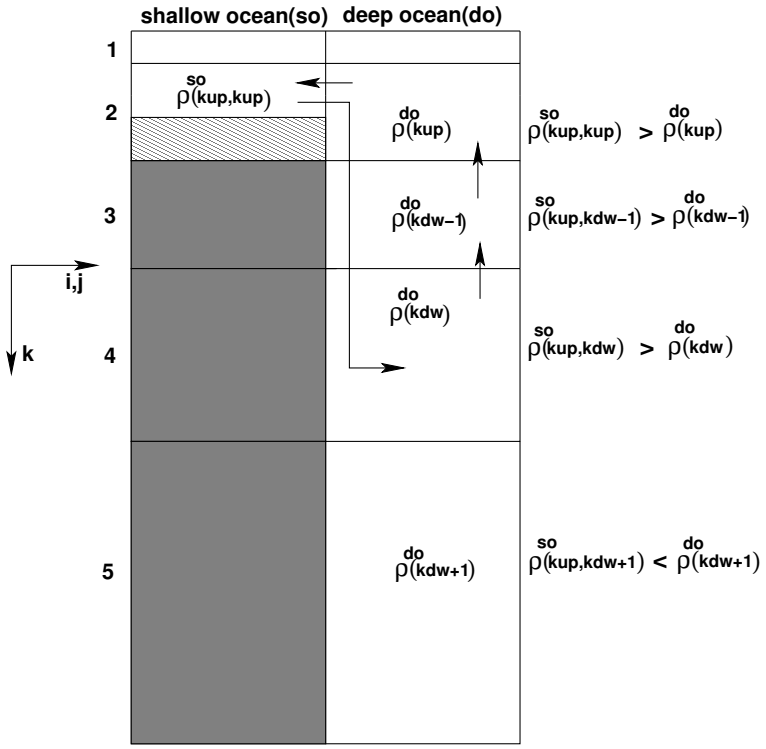

Figure 15.1: Schematic of the Campin and Goosse (1999) overflow method in the horizontal-vertical plane. The darkly filled region represents bottom topography using MOM4's full cells. The lightly filled region represents topography filled by a partial cell. Generally, the thickness of a cell sitting on top of a topographic feature, as the $k = 2$ cell in the "so" column, is thinner than the corresponding cell in the deep-ocean column (the $k = 2$ cell in the "do" column). Shown are tracer cells, with arrows representing the sense of the scheme's upstream advective transport. This figure is based on Figure 1 of Campin and Goosse (1999).

That is, we compute the density at the salinity and potential temperature of the shallow ocean parcel, $(s_{i,j,kup}, \theta_{i,j,kup})$, but at the *in situ* pressure for the respective grid cell in the deep column. The density is then compared to the density of the parcel at the *in situ* salinity, temperature, and pressure of the cells in the deep ocean column.

15.2.2 Prescribing the downslope flow

Following Campin and Goosse (1999), we assume that the dense parcel has a downslope momentum imparted to it. This momentum is proportional to the topographic slope, $H_{,x}$, the acceleration from gravity,g, the amount of fluid within the cell participating in the downslope flow,

$$0 \leq \delta \leq 1, \tag{15.6}$$

and the positive density difference

$$\Delta\rho = \rho^{so}(kup, kup) - \rho^{do}(kup) > 0. \tag{15.7}$$

The momentum is retarded by frictional dissipation, μ (in units of inverse time). These considerations then lead to the momentum balance[1]

$$\rho_o \, V^{(t)} \, \mu \, u^{slope} = g \, \delta \, V^{(t)} \, \Delta\rho \, |H_{,x}| \tag{15.8}$$

where

$$V^{(t)} = dxt * dyt * dht \tag{15.9}$$

is the volume of the dense parcel's tracer cell. Equation (15.8) is also used to determine a meridionally directed downslope transport, with the meridional topographic slope $H_{,y}$ replacing $H_{,x}$, and $\Delta\rho$ the density difference between meridionally adjacent parcels.

Solving equation (15.8) for the speed u^{slope} yields

$$u^{slope} = \left(\frac{g \, \delta}{\rho_o \, \mu} \right) \, |H_{,x}| \, \Delta\rho. \tag{15.10}$$

If the depth H refers to the depth of a tracer cell, then the absolute slope $|H_{,x}|$ is naturally defined at the zonal face of the tracer cell. Hence, the speed, u^{slope}, is likewise positioned at the zonal face. This is the desired position for an advective tracer transport velocity.

Campin and Goosse (1999) suggest the values $\mu = 10^{-4} \, \mathrm{sec}^{-1}$ and $\delta = 1/3$. These parameters are set as namelists in MOM4. Using these numbers, with an absolute topographic slope of $|H_{,x}| \approx 10^{-3}$ and density difference $\Delta\rho \approx 1 \, \mathrm{kg \, m}^{-3}$, leads to the speed

$$u^{slope} \approx .03 \, \mathrm{m \, sec}^{-1}. \tag{15.11}$$

Associated with this downslope speed is a volume transport of fluid leaving the cell

$$U^{slope} = u^{slope} \, dht_{min} \, dyt. \tag{15.12}$$

In this equation, dht_{min} is the minimum thickness of the shelf cell and the adjacent cell. This minimum operation is necessary when considering MOM4's bottom partial cells, whereby the bottom-most cell in a column can have arbitrary thickness (Figure 15.1). With $u^{slope} \approx .03 \mathrm{m \, s}^{-1}$ corresponding to the speed of fluid leaving a grid cell that is one-degree in width and 50 m in depth, we have a volume transport $U^{slope} \approx 0.2$Sv. Larger values are easily realized for steeper slopes, larger density differences, and larger grid cells.

15.2.3 Mass conservation and tracer transport

To conserve mass throughout the system, the mass flux exiting the shelf cell and entering the deep cell must itself be returned from the adjacent cell. This situation then sets up a mass flux throughout the participating cells, where there is zero convergence of the flux and so zero net increase or decrease in mass. For the Boussinesq fluid, mass conservation is replaced by volume conservation. This redirected plumbing is shown in Figure 15.1.

[1] The appearance of the constant density, ρ_o, on the left hand side, rather than the *in situ* density, ρ, is described in Chapter 3 as well as Griffies (2004). In those discussions we show that ρ_o is appropriate for either the Boussinesq or non-Boussinesq forms of MOM4.

The convergence-free seawater mass flux carries with it tracer mass. If there are differences in the tracer content of the cells, then the tracer flux will have a nonzero convergence, and so it moves tracer throughout the system. We use first-order upstream advective transport as a discretization of this process. First-order upstream advection is the simplest form of advection. Its large level of numerical diffusion is consistent with our belief that the bottom layer flows in the real ocean near steep topography are quite turbulent. Hence, although inappropriate for interior flows, we are satisfied with the use of upstream advection for the overflow scheme.

15.3 Implementation in MOM4

This section details the implementation of the Campin and Goosse (1999) scheme in MOM4.

15.3.1 Start of the integration

At the start of the model integration, it is necessary to determine those grid points where it is possible to have a downslope flow. For this purpose, we introduce the array $topog\_step(i, j, m)$, with $m = 1, 2, 3, 4$ specifying in a counter-clockwise direction the four surrounding columns whose depths are to be compared to that at the central (i, j) point. Figure 15.2 illustrates this notation. If the adjacent column is deeper than the central point, thus representing a possible direction for downslope flow, then $topog\_step(i, j, m)$ for this value of m is set to unity. Otherwise, $topog\_step(i, j, m)$ for this m is zero. Note that with partial bottom cells, it is possible for an adjacent column to be deeper yet for the number of vertical cells to be the same in both columns. To initiate the downslope scheme of Campin and Goosse (1999), we insist that there be at least one more grid cell in the adjacent column.

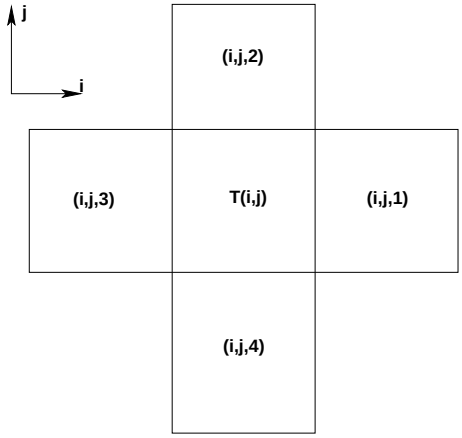

Figure 15.2: Plan view (x-y plane) of a tracer grid cell at (i, j) and its horizontally adjacent tracer cells. We label the adjacent cells $(i+1, j)$, $(i, j+1)$, $(i-1, j)$, $(i, j-1)$ as $m = 1, 2, 3, 4$. Notice that we do not consider downslope flow along a diagonal direction.

15.3.2 During a time step

During each time step, we locate where downslope flow is favorable for points sitting on the ocean bottom at $(i, j, kmt(i, j))$. For each of the four directions ($m = 1, 2, 3, 4$) where $topog\_step(i, j, m) = 1$, we check the density difference between the central point and the adjacent point. If the density of the central point is larger, then the Campin and Goosse (1999) scheme is used to initiate downslope transport. For these directions, we locate the depth of neutral buoyancy for the central point according to the discussion in Section 15.2.1, and so specify the number of vertical cells, kdw, participating in the transport. Note that we allow for downslope transport to occur in more than one direction, as occurs in those cases for a fixed (i, j) where $topog\_step(i, j, m)$ has more than a single nonzero element.

Our prescription is mindful of the possibility for the shallow-cell to be a partially filled cell sitting on the topography. For this reason, the convergence-free volume transport associated with the downslope flow is weighted by the minimum vertical thickness of the two cells (equation (15.12)). Otherwise, it would be possible to flood a thin partial cell with a huge amount of tracer (e.g., heat).

We incorporate the effects from the Campin and Goosse (1999) overflow scheme into MOM4's tracer source array. To derive the source, we proceed as for the river-mixing and cross-land mixing formulations (Chapter 12 and 13) by focusing on the time evolution due to just the overflow process. For the particular zonal-vertical case illustrated in Figure 15.2, we prescribe

$$\partial_t \, (V^{(t)} \, \rho \, C)^{so}_{i,j,kup} = \rho_o \, U^{slope} \, (C^{do}_{i+1,j,kup} - C^{so}_{i,j,kup}) \tag{15.13}$$

$$\partial_t \, (V^{(t)} \, \rho \, C)^{do}_{i+1,j,kup} = \rho_o \, U^{slope} \, (C^{do}_{i+1,j,kdw-1} - C^{do}_{i+1,j,kup}) \tag{15.14}$$

$$\partial_t \, (V^{(t)} \, \rho \, C)^{do}_{i+1,j,kdw-1} = \rho_o \, U^{slope} \, (C^{do}_{i+1,j,kdw} - C^{do}_{i+1,j,kdw-1}) \tag{15.15}$$

$$\partial_t \, (V^{(t)} \, \rho \, C)^{do}_{i+1,j,kdw} = \rho_o \, U^{slope} \, (C^{so}_{i,j,kup} - C^{do}_{i+1,j,kdw}), \tag{15.16}$$

where again $U^{slope} = u^{slope} \, dht_{min} \, dyt$, with

$$dht_{(min)} = \min(dht_{i,j,kup}, dht_{i+1,j,kup}) \tag{15.17}$$

the minimum thickness of the two cells at $k = kup$. For the Boussinesq case, ρ factors on the left hand side are set to the constant reference density ρ_o. Setting the tracer concentration to the same uniform value leads to vanishing time tendencies for $\rho \, V^{(t)}$ in each cell, thus reflecting volume/mass conservation. Additionally, summing these four equations leads to a vanishing right hand side, thus reflecting conservation of total tracer in the system. Since the downslope mixing has the form of an upstream advection, we discretize temporally by evaluating the tracer and density on the right hand side at the lagged time $\tau - 1$.

As implemented in MOM4, the tracer source array is modified in the following manner to account for the downslope flow from Campin and Goosse (1999)

$$[A^{(t)} \, \text{dht} \cdot \text{tracer-source}^{so}]_{i,j,kup} = U^{slope} \, (C^{do}_{i+1,j,kup} - C^{so}_{i,j,kup}) \tag{15.18}$$

$$[A^{(t)} \, \text{dht} \cdot \text{tracer-source}^{do}]_{i+1,j,kup} = U^{slope} \, (C^{do}_{i+1,j,kdw-1} - C^{do}_{i+1,j,kup}) \tag{15.19}$$

$$[A^{(t)} \, \text{dht} \cdot \text{tracer-source}^{do}]_{i+1,j,kdw-1} = U^{slope} \, (C^{do}_{i+1,j,kdw} - C^{do}_{i+1,j,kdw-1}) \tag{15.20}$$

$$[A^{(t)} \, \text{dht} \cdot \text{tracer-source}^{do}]_{i+1,j,kdw} = U^{slope} \, (C^{so}_{i,j,kup} - C^{do}_{i+1,j,kdw}) \tag{15.21}$$

where

$$A^{(t)} = dxt * dyt \tag{15.22}$$

is the time independent horizontal area of a tracer cell.

15.4 Comments on the two overflow schemes in MOM4

As mentioned at the start of this chapter, there are two methods implemented in MOM4 whose aim is to enhance the ability of the simulated fluid to form dense deep water: (1) the Campin and Goosse (1999) scheme described in this chapter, and (2) the sigma diffusion scheme from Beckmann and Döscher (1997) and Döscher and Beckmann (1999) as described in Chapter 14. Both are quasi-physical engineering approaches to the problem of simulating deep water formation near topography. Each provides plumbing routes beyond the local horizontal-vertical routes available in z-models. In this way, these methods provide a new means for *representing* the flows. Questions such as parameterizing the rates of entrainment, volume flux, etc. (e.g., Killworth and Edwards (1999)) are not directly addressed by these schemes.

Climate modelers generally gauge the utility of overflow schemes on the overall results: Do they indeed provide a route for deep water formation near topographic gradients in a manner expected from observations? Yet details of the transport are often not the first priority. This situation is unsatisfying from a process physics perspective. Given the coarseness of ocean climate models (circa year 2003) relative to the small scales of typical high-latitude overflow dynamics, we may not be able to do better with the z-models.

The density structure in Figure 15.3 illustrates a case where the Beckmann and Döscher (1997) scheme does not prescribe enhanced downslope transport. The reason is that their scheme only works with density within the bottommost tracer cell. For this example, density at the bottom of the deeper column is greater than that on the shelf, and so there is no enhanced transport prescribed. In contrast, the Campin and Goosse (1999) scheme prescribes a downslope transport, with the dense shelf water moving to its neutral buoyancy depth.

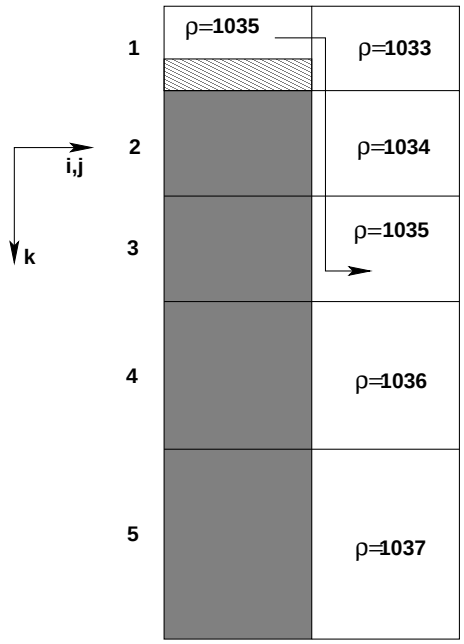

Figure 15.3: Schematic of a situation where a dense parcel sits on a shelf next to a column whose upper portion is light, but whose deeper portion is denser than the shelf. For this case, the Campin and Goosse (1999) scheme prescribes a transport between the shelf water at level 1 and the deeper water at level 3, with water bubbling upward to conserve mass as shown in Figure 15.1. In contrast, the Beckmann and Döscher (1997) scheme will not prescribe any enhanced transport, since here the bottom of the deep column is denser than the shelf.

Part VI

Some diagnostics

SOME DIAGNOSTICS

MOM4 makes extensive use of the FMS diagnostic manager, whereby any field that is carried by the model can be trivially output to a diagnostics file via the registration of that field with the diagnostics manager, and the associated entry of the field's name within the diagnostics table. This part of the MOM4 Guide does not describe this aspect of diagnostics. Instead, we focus here on the formulation and computation of certain diagnostics that have proven of use for research with z-coordinate models.

CHAPTER

SIXTEEN

Streamfunctions

Contents

The purpose of this chapter is to present the mathematical formulation of streamfunctions commonly used to summarize the overturning circulation as well as the vertically integrated circulation.

16.1 Meridional-overturning streamfunction

The meridional overturning streamfunction is commonly used to diagnose features of the thermohaline circulation. For the Boussinesq model, it provides a direct picture of zonally integrated volume transport for both steady-state and transient motions. For non-Boussinesq models, it provides a picture of mass transport only for steady-state motions.

16.1.1 Summary of continuity and notation

We follow the formulation of non-Boussinesq z-coordinate ocean models presented by Griffies (2004). In this case, a non-Boussinesq ensemble averaged fluid leads to the continuum model continuity equation

$$\rho_{,t} + \rho_o \nabla \cdot \mathbf{v} = 0. \tag{16.1}$$

In orthogonal horizontal coordinates, velocity field divergence takes the form (see Griffies (2004))

$$\nabla \cdot \mathbf{v} = (\mathrm{d}y\,\mathrm{d}z)^{-1}\,(\mathrm{d}y\,\mathrm{d}z\,u)_{,x} + (\mathrm{d}x\,\mathrm{d}z)^{-1}\,(\mathrm{d}x\,\mathrm{d}z\,v)_{,y} + (\mathrm{d}x\,\mathrm{d}y)^{-1}\,(\mathrm{d}x\,\mathrm{d}y\,w)_{,z} \tag{16.2}$$

which then leads to the continuity equation

$$(dV/\rho_o)\,\rho_{,t} + \mathrm{d}x\,(\mathrm{d}y\,\mathrm{d}z\,u)_{,x} + \mathrm{d}y\,(\mathrm{d}x\,\mathrm{d}z\,v)_{,y} + \mathrm{d}z\,(\mathrm{d}x\,\mathrm{d}y\,w)_{,z} = 0, \tag{16.3}$$

where

$$dV = \mathrm{d}x\,\mathrm{d}y\,\mathrm{d}z \tag{16.4}$$

corresponds to the volume of a model grid cell. Note that the volume of grid cells in the top levels of MOM4 are time dependent due to the use of a free surface. Hence, it is not generally valid to bring dV inside the time derivative.

To set the notation, the distance between two infinitesimally close points on the sphere is written

$$(\mathrm{d}x)^2 = (h_1\,\mathrm{d}\xi^1)^2 + (h_2\,\mathrm{d}\xi^2)^2 + (h_3\,\mathrm{d}\xi^3)^2 \tag{16.5}$$

when using generalized orthogonal coordinates (ξ^1, ξ^2, ξ^3). For a Traditional Approximation continuum system (see Griffies (2004)), the stretching functions h_1 and h_2 are dependent on horizontal position alone, and h_3 is unity. However, to allow the following manipulations to incorporate MOM4's partial cells, we maintain a horizontal and vertical position dependence to h_3.

16.1.2 Meridional and vertical transport

To proceed, introduce the transports

$$\mathcal{V} = (\mathrm{d}z)^{-1} \int_{\xi^1_a}^{\xi^1_b} \mathrm{d}x\,(v\,\mathrm{d}z) \tag{16.6}$$

$$\mathcal{W} = (\mathrm{d}y)^{-1} \int_{\xi^1_a}^{\xi^1_b} \mathrm{d}x\,(w\,\mathrm{d}y). \tag{16.7}$$

Integration is taken along a line of constant ξ^1, where ξ^1 is the generalized orthogonal coordinate corresponding to the spherical longitude λ. Integration endpoints ξ^1_a and ξ^1_b are assumed to be at land-sea boundaries, where u vanishes, or over a periodic domain. As in the spherical coordinate case, we refer to $\mathcal{V}$ as the generalized meridional transport. To motivate the definition of the transport streamfunction,

take the generalized meridional derivative of $\mathrm{d}z\,\mathcal{V}$ to render

$$\begin{aligned}(\mathrm{d}z\,\mathcal{V})_{,y} &= \partial_y\left(\int_{\xi^1_a}^{\xi^1_b}\mathrm{d}x\,(\mathrm{d}z\,v)\right)\\ &= \frac{1}{h_2}\int_{\xi^1_a}^{\xi^1_b}\partial_2\,(\mathrm{d}x\,\mathrm{d}z\,v)\\ &= \frac{1}{\mathrm{d}y}\int_{\xi^1_a}^{\xi^1_b}\mathrm{d}y\,(\mathrm{d}x\,\mathrm{d}z\,v)_{,y}\end{aligned} \tag{16.8}$$

These steps made use of the properties of orthogonal coordinates whereby ∂_2 commutes with the zonal integration, since it is orthogonal to the integration pathway taken along a line of constant ξ^1. However, ∂_2 does not commute with the distances $\mathrm{d}x$ and $\mathrm{d}z$, each of which can be functions of the generalized meridional coordinate ξ^2. Use of continuity in the form (16.3) yields

$$\begin{aligned}-\mathrm{d}y\,(\mathrm{d}z\,\mathcal{V})_{,y} &= \int_{\xi^1_a}^{\xi^1_b}[\mathrm{d}z\,(\mathrm{d}x\,\mathrm{d}y\,w)_{,z}+(dV/\rho_o)\,\rho_{,t}]\\ &= \mathrm{d}z\,(\mathrm{d}y\,\mathcal{W})_{,z}+\int_{\xi^1_a}^{\xi^1_b}(dV/\rho_o)\,\rho_{,t}.\end{aligned} \tag{16.9}$$

To reach this relation, we used

$$\int_{\xi^1_a}^{\xi^1_b}\mathrm{d}x\,(\mathrm{d}y\,\mathrm{d}z\,u)_{,x}=0, \tag{16.10}$$

which follows from the chosen zonal boundaries.

16.1.3 Overturning streamfunction

In summary, the zonally integrated transports satisfy the balance

$$(\mathrm{d}z)^{-1}\,(\mathrm{d}z\,\mathcal{V})_{,y}+(\mathrm{d}y)^{-1}\,(\mathrm{d}y\,\mathcal{W})_{,z}+(\mathrm{d}y\,\mathrm{d}z)^{-1}\int_{\xi^1_a}^{\xi^1_b}(dV/\rho_o)\,\rho_{,t}=0. \tag{16.11}$$

This relation indicates that meridional and vertical transports are balanced by fluctuations in mass. In a steady state, or for the Boussinesq models, the mass fluctuations vanish, thus leading to volume conservation manifesting as the two-dimensional non-divergence condition

$$\mathrm{d}y\,(\mathrm{d}z\,\mathcal{V})_{,y}+\mathrm{d}z\,(\mathrm{d}y\,\mathcal{W})_{,z}=\mathrm{d}\xi^2\,\mathrm{d}\xi^3\left(\frac{\partial(h_3\,\mathcal{V})}{\partial\xi^2}+\frac{\partial(h_2\,\mathcal{W})}{\partial\xi^3}\right)=0. \tag{16.12}$$

The second equality follows by the orthogonal nature of the coordinates, whereby

$$\frac{\partial(d\xi^2)}{\partial\xi^3} = \frac{\partial(d\xi^3)}{\partial\xi^2} = 0. \tag{16.13}$$

for the steady state , or for the Boussinesq models,We are thus motivated to introduce an overturning streamfunction that satisfies

$$\mathcal{V} = -\Psi_{,z} \tag{16.14}$$
$$\mathcal{W} = \Psi_{,y}. \tag{16.15}$$

The streamfunction Ψ summarizes the meridional-depth volume transport for a Boussinesq fluid, or for a steady-state non-Boussinesq fluid. It has dimensions volume/time, and so it represents the volume transport of water in the (y, z) plane. The typical dimensions are Sverdrups, where $1\,\text{Sv} = 10^6 \text{m}^3\,\text{sec}^{-1}$. Multiplication by ρ_o produces a mass transport streamfunction $\rho_o\,\Psi$ in units of $\text{kg}\,\text{sec}^{-1}$.

We can solve for the streamfunction via integration of its defining relation and setting a boundary condition. Integration of equation (16.14) leads to

$$\Psi(y,z) = \Psi(y,z_o) - \int_{z_o}^{z} \mathrm{d}z'\,\mathcal{V}(y,z'), \tag{16.16}$$

where z_o is a reference depth. Similar integration of equation (16.15) leads to

$$\Psi(y,z) = \Psi(y_o,z) + \int_{y_o}^{y} \mathrm{d}y'\,\mathcal{W}(y',z), \tag{16.17}$$

where y_o is a reference latitude. It is now possible to develop two equivalent expressions for the overturning streamfunction. The first is found through substituting the expression (16.16) into (16.17)

$$\Psi(y,z) = \Psi(y_o,z_o) - \int_{z_o}^{z} \mathrm{d}z'\,\mathcal{V}(y_o,z') + \int_{y_o}^{y} \mathrm{d}y'\,\mathcal{W}(y',z). \tag{16.18}$$

The second is found by substituting equation (16.17) into (16.16)

$$\Psi(y,z) = \Psi(y_o,z_o) - \int_{z_o}^{z} \mathrm{d}z'\,\mathcal{V}(y,z') + \int_{y_o}^{y} \mathrm{d}y'\,\mathcal{W}(y',z_o). \tag{16.19}$$

16.1.4 Choosing the reference values

The question is how to choose the reference values y_o and z_o to simplify the computation of the overturning streamfunction. In general, evaluation of the vertical transport term is more difficult than the meridional transport term. One is therefore motivated to focus on equation (16.19) when computing the streamfunction, rather than equation (16.18). For choosing the reference value z_o, it is useful to consider the water budget and how it closes. In the rigid lid, the water budget is closed within the ocean domain. As such, so long as the value of z_o corresponds to a value anywhere completely outside the ocean domain, the vertical transport term

$\int_{y_o}^{y} \mathrm{d}y' \; \mathcal{W}(y', z_o)$ vanishes. For the free surface, however, the possibility of surface water fluxes allows for an open water budget above the ocean surface. Since there is no attempt here to account for water cycling through the rock beneath the ocean, one can assume all water transport in rock vanishes. Hence, by taking z_o to be some value completely beneath the ocean bottom, the vertical transport term can again be dropped with the free surface. As a consequence, a general expression for the overturning streamfunction, valid for both the free surface and rigid lid, is given just by the meridional transport term

$$\Psi(y, z) = -\int_{z_o}^{z} \mathrm{d}z' \, \mathcal{V}(y, z') = -\int_{z_o}^{z} \int_{x_a}^{x_b} \mathrm{d}x \, \mathrm{d}z' \, v. \tag{16.20}$$

In practice, it is not necessary to evaluate the integral anyplace beneath the ocean bottom, since the water velocity vanishes there. On the bottom, the vertical coordinate takes on the non-constant value $z = -H(x, y)$. Therefore, when integrating just to the ocean bottom, it is necessary to perform the vertical integral first, and then the zonal integral

$$\Psi(y, z) = -\int_{x_a}^{x_b} \mathrm{d}x \int_{-H}^{z} \mathrm{d}z' \, v. \tag{16.21}$$

Beneath the ocean surface, the no-normal flow condition implies that the overturning streamfunction is a constant along the side and bottom land-sea boundaries. For the rigid lid, the absence of fresh water input to the ocean surface also implies that its overturning streamfunction is a constant at the ocean surface. The choice $\Psi(y_o, z_o) = 0$ means that the rid lid overturning streamfunction is zero along all the boundaries. For the free surface, however, the overturning streamfunction need not be a constant on the ocean surface, due to the presence of surface water fluxes, whereas it remains zero on the sides/bottom just as for the rigid lid.

16.1.5 Transport beneath an arbitrary surface

As shown in Section 40.9 of Pacanowski and Griffies (1999), we can extend the above considerations to the case of generalized vertical coordinates. In this case, we are concerned with the meridional transport of fluid beneath some generalized vertical coordinate surface. It is a straightforward matter to extend the definition of the overturning streamfunction to this case, where

$$\Psi(y, s) = -\int_{x_a}^{x_b} \int_{-s(H)}^{s(z)} \mathrm{d}x \, \mathrm{d}z' \, v, \tag{16.22}$$

with $s = s(x, y, z, t)$ the generalized vertical coordinate (see Griffies (2004) for details). Surfaces that are physically of interest include various potential density surfaces, which are especially relevant when the flow is adiabatic. See Section 40.9 of Pacanowski and Griffies (1999) for more discussion.

16.1.6 Transport from GM90

The parameterization of Gent et al. (1995) provides a volume transport in addition to the resolved scale Eulerian mean transport. The total meridional-overturning streamfunction takes the form

$$\Psi^{(tot)}(y,z) = -\int_{x_a}^{x_b} \mathrm{d}x \int_{-H}^{z} \mathrm{d}z' \, (v + v^{gm}), \tag{16.23}$$

where

$$v^{gm} = -\partial_z \left(\kappa \, S_y\right) \tag{16.24}$$

is the eddy-induced velocity with $S_y = -\partial_y \rho / \partial_z \rho$ the neutral slope in the y-direction and κ a diffusivity. Performing the vertical integral on the GM90 piece leads to

$$\Psi^{(tot)}(y,z) = \Psi(y,z) + \Psi^{gm}(y,z) \tag{16.25}$$

where

$$\Psi^{gm}(y,z) = \int_{x_a}^{x_b} \mathrm{d}x \, (\kappa \, S_y) \tag{16.26}$$

with $\kappa \, S_y = 0$ at $z = -H$. Hence, the Gent et al. (1995) parameterization adds a contribution that scales linearly with basin size, isopyncal slope, and diffusivity

$$\Psi^{gm} \sim L \, S \, \kappa. \tag{16.27}$$

As an example, let $\kappa = 10^3 \mathrm{m}^2 \, \mathrm{s}^{-1}$, $S = 10^{-3}$, and $L = 10^7$ m, which yields $\mathcal{T} \approx$ 10Sv. Such transport can represent a nontrivial addition to that from the resolved scale velocity field.

16.2 Vertically integrated transport

The purpose of this section is to discuss the streamfunction used to summarize the vertically integrated transport. Only when vertically integrated flow is non-divergent, such as for the Boussinesq rigid lid case, will a streamfunction be sufficient. In general, it only approximates the flow. However, for many cases the approximate streamfunction is quite useful.

16.2.1 Summary of the rigid lid

With the rigid lid method of Bryan (1969), it is assumed that the vertically integrated velocity in a Boussinesq fluid is non-divergent $\nabla \cdot \mathbf{U} = 0$. Hence, it can be described via a scalar streamfunction $\mathbf{U} = \hat{\mathbf{z}} \wedge \nabla \tilde{\psi}$. In this case, the vertically integrated advective transport between two points is given by

$$T_{ab} = \int_a^b dl \; \hat{\mathbf{n}} \cdot \int_{-H}^{0} \mathrm{d}z \; \mathbf{u} = \psi_a - \psi_b, \tag{16.28}$$

where dl is the line element along any path connecting the points a and b, and $\hat{\mathbf{n}}$ is a unit vector pointing perpendicular to the path in a rightward direction when facing

the direction of integration. As written, T_{ab} has units of volume per time, and so it represents a volume transport. Therefore, the difference between the streamfunction at two points represents the vertically integrated volume transport between the two points. It is for this reason that the streamfunction is sometimes called the *volume transport streamfunction*. Note that Bryan (1969) defined the barotropic streamfunction with an extra factor of the Boussinesq density ρ_o, such that his mass transport streamfunction has the dimensions of mass per time rather than volume per time. The difference is trivial for a Boussinesq fluid.

16.2.2 General case of divergent flow

The vertically integrated horizontal momentum density

$$\rho_o \, \mathbf{U} = \int_{-H}^{\eta} \rho \, \mathbf{u} \tag{16.29}$$

generally has a non-zero divergence due to fluctuations of mass and/or volume within the vertical column. Hence, it corresponds to both a streamfunction $\tilde{\psi}$ and a velocity potential χ

$$\mathbf{U} = \hat{\mathbf{z}} \wedge \nabla \tilde{\psi} + \nabla \chi. \tag{16.30}$$

Only for a Boussinesq rigid-lid model with zero fresh water flux will χ vanish. Hence, to compute the precise vertically integrated transport passing between two points, a direct evaluation of the integral

$$T_{ab} = \int_a^b dl \; \hat{\mathbf{n}} \cdot \mathbf{U} \tag{16.31}$$

is given. Although accurate and complete, this integral does not readily provide a horizontal map of transport, and so it looses much of the appeal associated with the transport streamfunction used with a rigid lid.

However, for many practical situations, maps of the function

$$\psi(x, y) = - \int_{y_o}^{y} \mathrm{d}y' \, U(x, y') \tag{16.32}$$

are quite useful, where the lower limit y_o is taken at the southern boundary of the domain, generally given by a solid wall for ocean climate models. By its definition, the meridional derivative of ψ yields the zonal transport

$$\psi_{,y} = U. \tag{16.33}$$

The zonal derivative, however, does not yield the meridional transport due to the divergent nature of the vertically integrated flow. To see what it does yield, let us restrict attention to the Boussinesq case with spherical coordinates, where

$$\frac{1}{R \, \cos\phi} \, \psi_{,\lambda} = V - \frac{R}{\cos\phi} \int_{\phi_o}^{\phi} d\phi' \, \cos\phi' \, \nabla \cdot \mathbf{U}. \tag{16.34}$$

To reach this result we used where $\cos\phi_o \, V(\lambda, \phi_o) = 0$. With volume conservation in the Boussinesq model leading to

$$\nabla \cdot \mathbf{U} = -\eta_t + q_w, \tag{16.35}$$

we see that $\nabla \cdot \mathbf{U}$ vanishes only when there is zero time tendency of the free surface height and zero fresh water flux through the surface. Hence, the zonal derivative leads to the meridional transport plus a term that vanishes in the case of a steady state ($\eta_t = 0$) and a zero fresh water flux. It is useful to see how large the extra term might be. For this purpose, zonally integrate the derivative $\psi_{,\lambda}$ to find

$$\begin{aligned} \psi(\lambda,\phi) - \psi(\lambda_o,\phi) &= R\,\cos\phi \int_{\lambda_o}^{\lambda} d\lambda'\, V(\lambda',\phi) \\ &- R^2 \int_{\lambda_o}^{\lambda} d\lambda' \int_{\phi_o}^{\phi} d\phi'\, \cos\phi'\,(-\eta_t + q_w). \end{aligned} \tag{16.36}$$

For example, with $-\eta_t + q_w = 1m/year$ applied over a $1000km \times 1000km$ area, the extra term contributes much less than a Sv to the streamfunction. Cases where the differences are larger certainly can be constructed. But for many diagnostic purposes, the differences are negligible.

By construction, ψ reduces to the transport streamfunction in the case of a rigid lid where $\nabla \cdot \mathbf{U} = 0$. However, this is not a unique choice and alternatives do exist. For example,

$$\psi^*(x,y) = \psi(x_o,y) + \int_{x_o}^{x} \mathrm{d}x'\, V(x',y), \tag{16.37}$$

gives

$$V = \psi^*_{,x}. \tag{16.38}$$

ψ^* has the advantage that zonal derivatives give the exact meridional transport, yet the meridional derivative deviates from the zonal transport. In the end, it might be useful to plot ψ and ψ^* and compare.

As each streamfunction is defined only up to an arbitrary constant, it is useful to specify this constant in a manner to correspond to that resulting from the rigid lid approximation. To do so, it is recommended that one normalizes each streamfunction by the value at $\lambda = 300^\circ$ and $\phi = -20^\circ$, which corresponds to a point over South America. This convention corresponds to taking the Americas as the zeroth island in the rigid lid method.

CHAPTER

SEVENTEEN

Diagnosing tracer transport

Contents

The purpose of this chapter is to present diagnostics of integrated forms for tracer transport.

17.1 Introduction

Diagnosing the transport of tracers across a particular section or through a straight provides a useful means to compare simulations with observations. It also allows one to summarize a large amount of information thus integrating together many processes. As described in various papers, such as Bryan (1987), one common integrated diagnostic is the meridional tracer transport. Furthermore, when coupling to an atmospheric model, Gordon et al. (2000) found it crucial to roughly match the ocean meridional heat transport to that expected by the atmospheric model. Motivated by the importance of meridional tracer transport to climate modeling, we focus mostly on meridional transport, though all results can be generalized to arbitrary directions. For the tripolar grid supported by MOM4 (Section 4.2), the following diagnostics represent true northward transport for regions south of $65^\circ N$.

17.2 Integrated mass budget

Prior to developing budgets for tracer, we revisit some issues discussed in Section 16.1 with mass budgets integrated over certain domains. For this purpose, recall that conservation of mass for an infinitesimal parcel of model fluid is given by (see Section 3.3)

$$\rho_{,t} + \rho_o \nabla \cdot \mathbf{v} = 0, \tag{17.1}$$

where ρ is the density and $\mathbf{v} = (\mathbf{u}, w)$ is the three-dimensional advection velocity discretized according to the needs of the energetic analysis described in Section 6.2. Integrating this local budget vertically over the depth of a fluid column leads to the budget

$$\partial_t \left(\int_{-H}^{\eta} dz\, \rho \right) + \rho_o \nabla \cdot \mathbf{U} = \rho_o\, q_w. \tag{17.2}$$

In this equation,

$$\mathbf{U} = \int_{-H}^{\eta} dz\, \mathbf{u} = (H + \eta)\, \overline{\mathbf{u}} \tag{17.3}$$

is the depth integrated velocity, q_w is the volume per area per time of fresh water entering the ocean surface ($q_w > 0$ means water enters the ocean domain), $z = -H$ is the ocean bottom, and is $z = \eta$ the free surface deviation from $z = 0$. Derivation of equation (17.2) required the use of the surface and bottom kinematic boundary conditions (see Section 3.4). In a semi-discrete form appropriate for the discrete numerical model, the column mass budget is given by

$$\partial_t \left(\sum_k h\, \rho \right) + \rho_o \nabla \cdot \mathbf{U} = \rho_o\, q_w \tag{17.4}$$

with h the tracer cell thickness.

Integrating zonally and assuming either no-normal flow at the side boundaries, or periodic boundary conditions, leads to the zonal and vertically integrated mass budget

$$\partial_t \left(\int_{x_w}^{x_e} dx \int_{-H}^{\eta} dz\, \rho \right) + \rho_o \int_{x_w}^{x_e} dx\, \partial_y V = \rho_o \int_{x_w}^{x_e} dx\, q_w. \tag{17.5}$$

At steady state, the zonally integrated divergence of the vertically integrated meridional velocity balances the zonally integrated fresh water flux

$$\int_{x_w}^{x_e} dx\, \partial_y V = \int_{x_w}^{x_e} dx\, q_w \qquad \text{steady state.} \tag{17.6}$$

If we first integrate from a southern latitude $y = y_s$ where $V(y_s) = 0$ northward to some latitude $y = y_n$, and then zonally, we have the balance

$$\partial_t \left(\int_{x_w}^{x_e} dx \int_{y_s}^{y_n} dy \int_{-H}^{\eta} dz\, \rho \right) + \rho_o \int_{x_w}^{x_e} dx\, V(y_n) = \rho_o \int_{x_w}^{x_e} \int_{y_s}^{y_n} dx\, dy\, q_w. \tag{17.7}$$

At steady state, the zonal and vertical integrated velocity at a particular latitude balances the zonal and vertical integrated fresh water flux

$$\int_{x_w}^{x_e} dx\, V(y_n) = \int_{x_w}^{x_e}\int_{y_s}^{y_n} dx\, dy\, q_w \qquad \text{steady state.} \tag{17.8}$$

In the absence of a fresh water flux,

$$\int_{x_w}^{x_e} dx\, V(y_n) = 0 \qquad \text{steady state with } q_w = 0. \tag{17.9}$$

17.3 Integrated tracer budget

Following in a manner similar to the mass budget, we recall that the budget of tracer for a semi-discrete parcel of model water (see Griffies (2004) for derivation)

$$\partial_t(\rho\, h\, T) = -\rho_o\, \nabla\cdot(h\, \mathbf{F}) - \rho_o\, h\, \partial_z\, F^z, \tag{17.10}$$

where we drop tracer source terms for simplicity. In this equation, h is the thickness of the model grid cell, and $\mathbf{F} = (\mathbf{F}^h, F^z)$ is the combined advective and sub-grid-scale tracer fluxes

$$\mathbf{F} = \mathbf{v}\, T + \mathbf{F}_{sgs}. \tag{17.11}$$

Integration over the depth of the ocean and along an i-line (the zonal direction when using spherical coordinates), and assuming either solid walls or periodic boundary conditions, renders

$$\partial_t \left(\sum_{i,k} dx\, dy\, h\, \rho\, T \right) = -\rho_o \sum_{i,k} \delta_j \left(dx\, h\, F^y\right) - \rho_o \sum_i dx\, dy\, F^z_{k=0}, \tag{17.12}$$

where

$$\delta_j\, \Phi = \Phi_{j+1} - \Phi_j \tag{17.13}$$

is a difference operator acting on the fluxes passing across the meridional faces of the tracer cells, and we employed the discrete divergence operator introduced in Section 6.2. The vertical flux at $k = 0$ is given by (see Griffies (2004))

$$F^z_{k=0} = -q_w\, T_w + Q^{turb}_T, \tag{17.14}$$

with T_w the tracer concentration in the fresh water, and Q^{turb}_T the turbulent flux of tracer associated with sub-grid-scale processes.

At a steady state, the zonal integrated surface flux at a particular latitude is balanced by the depth and zonal integrated meridional tracer flux convergence

$$\sum_{i,k} \delta_j \left(dx\, h\, F^y\right) = -\sum_i dx\, dy\, F^z_{k=0} \qquad \text{steady state.} \tag{17.15}$$

In the absence of surface tracer fluxes, the steady state flux moving northward must balance that moving southward. The result reduces to equation (17.8) in the case

of tracer concentration is uniform. Note that only for coordinates where dy is independent of i (such as spherical coordinates) can dy be transferred to the right hand side.

Now integrate from a southern row $j = js$ where the meridional flux vanishes, such as the Antarctic continent. At the northern row $j = jn$, the meridional and zonal integrated surface flux is balanced at steady state by the net meridional flux entering southward through the northern j-row boundary

$$\sum_{i,k} (dx\, h\, F^y)_{j=jn} = -\sum_i \sum_{j=js}^{j=jn} dx\, dy\, F^z_{k=0} \qquad \text{steady state.} \tag{17.16}$$

This result reduces to equation (17.9) in the case of uniform tracer concentration and zero surface tracer fluxes.

17.4 Northward tracer transport

In regions of the model where grid lines are spherically oriented, the zonally and vertically integrated northward tracer transport is given by

$$F^{north} = \rho_o \sum_{i,k} dx\, h\, F^y = \rho_o \sum_{i,k} dx\, (v\, h\, T + h\, F^y_{sgs}). \tag{17.17}$$

Typically this transport is dominated by the advective component. However, for regions such as the Southern Ocean, contributions from neutral physics, contained in F^y_{sgs}, can be nontrivial.

17.4.1 Decomposition of the meridional advective tracer flux

It is often useful to decompose the zonal and depth integrated meridional advective transport into various components. Because of the generally nontrivial bottom topography and surface height, we find it convenient to decompose the thickness weighted meridional velocity according to

$$v\, h = (v\, h - V/nk) + V/nk = \widehat{v\, h} + V/nk \tag{17.18}$$

where

$$\overline{\Phi} = \frac{1}{H+\eta} \int_{-H}^{\eta} dz\, \Phi \longrightarrow \frac{1}{H+\eta} \sum_{k=1}^{nk} h\, \Phi \tag{17.19}$$

is the depth average, and $\mathbf{U} = (U, V) = (H+\eta)\, \overline{\mathbf{u}}$ is the depth integrated horizontal velocity. With this decomposition, the northward advective tracer transport becomes

$$\rho_o^{-1}\, F^{north}_{advect} = \sum_i dx \sum_k (v\, h)\, T \tag{17.20}$$

$$= \sum_i dx \sum_k (V/nk + \widehat{v\, h})\, (\overline{T} + \widehat{T}) \tag{17.21}$$

$$= \sum_i dx\, V\, \overline{T} + \sum_i dx \sum_k \widehat{v\, h}\, \widehat{T}. \tag{17.22}$$

We now decompose fields according to their zonal mean and deviations therefrom

$$\Phi = (\Phi - \Phi^{\overline{x}}) + \Phi^{\overline{x}} = \Phi^{x'} + \Phi^{\overline{x}} \tag{17.23}$$

where

$$\Phi^{\overline{x}} = \frac{1}{L} \int_{x_1}^{x_2} dx\, \Phi \longrightarrow \frac{1}{L} \sum_i dx\, \Phi \tag{17.24}$$

is the zonal mean. Introducing this decomposition yields

$$\begin{aligned} \rho_o^{-1}\, F^{north}_{advect} &= \sum_i dx\, V\, \overline{T} + \sum_i dx \sum_k \widehat{v\,h}\, \widehat{T} \\ &= L_{k=0}\, V^{\overline{x}}\, \overline{T}^{\overline{x}} + \sum_i dx\, V^{x'}\, \overline{T}^{x'} + \sum_k \sum_i dx\, (\widehat{v\,h}^{\overline{x}}\, \widehat{T}^{\overline{x}} + \widehat{v\,h}^{x'}\, \widehat{T}^{x'}) \\ &= L_{k=0}\, V^{\overline{x}}\, \overline{T}^{\overline{x}} + \sum_i dx\, V^{x'}\, \overline{T}^{x'} + \sum_k L_k\, \widehat{v\,h}^{\overline{x}}\, \widehat{T}^{\overline{x}} + \sum_k \sum_i dx\, \widehat{v\,h}^{x'}\, \widehat{T}^{x'} \end{aligned} \tag{17.25}$$

where L_k is the distance as a function of vertical depth level over which the zonal integration takes place within sea water (i.e., land is not included).

17.4.2 Interpretation of terms

The utility of the above decomposition is that we can ascribe useful interpretations for the different terms.

17.4.2.1 Mean advecting mean

The term

$$F^{north}_{mean-mean} = \rho_o\, L_{k=0}\, V^{\overline{x}}\, \overline{T}^{\overline{x}} \tag{17.26}$$

represents the zonal and depth mean meridional velocity advecting the zonal and depth mean tracer. In a steady state with no surface forcing, equation (17.9) showed that mass conservation leads to $V^{\overline{x}} = 0$, and so $F^{north}_{mean-mean} = 0$. In general, however, this transport is not zero.

17.4.2.2 Barotropic gyre transport

The term

$$F^{north}_{bt-gyre} = \rho_o \sum_i dx\, V^{x'}\, \overline{T}^{x'} \tag{17.27}$$

is called the barotropic gyre transport. The *gyre* adjective refers to the presence of zonal anomalies in both the vertically integrated velocity and vertically integrated tracer. Such anomalies typically arise from wind forcing in ocean basins. This term vanishes in a domain with zero zonal anomalies and/or with zero vertically integrated flow.

17.4.2.3 Baroclinic overturning transport

The term

$$F^{north}_{bc-over} = \rho_o \sum_k L_k \, \widehat{v\,h}^{\overline{x}} \, \widehat{T}^{\overline{x}} \tag{17.28}$$

is called the baroclinic overturning transport. The *overturning* adjective refers to the presence of zonal averaged vertical shear terms for both the thickness weighted velocity and the tracer. This transport typically arises from zonally averaged overturning circulation, such as that associated with thermohaline forcing. Note that often one extracts from this term an Ekman component described in Section 17.4.3.

17.4.2.4 Baroclinic gyre transport

The term

$$F^{north}_{bc-gyre} = \rho_o \sum_k \sum_k dx \, \widehat{v\,h}^{x'} \, \widehat{T}^{x'} \tag{17.29}$$

is called the baroclinic gyre transport. Again, often one extracts from this term an Ekman component described in Section 17.4.3.

17.4.3 Ekman component

A further decomposition is often made to the shear component of the velocity $\widehat{v}$ in regions bounded away from the equator. Here, we decompose the velocity according to

$$\widehat{v} = (\widehat{v} - \widehat{v}_E) + \widehat{v}_E = \widehat{v}_B + \widehat{v}_E, \tag{17.30}$$

where

$$\widehat{v}_E = \frac{\tau^\lambda}{\rho_o \, f \, h_E} \tag{17.31}$$

is the meridional Ekman velocity over a depth of thickness h_E. The thickness of the Ekman layer is often taken as the thickness of the first model level, though this is not always appropriate, especially with models of fine vertical resolution.

CHAPTER

EIGHTEEN

Effective dianeutral diffusivity

Contents

The purpose of this chapter is to detail a method to quantify water mass mixing in MOM without detailed knowledge of the numerical transport scheme. The method is restricted to experiments with a Boussinesq fluid, flat bottom ocean, linear equation of state, and without buoyancy forcing. Extensions are possible, yet not implemented. Momentum forcing via winds is allowed. Much of the fundamentals in this chapter are guided by the work of Winters et al. (1995) and Winters

and D'Asaro (1995). Griffies et al. (2000b) applied these methods to various idealized model configurations.

We assume the linear equation of state for an incompressible fluid is written in the form

$$\rho = \rho_0 \, (1 - \alpha \, \theta), \tag{18.1}$$

where θ is potential temperature, ρ_o is a constant density associated with the Boussinesq approximation, and α is a constant thermal expansion coefficient. The system is open to momentum fluxes yet closed to buoyancy fluxes.

18.1 Potential energy and APE in Boussinesq fluids

The purpose of this section is to introduce the notion of a sorted density profile in the context of potential energy and available potential energy (APE). This profile is of particular relevance when considering the effective mixing occuring throughout a column of sorted fluid in Section 18.2.

Potential energy of the ocean is given by

$$E_p = \int \mathrm{d}V \, \rho \, \mathcal{P}, \tag{18.2}$$

where

$$\mathcal{P} = g \, z \tag{18.3}$$

is the potential energy per mass of a fluid parcel, g is the acceleration of gravity, z is the vertical position of a fluid parcel, and $\rho \, \mathrm{d}V = \rho \, \mathrm{d}x \, \mathrm{d}y \, \mathrm{d}z$ is the parcel mass.

Available potential energy (APE) is the difference between the potential energy of the fluid in its natural state, and the potential energy of a corresponding stably stratified *reference* state. The reference state is reached by adiabatically rearranging the fluid to a state of minimum potential energy, which is a state that contains zero horizontal gradients. This rearrangement, or *sorting*, provides a non-local mapping between the unsorted fluid density and the sorted density

$$\rho(\mathbf{x}, t) = \rho(z^*(\mathbf{x}, t), t). \tag{18.4}$$

The sorting map determines a vertical position field $z^*(\mathbf{x}, t)$ which is the vertical height in the sorted state occupied by a parcel at $(\mathbf{x}, t)$ in the unsorted state. Due to the monotonic arrangement of density in the sorted state, $z^*(\mathbf{x}, t)$ is a monotonic function of density $\rho(\mathbf{x}, t)$.

It is convenient to set the origin of the vertical coordinate at the ocean bottom so to keep potential energy of the unsorted state non-negative. This convention also allows for $z^*(\mathbf{x}, t)$ to be defined as a monotonically decreasing function of density. That is,

$$\rho(\mathbf{x}_1, t) < \rho(\mathbf{x}_2, t) \Rightarrow z^*(\mathbf{x}_1, t) > z^*(\mathbf{x}_2, t). \tag{18.5}$$

Conservation of volume in a flat bottom ocean implies that the sorted fluid state has the same vertical extent as the unsorted fluid, which renders

$$0 \leq z, z^* \leq H, \tag{18.6}$$

where H is the ocean depth.

In the following, it proves convenient to denote the density profile in the sorted reference state using the symbols

$$\rho(z^*, t) = \rho_{ref}(z = z^*, t). \tag{18.7}$$

Given this notation, the non-local sorting map between the unsorted and sorted fluid states provides the equivalence

$$\rho(\mathbf{x}, t) = \rho(z^*(\mathbf{x}, t), t) = \rho_{ref}(z = z^*, t). \tag{18.8}$$

In turn, potential energy for the sorted fluid state can be written in two equivalent manners

$$E_{ref} = g \int \mathrm{d}V \, z \, \rho_{ref}(z, t) \tag{18.9}$$

$$= g \int \mathrm{d}V \, z^*(\mathbf{x}, t) \, \rho(\mathbf{x}, t). \tag{18.10}$$

Equation (18.9) represents an integral over the sorted fluid state, in which the density of this state is a function only of the depth. The horizontal area integral is thus trivial to perform. Equation (18.10) represents an integral over the unsorted fluid state, where the density $\rho(\mathbf{x}, t)$ of an unsorted parcel is weighted by the vertical position $z^*(\mathbf{x}, t)$ that the parcel occupies in the sorted state. It follows that the APE can be written in two equivalent ways

$$E_{APE} = g \int \mathrm{d}V \, z \, [\rho(\mathbf{x}, t) - \rho_{ref}(z, t)] \tag{18.11}$$

$$= g \int \mathrm{d}V \, \rho(\mathbf{x}, t) \, [z - z^*(\mathbf{x}, t)]. \tag{18.12}$$

18.2 Effective dianeutral mixing

In this section we formulate a method to empirically quantify the effects on water masses arising from various simulated tracer transport processes. A similar application was advocated by Winters et al. (1995) and Winters and D'Asaro (1995) for the purpose of diagnosing mixing in direct numerical simulations of unstable fluid flows. Their focus was on physically motivated mixing such as that occuring with breaking waves. The main focus here is on spurious mixing due to numerical errors. The procedure is identical, however, in that for each case, one considers the evolution of the reference density profile, $\rho_{ref}(z, t)$, in a fluid system closed to buoyancy fluxes

$$\partial_t \, \rho_{ref} = \partial_{z^*} \, (\kappa_{eff} \, \partial_{z^*} \rho_{ref}). \tag{18.13}$$

Again, in this equation z^* is the vertical position in the sorted fluid state. Therefore, constant z^* surfaces represent constant density surfaces in the unsorted state. As such, the effective diffusivity κ_{eff} summarizes the total amount of mixing across constant density surfaces. If the simulation does not change the water mass distribution, then $D\rho/Dt = 0$, the sorted reference density is static $\partial_t \, \rho_{ref} = 0$, and the effective diffusivity is zero. In turn, any temporal change in the reference density represents changes in the water mass distribution. These changes are the result of dianeutral mixing, and so have an associated non-zero $\kappa_{eff}(z^*, t)$. This is the basic idea that is pursued in the following sections.

18.2.1 Global effective dianeutral diffusivity

In addition to the diffusivity $\kappa_{eff}(z^*,t)$, which is local in density space, it is useful to garner a summary of the overall dianeutral mixing occuring in an ocean model. A vertical integral of $\kappa_{eff}(z^*,t)$ would provide such information. A quicker computation of a global effective dianeutral diffusivity can be obtained by inverting the variance equation for the sorted density

$$\partial_t \int \mathrm{d}V\ \rho_{ref}^2 = -2 \int \mathrm{d}V\ \kappa_{eff}\ (\partial_z \rho_{ref})^2. \tag{18.14}$$

This result, derived for a closed fluid system, suggests the introduction of a global effective diffusivity

$$\kappa_{global}(t) = -\left(\frac{\partial_t \int \mathrm{d}V\ \rho_{ref}^2}{2 \int \mathrm{d}V\ (\partial_z \rho_{ref})^2} \right). \tag{18.15}$$

This diffusivity provides one number that can be used to represent the total amount of dianeutral diffusion acting over the full model domain. It vanishes when the simulation is adiabatic, as does the effective diffusivity $\kappa_{eff}(z^*,t)$. However it is generally different from the vertical average of $\kappa_{eff}(z^*,t)$.

18.2.2 Finite difference approximation

In the following, assume that the discrete sorted density is equally spaced in the vertical with a separation Δz^*, and let the vertical coordinate increase upwards from zero at the flat bottom ocean floor. Note that in general, $\Delta z^* << \Delta z$, where Δz is the ocean model's grid spacing. The reason is that *all* the $N_x \times N_y \times N_z$ grid points in the ocean model are sorted into the reference vertical profile, which has a vertical range over the same extent as the ocean model: $0 \le z, z^* \le H$. As a consequence, the vertical resolution of the sorted profile is $N_x \times N_y$ times finer than the N_z points resolving the profile at a particular horizontal position in the unsorted state.

On the discrete lattice, the vertical diffusive flux of the sorted density

$$F^{z^*}(z^*,t) = -\kappa_{eff}(z^*,t)\, \partial_{z^*} \rho_{ref}(z^*,t) \tag{18.16}$$

is naturally defined at the top face of the density cell whose center is at z^*. As such, the diffusion operator at the lattice point z^*, which is constructed as the convergence of the diffusive flux across a density grid cell, takes the discrete form

$$-(\partial_{z^*} F^{z^*})(z^*,t) \approx -\left(\frac{F^{z^*}(z^*,t-\Delta t) - F^{z^*}(z^*-\Delta z^*, t-\Delta t)}{\Delta z^*} \right). \tag{18.17}$$

The time lag is necessary to provide for a stable discretization of the diffusion equation. The discretization of the flux is given by

$$\begin{aligned} F^{z^*}(z^*,t) &= -\kappa_{eff}(z^*,t)\ \partial_{z^*} \rho_{ref}(z^*,t) \\ &\approx -\kappa_{eff}(z^*,t)\ \left(\frac{\rho_{ref}(z^* + \Delta^* z, t) - \rho_{ref}(z^*,t)}{\Delta z^*} \right). \end{aligned} \tag{18.18}$$

Since the flux is located at the top face of the density grid cell whose center is at the position z^*, the effective diffusivity is located at this face as well. Each of these difference operators is consistent with those used in MOM when discretizing the diffusion equation for the unsorted fluid.

As with the unsorted tendency, the time derivative in the effective diffusion equation can be approximated using a leap-frog differencing:

$$\partial_t \rho_{ref}(z^*, t) \approx \frac{\rho_{ref}(z^*, t + \Delta t) - \rho_{ref}(z^*, t - \Delta t)}{2\Delta t}. \tag{18.19}$$

Piecing these results together yields the expression for the vertical flux at the top of the density cell $z^* + \Delta z^*$

$$F^{z^*}(z^*, t - \Delta t) = F^{z^*}(z^* - \Delta z^*, t - \Delta t) - \frac{\Delta z^*}{2\Delta t}\left[\rho_{ref}(z^*, t + \Delta t) - \rho_{ref}(z^*, t - \Delta t)\right]. \tag{18.20}$$

This flux can be determined starting from the ocean bottom, where is vanishes, and working upwards. Without surface buoyancy fluxes, it also vanishes at the top of the water column, resulting in conservation of $\int dz^* \rho_{ref}(z^*, t)$. After diagnosing the flux from the tendency, the effective diffusivity can be diagnosed from

$$\kappa_{eff}(z^*, t) = -F^{z^*}(z^*, t)\left(\frac{\Delta z^*}{\rho_{ref}(z^* + \Delta z^*, t) - \rho_{ref}(^*z, t)}\right). \tag{18.21}$$

The issues of what to do when the density gradient becomes small, as in weakly stratified regions, is discussed in Sections 18.2.3 and 18.2.5.

18.2.3 Relevant vertical stratification range

In the stratified portions of the upper ocean, periods $2\pi/N$ for buoyancy oscillations are roughly 10-30 minutes, smaller in the pycnocline, and in the deep ocean periods are roughly 5-6 hours (see pages 55-56 of Pickard and Emery (1990)). The squared buoyancy frequency for the sorted reference state is given by

$$\begin{aligned} N_*^2 &= -\frac{g}{\rho_o}\frac{d\rho_{ref}}{dz^*} \\ &= -\frac{g}{1000\,\rho_o}\frac{d\sigma_{ref}}{dz^*}, \end{aligned} \tag{18.22}$$

where $\sigma_{ref} = 1000\,(\rho_{ref} - 1)$ is the sigma value for the sorted density $\rho_{ref}(g/cm^3)$. Working with σ_{ref} is desirable for accuracy reasons. The observed range in buoyancy periods provides a range over the sorted vertical profile's stratification for which a calculation of the model's effective diffusivity will be performed:

$$\frac{d\rho_{ref}}{dz^*} = -\frac{1.035 g/cm^3}{980 cm/sec^2}\frac{4\pi^2}{T^2}, \tag{18.23}$$

where $T(sec)$ is the period. With $1 \times 60 secs < T < 6 \times 60 \times 60 secs$ defining the period range, the corresponding vertical density gradient range is

$$10^{-10} g/cm^4 \le \left|\frac{d\rho_{ref}}{dz}\right| \le 10^{-5} g/cm^4, \tag{18.24}$$

and the corresponding range for the sigma gradient is

$$10^{-7} g/cm^4 \leq \left| \frac{d\sigma_{ref}}{dz} \right| \leq 10^{-2} g/cm^4. \tag{18.25}$$

18.2.4 A useful test case

When coding the effective diffusivity algorithm, it has been found useful to compare results with those from a different approach. Here, we horizontally average (i.e., homogenize) the density field along a particular depth surface. In a model with stable stratification, rigid lid, flat bottom, no-flux boundary, potential density evolution takes the form

$$\partial_t \langle \rho \rangle^{x,y} = -\partial_z \langle w \, \rho \rangle^{x,y} + \partial_z \langle \kappa \, \rho_{,z} \rangle^{x,y} \tag{18.26}$$

where κ is a vertical diffusivity and the angled-brackets indicate horizontally averaged quantities. With zero advection, evolution occurs solely via vertical diffusion. Hence, backing out an effective diffusivity for this horizontally homogenized system yields κ, regardless the horizontal/vertical stratification. It turns out that this algorithm is far simpler to implement numerically, since it does not require sorting nor interpolation to a prespecified sorted coordinate z^*. Its results are in turn more robust. Yet, importantly, they are relevant only for the case of no-advection, which is not so interesting in general yet serves as a good check for specific cases.

18.2.5 Computational precision

Models run with pure horizontal and/or vertical diffusion theoretically show $\kappa_{eff} \geq 0$ (see Winters and D'Asaro (1995) and Griffies et al. (2000b)). However, if the stratification range given by equations (18.24) or (18.25) is violated by more than roughly an order of magnitude, then spurious values of κ_{eff} tend to arise. These spurious values include unreasonably large values for κ_{eff} in regions of very low stratification, and negative values in regions of very large stratification. However, within the range given by equations (18.24) or (18.25), the computation yields reasonable values. For stratification outside this range, κ_{eff} is arbitrarily set to zero.

Another point to consider is that the stratification of ρ_{ref} shows much fine-scale step-liked structure. Computing an effective diffusivity based on such a profile will in turn show lots of noise. Averaging over the fine scales is therefore necessary to garner robust answers. That is, the spurious mixing diagnostic is smoother when having coarser vertical resolution. An objective means of averaging is to average ρ_{ref} vertically onto the same vertical grid used by the forward model in computing the unsorted density state. If this vertical stratification is itself very fine, then spurious values of κ_{eff} may still result, again due to not enough points of ρ_{ref} averaged into a single layer.

18.2.6 Negative κ_{eff}

Those advection schemes which contain dispersion, such as centered differenced advection, have leading order error terms that are not second order, but rather third order differential operators. Hence, the diagnosis of κ_{eff} for these schemes

will likely to contain a fair amount of negative values. In turn, negative κ_{eff} may be interpreted as a sign of dispersion errors, which can create or destroy water masses. Upon introducing convection into the model, much of these *undershoots* and *overshoots* created by dispersion are rapidly mixed. In turn, the resulting κ_{eff} should become positive upon introducing convection.

Another source of negative κ_{eff} apparently can arise simply due to the finite sampling time and discrete grid, even in the case of pure diffusion. For example, if there is a mixing event, and if this event is under-sampled in time, it is possible that the sorted state may have density appear in a non-local manner. Such mixing events will lead to negative κ_{eff}. The ability to realize such values for κ_{eff} motivates a sampling time Δt equal to time step used to evolve the unsorted density.

18.2.7 A comment on convection

Although the relaxation experiments allow for a focus on adiabatic physics, in a z-coordinate model there is no guarantee that an experiment will remain vertically stable, especially if running with a nonzero wind stress. If convective adjustment is then allowed, water mass mixing will occur. Hence, the experiments which focus on advection must remove convective adjustment. In turn, the presence of convection is actually quite an important element in determining the effective amount of spurious water mass mixing occuring in the model. The reason is that certain advection schemes, through dispersion errors, introduce unstable water which is then mixed-out through convection. After determining the effective diffusivity from the pure advection experiments, it is appropriate to then allow convection to occur and to compare the amount of convection appearing with the various advection discretizations.

18.2.8 The experimental design

The framework developed in this section applies most readily to an ocean model with a linear equation of state run without any buoyancy forcing. Since the model is to be run with zero buoyancy forcing, it is necessary to spin-up to some interesting state and perform various relaxation experiments. As a test of the algorithm to compute κ_{eff}, it is useful to run a set of tests with pure horizontal and vertical diffusion; no advection or convection. These experiments are necessary to establish a baseline for later comparison. After being satisfied, a set of relaxation experiments should be run with advection and/or other transport processes enabled.

18.3 An example with vertical density gradients

It is useful to present some examples which can be readily worked through by hand. These examples highlight many of the points raised in the previous discussion, and provide some guidance for interpreting the three-dimensional MOM results. Each of these examples considers the dynamics of the unsorted and sorted density fields when the unsorted field is affected by vertical and horizontal diffusion.

The first example considers the initial density field shown in Figure 18.1. There are a total of $N = N_x\, N_y\, N_z = (4 \times 1) \times 3$ grid cells in this two-dimensional example. The density field has zero baroclinicity. So the question is: How does this state,

and the corresponding sorted density state, evolve under the effects of vertical diffusion? Note the grid dimensions for the two states are related through

$$\Delta z = 4\,\Delta z^*, \tag{18.27}$$

where z is the vertical coordinate for the unsorted state, and z^* is the vertical coordinate for the sorted state. For the following, it is convenient to define this state as that at time $(t - \Delta t)$. The potential energies of the unsorted and sorted states are easily computed to be

$$\begin{aligned} E_p(t-\Delta t) &= 56\,\rho_o\,g\,\Delta z\,V & (18.28)\\ E_{ref}(t-\Delta t) &= 56\,\rho_o\,g\,\Delta z\,V & (18.29)\\ E_{APE}(t-\Delta t) &= 0 & (18.30) \end{aligned}$$

where V is the volume of the grid cells, and ρ_o is the density scale. The zero APE is due to the absence of horizontal density gradients.

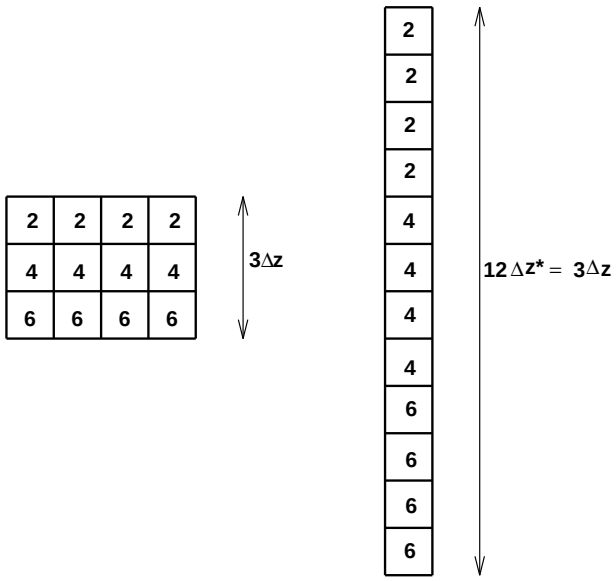

Figure 18.1: The initial density field for the first example. The number in each box represents the density, given in units of ρ_o. The left panel shows the density $\rho(x, z, t - \Delta t)$ in the unsorted fluid state, and the right panel shows the density $\rho_{ref}(z^*, t - \Delta t)$ in the sorted state. Note that the vertical scale $\Delta z^* = \Delta z/4$ for the sorted state has been expanded for purposes of display.

18.3.1 Evolution of the unsorted state

Evolution of the unsorted density is given by the discrete equation

$$\rho(x,z,t+\Delta t) = \rho(x,z,t-\Delta t) - \left(\frac{2\,\Delta t}{\Delta z}\right)\left[F^z(x,z,t-\Delta t) - F^z(x,z-\Delta z,t-\Delta t)\right], \tag{18.31}$$

where the vertical diffusive flux is given by

$$\begin{aligned} F^z(x,z,t) &= -\kappa\, \delta_z \rho(x,z,t) \\ &\approx -\kappa \left(\frac{\rho(x,z+\Delta z,t) - \rho(x,z,t)}{\Delta z} \right). \end{aligned} \tag{18.32}$$

$F^z(x,z,t)$ is defined at the top face of the density grid cell whose center has position (x,z). In the following, it is useful to introduce the dimensionless quantity

$$\delta_{(v)} = 2\,\kappa\,\Delta t/(\Delta z)^2. \tag{18.33}$$

This number arises from the chosen discretization of the diffusion equation. For linear stability of the discretization, $\delta_{(v)} < 1$ must be maintained.

The top panel of Figure 18.2 shows the vertical diffusive flux through the cell faces at time $t - \Delta t$, and the bottom panel shows the resulting density field $\rho(z,z,t+\Delta t)$. Density in the middle row does not change, whereas the upper row density increases and the lower row density decreases. The potential energy of this state is

$$E_p(t+\Delta t) = \rho_o\, g\, \Delta z\, V\, (56 + 8\,\delta_{(v)}). \tag{18.34}$$

This increase in potential energy is a result of the raised center of mass arising from the vertical diffusive fluxes.

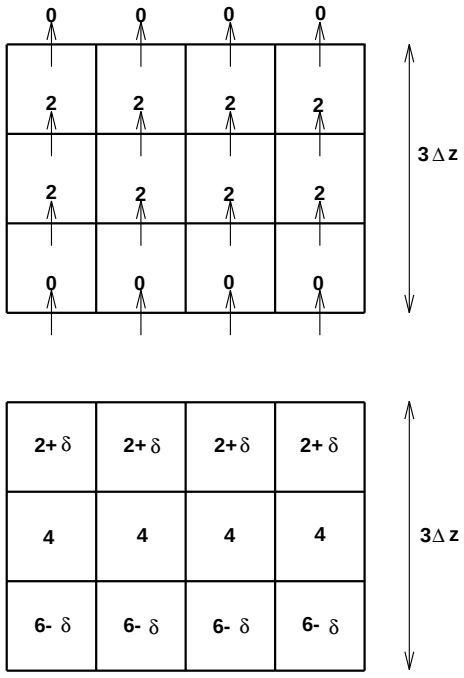

Figure 18.2: Top panel: The vertical diffusive flux $F^z(x,z,t-\Delta t)$, in units of $\rho_o\,\kappa/\Delta z$, passing through the faces of the unsorted density grid cells. Bottom panel: The unsorted density field $\rho(x,z,t+\Delta t)$, in units of ρ_o, where the dimensionless increment δ is given by $\delta = 2\delta_{(v)} = 4\,\kappa\,\Delta t/(\Delta z)^2$. This density field results from the vertical convergence of the flux $F^z(x,z,t-\Delta t)$.

18.3.2 Evolution of the sorted state

Corresponding to the evolution of the unsorted density, there is an evolution of the sorted density

$$\rho_{ref}(z^*, t+\Delta t) = \rho_{ref}(z^*, t-\Delta t) - \left(\frac{2\,\Delta t}{\Delta z^*}\right)\left[F^{z^*}(z^*, t-\Delta t) - F^{z^*}(z^*-\Delta z^*, t-\Delta t)\right]. \tag{18.35}$$

The dianeutral diffusive flux is

$$\begin{aligned} F^{z^*}(z^*, t) &= -\kappa_{eff}(z^*, t)\ \delta_{z^*}\rho_{ref}(z^*, t) \\ &\approx -\kappa_{eff}(z^*, t)\ \left(\frac{\rho_{ref}(z^*+\Delta z^*, t) - \rho_{ref}(z^*, t)}{\Delta z^*}\right), \end{aligned} \tag{18.36}$$

where $\rho_{ref}(z^*, t)$ is the sorted state's density. $F^{z^*}(z^*, t)$ is defined at the top face of the sorted density grid cell whose center has height z^*. Given the time tendency for the sorted state, the flux is diagnosed through

$$F^{z^*}(z^*, t-\Delta t) = F^{z^*}(z^*-\Delta z^*, t-\Delta t) - \left(\frac{\Delta z^*}{2\Delta t}\right)\left[\rho_{ref}(z^*, t+\Delta t) - \rho_{ref}(z^*, t-\Delta t)\right]. \tag{18.37}$$

The left panel of Figure 18.3 shows the sorted density field $\rho_{ref}(z^*, t+\Delta t)$, and the second panel shows the diagnosed vertical diffusive flux $F^{z^*}(z^*, t-\Delta t)$. The third panel shows the vertical density gradient $[\rho_{ref}(z^*+\Delta z^*, t-\Delta t) - \rho_{ref}(z^*, t-\Delta t)]/\Delta z^*$. The fourth panel shows the effective diffusivity $\kappa_{eff}(z^*, t-\Delta t)$, which is diagnosed from the relation

$$\kappa_{eff}(z^*, t-\Delta t) = -F^{z^*}(z^*, t-\Delta t)\left(\frac{\Delta z^*}{\rho_{ref}(z^*+\Delta z^*, t-\Delta t) - \rho_{ref}(z^*, t-\Delta t)}\right). \tag{18.38}$$

The units for $\kappa_{eff}(z^*, t-\Delta t)$ are $(\Delta z^*)^2/\Delta t$. Hence, a value for $\kappa_{eff}(z^*, t-\Delta t)$ of $2\,\delta$ in Figure 18.3 indicates a dimensional value of

$$\begin{aligned} \kappa_{eff}(z^*, t-\Delta t) &= 2\,\delta\,\frac{(\Delta z^*)^2}{\Delta t} \\ &= \kappa\,\frac{4\,\Delta t}{(\Delta z)^2}\,\frac{(\Delta z^*)^2}{\Delta t} \\ &= \kappa/4. \end{aligned} \tag{18.39}$$

This example illustrates a problem with unstratified parts of the sorted profile. As evident from Figures 18.1 and 18.3, the 12 sorted boxes are actually three larger homogeneous boxes, and so the calculation should compute fluxes and diffusivities for these three boxes rather than for the 12 boxes. Figure 18.4 shows such a combined system, where there are three boxes each of height Δz comprising the sorted state. Repeating the previous calculation for this configuration recovers the expected $\kappa_{eff} = \kappa$ on the two interior interfaces. Note that there is no *ad hoc* setting to zero certain values of κ_{eff} associated with unstratified portions of the profile.

As a final note, the potential energy of the sorted state at time $t+\Delta t$ is

$$E_{ref}(t+\Delta t) = \rho_o\, g\, \Delta z\, V\, (56 + 16\,\delta_{(v)}), \tag{18.40}$$

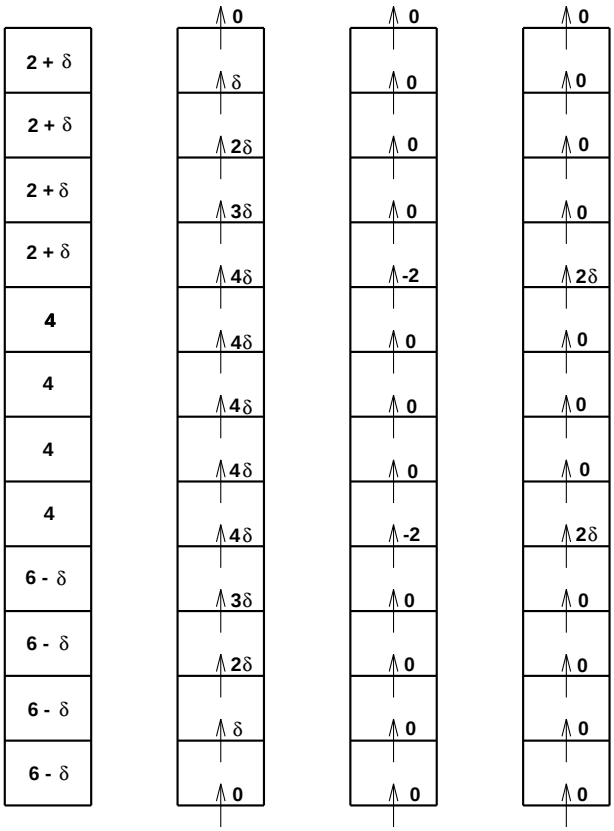

Figure 18.3: First panel (left): The sorted density field $\rho_{ref}(z^*, t + \Delta t)$, in units of ρ_o. Second panel: The vertical diffusive flux $F^{z^*}(z^*, t - \Delta t)$, in units of $\rho_o \, \Delta z^* / (2 \, \Delta t)$, passing through the faces of the sorted density grid cells. Third panel: The vertical density gradient $[\rho_{ref}(z^* + \Delta z^*, t - \Delta t) - \rho_{ref}(z^*, t - \Delta t)]/\Delta z^*$ in units of $\rho_o / \Delta z^*$. Fourth panel: The effective diffusivity $\kappa_{eff}(z^*, t - \Delta t)$ in units of $(\Delta z^*)^2 / \Delta t$.

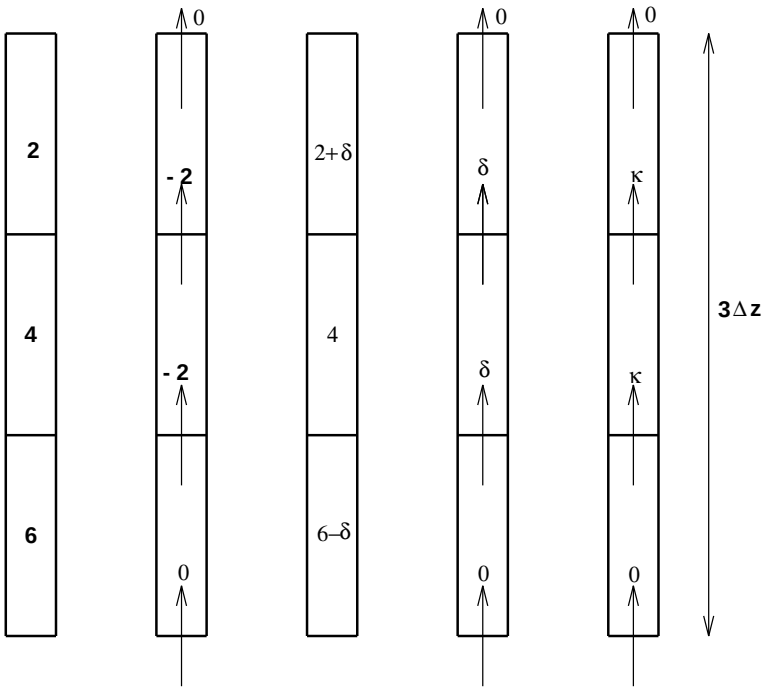

Figure 18.4: First panel (far left): The initial density field $\rho_{ref}(z^*, t - \Delta t)$, consisting of the combination of the three groups of four homogeneous cells. The values are given in units of ρ_o. In this recombined arrangement, $\Delta z^* = \Delta z$. Second panel: The vertical density gradient $[\rho_{ref}(z^* + \Delta z^*, t - \Delta t) - \rho_{ref}(z^*, t - \Delta t)]/\Delta z^*$, in units of $\rho_o/\Delta z^*$. Third panel: The density $\rho_{ref}(z^*, t + \Delta t)$ in units of ρ_o. Fourth panel: The diffusive flux $F^{z^*}(z^*, t - \Delta t)$. Fifth panel (far right): The effective diffusivity $\kappa_{eff}(z^*, t - \Delta t)$.

which is higher than the initial potential energy as a result of the raised center of mass. The APE remains unchanged

$$E_{APE}(t + \Delta t) = 0, \tag{18.41}$$

as it should since there remains zero baroclinicity in the final state.

18.3.3 Caveat about weakly stratified regions

Note that in this example, the same set of boxes are perfectly homogenized at each time step. As such, it is straightforward to combine the boxes in order to derive their effective diffusivities. In general, this simple situation will not be true, and so the effective height of the combined boxes will differ. Furthermore, most cases of homogenization are approximate (Sections 18.2.3 and 18.2.5), which introduces even more time dependence to the interfaces between effectively homogeneous boxes. In order to compute an effective diffusivity, however, our algorithm needs to evaluate all quantities at the same depth level z^*. Time dependent z^* is problematical.

The current example suggestes that one possibile way to account for homogenization is to count the number of nearly homogeneous boxes occuring in a particular section of the sorted column. When the first interface is reached that has a nontrivial stratification, then the effective diffusivity computed for this interface is multiplied by the number of trailing boxes which are homogeneous. This trick works for the example just considered ($\kappa/4 \times 4 = \kappa$). However, in the example considered in Section 18.4.2, it leads to an effective diffusivity which can be larger than the horizontal diffusivity. Such is not possible, and so one is led to reject the proposed patch. A clean way to proceed is to try to resolve as best as possible the stratification within the sorted fluid state. For those regions which are simply too weakly stratified, it must be recognized that the computed effective diffusivity might be smaller than a more refined computation.

An alternative approach is to average the sorted density field onto the discrete levels realized in the unsorted state. Indeed, this resolution of the sorted state is arguably that which is relevant for diagnosing the effective diffusivity. This is the approach taken with the MOM experiments documented in Griffies et al. (2000b).

18.4 An example with vertical and horizontal gradients

This example considers the initial unsorted density configuration is shown in Figure 18.5. There are three rows of four boxes stacked on top of one another, and there are both vertical and horizontal density gradients. Also shown is the corresponding sorted state. As with the example in Section 18.3, the grid dimensions for the two states are related through $\Delta z = 4\,\Delta z^*$, where z is the vertical coordinate for the unsorted state, and z^* is the vertical coordinate for the sorted state. The potential energies are

$$E_p(t - \Delta t) = 110\,\rho_o\,g\,\Delta z\,V \tag{18.42}$$

$$E_{ref}(t - \Delta t) = 98\,\rho_o\,g\,\Delta z\,V \tag{18.43}$$

$$E_{APE}(t - \Delta t) = 12\,\rho_o\,g\,\Delta z\,V, \tag{18.44}$$

where V is the volume of the boxes and ρ_o is the density scale.

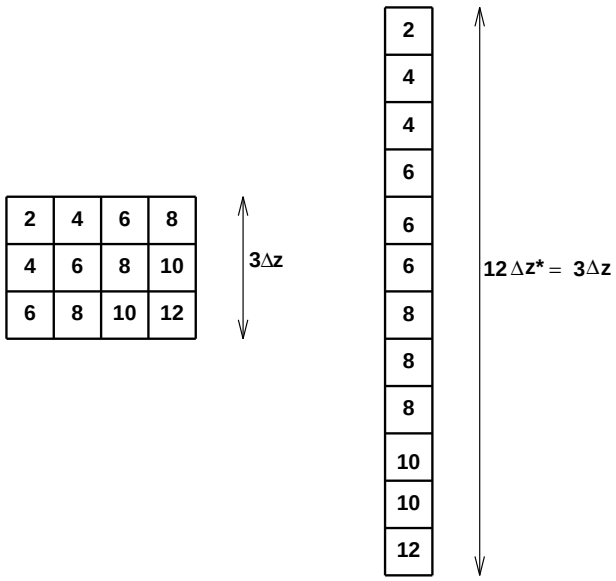

Figure 18.5: The initial density field for the horizontal and vertical diffusion examples. The number in each box represents the density, given in units of ρ_o. The left panel shows the density $\rho(x, z, t - \Delta t)$ in the unsorted fluid state, and the right panel shows the density $\rho_{ref}(z^*, t - \Delta t)$ in the sorted state. Note that the vertical scale $\Delta z^* = \Delta z/4$ for the sorted state has been expanded for purposes of display.

18.4.1 Vertical diffusion

Consider first just vertical diffusion acting on the unsorted state. The vertical diffusivity κ acting on the unsorted state is assumed to be uniform and constant.

18.4.1.1 Evolution of the unsorted state

Evolution of the unsorted density is given by the discrete equation

$$\rho(x, z, t + \Delta t) = \rho(x, z, t - \Delta t) - \left(\frac{2\,\Delta t}{\Delta z}\right)\left[F^z(x, z, t - \Delta t) - F^z(x, z - \Delta z, t - \Delta t)\right], \tag{18.45}$$

where the vertical diffusive flux is given by

$$\begin{aligned} F^z(x, z, t) &= -\kappa\, \delta_z \rho(x, z, t) \\ &\approx -\kappa \left(\frac{\rho(x, z + \Delta z, t) - \rho(x, z, t)}{\Delta z}\right). \end{aligned} \tag{18.46}$$

$F^z(x, z, t)$ is defined at the top face of the density grid cell whose center has height z. The top panel of Figure 18.6 shows the vertical diffusive flux through these faces at time $t - \Delta t$, and the bottom panel shows the resulting density field $\rho(x, z, t +$

Δt). Density in the middle row does not change, whereas the upper row density increases and the lower row density decreases. The potential energy of this state is

$$E_p(t+\Delta t) = \rho_o\, g\, \Delta z\, V\, (110 + 16\, \delta_{(v)}), \tag{18.47}$$

which is higher than the initial potential energy as a result of the raised center of mass.

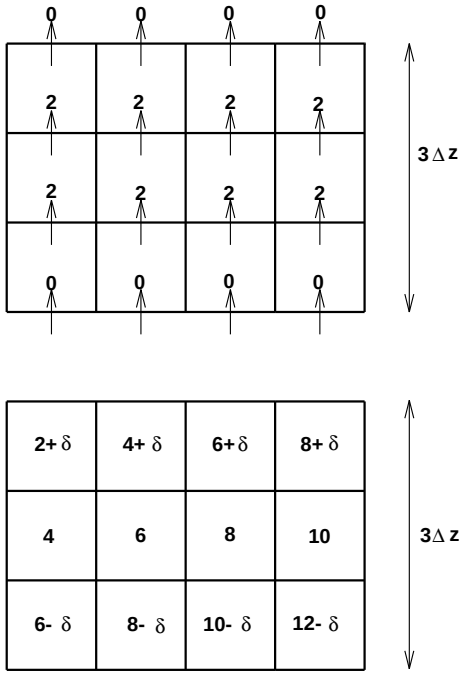

Figure 18.6: Top panel: The vertical diffusive flux $F^z(x,z,t-\Delta t)$, in units of $\rho_o\,\kappa/\Delta z$, passing through the faces of the unsorted density grid cells. Bottom panel: The unsorted density field $\rho(x,z,t+\Delta t)$, in units of ρ_o, where $\delta = 2\,\delta_{(v)} = 4\,\kappa\,\Delta t/(\Delta z)^2$. This is the density field resulting from the vertical convergence of the flux $F^z(x,z,t-\Delta t)$. The potential energy of this field is $E_p(t+\Delta t) = \rho_o\, g\, \Delta z\, V\, (110 + 16\delta_{(v)})$.

18.4.1.2 Evolution of the sorted state

Corresponding to the evolution of the unsorted density, there is an evolution of the sorted density which is given by

$$\rho_{ref}(z^*, t+\Delta t) = \rho_{ref}(z^*, t-\Delta t) - \left(\frac{2\,\Delta t}{\Delta z^*}\right)\left[F^{z^*}(z^*, t-\Delta t) - F^{z^*}(z^*-\Delta z, t-\Delta t)\right]. \tag{18.48}$$

The dianeutral diffusive flux is given by

$$\begin{aligned} F^{z^*}(z^*,t) &= -\kappa_{eff}(z^*,t)\ \delta_{z^*}\rho_{ref}(z^*,t) \\ &\approx -\kappa_{eff}(z^*,t)\ \left(\frac{\rho_{ref}(z^*+\Delta z^*,t) - \rho_{ref}(z^*,t)}{\Delta z^*}\right), \end{aligned} \tag{18.49}$$

where $\rho_{ref}(z^*, t)$ is the sorted state's density. $F^{z^*}(z^*, t)$ is defined at the top face of the sorted density grid cell whose center has height z^*. Given the time tendency for the sorted state, the flux is diagnosed through

$$F^{z^*}(z^*, t-\Delta t) = F^{z^*}(z^*-\Delta z^*, t-\Delta t) - \left(\frac{\Delta z^*}{2\Delta t}\right)[\rho_{ref}(z^*, t+\Delta t) - \rho_{ref}(z^*, t-\Delta t)]. \tag{18.50}$$

The left panel of Figure 18.7 shows the sorted density field $\rho_{ref}(z^*, t+\Delta t)$, and the second panel shows the diagnosed vertical diffusive flux $F^{z^*}(z^*, t-\Delta t)$. The third panel shows the vertical density gradient $[\rho_{ref}(z^*+\Delta z^*, t-\Delta t) - \rho_{ref}(z^*, t-\Delta t)]/\Delta z^*$. Note the regions of zero stratification. The fourth panel shows the effective diffusivity $\kappa_{eff}(z^*, t-\Delta t)$, which is diagnosed from the relation

$$\kappa_{eff}(z^*, t-\Delta t) = -F^{z^*}(z^*, t-\Delta t)\left(\frac{\Delta z^*}{\rho_{ref}(z^*+\Delta z^*, t-\Delta t) - \rho_{ref}(z^*, t-\Delta t)}\right). \tag{18.51}$$

The units for $\kappa_{eff}(z^*, t-\Delta t)$ are $(\Delta z^*)^2/\Delta t$. In addition, consistent with the discussion in Section 18.3.2, the effective diffusivity for the interfaces on top of unstratified water are multiplied by the number of unstratified boxes. A value for $\kappa_{eff}(z^*, t-\Delta t)$ of δ in Figure 18.7 indicates a dimensional value of

$$\begin{aligned}\kappa_{eff}(z^*, t-\Delta t) &= \delta\,\frac{(\Delta z^*)^2}{\Delta t} \\ &= \kappa\,\frac{4\,\Delta t}{(\Delta z)^2}\,\frac{(\Delta z^*)^2}{\Delta t} \\ &= \kappa/4. \end{aligned} \tag{18.52}$$

As a final note, the potential energy of the sorted state at time $t+\Delta t$ is

$$E_{ref}(t+\Delta t) = \rho_o\, g\, \Delta z\, V\, (98 + 7\,\delta_{(v)}), \tag{18.53}$$

which is higher than the initial potential energy as a result of the raised center of mass. The APE is therefore given by

$$E_{APE}(t+\Delta t) = \rho_o\, g\, \Delta z\, V\, (12 + 11\,\delta_{(v)}), \tag{18.54}$$

which is larger than $E_{APE}(t-\Delta t)$ given in equation (18.44).

18.4.2 Horizontal diffusion

Consider now just horizontal diffusion acting on the unsorted state. The horizontal diffusivity A acting on the unsorted state is assumed to be uniform and constant.

18.4.2.1 Evolution of the unsorted state

Evolution of the unsorted density is given by the discrete equation

$$\rho(x, z, t+\Delta t) = \rho(x, z, t-\Delta t) - \left(\frac{2\,\Delta t}{\Delta x}\right)[F^x(x, z, t-\Delta t) - F^x(x-\Delta x, z, t-\Delta t)], \tag{18.55}$$

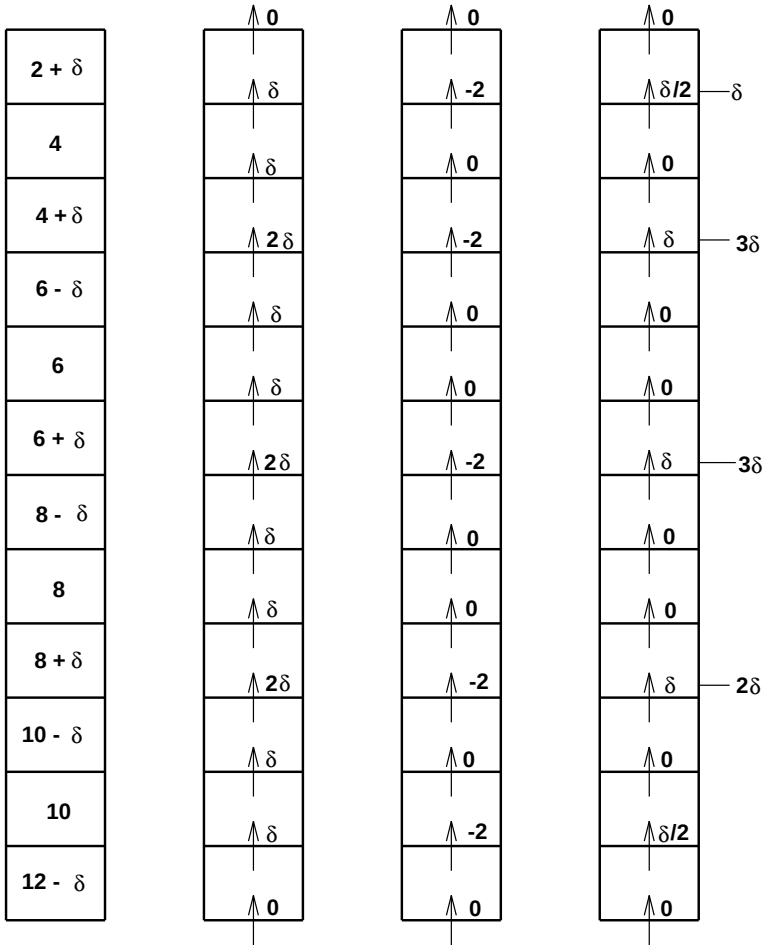

Figure 18.7: Left panel: The sorted density field $\rho_{ref}(z^*, t + \Delta t)$, in units of ρ_o. Second panel: The vertical diffusive flux $F^{z^*}(z^*, t - \Delta t)$, in units of $\rho_o \, \Delta z^* / \Delta t$, passing through the faces of the sorted density grid cells. Third panel: The vertical density gradient $[\rho_{ref}(z^* + \Delta z^*, t - \Delta t) - \rho_{ref}(z^*, t - \Delta t)]/\Delta z^*$ in units of $\rho_o / \Delta z^*$. Fourth panel: The effective diffusivity $\kappa_{eff}(z^*, t - \Delta t)$ in units of $(\Delta z^*)^2 / \Delta t$. The four κ_{eff} values which are on top of unstratified portions of the $\rho_{ref}(z^*, t - \Delta t)$ profile have been multiplied by the number of unstratified boxes which lie directly beneath it.

where the horizontal diffusive flux is given by

$$\begin{aligned} F^x(x,z,t) &= -A\ \delta_x \rho(x,z,t) \\ &\approx -A\ \left(\frac{\rho(x+\Delta x,z,t) - \rho(x,z,t)}{\Delta x} \right). \end{aligned} \tag{18.56}$$

$F^x(x,z,t)$ is defined at the east face of the density grid cell whose center has position (x,z). The top panel of Figure 18.8 shows the horizontal diffusive flux through these faces at time $t-\Delta t$, and the bottom panel shows the resulting density field $\rho(x,z,t+\Delta t)$. The potential energy of this state is the same as the initial potential energy, since the horizontal fluxes are parallel to the geopotential

$$E_p(t+\Delta t) = E_p(t-\Delta t) = 110\,\rho_o\,g\,\Delta z\,V. \tag{18.57}$$

18.4.2.2 Evolution of the sorted state

Corresponding to the evolution of the unsorted density, there is an evolution of the sorted density which is given by

$$\rho_{ref}(z^*,t+\Delta t) = \rho_{ref}(z^*,t-\Delta t) - \left(\frac{2\,\Delta t}{\Delta z^*} \right) [F^{z^*}(z^*,t-\Delta t) - F^{z^*}(z^*-\Delta z,t-\Delta t)]. \tag{18.58}$$

The dianeutral diffusive flux is given by

$$\begin{aligned} F^{z^*}(z^*,t) &= -\kappa_{eff}(z^*,t)\ \delta_{z^*}\rho_{ref}(z^*,t) \\ &\approx -\kappa_{eff}(z^*,t)\ \left(\frac{\rho_{ref}(z^*+\Delta z^*,t) - \rho_{ref}(z^*,t)}{\Delta z^*} \right), \end{aligned} \tag{18.59}$$

where $\rho_{ref}(z^*,t)$ is the sorted state's density. $F^{z^*}(z^*,t)$ is defined at the top face of the sorted density grid cell whose center has height z^*. Given the time tendency for the sorted state, the flux is diagnosed through

$$F^{z^*}(z^*,t-\Delta t) = F^{z^*}(z^*-\Delta z^*,t-\Delta t) - \left(\frac{\Delta z^*}{2\Delta t} \right) [\rho_{ref}(z^*,t+\Delta t) - \rho_{ref}(z^*,t-\Delta t)]. \tag{18.60}$$

The left panel of Figure 18.4.2.2 shows the sorted density field $\rho_{ref}(z^*,t+\Delta t)$, and the second panel shows the diagnosed vertical diffusive flux $F^{z^*}(z^*,t-\Delta t)$. The third panel shows the vertical density gradient $[\rho_{ref}(z^*+\Delta z^*,t-\Delta t) - \rho_{ref}(z^*,t-\Delta t)]/\Delta z^*$. Note the regions of zero stratification. The fourth panel shows the effective diffusivity $\kappa_{eff}(z^*,t-\Delta t)$, which is diagnosed from the relation

$$\kappa_{eff}(z^*,t-\Delta t) = -F^{z^*}(z^*,t-\Delta t) \left(\frac{\Delta z^*}{\rho_{ref}(z^*+\Delta z^*,t-\Delta t) - \rho_{ref}(z^*,t-\Delta t)} \right). \tag{18.61}$$

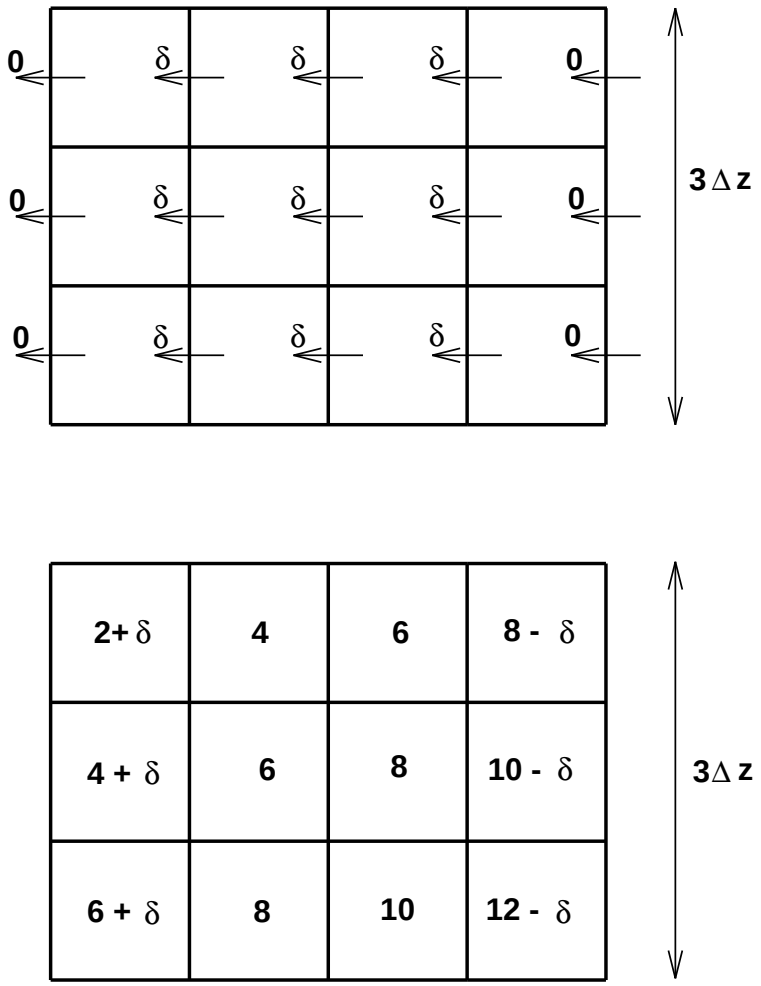

Figure 18.8: Top panel: The horizontal diffusive flux $F^x(x, z, t - \Delta t)$, in units of $\rho_o\, A/\Delta x$, passing through the faces of the unsorted density grid cells. Bottom panel: The unsorted density field $\rho(x, z, t + \Delta t)$, in units of ρ_o, where $\delta = 2\,\delta_{(h)} = 4\,A\,\Delta t/(\Delta x)^2$. This is the density field resulting from the vertical convergence of the flux $F^x(x, z, t - \Delta t)$. The potential energy of this field is $E_p(t + \Delta t) = 110\,\rho_o\, g\, \Delta z\, V$.

The units for $\kappa_{eff}(z^*, t-\Delta t)$ are $(\Delta z^*)^2/\Delta t$. For example, a value for $\kappa_{eff}(z^*, t-\Delta t)$ of $3\delta/2$ in Figure 18.4.2.2 indicates a dimensional value of

$$\begin{aligned} \kappa_{eff}(z^*, t-\Delta t) &= (3\,\delta/2)\,\frac{(\Delta z^*)^2}{\Delta t} \\ &= 6\,A\,\frac{\Delta t}{(\Delta x)^2}\,\frac{(\Delta z^*)^2}{\Delta t} \\ &= 6\,A\,\left(\frac{\Delta z^*}{\Delta x}\right)^2. \end{aligned} \tag{18.62}$$

For the special case of $\Delta x = \Delta z = 4\Delta z^*$, the effective diffusivity is $3A/8$. Note that if the patch proposed in Section 18.3.3 is used, then the $3\delta/2$ diffusivity would become $9\delta/2$, leading to the possibility for an effective diffusivity of $9\,A/8$, which is impossible.

As a final note, the potential energy of the sorted state at time $t+\Delta t$ is

$$E_{ref}(t+\Delta t) = \rho_o\, g\, \Delta z\, V\, (98 + 19\,\delta_{(h)}/2), \tag{18.63}$$

which is higher than the initial potential energy as a result of the raised center of mass. The APE is given by

$$E_{APE}(t+\Delta t) = \rho_o\, g\, \Delta z\, V\, (12 - 19\,\delta_{(h)}/2), \tag{18.64}$$

which is smaller than $E_{APE}(t-\Delta t)$ given in equation (18.44).

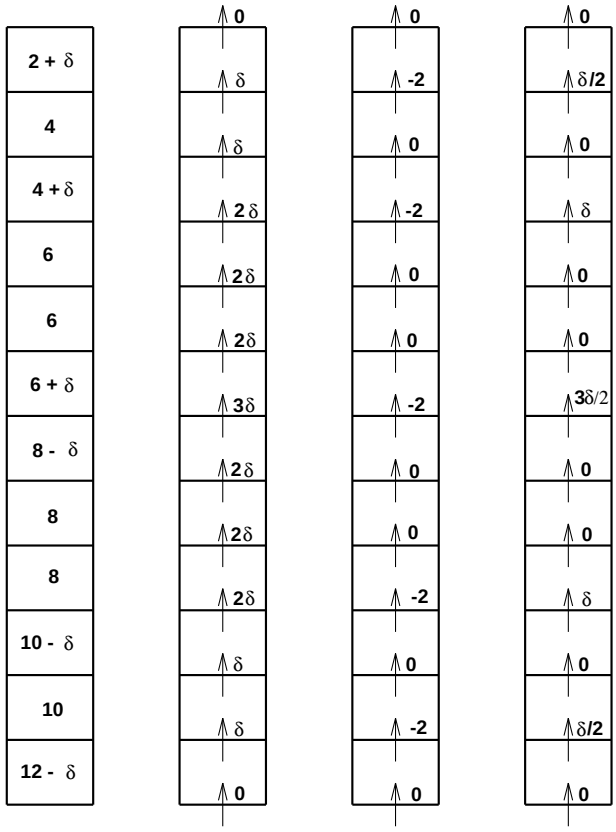

Figure 18.9: First panel (far left): The sorted density field $\rho_{ref}(z^*, t + \Delta t)$ in units of ρ_o. Second panel: The vertical diffusive flux $F^{z^*}(z^*, t - \Delta t)$, in units of $\rho_o \, \Delta z^* / \Delta t$, passing through the faces of the sorted density grid cells. Third panel: The vertical density gradient $[\rho_{ref}(z^* + \Delta z^*, t - \Delta t) - \rho_{ref}(z^*, t - \Delta t)]/\Delta z^*$ in units of $\rho_o / \Delta z^*$. Fourth panel: The effective diffusivity $\kappa_{eff}(z^*, t - \Delta t)$ in units of $(\Delta z^*)^2 / \Delta t$. The four κ_{eff} values which are on top of unstratified portions of the $\rho_{ref}(z^*, t - \Delta t)$ profile have been multiplied by the number of unstratified boxes which lie directly beneath it.

CHAPTER

NINETEEN

Age tracers

Contents

Age tracers are perhaps the simplest nontrivial passive tracers commonly used in ocean modeling. They provide the modeler with a visual means to deduce the time that a water parcel has spent circulating after having been in contact with a certain part of the domain. The purpose of this chapter is to present the basics for how mom4 computes age tracers.

19.1 Fundamental considerations

Fluid parcels generally contain material constituents that are transported as the parcel moves through the ocean. These constituents are commonly termed *tracers* since they are useful for *tracing* pathways of fluid transport.

Material tracers have a total mass within a fluid parcel written

$$\mathrm{d}M_C = (\mathrm{d}M)\, C = (\rho\, \mathrm{d}V)\, C, \tag{19.1}$$

where $\mathrm{d}M = \rho\, \mathrm{d}V$ is the total mass of the parcel of seawater, and $C = \mathrm{d}M_C/\mathrm{d}M$ is the mass of tracer per mass of seawater. C is often termed the *tracer concentration* or *tracer mass fraction*. Notably, since the seawater mass and tracer mass are both scalar quantities, the tracer concentration is likewise a scalar field. Hence, tracers are often called *scalars* in the fluid dynamics literature. Additionally, when the tracer concentration C is uniform throughout the ocean, the budget for tracer mass reduces to the budget for seawater mass. This observation, which follows from the definition of C, provides an important compatibility constraint between mass and tracer budgets that should be maintained in numerical simulations. Otherwise, spurious source/sinks can cause tracer or mass to form in unphysical manners.

Conserving tracer mass within a parcel of seawater leads to the conservation statement

$$\begin{aligned} \frac{\mathrm{d}\left[(\rho\,\mathrm{d}V)\,C\right]}{\mathrm{d}t} &= (\rho\,\mathrm{d}V)\,\frac{\mathrm{d}C}{\mathrm{d}t} \\ &= 0, \end{aligned} \tag{19.2}$$

where we used mass conservation $\mathrm{d}(\rho\,\mathrm{d}V)/\mathrm{d}t = 0$. Combining the Eulerian form of material tracer conservation $\mathrm{d}C/\mathrm{d}t = (\partial_t + \mathbf{v}\cdot\nabla)\,C = 0$ with mass conservation $\rho_{,t} + \nabla\cdot(\rho\,\mathbf{v}) = 0$ leads to the Eulerian conservation law for tracer mass per volume $\rho\,C$ within in a seawater parcel

$$(\rho\,C)_{,t} + \nabla\cdot(\rho\,C\,\mathbf{v}) = 0. \tag{19.3}$$

Additional terms appear on the right hand side when sources or sinks of tracer are found within the fluid or at the boundaries.

For purposes of establishing the momentum and tracer budgets, the mass of a Boussinesq seawater parcel is given by $\mathrm{d}M = \rho_o\,\mathrm{d}V$. Material conservation of tracer mass $(\rho_o\,\mathrm{d}V)\,C$ still leads to material conservation of tracer concentration: $\mathrm{d}C/\mathrm{d}t = 0$, since now the parcel's volume is conserved. Combining material conservation of tracer concentration with parcel volume conservation, $\nabla\cdot\mathbf{v} = 0$, leads to the Eulerian conservation law

$$C_{,t} + \nabla\cdot(\mathbf{v}\,C) = 0. \tag{19.4}$$

There are two main ways that the mass of tracer within a seawater parcel can change. First, there can be tracer-dependent sources or sinks of tracer mass $\rho\,\mathcal{S}^{(C)}$ within the fluid domain or at the boundaries. Second, there can be irreversible molecular or turbulent mixing effects that move tracer mass between parcels. Many of these mixing effects can be mathematically represented by the convergence of a density weighted tracer flux $\rho\,\mathbf{F}$. Hence, for a non-Boussinesq fluid, the time tendency for density weighted tracer concentration is written

$$(\rho\,C)_{,t} = -\nabla\cdot(\rho\,C\,\mathbf{v} + \rho\,\mathbf{F}) + \rho\,\mathcal{S}^{(C)}, \tag{19.5}$$

whereas for a Boussinesq fluid it is

$$C_{,t} = -\nabla\cdot(C\,\mathbf{v} + \mathbf{F}) + \mathcal{S}^{(C)}. \tag{19.6}$$

19.2 Age tracers

As discussed in many places, such as Thiele and Sarmiento (1990) and England (1995), age tracers are defined by the source term $\mathcal{S}^{(C)}$ appearing in equations (19.5) and (19.6), as well as the initial and boundary conditions. The source is set to unity everywhere within the ocean fluid

$$\mathcal{S}^{(C)} = 1. \tag{19.7}$$

This prescription specifies that the age field C has units of time. Hence, the age tracer is somewhat distinct from the material tracers discussed in Section 19.1,

where C for material tracers is a dimensionless field (such as salinity). At a region of interest, say the ocean surface, the boundary condition for the age tracer is zero. In mom4, one defines various age tracers that differ by the region that their boundary condition is set to zero. For all of the age tracers, the age is set to zero at the initial time of the experiment.

Given these prescriptions, C measures the age, in units of time, that a water parcel has spent away from the region where it was set to zero. Therefore, visual maps of C are useful to deduce such physically interesting properties as ventilation times.

Part VII

Miscellaneous Topics

MISCELLANEOUS TOPICS

This part of the MOM4 Guide contains discussions of various topics that do not cleanly fall into other parts.

CHAPTER

TWENTY

Equation of state considerations

Contents

The purpose of this chapter is to present certain issues related to the equation of state used to compute density and its partial derivatives.

20.1 Introduction

Density is needed to compute the hydrostatic pressure. Additionally, it determines the static stability of a vertical fluid column. Finally, its derivatives with respect to potential temperature and salinity

$$\rho_{,\theta} = \left(\frac{\partial \rho}{\partial \theta}\right)_{p,s} \tag{20.1}$$

$$\rho_{,s} = \left(\frac{\partial \rho}{\partial s}\right)_{p,\theta} \tag{20.2}$$

set the neutral directions used for sub-grid-scale tracer transport. Therefore, it is important that the equation of state be accurate over the range of temperature, salinity, and pressure values occurring in ocean simulations.

In early versions of MOM, density was computed according to the Bryan and Cox (1972) cubic polynomial approximation to the UNESCO equation of state (Gill (1982)). That approach was quite useful for certain problems. Unfortunately, it has limitations that are no longer acceptable for global climate modeling. First, the polynomials are fit at discrete depth levels. The use of partial cells makes this approach cumbersome since with partial cells it is necessary to generally compute density at arbitrary depths. Second, the cubic approximation is inaccurate for many

regimes of ocean climate modeling, such as wide ranges in salinity associated with rivers and sea ice. For these two reasons, a more accurate method is desired.

Two equations of state (EOS) are currently available in MOM4 for computing density. The first is a linear equation of state whereby density is a linear function only of potential temperature. This EOS is relevant only for idealized simulations with the Boussinesq approximation. The second EOS is that proposed by McDougall et al. (2003). As they argue, their EOS is more accurate than the UNESCO EOS due to the use of more accurate empirical data as reported in Feistel (1993) and Feistel and Hagen (1995). Even given its high degree of accuracy, this EOS has been found to be quite efficient.

20.2 Comments on highly accurate equations of state

Although there are portions of ocean climate models that are computed less accurately than density resulting from the McDougall et al. (2003) equation of state, there is little reason to compromise the integrity of the density calculation to remain equitable with the less accurate algorithms. In particular, there are three main reasons favoring the use of accurate EOS formulations.

- Many important details of deep water transformations, thermal wind computations, and tracer transport depend on an accurate EOS. Furthermore, realistic ocean climate models with increasing resolutions are put into regimes where temperature, salinity, and pressures vary over broad ranges. Hence, it is important to employ an EOS that can span this range without compromising the integrity of the computed density or density partial derivatives.

- The McDougall et al. (2003) EOS is very efficient, so its cost is much less than earlier experiences coding the UNESCO form taken from Gill (1982) or Jackett and McDougall (1995).

- Use of a realistic EOS in a z-coordinate model comes without the price of complex algorithms, in contrast to the situation with isopycnal models. Hence, it makes sense to provide z-models with the capability of computing highly accurate equilibrium thermodynamic properties.

20.3 Linear equation of state

The linear equation of state in MOM4 assumes that density is a linear function of potential temperature. There is no salinity nor pressure dependence. The form used is

$$\rho(\mathbf{x}, t) = \rho_0 - \tilde{\alpha}\,\theta(\mathbf{x}, t) \tag{20.3}$$

with

$$\tilde{\alpha} = 0.255\,\mathrm{kg/m^3/^\circ K} \tag{20.4}$$

$$\rho_0 = 1035\,\mathrm{kg/m^3}. \tag{20.5}$$

Hence, the density partial derivatives are given by

$$\rho_{,\theta} = -\tilde{\alpha} \tag{20.6}$$
$$\rho_{,s} = 0. \tag{20.7}$$

Due to the absence of pressure effects, this density is most correctly thought of as a potential density. Hence, without compressibility, its use for computing pressure is self-consistent only when employing the Boussinesq approximation.

20.4 McDougall, Jackett, Wright, and Feistel's EOS

Feistel (1993) and Feistel and Hagen (1995) studied the equilibrium thermodynamics of seawater and produced a more accurate EOS than UNESCO by using more recent empirical data. McDougall et al. (2003) produced a fit to Feistel and Hagen to render an expression convenient for use in ocean models. Their EOS is highly recommended for purposes of realistic ocean climate simulations, where accuracy over a wide range temperature, salinity, and pressure is crucial. The following equation has been fit over the range

$$0\text{psu} \leq s \leq 40\text{psu} \tag{20.8}$$
$$-3^\circ\text{C} \leq \theta \leq 40^\circ\text{C} \tag{20.9}$$
$$0\text{db} \leq p \leq 8000\text{db}. \tag{20.10}$$

The EOS has 25 terms. Its general form is motivated by that of Wright (1997). Appendix B to McDougall et al. (2003) provides the following equation for *in situ* density ρ written in terms of pressure, salinity, and potential temperature

$$\rho(s, \theta, p) = \frac{P_1(s, \theta, p)}{P_2(s, \theta, p)}, \tag{20.11}$$

where p is the local pressure in units of decibars, θ is the potential temperature referenced to zero pressure in units of *Celsius*, and s is salinity in *psu*. Note the conversion between mks pressure and decibars is given by

$$10^{-4}\,\text{db} = 1\,\text{Pa}. \tag{20.12}$$

A check value for this equation is $\rho = 1033.213387\,\text{kg.m}^{-3}$ with $s = 35$psu, $\theta = 20^\circ C$, and $p = 2000\text{db} = 2 \times 10^7\text{Pa}$. The polynomial functions P_1 and P_2 are given by

$$\begin{aligned} P_1 &= a_o + a_1\,\theta + a_2\,\theta^2 + a_3\,\theta^3 + a_4\,s + a_5\,s\,\theta + a_6\,s^2 \\ &\quad + a_7\,p + a_8\,p\,\theta^2 + a_9 p\,s + a_{10}\,p^2 + a_{11}\,p^2\,\theta^2 \end{aligned} \tag{20.13}$$

$$\begin{aligned} P_2 &= b_o + b_1\,\theta + b_2\,\theta^2 + b_3\,\theta^3 + b_4\,\theta^4 + b_5\,s + b_6\,s\,\theta + b_7\,s\,\theta^3 + b_8\,s^{3/2} + b_9\,s^{3/2}\,\theta^2 \\ &\quad + b_{10}\,p + b_{11}\,p^2\,\theta^3 + b_{12}\,p^3\,\theta. \end{aligned} \tag{20.14}$$

The coefficients a_n and b_n are tabulated in Appendix B of McDougall et al. (2003). Rearrangement in order to reduce multiplications leads to

$$P_1 = a_o + \theta\,(a_1 + \theta\,(a_2 + a_3\,\theta)) + s\,(a_4 + a_5\,\theta + a_6\,s) + p\,(a_7 + a_8\,\theta^2 + a_9\,s + p\,(a_{10} + a_{11}\,\theta^2)) \tag{20.15}$$

$$P_2 = b_o + \theta\,(b_1 + \theta\,(b_2 + \theta\,(b_3 + \theta\,b_4))) + s\,(b_5 + \theta\,(b_6 + b_7\,\theta^2) + s^{1/2}\,(b_8 + b_9\,\theta^2)) + p\,(b_{10} + p\,\theta\,(b_{11}\,\theta^2 + b_{12}\,p)). \tag{20.16}$$

The density partial derivatives are

$$\left(\frac{\partial\rho}{\partial\theta}\right)_{s,p} = \rho\left(\frac{1}{P_1}\left(\frac{\partial P_1}{\partial\theta}\right)_{s,p} - \frac{1}{P_2}\left(\frac{\partial P_2}{\partial\theta}\right)_{s,p}\right) \tag{20.17}$$

$$\left(\frac{\partial\rho}{\partial s}\right)_{\theta,p} = \rho\left(\frac{1}{P_1}\left(\frac{\partial P_1}{\partial s}\right)_{\theta,p} - \frac{1}{P_2}\left(\frac{\partial P_2}{\partial s}\right)_{\theta,p}\right). \tag{20.18}$$

Since divisions are computationally more expensive than multiplications, we find it useful to rearrange these results to

$$\left(\frac{\partial\rho}{\partial\theta}\right)_{s,p} = (P_2)^{-1}\left[\left(\frac{\partial P_1}{\partial\theta}\right)_{s,p} - \rho\left(\frac{\partial P_2}{\partial\theta}\right)_{s,p}\right] \tag{20.19}$$

$$\left(\frac{\partial\rho}{\partial s}\right)_{\theta,p} = (P_2)^{-1}\left[\left(\frac{\partial P_1}{\partial s}\right)_{\theta,p} - \rho\left(\frac{\partial P_2}{\partial s}\right)_{\theta,p}\right] \tag{20.20}$$

where $(P_2)^{-1}$ can be saved in a temporary array, thus reducing the number of divisions from four to one.[1] The partial derivatives are given by

$$\left(\frac{\partial P_1}{\partial\theta}\right)_{s,p} = a_1 + 2\,a_2\,\theta + 3\,a_3\,\theta^2 + a_5\,s + 2\,a_8\,p\,\theta + 2\,a_{11}\,p^2\,\theta \tag{20.21}$$

$$\left(\frac{\partial P_1}{\partial s}\right)_{\theta,p} = a_4 + a_5\,\theta + 2\,a_6\,s + a_9\,p \tag{20.22}$$

$$\left(\frac{\partial P_2}{\partial\theta}\right)_{s,p} = b_1 + 2\,b_2\,\theta + 3\,b_3\,\theta^2 + 4\,b_4\,\theta^3 + b_6\,s + 3\,b_7\,s\,\theta^2 + 2\,b_9\,s^{3/2}\,\theta + 3\,b_{11}\,p^2\,\theta^2 + b_{12}\,p^3 \tag{20.23}$$

$$\left(\frac{\partial P_2}{\partial s}\right)_{\theta,p} = b_5 + b_6\,\theta + b_7\,\theta^3 + (3/2)\,b_8\,s^{1/2} + (3/2)\,b_9\,s^{1/2}\,\theta^2 \tag{20.24}$$

[1] We thank Trevor McDougall for pointing out this simplification.

with rearrangement leading to

$$\left(\frac{\partial P_1}{\partial \theta}\right)_{s,p} = a_1 + \theta\,(2\,a_2 + 3\,a_3\,\theta) + a_5\,s + 2\,p\,\theta\,(a_8 + a_{11}\,p) \tag{20.25}$$

$$\left(\frac{\partial P_1}{\partial s}\right)_{\theta,p} = a_4 + a_5\,\theta + 2\,a_6\,s + a_9\,p \tag{20.26}$$

$$\left(\frac{\partial P_2}{\partial \theta}\right)_{s,p} = b_1 + \theta\,(2\,b_2 + \theta\,(3\,b_3 + 4\,b_4\,\theta)) + s\,(b_6 + \theta\,(3\,b_7\,\theta + 2\,b_9\,s^{1/2})) \tag{20.27}$$
$$+ p^2\,(3\,b_{11}\,\theta^2 + b_{12}\,p)$$

$$\left(\frac{\partial P_2}{\partial s}\right)_{\theta,p} = b_5 + \theta\,(b_6 + b_7\,\theta^2) + (3/2)\,s^{1/2}\,(b_8 + b_9\,\theta^2). \tag{20.28}$$

CHAPTER

TWENTYONE

Open boundary conditions

Contents

The purpose of this chapter is to present the method used in mom4 for prescribing open boundary conditions. This chapter was written by Martin Schmidt (martin.schmidt@io-warnemuende.de) and it is under revision.

21.1 Introduction

Numerical circulation models of marginal seas with biological, chemical and sediment dynamic components require a high model resolution and involve a large number of variables. Hence, a regional model is the only realistic implementation

with a reasonable amount of computer resource consumption. In most cases the exchange of mass, heat, momentum and dissolved or suspended matter with the outer ocean is important. In this case at the model boundary an open boundary condition (OBC) must apply, which permits flux out of - and into the model area.

The formulation of boundary condition at the boundary of the model domain reveals as a complex problem. For an ocean, which is for example subdivided into a western and an eastern subbasin by a virtual boundary the information on events in the eastern part, which are forcing some flow, i.e. by wind or fresh water flux, is spread from the eastern part to the west by waves propagating with a wave speed c. It reflects causality that it needs some time $t = \frac{s}{c}$, where s is the distance to the source of the wave, until a signal from the remote event can be detected at a fixed point in the western model part. Such waves spreading through the virtual boundary can be described solely from the dynamics of the eastern model part.

The assumption, that the ocean dynamics at the model boundary is mainly influenced by the model interiour may be a desirable model property but is valid in special cases only. In the general case of realistic model applications signals from outside the model domain have a strong influence. Hence, some boundary values of the quantities of interest must be prescribed. Usually, little is known about processes outside the model domain and rough approximations for the boundary values must be used. However, even if sufficient boundary values are available, the prescribed data could be inconsistent with the interiour model dynamics.

Hence, motion at the model boundary is governed by internal processes which are known from the model integration and be external processes, which are only partly known. The problem is, that the model equations can not separate incoming and outgoing waves at the boundary. Hence, prescribed quantities disturb outgoing waves and may lead to unphysical wave reflections at the boundary. On the other hand, neglection of incoming waves may disregard important processes within the model domain driven or triggered from outside. Consequently, the numerical scheme at the open boudary is a compromise. For processes in the model domain, the boundary should be "passive", i.e., waves from the model interior must leave the model domain without distortion. For processes outside the model domain which are important for the model dynamics, the boundary must be "active", the model dynamics must get information on processes outside of the model domain. This is not an "either-or " the open boundary must behave as "passive" and "active" at the same time.

It is easy to find examples for open boundaries which are "passive" and "active" at the same time. Consider a semi-enclosed or marginal sea where the model domain ends at a narrow or shallow connection to the open ocean. If wind forcing over the model domain drives water into the model area, Kelvin waves propagate towards the boundary switching on inflow there. In this case the boundary must be "passive" and these waves should leave the model domain without reflection. At the same time the boundary must be "active" for heat- or saltflux, since information on the properties of the inflowing water is needed.

To maintain this principle contradiction, a different boundary condition must be applied for both the flow contributions driven inside and from outside the model domain. This requires that both the flow components in the boundary region must be separated. This is done by means of a Sommerfeld radiation condition.

As such, the boundary condition is not the implementation of exact physical

laws but requires many assumptions and approximations. Differently from the other model components it should be considered as an engineering tool, which must be tuned to find a reasonable compromise for the special model purposes.

The implementation of OBC ihas been subject of many papers and technical reports. The implementation depends strongly on the model grid, the present scheme is for the Arakaw B-grid and follows in general the approach of Stevens (1991). It has been tested successfully in the FRAM model (Stevens, 1991) and in the *community modeling effort (CME)* , (e.g., Döscher and Redler, 1995). They have also been used in a GFDL-model of the North Atlantic in the framework of *MAST2-DYNAMO* (Dynamo, 1994) as well as in a regional model of the subpolar North Atlantic (Redler and Böning, 1996). These experiments were based on Redlers implementation of OBC in MOM-1.

ROMS others ...

For the explicit free surface code used in MOM-3 the implementation of open boundary conditions was modified. Especially the calculation of the phase speed of barotropic waves must be refined. The modifications of the free surface open boundary conditions in MOM-3 are based on the experience with the methods developed by A. Mutzke (Mutzke, 1996) for a circulation model of the Baltic Sea (Seifert, Schmidt, Fennel, 1999). driven by 3 hourly gauges in the Skagerak.

21.2 One-dimensional, linear, non-rotating waves

Before we inverstigate the implementation of numerical schemes for open boundaries, the mathematical problems at open boundaries should be shortly discussed. As the first item we consider the behaviour of waves near an open boundary. As a simple example we consider a long zonal channel and study nonrotating, linearized, frictionless and barotropic gravity waves. The basic equations are the momentum equations for the vertically integrated flow U, V

$$\dot{U} + gH\frac{\partial \eta}{\partial x} = X, \tag{21.1}$$

$$\dot{V} + gH\frac{\partial \eta}{\partial y} = Y \tag{21.2}$$

and the equation of continuity

$$\dot{\eta} = Q - \left(\frac{\partial U}{\partial x} + \frac{\partial V}{\partial y}\right). \tag{21.3}$$

η denotes the sea level elevation, X and Y are the wind stress components, Q is a fresh water flux, H the total depth and g the gravitational accelleration. These equations can be combined to a single equation for the sea level elevation,

$$-\ddot{\eta} + \frac{\partial}{\partial x}\left(gH\frac{\partial \eta}{\partial x}\right) + \frac{\partial}{\partial y}\left(gH\frac{\partial \eta}{\partial y}\right) = \frac{\partial X}{\partial x} + \frac{\partial Y}{\partial y} - \dot{Q}. \tag{21.4}$$

We consider an initial value problem for time $t = 0$. The sea surface has a well

defined shape η_0, the velocity is assumed to be zero.

$$\begin{aligned} \eta(xy0) &= \eta_0(xy), && (21.5)\\ U(xy0) &= V(xy0) = 0, && (21.6)\\ \dot{\eta}(xy0) &= \dot{\eta_0}(xy) = Q(xy0) && (21.7) \end{aligned}$$

Introducing the one sided Fourier transforms

$$\begin{aligned} \int_0^\infty dt\, e^{i\omega t}\eta(t) &= \eta(\omega), && (21.8)\\ \int_0^\infty dt\, e^{i\omega t}\dot{\eta}(t) &= -\eta_0 - i\omega\eta(\omega), && (21.9)\\ \int_0^\infty dt\, e^{i\omega t}\ddot{\eta}(t) &= -\dot{\eta}_0 + i\omega\eta_0 - \omega^2\eta(\omega), && (21.10) \end{aligned}$$

the initial condition appear as sources in the equation of η,

$$\omega^2\eta + \frac{\partial}{\partial x}\left(gH\frac{\partial\eta}{\partial x}\right) + \frac{\partial}{\partial y}\left(gH\frac{\partial\eta}{\partial y}\right) = F(x,y,\omega), \tag{21.11}$$

with

$$F(x,y,\omega) = \frac{\partial X}{\partial x} + \frac{\partial Y}{\partial y} + i\omega(\eta_0 + Q), \tag{21.12}$$

To ensure causality, a small positive imaginary part has been added to the frequency ω, i.e., ω means $\omega + i\varepsilon$. It will not be written explicitely but is needed for the inverse Fourier transforms.

For the discussion of the open boundary problem it is sufficient, to consider simplified examples. Hence, we assume that the meridional wind is zero and the initial sea level elevation depends on the zonal co-ordinate only. In this case we have a one-dimensional problem since all variables depend on the zonal co-ordinate x only.

The sea surface elevation should be small compared with the depth. Hence, for a flat bottom the depth is approximately constant, $H = H_0 + \eta \approx H_0$, and all waves spread with a constant phase speed c

$$c = \sqrt{gH_0}. \tag{21.13}$$

A general solution of equation (21.11) can be found by means of a Green function. The Green function is defined by the equation

$$\left(\omega^2 + c^2\frac{\partial^2}{\partial x'^2}\right) G(x,x',\omega) = \delta(x - x'). \tag{21.14}$$

The boundary conditions at the edge of the model area will be specified later.

Subtracting equation (21.14) multiplied with G from equation (21.11) multiplied with η, integrating over x' the general solution reads

$$\eta(x\omega) = \int_{x_l}^{x_r} dx'\, G(x,x',\omega)F(x'\omega) + c^2\left(\eta(x')\frac{\partial G(x,x',\omega)}{\partial x'} - G(x,x',\omega)\frac{\partial\eta(x')}{\partial x'}\right)\Bigg|_{x'=x_l}^{x'=x_r} \tag{21.15}$$

x_l and x_r are the left and the right boundary of the channel. Hence, specifying appropriate boundary conditions for the Green function at $x' = x_l$ and $x' = x_r$ may help to simplify the problem considerably.

21.2.1 A very long channel

As first example we consider an infinitely long channel, i.e., $x_l = -\infty$, $x_r = +\infty$, which will serve as a reference solution for the open boundary problem. Owing for solutions which describe surface waves forced in a limited area near the origin we reqiuire, that η vanishes at large distances from the origin,

$$\eta(x) = 0, \quad \text{for} \quad x \to \pm\infty. \tag{21.16}$$

For the Green function we require the boundary condition

$$G(x, x') = 0, \quad \text{for} \quad x' \to \pm\infty, \tag{21.17}$$

and find for the Green function

$$G(xx'\omega) = \frac{1}{2i\omega c} e^{i\frac{\omega}{c}|x-x'|}. \tag{21.18}$$

The general result for the seal level η is

$$\eta(x\omega) = \int_{x_l}^{x_r} dx'\, G(xx', \omega) F(x'\omega) \tag{21.19}$$

To discuss the open boundary problem we split the channel at $x = a$ and ask only for the sea level within an area of interest, say at $x > a$. The point $x = a$ is the open boundary. The sea level elevation at all points $x > a$ consists now of two contributions, η_l describes waves propagating eastward from the area left of the boundary and η_r which stands for all waves generated at all points $x > a$ within the area of interest. Also the forcing function F can be devided formally in two parts,

$$F(x\omega) = \theta(x-a)F_r(x\omega) + \theta(a-x)F_l(x\omega) \tag{21.20}$$

F_r is the forcing in the area east of $x = a$, F_l decribes all forcing west of $x = a$. η_l reads

$$\begin{aligned} \eta_l(x\omega) &= \frac{1}{2i\omega c} \int_{-\infty}^{a} dx'\, e^{i\omega\frac{x-x'}{c}} F_l(x'\omega), \\ &= \eta_l(a\omega) e^{i\frac{\omega}{c}(x-a)}. \end{aligned} \tag{21.21}$$

the result for η_r is

$$\eta_r(x\omega) = \frac{1}{2i\omega c} \int_{a}^{\infty} dx'\, e^{i\omega\frac{|x-x'|}{c}} F_r(x'\omega). \tag{21.22}$$

The inverse Fourier transforms are

$$\begin{aligned} \eta_l(xt) &= \int \frac{d\omega}{2\pi} \frac{1}{2i\omega c} \int_{-\infty}^{a} dx'\, e^{-i\omega\left(t-\frac{x-x'}{c}\right)} F_l(x'\omega) \\ &= \eta_l\left(a, t - \frac{x-a}{c}\right) \end{aligned} \tag{21.23}$$

$$\eta_r(xt) = \eta_r^<(xt) + \eta_r^>(xt)$$

with

$$\begin{aligned}
\eta_r^<(xt) &= \int \frac{d\omega}{2\pi}\frac{1}{2i\omega c}\int_a^x dx'\, e^{-i\omega\left(t-\frac{x-x'}{c}\right)}F_r(x'\omega) \\
\eta_r^>(xt) &= \int \frac{d\omega}{2\pi}\frac{1}{2i\omega c}\int_x^\infty dx'\, e^{-i\omega\left(t+\frac{x-x'}{c}\right)}F_r(x'\omega)
\end{aligned} \tag{21.24}$$

Hence, considering the sea level elevation $\eta = \eta_l + \eta_r$ at a certain point x, it is the superposition of three contributions. η_l depends on $x - ct$ and decribes eastward travelling waves generated somewhere at locations $x < a$. The first contribution of η_r, $\eta_r^<(x-ct)$ depending on $x - ct$ is a superposition of waves generated at locations between a and x travelling eastward, the second contribution of η_r, $\eta_r^>(x+ct)$, describes westward moving waves coming from locations eastward of x. From a mathematical point of view the problem is solved, if the Green function and all forces for $x > a$ are known, and a time series of incoming waves at $x = a$ is prescribed. However, the separation of the solution in incoming and outgoing waves is not part of a numerical scheme.

21.2.2 A general approach with open boundaries

A more general approach to the open boundary problem can be derived directly from eq. (21.15). We assume $x_r = \infty$ and get

$$\eta(x\omega) = \eta_r(x\omega) - c^2\left(\eta(x')\frac{\partial G(xx',\omega)}{\partial x'} - G(xx',\omega)\frac{\partial \eta(x')}{\partial x'}\right)\Big|_{x'=a}. \tag{21.25}$$

A similar equation follows for the derivative

$$\frac{\partial \eta(x\omega)}{\partial x} = \frac{\partial \eta_r(x\omega)}{\partial x} - c^2\left(\eta(x')\frac{\partial G^2(xx',\omega)}{\partial x\partial x'} - \frac{\partial G(xx',\omega)}{\partial x}\frac{\partial \eta(x')}{\partial x'}\right)\Big|_{x'=a} \tag{21.26}$$

With

$$c^2\left.\frac{\partial G(xx',\omega)}{\partial x'}\right|_{x'=a} = -\frac{1}{2}e^{i\frac{\omega}{c}(x-a)} \tag{21.27}$$

$$c^2\left.\frac{\partial G(xx',\omega)}{\partial x}\right|_{x'=a} = \frac{1}{2}e^{i\frac{\omega}{c}(x-a)} \tag{21.28}$$

$$c^2\left.\frac{\partial G^2(xx',\omega)}{\partial x\partial x'}\right|_{x'=a} = -\frac{i\omega}{2c}e^{i\frac{\omega}{c}(x-a)} \tag{21.29}$$

$$\tag{21.30}$$

we find the two equations

$$\eta(a\omega) = 2\eta_r(a\omega) + \frac{c}{i\omega}\frac{\partial \eta(x\omega)}{\partial x}|_{x=a} \tag{21.31}$$

$$\frac{\partial \eta(x\omega)}{\partial x}|_{x=a} = 2\frac{\partial \eta_r(x\omega)}{\partial x}|_{x=a} + \frac{i\omega}{c}\eta(a\omega) \tag{21.32}$$

The determinant of the coefficient matrix is zero and the above equations cannot be used to calculate the sea level at $x = a$. This is clear from the previous section,

since $\eta(a\omega)$ is influenced also from the area at $x < a$. However, with the help of the above relations equation (21.25) can be rewritten where either the sea level or alternatively the sea level gradient at $x = a$ must be prescribed.

$$\begin{aligned} \eta(x\omega) &= \eta_r(x\omega) + e^{i\frac{\omega}{c}(x-a)}\left(\eta(a\omega) - \eta_r(a\omega)\right) && (21.33)\\ &= \eta_r(x\omega) + e^{i\frac{\omega}{c}(x-a)}\eta_l(a\omega) && (21.34)\end{aligned}$$

This is the same form as equation (21.21) but $\eta_l(a\omega)$ is now an unknown boundary value which must be prescribed. Alternatively, the gradient of η_l can be prescribed,

$$\eta(x\omega) = \eta_r(x\omega) + \frac{c}{i\omega}e^{i\frac{\omega}{c}(x-a)}\frac{\partial\eta_l(x\omega)}{\partial x}|_{x=a}. \quad (21.35)$$

21.2.2.1 Example: initial step like sea surface elevation

An illustrative example is a step like initial surface elevation,

$$\eta_0(x) = \eta_0\theta(x - x_0), \quad (21.36)$$

where the sea surface has a level η_0 east of $x = x_0$ and 0 elsewhere. To position of the initial step is assumed within the model domain, $x_0 > a$. Hence, at least for small times $\eta_l = 0$ should be valid.

$$\eta_r(x\omega) = \frac{i\,\eta_0}{2\omega}\left(\theta(x - x_0)\left(2 - e^{i\frac{\omega}{c}(x-x_0)}\right) + \theta(x_0 - x)\left(e^{i\frac{\omega}{c}(x_0-x)}\right)\right) \quad (21.37)$$

solution follows

21.2.3 The Sommerfeld radiation condition

The set of equations (21.32) and (21.32) can be rewritten as

$$\begin{aligned} \eta_r(a\omega) &= -\frac{c}{i\omega}\frac{\partial\eta_r(x\omega)}{\partial x}|_{x=a} && (21.38)\\ \eta_l(a\omega) &= \frac{c}{i\omega}\frac{\partial\eta_l(x\omega)}{\partial x}|_{x=a}. && (21.39)\end{aligned}$$

This is equivalent to

$$\begin{aligned} \frac{\partial\eta_r(at)}{\partial t} &= c\,\frac{\partial\eta_r(xt)}{\partial x}|_{x=a},\\ \frac{\partial\eta_l(at)}{\partial t} &= -c\,\frac{\partial\eta_l(xt)}{\partial x}|_{x=a}. && (21.40)\\ & && (21.41)\end{aligned}$$

It means, that η_r at the boundary $x = a$ consists of westward going waves only but η_l is spreading only eastward. Hence, requiring for the total solution η

$$\frac{\partial\eta(xt)}{\partial t}|_{x=a} = c\,\frac{\partial\eta(xt)}{\partial x}|_{x=a}, \quad (21.42)$$

is equivalent with $\eta_l(a) = 0$ which means, that no eastward going waves are in the open boundary and the domain $x > a$ is influenced only from forces acting

at $x > a$. A similar boundary condition was originally derived for the theory of electromagnetic waves to remove incoming waves from the far field solution for an oscillating dipole antenna and is called commonly Sommerfeld radiation condition (see e.g. Sommerfeld, 1966).

In the context of our Greens function approach, the equations (21.40) and (21.40) have been derived and reflect the boundary conditions applied for the Greens function, which means, that all relevant sources of waves must have a finite distance from the origin. Hence, here these equations are not a boundary condition but a general property of the wave field. On the other hand equation (21.42) restricts the manifold of solutions of the wave equation. It corresponds to $\eta_l(a) = 0$ and is suitable as boundary condition which filters out incoming waves.

21.2.4 Is this an ill-posed problem?

From the viewpoint of mathematical analysis all quantities are well defined and a unique solution can be found. But this requires to separate the solution in the components η_r and η_l which is more or less impossible for realistic applications and numerical solution procedures. For practical applications the problem reveals differently: find a solution of the equations for an initial state and forcing given within the model domain and some prescribed boundary values. To sea the problems related to this approach let us return to equations (21.33) and (21.34). As long as the component $\eta_l(a)$ at the right hand side is known, the solution is well defined. However, if $\eta_l(a)$ is diagnosed from a prescribed value $\eta(a) = \eta^{ext}$ by

$$\eta_l(a) \quad = \quad \eta^{ext} - \eta_r(a), \tag{21.43}$$

the solution reads

$$\eta(x\omega) \quad = \quad \eta_r(x\omega) + e^{i\frac{\omega}{c}(x-a)} \left(\eta^{ext}(\omega) - \eta_r(a\omega)\right). \tag{21.44}$$

All deviations between the prescribed and the internally forced sealevel generate waves propagating into the model domain. Only if the prescribed sealevel is the exact solution no inwards propagating waves occur. Hence, boundary values and forcing must be consistent data sets to avoid artificial values for $\eta_l(a)$ and artificial waves by reflection of the internal solution at the model boundary. This is an unrealistic constraint for oceanographic applications where boundary data are taken in most cases from other models or measurements. Surface gravity waves are varying at timescales of seconds to minutes but boundary values are mostly availabe with timescales of hours, days or even month. An open boundary with prescribed slowly varying external values would simply reflext outgoing waves back into the model area.

From this point of view the problem to find the sealevel within a given model domain from the equations, initial values, the forcing and prescribed boundary values is an ill-posed problem which can be solved only approximately. As a guide how this can be accomplished, the special case of no incoming waves can be used. In this case the Sommerfeld radiation condition applies to the total solution and no boundary values are needed. Hence, time tendency of the total η at the boundary $x = a$ consists of an contribution governed by a Sommerfeld radiation condition

and an external contribution. The latter is only present, when the internal time tendency leads to an result different from the prescribed extrenal value,

$$\frac{\partial \eta(xt)}{\partial t}|_{x=a} = c\,\frac{\partial \eta(xt)}{\partial x}|_{x=a} + \frac{\eta^{ext}(t) - \eta(at)}{\tau}. \tag{21.45}$$

This equation can be read as follows. If the solution follows the externally prescribed value η^{ext}, there are no externally driven incoming waves. If there is a difference, the solution at the boundary is slowly relaxed to the prescribed value, the parameter τ rules the relaxation time. In more refined schemes (Orlanski ...) parameterisations like $\tau = \tau(c)$ is used to relax only, if incoming waves are detected.

21.3 The rotating case

The Sommerfeld radiation condition (21.40) applies only if all wave components with different wave numbers have the same phase speed, i.e., if $\omega \sim k$. In realistic ocean dynamics the Coriolis force plays an important role and rules also the dispersion relation of most waves. For Poincaré waves the disperion relation reads

$$\omega^2 = f^2 + k^2 c_n^2 \tag{21.46}$$

c_n is the maximum wave speed of vertical Eigenmodes. This implies a general form of the phase function of waves

$$\Phi = f\sqrt{t^2 - \frac{x^2}{c_n^2}} \tag{21.47}$$

and

$$\Phi_t^2 = f^2 + \Phi_x^2 c_n^2, \quad \frac{\Phi_t}{\Phi_x} = -\frac{t\,c_n^2}{x} \tag{21.48}$$

Generally, a Sommerfeld radiation condition is not valid since the waves are dispersive because of rotation. Only for large wave numbers k rotation plays a minor role and $\omega \sim k$. Nevertheless, a radiation condition may apply apprimately for a short time after the front has passed through a point x. In this case the ratio of phases is approximately

$$\frac{\Phi_t}{\Phi_x} \approx -c_n \tag{21.49}$$

which resembles a Sommerfeld radiation condition.

However, the large scale flow needs not to be wave like. It is well known that for times greater than the inertial period f^{-1} the flow becomes geostrophic, i.e., pressure gradients balance the Coriolis force.

21.4 The geometry of open boundaries

The geometric setup of open model boundaries in shown in Figures 21.4 and 21.4. The numerical scheme in Arakawa B-grid requires that the out-most points must be alway tracer points.

The following index convention for the variables is used:

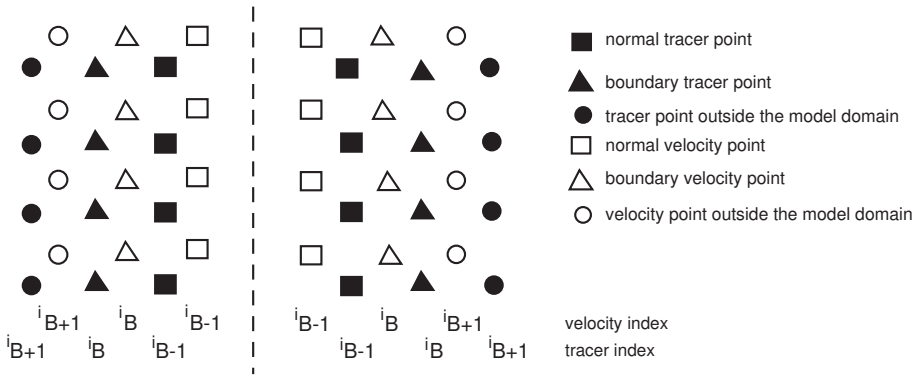

Figure 21.1: The geometry of western (left) and eastern (right) open boundaries. Note the index convention explained below.

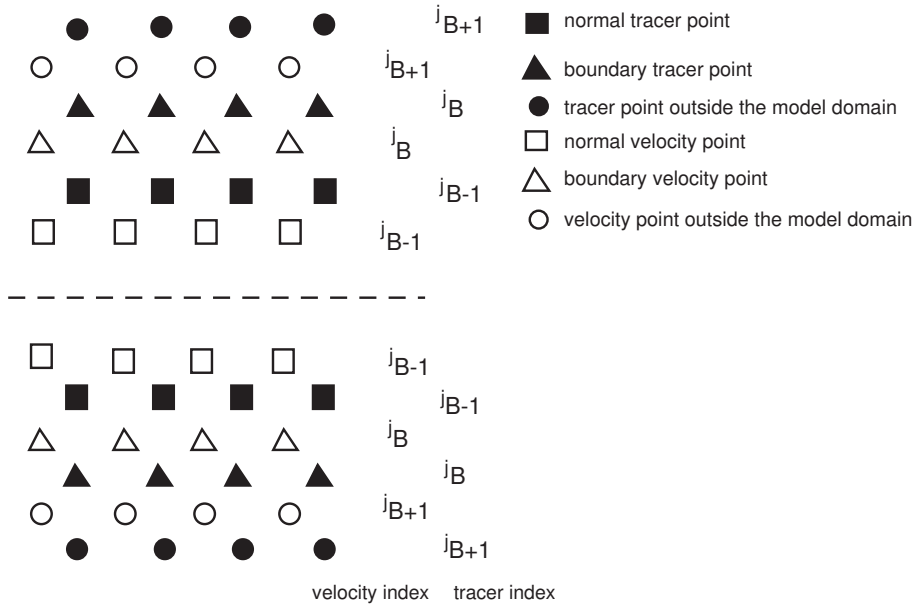

Figure 21.2: The geometry of southern (lower) and northern (upper) open boundaries. Note the index convention explained below.

- the index "B" means "boundary point"
- For a western boundary at $i = i_B$, $T_B = T_{i_B}$ and $u_B = u_{i_B}$.
- For an eastern boundary the out-most point is a tracer point. Hence for a boundary at $i = i_B$, $T_B = T_{i_B}$ and $u_B = u_{i_B-1}$.
- A similar convention is used for southern and norther boundaries.
- The index "$B-1$" points to the first internal model point.
- The index "$B+1$" points to the first grid point outside the model domain.

This is illustrated by Figure 21.4 and 21.4. For example at a western boundary with $i = 3$ the following relations hold

$$T_B = T_{i=3}, \quad T_{B-1} = T_{i=4}, \quad T_{B+1} = T_{i=2}, \tag{21.50}$$
$$u_B = u_{i=3}, \quad u_{B-1} = u_{i=4}, \quad u_{B+1} = u_{i=2}, \tag{21.51}$$
$$\tag{21.52}$$

for a southern boundary at $j = 90$ one has

$$T_B = T_{j=90}, \quad T_{B-1} = T_{j=89}, \quad T_{B+1} = T_{j=91}, \tag{21.53}$$
$$u_B = u_{j=89}, \quad u_{B-1} = u_{j=88}, \quad u_{B+1} = u_{j=90}. \tag{21.54}$$
$$\tag{21.55}$$

From a first point of view this seems to be confusing but avoids a lot of case discussions in the calculation of phase velocities.

21.5 Momentum equations

Since the velocity points at the boundary are surrounded by valid tracer points, most contributions to the momentum time tendency as pressure gradients, wind forcing, bottom friction and Coriolis force can be calculated. Only the divergence of the advective and diffusive momentum flux is unknown, since the velocity on points beyond the boundary is needed, but not defined. If the velocity at these points can be prescribed, i.e. from another model, the numerical scheme is complete. But there remain the well known nesting problems, which arise from differences in model resolution and forcing.

If nothing can be prescribed, the fact, that many flow is quasi-geostrophic helps to find an approximation. Since friction and advection are small friction is calculated by extrapolation from the model interior and the divergence of the advection operator is set to zero. The horizontal momentum equations with reduced physics used on the velocity boundary points (red crosses) are

$$u_t = v\left(f + \frac{u\tan\phi}{a}\right) - \left(\frac{1}{a\,\rho_\circ \cdot \cos\phi}\right) p_\lambda + (\kappa_m u_z)_z + F^u \tag{21.56}$$

$$v_t = -u\left(f + \frac{u\tan\phi}{a}\right) - \left(\frac{1}{a\,\rho_\circ}\right) p_\phi + (\kappa_m v_z)_z + F^v \tag{21.57}$$

For the friction operator F simple friction is assumed. The unknown velocity at points outside the boundary is set by extrapolation.

21.6 Tracer equation

The important contributions to the advection-diffusion equation for tracers cannot be found from simple approximations. One of the requirements for the boundary condition is , that the boundary must be "passive" for outgoing waves. Following Orlanski (1976) the tracer field near the boundary is considered as the result of traveling linear waves and advection. Assuming, that the waves and advection are perpendicularly to the open boundary, the tracer field should have the general form

$$T(q_{\parallel}, q_{\perp}, t) = T\left(q_{\parallel}, q_{\perp} \pm (c + v_{ad})\, t\right) \tag{21.58}$$

Here $q_{\parallel}$ and $q_{\perp}$ are the spatial coordinates parallel or perpendicularly to the boundary, c is the wave phase speed and v_{ad} the advection velocity. Assuming v_{ad} to be constant T obeys the differential equation

$$\frac{\partial T}{\partial t} = \pm (c + v_{ad}) \frac{\partial T}{\partial q_{\perp}}. \tag{21.59}$$

The negative sign corresponds to waves traveling in the direction of $q_{\perp}$, the positive sign corresponds to waves traveling in the opposite direction. Thus, choosing either the positive or the negative sign waves entering the model area from outside can be removed from the solution keeping only outgoing waves. This so called Sommerfeld radiation condition (see e.g. Sommerfeld, 1966) was originally derived for the theory of electromagnetic waves to remove incoming waves from the far field solution for an oscillating dipole antenna.

Hence, the modified tracer equation at an open boundary point is the superposition of the radiation condition and the diffusion term and reads

$$\frac{\partial T}{\partial t} + \frac{c_T + v_{ad}}{a} \frac{\partial T}{\partial \phi} = F^T + S^T, \quad c_T = -a \frac{\partial T}{\partial t} / \frac{\partial T}{\partial \phi} \tag{21.60}$$

$$\frac{\partial T}{\partial t} + \frac{c_T + u_{ad}}{a \cos\phi} \frac{\partial T}{\partial \lambda} = F^T + S^T, \quad c_T = -a \cos\phi \frac{\partial T}{\partial t} / \frac{\partial T}{\partial \lambda} \tag{21.61}$$

Equation (21.60) applies for a northern or southern boundary, equation(21.61) is valid for an eastern or western boundary respectively. The phase speed acts in the same manner as an outward directed advection. u_{ad} and v_{ad} is the advection velocity calculated from u_B and v_B respectively.

The numerical approximation c^n_{num} for the phase velocities is calculated in the model interior,

$$c^n_{num} = -\frac{T^n_{B-1} - T^{n-1}_{B-1}}{T^n_{B-1} - T^n_{B-2}} \frac{q_{\perp,B-1} - q_{\perp,B-2}}{t^n - t^{n-1}}, \tag{21.62}$$

where the superscript "n" denotes the time step. The CFL-criterion provides a limit c_{max} for the phase speed,

$$c_{max} = \frac{q_{\perp,B-1} - q_{\perp,B-2}}{2\Delta t}. \tag{21.63}$$

It may happen that the phase speed is directed into the model domain. In this case it is set to zero.

$$c_T^n = c_{max}, \quad |c_{num}^n| \geq |c_{max}^n|, \quad \text{outgoing waves} \tag{21.64}$$
$$c_T^n = c_{num}^n, \quad |c_{num}^n| < |c_{max}^n|, \quad \text{outgoing waves} \tag{21.65}$$
$$c_T^n = 0, \quad \text{incoming waves} \tag{21.66}$$

For outgoing waves, the gradient of T in the advective term is calculated from T_B and T_{B-1}

The diffusion operator F^T requires the knowledge of T_{B+1}. For a passive boundary the approximation

$$T_{B+1} = T_B \tag{21.67}$$

is used. Other approximations, i.e.,

$$T_{B+1} = 0.5\,(T_B + T_{B-1}) \tag{21.68}$$

are possible.

This "passive" boundary condition may not be sufficient for many purposes. After running a "passive" boundary over a long period, the tracer near the boundary will be determined completely by processes in the model domain. As an example consider a marginal sea with a strong fresh water surplus. There will be an estuarine circulation with a more or less permanent outflow of brackish water in a surface layer and inflow near the bottom. However, the salinity of the inflowing water will be reduced too after some time by vertical mixing processes and the model results will suffer from underestimated stratification.

To overcome this problem information on the tracer concentration in the adjacent sea must be provided for the model. The simple approximation

$$T_{B+1} = T_0, \tag{21.69}$$

where T_0 may stem from an appropriate database, improves the performance of the diffusion operator which in turn may invoke wave like processes traveling from the boundary into the model. Using an upstream formulation for the tracer gradient in the advective term, this can switch on an inflow through the open boundary. However, waves of a small amplitude but with a high phase speed may disturb this scheme. Thus, the source term S^T can be used for a controlled restoring to prescribed boundary values.

21.7 The sea level

21.7.1 The passive properies of the boundary

Notably, if the out-most points would be velocity points, the sea level equation would be complete and no open boundary condition for η would be necessary. However, in practice the velocity field is difficult to measure but information on the sea level is known in form of tidal tables, coastal gauges or altimeter data. Thus, the sea level is the appropriate quantity for an open boundary condition.

21.7.1.1 The Sommerfeld radiation condition for the sea level

Assuming barotropic, linear surface waves and neglecting Coriolis force, the sea level elevation η has the general form

$$\eta = \eta(\vec{k} \cdot \vec{r} - \omega t) \tag{21.70}$$

and depends only on the argument $\alpha = \vec{k} \cdot \vec{r} - \omega t$ where $\vec{k}$ is the wave number and ω is the wave frequency. The waves move with phase velocity

$$\vec{c} = \frac{\omega}{k}\frac{\vec{k}}{k}. \tag{21.71}$$

From the derivatives (in Cartesian co-ordinates)

$$\begin{aligned} \eta_t &= -\omega\eta_\alpha \\ \eta_x &= k_x\eta_\alpha \\ \eta_y &= k_y\eta_\alpha \end{aligned} \tag{21.72}$$

follows the identity

$$\eta_t = -c_x\eta_x - c_y\eta_y. \tag{21.73}$$

with

$$\begin{aligned} c^2 &= \frac{\omega^2}{k^2}, \\ a_x &= \frac{\omega}{k_x} = -\frac{\eta_t}{\eta_x}, \\ a_y &= \frac{\omega}{k_y} = -\frac{\eta_t}{\eta_y}, \\ c_x &= -\frac{c^2}{a_x} = -\frac{\eta_t\eta_x}{\eta_y^2 + \eta_x^2}, \\ c_y &= -\frac{c^2}{a_y} = -\frac{\eta_t\eta_y}{\eta_y^2 + \eta_x^2}, \end{aligned} \tag{21.74}$$

Notable, c^2 is obeys

$$c^{-2} = a_x^{-2} + a_y^{-2}, \tag{21.75}$$

$$c^2 = c_x^2 + c_y^2, \tag{21.76}$$

$$\tag{21.77}$$

For free, barotropic, linear surface waves without Coriolis force, the velocity components depend also only on α and an equation like equation (21.73) can be derived also directly from the sea level equation

$$\eta_t = -U_x - V_y + q_w, \tag{21.78}$$

$$\eta_t = -c_x\eta_x - c_y\eta_y + q_w, \tag{21.79}$$

The more general form with the additional contribution from the fresh water flux, q_w, could be found also from equation (21.70) considering the quantity $\tilde{\eta} = \eta(\vec{k} \cdot \vec{r} - \omega t) + q_w t$.

So far, in its differential form equation(21.79) is an identity. To transform it into a prognostic equation to be used at the boundary, the phase speed must be diagnosed near the model boundary. Icoming waves are suppressed by the radiation condition

$$\vec{c} \cdot \vec{n} \quad > \quad 0, \tag{21.80}$$

where $\vec{n}$ is a vector directed outward of the model domain normally to the boundary and $\vec{c}$ has the components (c_x, c_y).

Considering a western boundary, the condition $c_x < 0$ permits only outgoing waves, at an eastern boundary $c_x > 0$ is required. In the same manner, at a northern boundary $c_y > 0$ and at a southern boundary $c_y < 0$ applies.

In geophysical co-ordinates, equation(21.79) reads

$$\frac{\partial \eta_t}{\partial t} = -\left(\frac{1}{a\, c_\phi}\frac{\partial \eta}{\partial \phi} + \frac{1}{a\, c_\lambda \cos\phi}\frac{\partial \eta}{\partial \lambda}\right) + q_w, \tag{21.81}$$

$$c_\phi = -\frac{\frac{\partial \eta}{\partial t}\,\frac{1}{a}\frac{\partial \eta}{\partial \phi}}{\left(\frac{1}{a}\frac{\partial \eta}{\partial \phi}\right)^2 + \left(\frac{1}{a\cos\phi}\frac{\partial \eta}{\partial \phi}\right)^2} \tag{21.82}$$

$$c_\lambda = -\frac{\frac{\partial \eta}{\partial t}\,\frac{1}{a\cos\phi}\frac{\partial \eta}{\partial \lambda}}{\left(\frac{1}{a}\frac{\partial \eta}{\partial \phi}\right)^2 + \left(\frac{1}{a\cos\phi}\frac{\partial \eta}{\partial \phi}\right)^2}. \tag{21.83}$$

(21.84)

21.7.1.2 Numerical scheme

For the spatial derivatives perpendicularly to the boundary a forward or backward scheme is used, derivatives along the boundary are calculated with centered diferences. The time stepping of η at the boundary follows basically the leapfrog scheme as used in MOM, η at time level $\tau + 1$ is calculated from η at time level $\tau - 1$ from phases at time level τ. However, for numerical stability, the gradient of η is calculated implicitely at $\tau + 1$, hence, for a western or eastern boundary

$$\frac{\eta^{n+1}_{B,j} - \eta^{n-1}_{B,j}}{2\Delta t} = -\frac{1}{a}\left(c_\phi \frac{\eta^{n}_{B-1,j+1} - \eta^{n}_{B-1,j-1}}{\phi_{j+1} - \phi_{j-1}} + \frac{c_\lambda}{\cos\phi_j}\frac{\eta^{n+1}_{B,j} - \eta^{n+1}_{B-1,j}}{\lambda_B - \lambda_{B-1}}\right) + q_w, \tag{21.85}$$

(21.86)

and for a southern or northern boundary

$$\frac{\eta^{n+1}_{i,B} - \eta^{n-1}_{i,B}}{2\Delta t} = -\frac{1}{a}\left(c_\phi \frac{\eta^{n+1}_{i,B} - \eta^{n+1}_{i,B-1}}{\phi_B - \phi_{B-1}} + \frac{c_\lambda}{\cos\phi_{B-1}}\frac{\eta^{n}_{i+1,B-1} - \eta^{n}_{i-1,B-1}}{\lambda_{i+1} - \lambda_{i-1}}\right) + q_w, \tag{21.87}$$

(21.88)

The phase speed is calculated implicitely, for a western or eastern boundary

$$c_\phi = -\frac{\eta^{n+1}_{B-1,j} - \eta^{n-1}_{B-1,j}}{\eta^{n}_{B-1,j+1} - \eta^{n}_{B-1,j-1}} \frac{a\left(\phi_{j+1} - \phi_{j-1}\right)}{2\Delta t} \tag{21.89}$$

$$c_\lambda = -\frac{\eta^{n+1}_{B-1,j} - \eta^{n-1}_{B-1,j}}{\eta^{n}_{B-1,j} - \eta^{n}_{B-2,j}} \frac{a\,\cos\phi_j\left(\lambda_{B-1} - \lambda_{B-2}\right)}{2\Delta t}, \tag{21.90}$$

and for a southern or northern boundary

$$c_\phi = -\frac{\eta^{n+1}_{i,B-1} - \eta^{n-1}_{i,B-1}}{\eta^{n}_{i,B-1} - \eta^{n}_{i,B-2}} \frac{a\left(\phi_{B-1} - \phi_{B-2}\right)}{2\Delta t} \tag{21.91}$$

$$c_\lambda = -\frac{\eta^{n+1}_{i,B-1} - \eta^{n-1}_{i,B-1}}{\eta^{n}_{i+1,B-1} - \eta^{n}_{i-1,B-1}} \frac{a\,\cos\phi_{B-1}\left(\lambda_{i+1} - \lambda_{i-1}\right)}{2\Delta t} \tag{21.92}$$

As for the tracers, the numerical approximation c^n_{num} for the phase speed at time step n is calculated in the model interior,

$$c^n_{num} = -\frac{\eta^{n}_{B-1} - \eta^{n-1}_{B-1}}{\eta^{n}_{B-1} - \eta^{n}_{B-2}} \frac{q_{\perp,B-1} - q_{\perp,B-2}}{t^n - t^{n-1}}, \tag{21.93}$$

The upper limit c_{max} for the phase speed is,

$$c_{max} = \sqrt{gH}. \tag{21.94}$$

It is assumed, that the time step is small enough for the CFL-criterion of barotropic waves.

The calculation of the phases for η appears to more complex than for tracers. The phase speed is very noisy and needs smoothing. This is done by accumulation

$$c^n_\eta = 0.9c^{n-1}_\eta + 0.1c^{new}_\eta \tag{21.95}$$

with

$$c^{new}_\eta = c_{max}, \qquad |c^n_{num}| \geq |c^n_{max}|, \quad \text{outgoing waves} \tag{21.96}$$

$$c^{new}_\eta = c^n_{num}, \qquad |c^n_{num}| < |c^n_{max}|, \quad \text{outgoing waves} \tag{21.97}$$

$$c^{new}_\eta = 0, \qquad \text{incoming waves} \tag{21.98}$$

For a very small sea level gradient, the phase cannot be calculated. In this case the approximation

$$c^n_\eta = 0.99c^{n-1}_\eta \tag{21.99}$$

is used.

21.7.2 Relaxation of the sea level

All equations for the open boundary condition as described previously relate the sea level change at the boundary with processes in the model domain. A such

the model is selfreferencing and small errors in the open boundary conditions may accumulte and cause large errors in the mass and tracer bilance of the model.

Hence, an appropriate relaxation procedure is needed to correct this model shortcoming. However, the sea level profile along the open boundary prescribes the mass transport trough the boundary. Near the coast the sea level profile is mainly adjusted by Kelvin waves traveling along the coast and leaving behind the wave fronts a geostrophically adjusted alongshore corrent and the corresponding sea level profile. As such the relaxation should not disturb the sea level profile at the boundary but this profile should be generated by the model itself.

As such the relaxation is not done in the sea level equation but in the pressure gradient term of the barotropic momentum equation at the open boundary. The sea level at the boundary itself is adjusted only by the Orlanki condition.

To achieve this, the pressure gradients in the equation for the momentum perpendicularly to the boundary is modified according

$$\frac{1}{\rho_o}(p_s)_{q_\perp} \rightarrow \frac{1}{\rho_o}(p_s)_{q_\perp} + (\eta_r)_{q_\perp} \tag{21.100}$$

with

$$(\eta_r)_{q_\perp} = \frac{\eta_{rel}^{n-1} - \eta_{B-1}^{n-1}}{\Delta q_{bot}} a_\eta. \tag{21.101}$$

a_η is a relaxation coefficient $0 < a_\eta < 1$. Several approximations can be used for η_{rel}^{n-1}. A simple scheme relaxes the mean sea level at the boundary $\overline{\eta_{B-1}^{n-1}}$ towards the reference level η_0,

$$\eta_{rel}^{n-1} = \eta_{B-1}^{n-1} - \left(\overline{\eta_{B-1}^{n-1}} - \eta_0\right). \tag{21.102}$$

More sophisticated schemes can be designed but will be nevertheless rough approximations which neglect important aspects of the dynamics of the flow across the boundary.

21.7.3 Prescribed boundary conditions

In some cases information on gauges at both sides of the open boundary is known. For example a model of the Baltic Sea can have an open boundary to the North Sea in the Skagerak. The relaxation can be done with gauge date from Hirtshals η_H at latitude ϕ_H (Denmark) and Mondal η_M at ϕ_M(Norway), by a linear interpolation

$$\eta_{rel}^{n-1}(\phi) = \frac{\phi - \phi_H}{\phi_M - \phi_H}\eta_M - \frac{\phi - \phi_M}{\phi_M - \phi_H}\eta_H \tag{21.103}$$

However, if the model interiour is not commensurable with the prescribed boundary conditions large artificial currents may occur near the boundary.

CHAPTER

TWENTYTWO

Tidal forcing from the moon and sun

Contents

The purpose of this chapter is to describe the formulation of lunar and solar tidal forcing implemented in mom4. This chapter was written by Harper Simmons (hsimmons@iarc.uaf.edu)

22.1 Tidal consituents and tidal forcing

Without tidal forcing, the equation for the vertically integrated transport, $\mathbf{U}$, in MOM4 takes the form (Griffies (2004))

$$(\partial_t + f\,\hat{\mathbf{z}}\wedge)\mathbf{U} = -(H+\eta)\,\nabla(p_s + p_a)/\rho_o + \mathbf{G}, \tag{22.1}$$

where $\mathbf{G}$ is the vertically integrated forcing arising from baroclinic effects, p_s is the pressure associated with undulations of the surface height, p_a is the atmospheric pressure, H is the depth of the ocean, and η is the surface height deviation from a resting state with $z = 0$.

Tidal forcing arising from the eight primary constituents (M2, S2, N2, K2, K1, O1, P1, Q1) (see Gill (1982)) have been added to the forcing for $\mathbf{U}$. The formulation follows Marchuk and Kagan (1989), by considering a tide generating potential ($g\eta_{\rm eq}$) with corrections due to both the earth tide ($1+k-h$) and self-attraction and loading (α). In this approach, we have

$$\nabla\,(p_s + p_a) \to \nabla(p_s + p_a) + g\,\nabla\left[(1-\alpha)\eta - (1+k-h)\eta_{\rm eq}\right]. \tag{22.2}$$

The *equilibrium tide*, η_{eq}, arises from the astronomically derived gravity producing forces. It is modified by several factors. The Love numbers, k and h, named for the physicist A.L. Love, account for the reduction of the ocean tide because of the deformation of the solid earth by tidal forces. The Love numbers are frequency dependent, with $1+k-h$ generally close to 0.7 (Wahr (1998)).

The term α in equation (22.2) accounts for a modification of the ocean's tidal response as a result of self-attraction and loading (SAL) (Hendershott (1972)). Self attraction is the modification of the tidal potential as a result of the redistribution of the earth and ocean due to the equilibrium tidal forcing. Loading refers to the depression of the earth's crust by the mounding of tides. Calculation of the SAL term requires an extremely cumbersome integration over the earth surface, rendering equation (22.2) an integro-differential equation (Ray (1998)).

Instead of solving the integro-differential form of equation (22.2), MOM4 uses the scalar approximation to SAL. We feel this is justified since our purpose in introducing tidal forcing is to study the *effects* of tides on the general circulation, not the details of the tides themselves. The conjecture is that precise calculation of the SAL term is not needed for to understand tidal effects on the general circulation. For the scalar approximation, α is usually set between $0.940 - 0.953$. MOM4 uses $\alpha = 0.948$. Limitations of the scalar approximation to SAL are discussed by Ray (1998), who concluded that the scalar approximation introduces phase errors of up to 30° and amplitude errors of 10% into a global scale tidal simulation.

22.2 Implementation in MOM4

The equilibrium tide is written for the n^{th} diurnal tidal constituent as

$$\eta_{eq,n} = H_n \sin 2\phi \cos(\omega_n t + \lambda), \tag{22.3}$$

and for the n^{th} semi-diurnal constituent as

$$\eta_{eq,n} = H_n \cos^2 \phi \cos(\omega_n t + 2\lambda), \tag{22.4}$$

where ϕ is latitude and λ is longitude. Recognizing that equation (22.3) and (22.4) require the evaluation of trigonometric functions at every grid point and every time-step, tidal forcing is introduced into MOM4 in the following mathematically equivalent form. Making use of the identity

$$\cos(A + B) = \cos(A)\ \cos(B) - \sin(A)\ \sin(B), \tag{22.5}$$

we can write the eight tidal forcing constituents as

$$\begin{aligned} \eta_{\rm eq} = \Sigma_{n=1}^{4} \Big[& \beta_n \quad a_n \quad \cos^2 \phi \, [\cos(\omega_n \quad t) \cos 2\lambda - \sin(\omega_n \quad t) \sin 2\lambda] + \\ & \beta_{n+4} a_{n+4} \sin 2\phi \, [\cos(\omega_{n+4} t) \cos 2\lambda - \sin(\omega_{n+4} t) \sin 2\lambda] \, \Big], \end{aligned} \tag{22.6}$$

which allows all the trigonometric functions of ϕ and λ to be precomputed. Note that we have written $\beta_n = 1 + k_n - h_n$. The frequencies (ω_n), amplitudes (a_n) and Love numbers are listed in Table 22.1.

constituent	name	origin	ω (1/day)	$1+k-h$	a (m)
1	K_1	Luni-solar declinational	0.7292117	0.736	0.141565
2	O_1	Principal lunar declinational	0.6759774	0.695	0.100661
3	P_1	Principal solar declinational	0.7252295	0.706	0.046848
4	Q_1	Larger lunar elliptic	0.6495854	0.695	0.019273
5	M_2	Principal lunar	1.405189	0.693	0.242334
6	S_2	Principal solar	1.454441	0.693	0.112743
7	N_2	Largerl lunar elliptic	1.378797	0.693	0.046397
8	K_2	Luni-solar declinational	1.458423	0.693	0.030684

Table 22.1: Frequencies, Love numbers, and amplitude functions for the eight principle constituents of tidal forcing available in MOM4.

CHAPTER

TWENTYTHREE

Eddy-topography interaction via Neptune

Contents

The purpose of this chapter is to present a method for parameterizing the interactions between unresolved mesoscale eddies and topography.

23.1 Introduction

Based on statistical mechanics arguments, Holloway (1992) proposed that interactions between mesoscale eddies and topography result in a stress on the ocean with two important consequences: (1) the ocean is not driven toward a state of rest, (2) the resulting motion may have scales much larger than the eddy scales. That is, eddy-topography interactions can generate coherent mean flows on the scale of the topography. When Holloway described coastal currents that persistently flow against both the wind forcing and pressure gradient, the response was that it must be due to King Neptune. Who else? Hence, the effect is referred to colloquially as the *Neptune effect*.

The magnitude of the associated topographic stress is dependent on the correlation between pressure p and topographic gradients ∇H, and this correlation is largely unknown. But even if it is no larger than 0.1, the resulting topographic stress could be comparable in magnitude to that from the surface wind.

23.2 Basics of the parameterization

If the view is taken that equations of motion are solved for moments of probable flow, then those moments are forced in part by derivatives of the entropy distribution with respect to the realized moments. The entropy gradient is estimated as proportional to a departure of the realized moments from a state in which the

entropy gradient is weak. This latter state is approximated by a transport streamfunction ψ^{nep} and maximum entropy velocity $\mathbf{u}^{nep}$ given by

$$\begin{aligned} \psi^{nep} &= -f\, L\, H \\ \mathbf{u}^{nep} &= \hat{\mathbf{z}} \wedge \nabla \psi^{nep} \end{aligned} \tag{23.1}$$

where f is the Coriolis parameter, H is the ocean depth, and L is an adjustable length scale on the order of 10 km. If model resolution is coarse relative to the first deformation radius, $\mathbf{u}^{nep}$ is roughly depth independent. Depth independence is assumed in the MOM4 implementation of Neptune. To parameterize the unresolved driving of the mean flow by eddy-topography interactions, the Neptune parameterization drives flow towards towards $\mathbf{u}^{nep}$ using an eddy stress proportional to $(\mathbf{u}^{nep} - \mathbf{u})$.

23.3 As implemented in MOM4

The Neptune parameterization is implemented in MOM4 for Laplacian friction.[1] Neptune systematically damps the deformation rates towards a state of approximate maximum entropy. Notably, Neptune increases the kinetic energy as it damps the flow toward its maximum entropy state. Such occurs even for flows at rest experiencing no external forcing. As a result. Neptune spins-up the flow with shallow depths to the right of the downstream direction.

Kinetic energy input via a sub-grid scale (SGS) parameterization is perhaps the central weakness of the Neptune parameterization, where a more complete theory provides for total energy conservation (forcing and dissipation) at the SGS. Notably, no such SGS theory presently exists. Instead, numerical modelers traditionally employ energy sinks via frictional dissipation toward a state of rest, as well as thickness diffusion to a state of zero available potential energy, both with no corresponding source except that available via forcing by surface momentum and buoyancy fluxes. Holloway (1992) argues that such is not an appropriate modeling practice, thus motivating the use of Neptune as a interim approach until a more complete theory is available.

There is concern about the stepwise representation of bottom topography in z-coordinate models. The use of partial cells in MOM4 enhances the model's ability to represent the topographic slope in a more faithful manner than with full cells. In general, however, the Neptune parameterization is an attempt to instruct the simulation about physical consequences due to eddy-topography interactions. The hope is that if the model can be suitably informed about these effects, it matters little that topography is only approximately represented.

[1] It could be easily generalized to biharmonic friction.

CHAPTER

TWENTYFOUR

Temporal treatment of the Coriolis force

Contents

The purpose of this chapter is to present the two methods used in MOM4 for temporally discretizing the Coriolis force.

24.1 Inertial oscillations

The inviscid momentum equation in the absence of pressure is given by

$$(\mathrm{d}/\mathrm{d}t + f\,\hat{\mathbf{z}}\wedge)\,\mathbf{u} = 0, \tag{24.1}$$

which is equivalent to the second order free oscillator equation

$$(\mathrm{d}^2/\mathrm{d}t^2 + f^2)\,\mathbf{u} = 0. \tag{24.2}$$

Here, $\mathrm{d}/\mathrm{d}t$ is the material time derivative relevant for Lagrangian observers. Motions which satisfy this equation are termed *inertial oscillations* and they have period given by

$$T_{inertial} = \frac{2\,\pi}{f} = \frac{11.97}{\sin\phi}\,\text{hour} \tag{24.3}$$

where $\Omega = 7.292 \times 10^{-5}\text{s}^{-1}$ is the earth's angular speed. The period of inertial oscillations is smallest at the North pole where $\phi = \pi/2$ and $T_{smallest} \approx 12\,\text{hour}$.

An explicit temporal discretization of the inertial oscillation equation (24.1) will be unstable if the time step is longer than some fraction of the inertial period, where

the fraction depends on details of the time stepping. Coarse resolution models (models with resolutions on the order of 4-5 degrees) may find this time step constraint is the most stringent of the model's baroclinic momentum processes. To get around this limitation, a semi-implicit temporal treatment has been traditionally considered, as in Bryan (1969).

Additional issues with coupling to sea ice may warrant an implicit treatment even for ocean models run with a momentum time step that well resolves the inertial period. In these cases, temporal details of ocean-ice coupling have been found to cause enhanced energy at the inertial period. Semi-implicit time stepping of the Coriolis force may assist in damping this energy.

It is for these reasons that MOM4 provides an option to time step the Coriolis force either explicitly or semi-implicitly in the baroclinic portion of the model. The namelist parameter *acor* sets the level of implicitness, as described in Section 24.4.2.

24.2 Explicit temporal discretization

Consider now just the linear part of the inertial oscillation equation, where advection is dropped

$$(\partial_t + \hat{\mathbf{z}} \wedge)\mathbf{u} = 0. \tag{24.4}$$

Following the time integration discussions in O'Brien (1986) and Bryan (1989) (see also Section 2.3 of Durran (1999)), introduce the complex velocity

$$w = u + i\, v \tag{24.5}$$

where $i = \sqrt{-1}$ and w should not be confused with the vertical velocity component. In terms of w, equation (24.4) takes the form

$$\partial_t\, w = -i\, f\, w \tag{24.6}$$

which has an oscillatory solution

$$w = w_o\, e^{ift} \tag{24.7}$$

with period

$$T_{inertial} = 2\,\pi\, f^{-1}. \tag{24.8}$$

Time discretizing equation (24.6) with a centered leap-frog scheme leads to

$$w(\tau + \Delta\tau) = w(\tau - \Delta\tau) - i\lambda\, w(\tau) \tag{24.9}$$

with

$$\lambda = 2\, f\, \Delta\tau \tag{24.10}$$

a dimensionless number. We can write the finite difference solution in terms of an amplification factor

$$w(\tau + \Delta\tau) = G\, w(\tau). \tag{24.11}$$

Substituting this *ansatz* into equation (24.9) leads to the quadratic equation

$$G^2 + i\,\lambda\, G - 1 = 0 \tag{24.12}$$

whose solution is

$$G = \frac{-i\,\lambda \pm \sqrt{-\lambda^2 + 4}}{2}. \tag{24.13}$$

If

$$\lambda/2 = f\,\Delta\tau < 1, \tag{24.14}$$

then $|G| = 1$, which means the two finite difference solutions are neutral and stable. One root is an unphysical mode, known as the leap-frog *computational mode*, and the other corresponds to the physical solution. If $\lambda > 2$ then $|G| > 1$ which means both roots are unstable. Hence, stability requires a time step satisfying

$$\Delta\tau < f^{-1}. \tag{24.15}$$

That is,

$$\frac{T_{inertial}}{\Delta\tau} = \frac{2\,\pi}{f\,\Delta\tau} > 2\,\pi, \tag{24.16}$$

meaning the leap-frog scheme remains stable if there are at least $2\,\pi$ time steps per inertial period. At the North Pole, this constraint means

$$\Delta\tau < 1.9\,\text{hours}. \tag{24.17}$$

For the baroclinic part of the model algorithm, $\Delta\tau < 1.9$ hours can be the limiting time step for coarse resolution global models, thus motivating an alternative approach discussed in Section 24.3.

24.3 Semi-implicit temporal discretization

To overcome the time-step constraint (24.17) on the baroclinic time step, we now consider a semi-implicit time stepping scheme within the leap-frog portion of the baroclinic algorithm. As with any implicit approach, stability can be enhanced relative to explicit schemes. The price to pay is dissipation of the inertial motions. See section 2.3 of Durran (1999) for discussion.

A semi-implicit treatment of the Coriolis force, within a leap-frog scheme, leads to

$$w(\tau + \Delta\tau) - w(\tau - \Delta\tau) = -i\,\lambda\,[(1-\gamma)\,w(\tau - \Delta\tau) + \gamma\,w(\tau + \Delta\tau)] \tag{24.18}$$

where $0 \leq \gamma \leq 1$ is a dimensionless number whose value is set according to stability considerations. We can write $w(\tau + \Delta\tau) = G\,w(\tau - \Delta\tau)$, with the semi-implicit scheme yielding the amplification factor

$$G = \frac{1 - i\,\lambda\,(1-\gamma)}{1 + i\,\lambda\,\gamma}. \tag{24.19}$$

The squared modulus $|G|^2$ is used to determine conditions for stability

$$|G|^2 = \frac{[1 - \gamma\,\lambda^2\,(1-\gamma)]^2 + \lambda^2}{[1 + (\gamma\,\lambda)^2]^2}. \tag{24.20}$$

For $\gamma = 0$, $|G| > 1$ which leads to an unstable scheme. For $\gamma = 1/2$, $|G| = 1$ and so the scheme is neutral. With $1/2 < \gamma \leq 1$, $|G| < 1$, and so the scheme is

unconditionally stable. Hence, we arrive at the stability range for the semi-implicit parameter

$$1/2 \leq \gamma \leq 1, \tag{24.21}$$

with $\gamma = 1$ yielding the most stable scheme.

24.4 As implemented in MOM4

Both an explicit and semi-implicit treatment of the Coriolis force in the baroclinic equations are available in MOM4. The semi-implicit piece is handled at the end of a baroclinic time step, after the implicit treatment of vertical mixing. The logic used in the code is a bit confusing, so it is useful to expose some details here.

24.4.1 Algorithm in the code

Let us separate that portion of the Coriolis force proportional to γ from the portion independent of γ in order to ease coding for the case with a fully explicit Coriolis force. Hence, we temporally discretize the Coriolis force as

$$\begin{aligned} -f\,\hat{\mathbf{z}} \wedge \mathbf{u} &\rightarrow -f\,\hat{\mathbf{z}} \wedge [(1-\gamma)\,\mathbf{u}(\tau-\Delta\tau) + \gamma\,\mathbf{u}(\tau+\Delta\tau)] \\ &= -f\,\hat{\mathbf{z}} \wedge \mathbf{u}(\tau-\Delta\tau) - f\,\gamma\,\hat{\mathbf{z}} \wedge (\mathbf{u}[\tau+\Delta\tau) - \mathbf{u}(\tau-\Delta\tau)]. \end{aligned} \tag{24.22}$$

For the explicit case, $\gamma = 0$ and

$$-f\,\hat{\mathbf{z}} \wedge \mathbf{u} \rightarrow -f\,\hat{\mathbf{z}} \wedge \mathbf{u}(\tau). \tag{24.23}$$

We now consider time stepping the velocity using all accelerations except that portion of the Coriolis force proportional to γ. The corresponding time tendency is given by

$$\delta_\tau \mathbf{u}^* = 2\,\Delta\tau\,\mathbf{F} \tag{24.24}$$

where $\mathbf{F}$ includes the acceleration from advection, horizontal pressure gradient force, friction force (both explicit and implicit), as well as that piece of the Coriolis force independent of γ. If the Coriolis force is computed explicitly, then $\delta_\tau \mathbf{u}^*$ is the full time tendency for the baroclinic velocity. For the semi-implicit treatment, we require those contributions proportional to γ, thus leading to

$$\mathbf{u}(\tau+\Delta\tau) = \mathbf{u}(\tau-\Delta\tau) + 2\,\Delta\tau\,\delta_\tau \mathbf{u}^* - \lambda\,\gamma\,\hat{\mathbf{z}} \wedge (\mathbf{u}[\tau+\Delta\tau) - \mathbf{u}(\tau-\Delta\tau)] \tag{24.25}$$

where again

$$\lambda = 2\,f\,\Delta\tau. \tag{24.26}$$

Writing out the components leads to

$$u(\tau+\Delta\tau) = u(\tau-\Delta\tau) + 2\,\Delta\tau\,\delta_\tau u^* + \lambda\,\gamma\,[v(\tau+\Delta\tau) - v(\tau-\Delta\tau)] \tag{24.27}$$

$$v(\tau+\Delta\tau) = v(\tau-\Delta\tau) + 2\,\Delta\tau\,\delta_\tau v^* - \lambda\,\gamma\,[u(\tau+\Delta\tau) - u(\tau-\Delta\tau)], \tag{24.28}$$

and solving for $\mathbf{u}(\tau+\Delta\tau)$ renders

$$u(\tau+\Delta\tau) = u(\tau-\Delta\tau) + 2\,\Delta\tau\,\left(\frac{\delta_\tau u^* + \lambda\,\delta_\tau v^*}{1+(\lambda\,\gamma)^2}\right) \tag{24.29}$$

$$v(\tau+\Delta\tau) = v(\tau-\Delta\tau) + 2\,\Delta\tau\,\left(\frac{\delta_\tau v^* - \lambda\,\delta_\tau u^*}{1+(\lambda\,\gamma)^2}\right). \tag{24.30}$$

24.4.2 Namelist parameters

In the code,

$$\Delta\tau = \text{dtuv} \tag{24.31}$$

is the baroclinic time step, and

$$\gamma = \text{acor} \tag{24.32}$$

is a namelist parameter setting the level of implicit treatment for the Coriolis force. The method for discretizing the Coriolis force in the baroclinic part of the model is set according to the value of acor, with

$$\text{acor} = 0 \Rightarrow \text{fully explicit Coriolis} \tag{24.33}$$

$$1/2 \leq \text{acor} \leq 1 \Rightarrow \text{semi-implicit Coriolis.} \tag{24.34}$$

As the vertically integrated part of the model algorithm typically uses a time step much smaller than f^{-1}, MOM4 discretizes the Coriolis force explicitly when time stepping the vertically integrated equations. That is, acor is relevant *only* for the baroclinic equations.

24.4.3 Energy analysis

In the continuum, the Coriolis force does no work on a fluid parcel since it is always directed orthogonal to the flow direction

$$\mathbf{v} \cdot f\,\hat{\mathbf{z}} \wedge \mathbf{u} = 0. \tag{24.35}$$

This property is respected on the B-grid when we discretize the Coriolis force explicitly in time

$$\mathbf{v}(\tau) \cdot f\,\hat{\mathbf{z}} \wedge \mathbf{u}(\tau) = 0. \tag{24.36}$$

However, the semi-implicit treatment does not respect this property since in general the product

$$\mathbf{v}(\tau) \cdot f\,\hat{\mathbf{z}} \wedge [(1-\gamma)\,\mathbf{u}(\tau - \Delta\tau) + \gamma\,\mathbf{u}(\tau + \Delta\tau)] \tag{24.37}$$

does not vanish. The only time it will vanish is when the flow is in a steady state. This limitation of the semi-implicit approach is to be expected, since implicit time discretizations generally do not conserve energy.

CHAPTER

TWENTYFIVE

Checkerboard null mode

Contents

The purpose of this chapter is to discuss issues related to the presence of a checker-board null mode present with a B-grid that appears most prominently in the surface height field. Much of this discussion follows that given by Pacanowski and Griffies (1999).

25.1 Introduction

As discussed by Killworth et al. (1991), discretization of gravity waves on a B-grid can admit a stationary grid scale checkerboard pattern (see also Messinger (1973) and Janjić (1974) for atmospheric discussions). This pattern is associated with an unsuppressed grid splitting that can be initiated through grid scale forcing, such as topography. That is, the discrete equations admit a checkerboard null mode. Beckers (1999) also discusses subtleties associated with traditional linear stability. In our experience, when the model goes unstable due to CFL violations, this grid mode is the spatial pattern associated with the instability.

Strictly, the grid mode is present *only* when the surface pressure gradient takes the form $\nabla_h p_s = \overline{\rho}\, g\, \nabla_h \eta$, where $\overline{\rho}$ is an averaged surface density. For example, in the implementation of Killworth et al. (1991), $\nabla_h p_s = \rho_o\, g\, \nabla_h \eta$, and so the null mode is always present. Tests with the alternative expression $p_s = \rho_{k=1}\, g\, \eta$ used in MOM, in which surface pressure gradients arise from gradients in both the surface

density $\rho_{k=1}$ and surface height, suggest that the null mode is slightly suppressed. A more significant means to suppress the mode, however, is provided through the use of time averaging over the barotropic time steps, as well as with nonlinearity in the shallow water system present when the undulating surface height is fully incorporated to the dynamics.

Hence, for many purposes, the grid mode is absent or mild. Nonetheless, some experiments do experience a nontrivial checkerboard pattern in the surface height, especially in enclosed seas such as the Mediterranean Sea and Hudson Bay. In this case, the checkerboard mode is continually excited by surface forcing and topography, yet there is not enough grid resolution to allow the noise to radiate outward or as boundary waves. The checkerboard pattern can also be initiated by fresh water forcing. Although the typical forcing from the atmosphere is large scale, there will always be some projection onto the grid scale, thus pumping energy into the null mode. In this case, we have seen the checkerboard pattern appear even over large basins.

For those cases where the noise is unacceptable, we have considered various means to suppress it. The following relates our experience provides suggestions and caveats. We remain incompletely satisfied with the following methods, and so welcome other suggestions.

25.2 Experiences with the checkerboard null mode

Under certain circumstances, Killworth et al. (1991) noted that the checkerboard pattern can appear in the vertically integrated velocity. In order to dissipate this mode, they suggested that horizontal friction acting on the barotropic velocity be updated each barotropic time step, instead of only during the baroclinic time steps. This approach was found to be especially appropriate in simulations with strong eddy activity.

Updating frction on each barotropic time step can be quite costly. Therefore, in practice, one is restricted to the use of a constant viscosity Laplacian friction for both the barotropic and baroclinic modes. Notably, use of a biharmonic viscosity, updated each barotropic time step, could be prohibitively costly. As discussed by such authors as Semtner and Mintz (1977) and Griffies and Hallberg (2000), Laplacian friction for eddy-permitting simulations significantly under-utilizes the model grid as it strongly suppresses mesoscale eddy formation. Hence, restricting the model to constant viscosity Laplacian friction is not an acceptable solution to the grid splitting problem. Relatedly, barotropically updating a depth dependent viscosity, such as that arising from the Smagorinsky scheme (Griffies and Hallberg (2000)), is very cumbersome due to the need to maintain self-consistency between friction applied in the barotropic and baroclinic equations.

For the time stepping procedure used in MOM4, regions where the barotropic fields are evolving experience an effective spatial averaging associated with the barotropic time averaging. Eddy-rich regions are therefore preferentially smoothed. Consequently, time averaging provides for an effective suppression of the grid splitting in both the surface height and vertically integrated velocity.

Since the surface height evolution is given by the inviscid continuity equation, the checkerboard pattern tends to appear most prominently in this field. To sup-

press the surface height noise, Killworth et al. (1991) proposed the addition of the so-called "del-plus / del-cross" operator to the prognostic equation for the free surface height. Their approach is an extension of that suggested by Janjić (1974). The operator is basically the difference between Laplacians computed in two different manners, and it preferentially removes the checkerboard pattern by coupling the grids. This coupling occurs in a scale-selective manner so that the larger scales are only modestly affected. The construction of this operator requires the definition of time dependent image points over land to allow for it to conserve volume.

25.2.1 A caveat concerning filtering the surface height

Various surface height filters have been tested, such as the del-plus / del-cross operator, as well as a two-dimensional Shapiro filter designed to conserve volume with arbitrary geography. Either spatial filter successfully removes noisy patterns from the surface height. However, their effects on other model fields, such as vertical velocity, can be dependent on the strength of the surface height filter. In particular, for many cases where the filter was sufficient to suppress noise in the surface height, it had detrimental effects on the vertical velocity.

The reason for this sensitivity can be seen by considering the equations for gravity waves on a B-grid using a forward-backward time stepping scheme as in MOM3 (the following considerations do not depend on the choice of time stepping schemes). To better expose the main points, assume $p_s = \rho_o \, g \, \eta$, $D = H + \eta \approx H$, and omit fresh water forcing. The discretized equations take the form

$$\eta(t_{n+1}) = \eta(t_n) - \Delta t \, [\nabla_h \cdot \mathbf{U}(t_n) - F(\eta)\,] \tag{25.1}$$

$$U(t_{n+1}) = U(t_n) - H \, g \, \Delta t \, \delta_x \overline{\eta(t_{n+1})}^{\,y} \tag{25.2}$$

$$V(t_{n+1}) = V(t_n) - H \, g \, \Delta t \, \delta_y \overline{\eta(t_{n+1})}^{\,x}, \tag{25.3}$$

where $F(\eta)$ represents a spatial filter applied to the surface height.

Consider a case in which the free surface contains power in the checkerboard pattern, as well as longer waves, yet there is no spatial filter and so $F = 0$. The discretized surface pressure gradient does not feel the checkerboard pattern since this pattern is a null mode of the discrete derivative operators $\delta_x \overline{()}^{\,y}$ and $\delta_y \overline{()}^{\,x}$. Therefore, discrete pressure gradients are determined only by longer waves, and so the gradients are smooth. Since the checkerboard pattern is stationary in time, it does not contribute to the vertical velocity. Neglecting the time varying top cell volume in the baroclinic and tracer equations, as in the constant volume free surface methods of Killworth et al. (1991) and Dukowicz and Smith (1994), renders the checkerboard pattern dynamically irrelevant. Instead, it is simply an esthetic nuisance. Yet when solving the more general equations with undulating top cell thicknesses, as in MOM4, the noise cannot be ignored as it potentially will influence the other model fields.

Now consider the addition of a spatial filter designed to preferentially remove the checkerboard grid noise in the surface height. Unlike the unfiltered and noisy η, the filter F will generally not be invisible to the discretized pressure gradients, and so these gradients are now affected by a new source. In practice, these new sources can be nontrivial, especially when using the Shapiro filter, which is the strongest

available grid scale filtering. Tests in MOM3 with the del plus / del minus filter, using the weighting factor suggested by Killworth et al. (1991), transformed large amount of noise to the vertical velocity field near the surface. Again, the reason is that this filter is not invisible to the discretized gradients, and so while it acts to smooth the surface height, it correspondingly adds noise to the surface pressure gradients which then affect the barotropic velocity.

One attempt to suppress the transfer of noise was to also filter $\nabla_h \cdot \mathbf{U}$ in order to counteract the noisy pressure gradients. Unfortunately, this approach is problematic, since doing so breaks the precise connection between the barotropic and baroclinic systems. As a result, spatially filtering $\nabla_h \cdot \mathbf{U}$ produces a nontrivial spurious vertical velocity throughout the ocean, and in particular it creates unacceptable spurious advective fluxes through the ocean bottom.

25.2.2 Suggestions

As mentioned at the beginning of this section, we find the need for filtering to be greatly reduced due to the use of a nonlinear free surface in which the barotropic time steps are time averaged. Nevertheless, for those cases in which filtering is needed, such as for inland seas and when using fresh water forcing, we have found it sufficient to add a straightforward Laplacian to the free surface height equation with a reasonably small diffusivity. The more sophisticated Shapiro filter or del-plus minus del-minus operator have been found to be no better, and often much worse in their affects on vertical velocity. Note that a Laplacian, using no-flux boundary conditions, conserves volume. Therefore, adding a Laplacian to the free surface equation is trivial to implement relative to the del plus / del minus operator, which requires the specification of time dependent image points in order to preserve volume in arbitrary geometry.

25.2.2.1 Laplacian at the end of the barotropic loop

One way to apply the filter to the surface height is at the end of the barotropic time steps. In addition to the Laplacian added to the surface height, the needs of total tracer conservation necessitate a compensating additional horizontal diffusion be added to tracers in the surface model grid cells. Similar issues of tracer and volume/mass compatibility were described for the cross-land mixing scheme in Chapter 13. This approach has lost favor among the developers due to the nontrivial effects it has on tracer concentration in the $k = 1$ level.

25.2.2.2 Laplacian added within the barotropic loop

Another way to add a Laplacian filter is to filter the surface height within the barotropic time loop. In this way, the surface height is continually being smoothed. This method increases the cost of the barotropic system due to the added computations and extra communication (for parallel computers). Yet it removes the need to concern ourselves with tracers, since compatibility is not a problem so long as the surface height is updated consistenty with the tracer (see chapter 7). This is the approach implemented in MOM4.

25.3 Polar filtering

The CFL time step requirements for the barotropic mode can be quite stringent when reaching the pole on a spherical grid. Instead of reducing the time steps, it is common to prescribe a spatial filtering in order to remove the small scale features. This filtering traditionally takes the form of Fourier filtering (e.g., Bryan et al. (1975)). Experience in MOM3 indicates that one-dimenstional Shapiro filtering is preferable due to its increased speed. Nevertheless, as such filtering is necessary for each of the small barotropic mode time steps, the computational cost can be high and it can render strong load imbalances between adjacent parallel computer processors. Indeed, the cost can be higher than the cost of simply reducing the barotropic time step in order to satisfy the CFL constraint. Additionally, for reasons related to the mechanism discussed above, tests have shown that polar filtering of the surface height can result in a nontrivial amount of grid noise in the vertical velocity field within the polar filtering regions. As a result, polar filtering the barotropic fields is not recommended, even when using the spherical form of MOM4. Indeed, polar filtering is supported in MOM4 only for use within the tracer equation. In general, polar filtering is not recommended, and it is becoming obsolete in ocean climate models via the use of non-spherical grids such as the tripolar grid discussed in Chapter 4.

25.4 The checkerboard damping module in MOM4-beta

As mentioned in Section 13.8, some care must be exercised in the specification of points between which the cross-land mixing scheme is used. Otherwise, mixing surface height can add to the problems associated with the checker-board null mode. Turning this problem into a solution is something that the researcher may wish to investigate. That is, cross-land mixing can be considered an *ad hoc* method to suppress the checker-board mode in enclosed seas. By construction, this scheme allows for one to mix in a manner that conserves total tracer. Taking this approach globally is what the MOM4-beta checkerboard module does, where now the module introduces a local Laplacian mixing of surface height aimed to suppress the mode. As discussed in Section 13.2 when describing the cross-land mixing scheme, mixing surface height must be accompanied by a mixing of tracer in the ocean's surface grid cell in order to conserve total model tracer. It is because of this added tracer mixing in the surface cell, which can generally be nontrivial, that the checkerboard module has recently grown out of favor with researchers at GFDL. Indeed, it is not supported in MOM4.0, though it is available in the beta releases of MOM4.

BIBLIOGRAPHY

Adcroft, A., C. Hill, and J. Marshall, 1999: A new treatment of the coriolis terms in c-grid models at both high and low resolutions. *Monthly Weather Review*, 127, 1928–1936.

Aris, R., 1962: *Vectors, Tensors and the Basic Equations of Fluid Mechanics*. Dover Publishing, 262 pp.

Beckers, J. M., 1999: On some stability properties of the discretisation of the damped propagation of shallow-water intertia-gravity waves on the arakawa b-grid. *Ocean Modelling*, 1, 53–69.

Beckmann, A., and R. Döscher, 1997: A method for improved representation of dense water spreading over topography in geopotential–coordinate models. *Journal of Physical Oceanography*, 27, 581–591.

Bryan, F., 1987: Parameter sensitivity of primitive equation ocean general circulation models. *Journal of Physical Oceanography*, 17, 970–985.

Bryan, K., 1969: A numerical method for the study of the circulation of the world ocean. *Journal Computational Physics*, 4, 347–376.

Bryan, K., 1984: Accelerating the convergence to equilibrium of ocean-climate models. *Journal of Physical Oceanography*, 14, 666–673.

Bryan, K., 1989: The design of numerical models of the ocean circulation. J. W. David L.T. Anderson, Ed., *Oceanic circulation models: combining data and dynamics*, Vol. 44, Kluwer Academic Publishers, 465–511.

Bryan, K., and M. D. Cox, 1972: An approximate equation of state for numerical models of the ocean circulation. *Journal of Physical Oceanography*, 4, 510–514.

Bryan, K., and L. J. Lewis, 1979: A water mass model of the world ocean. *Journal of Geophysical Research*, 84, 2503–2517.

Bryan, K., S. Manabe, and R. C. Pacanowski, 1975: A global ocean-atmosphere climate model. part ii. the oceanic circulation. *Journal of Physical Oceanography*, 5, 30–46.

Campin, J.-M., and H. Goosse, 1999: Parameterization of density-driven downsloping flow for a coarse-resolution ocean model in z-coordinate. *Tellus*, 51A, 412–430.

Cox, M. D., 1984: *A primitive equation, 3-dimensional model of the ocean*. NOAA/Geophysical Fluid Dynamics Laboratory.

Danabasoglu, G., J. C. McWilliams, and W. G. Large, 1996: Approach to equilibrium in accelerated global oceanic models. *Journal of Climate*, 9, 1092–1110.

Denman, K., 1973: A time-dependend model of the upper ocean. *Journal of Physical Oceanography*, 3, 173–184.

Dewar, W. K., Y. Hsueh, T. J. McDougall, and D. Yuan, 1998: Calculation of pressure in ocean simulations. *Journal of Physical Oceanography*, 28, 577–588.

Döscher, R., and A. Beckmann, 1999: Effects of a bottom boundary layer parameterization in a coarse-resolution model of the north atlantic ocean. *Journal of Atmospheric and Oceanic Technology*, 17, 698–707.

Dukowicz, J. K., and R. D. Smith, 1994: Implicit free-surface method for the Bryan-Cox-Semtner ocean model. *Journal of Geophysical Research*, 99, 7991–8014.

Dukowicz, J. K., R. D. Smith, and R. C. Malone, 1993: A reformulation and implementation of the Bryan-Cox-Semtner ocean model on the connection machine. *Journal of Atmospheric and Oceanic Technology*, 10, 195–208.

Durran, D. R., 1999: *Numerical Methods for Wave Equations in Geophysical Fluid Dynamics*. Springer Verlag.

England, M. H., 1995: The age of water and ventilation timescales in a global ocean model. *Journal of Physical Oceanography*, 25, 2756–2777.

Favre, A., 1965: équations des gaz turbulents compressibles i and ii. *Journel de Méchanic*, 4, 361–421.

Feistel, R., 1993: Equilibrium thermodynamics of seawater revisited. *Progress in Oceanography*, 31, 101–179.

Feistel, R., and E. Hagen, 1995: On the Gibbs thermodynamic potential of seawater. *Progress in Oceanography*, 36, 249–327.

Gent, P. R., and J. C. McWilliams, 1990: Isopycnal mixing in ocean circulation models. *Journal of Physical Oceanography*, 20, 150–155.

Gent, P. R., J. Willebrand, T. J. McDougall, and J. C. McWilliams, 1995: Parameterizing eddy-induced tracer transports in ocean circulation models. *Journal of Physical Oceanography*, 25, 463–474.

Gill, A., 1982: *Atmosphere-Ocean Dynamics*. International Geophysics Series, Vol. 30, Academic Press Inc.

Goosens, M., F. Mittelbach, and A. Samarin, 1994: *The LaTeXCompanion*. Addison-Wesley.

Gordon, C., C. Cooper, C. A. Senior, H. Banks, T. C. J. J. M. Gregory, J. F. B. Mitchell, and R. A. Wood, 2000: The simulation of SST, sea ice extents and ocean heat transports in a version of the Hadley Centre coupled model without flux adjustments. *Climate Dynamics*, 16, 147–168.

Greatbatch, R. J., Y. Lu, and Y. Cai, 2001: Relaxing the Boussinesq approximation in ocean circulation models. *Journal of Atmospheric and Oceanic Technology*, 18, 1911–1923.

Griffies, S. M., 1998: The Gent-McWilliams skew-flux. *Journal of Physical Oceanography*, 28, 831–841.

Griffies, S. M., 2004: *Fundamentals of ocean climate models*. Princeton University Press.

Griffies, S. M., and Coauthors, 2000a: Developments in ocean climate modelling. *Ocean Modelling*, 2, 123–192.

Griffies, S. M., A. Gnanadesikan, R. C. Pacanowski, V. Larichev, J. K. Dukowicz, and R. D. Smith, 1998: Isoneutral diffusion in a z-coordinate ocean model. *Journal of Physical Oceanography*, 28, 805–830.

Griffies, S. M., and R. W. Hallberg, 2000: Biharmonic friction with a Smagorinsky viscosity for use in large-scale eddy-permitting ocean models. *Monthly Weather Review*, 128, 2935–2946.

Griffies, S. M., R. C. Pacanowski, and R. W. Hallberg, 2000b: Spurious diapycnal mixing associated with advection in a z-coordinate ocean model. *Monthly Weather Review*, 128, 538–564.

Griffies, S. M., R. C. Pacanowski, R. M. Schmidt, and V. Balaji, 2001: Tracer conservation with an explicit free surface method for z-coordinate ocean models. *Monthly Weather Review*, 129, 1081–1098.

Hallberg, R. W., 1997: Stable split time stepping schemes for large-scale ocean modeling. *Journal Computational Physics*, 135, 54–65.

Haltiner, G. T., and R. T. Williams, 1980: *Numerical Prediction and Dynamic Meteorology*. John Wiley and Sons.

Held, I. M., and V. D. Larichev, 1996: A scaling theory for horizontally homogeneous baroclinically unstable flow on a beta plane. *Journal of Atmospheric Sciences*, 53, 946–952.

Hendershott, M., 1972: The effects of solid earth deformation on global ocean tide. *Geophysical Journal of the Royal Astronomical Society*, 29, 389–402.

Hinze, J. O., 1975: *Turbulence*. McGraw-Hill Publishers.

Holland, W. R., J. C. Chow, and F. O. Bryan, 1998: Application of a third-order upwind scheme in the ncar ocean model. *Journal of Climate*, 11, 1487–1493.

Holloway, G., 1992: Representing topographic stress for large-scale ocean models. *Journal of Physical Oceanography*, 22, 1033–1046.

Huang, R. X., 1993: Real freshwater flux as a natural boundary condition for the salinity balance and thermohaline circulation forced by evaporation and precipitation. *Journal of Physical Oceanography*, 23, 2428–2446.

Jackett, D. R., and T. J. McDougall, 1995: Minimal adjustment of hydrographic profiles to achieve static stablilty. *Journal of Atmospheric and Oceanic Technology*, 12, 381–389.

Janjić, Z. I., 1974: A stable centered difference scheme free of two-grid-interval noise. *Monthly Weather Review*, 102, 319–323.

Jerlov, N. G., 1968: *Optical Oceanography*. Elsevier, 194 pp.

Killworth, P. D., 1989: On the parameterisation of deep convection in ocean models. *Parameterizing small scale processes in the ocean: Proceeding of the 'Aha Huliko 'a Hawaiian Winter Workshop*, 'Aha Huiliko'a, University of Hawaii at Manoa.

Killworth, P. D., and N. Edwards, 1999: A turbulent bottom boundary layer code for use in numerical ocean models. *Journal of Physical Oceanography*, 29, 1221–1238.

Killworth, P. D., J. M. Smith, and A. E. Gill, 1984: Speeding up ocean circulation models. *Ocean Modelling*, 56, 1–5.

Killworth, P. D., D. Stainforth, D. J. Webb, and S. M. Paterson, 1991: The development of a free-surface Bryan-Cox-Semtner ocean mode. *Journal of Physical Oceanography*, 21, 1333–1348.

Klinger, B. A., J. Marshall, and U. Send, 1996: Representation of convective plumes by vertical adjustment. *Journal of Geophysical Research*, 101, 18 175–18 182.

Lamport, L., 1994: *LaTeX: A Documentation Preparation System User's Guide and Reference Manual*. Addison-Wesley.

Landau, L. D., and E. M. Lifshitz, 1987: *Fluid Mechanics*. Pergamon Press.

Large, W. G., G. Danabasoglu, J. C. McWilliams, P. R. Gent, and F. O. Bryan, 2001: Equatorial circulation of a global ocean climate model with anisotropic horizontal viscosity. *Journal of Physical Oceanography*, 31, 518–536.

Large, W. G., J. C. McWilliams, and S. C. Doney, 1994: Oceanic vertical mixing: A review and a model with a nonlocal boundary layer parameterization. *Reviews of Geophysics*, 32, 363–403.

Levitus, S., 1982: Climatological atlas of the world ocean. U.S. Government Printing Office 13, NOAA, Washington, D.C. 163 pp.

KEY: Levitus82
ANNOTATION: 17 mircofiches

Lin, S. J., and R. B. Rood, 1996: Multidimensional flux-form semi-lagrangian transport schemes. *Monthly Weather Review*, 124, 2046–2070.

Losch, M., A. Adcroft, and J.-M. Campin, 2003: How sensitive are coarse general circulation models to fundamental approximations in the equations of motion? *Journal of Physical Oceanography*.

Lu, Y., 2001: Including non-Boussinesq effects in Boussinesq ocean circulation models. *Journal of Physical Oceanography*, 31, 1616–1622.

Marchuk, and Kagan, 1989: *Dynamics of Ocean Tides*. Kluwer Academic, 327 pp.

Marotzke, J., 1991: Influence of convective adjustment on the stability of the thermohaline circulation. *Journal of Physical Oceanography*, 21, 903–907.

Marshall, J., A. Adcroft, J.-M. Campin, and C. Hill, 2003: Atmosphere-ocean modeling exploiting fluid isomorphisms. *Journal of Physical Oceanography*.

Marshall, J., C. Hill, L. Perelman, and A. Adcroft, 1997: Hydrostatic, quasi-hydrostatic, and nonhydrostatic ocean modeling. *Journal of Geophysical Research*, 102, 5733–5752.

McDougall, T. J., R. J. Greatbatch, and Y. Lu, 2002: On conservation equations in oceanography: How accurate are Boussinesq ocean models? *Journal of Physical Oceanography*, 32, 1574–1584.

McDougall, T. J., D. R. Jackett, D. G. Wright, and R. Feistel, 2003: Accurate and computationally efficient algorithms for potential temperature and density of seawater. *Journal of Atmospheric and Oceanic Technology*, 20, 730–741.

Messinger, F., 1973: A method for construction of second-order accurate difference schemes permitting no false two-grid-interval waves in the height field. *Tellus*, 25, 444–457.

Morel, A., 1988: Optical modeling of the upper ocean in relation to its biogenous matter content (case-i waters). *JGR*, 93, 10 749–10 768.

Morel, A., and D. Antoine, 1994: Heating rate within the upper ocean in relation to its biooptical state. *Journal of Physical Oceanography*, 24, 1652–1665.

Morel, A., and J.-F. Berthon, 1989: Surface pigments, algal biomass profiles, and potential production of the euphotic layer: relationship reinvestigated in view of remote-sensing applications. *Limnology and Oceanography*, 34, 1542–1562.

Murray, R. J., 1996: Explicit generation of orthogonal grids for ocean models. *Journal Computational Physics*, 126, 251–273.

O'Brien, J. J., 1986: *Advanced Physical Oceanographic Numerical Modelling*. D. Reidel Publishing Company,, 608 pp.

Ohlmann, J., and D. Siegel, 2000: Ocean radiant heating. part i: Optical influences. *JPO*, 30, 1833–1848.

Pacanowski, R. C., 1995: *MOM2 Documentation, User's Guide, and Reference Manual*. NOAA/Geophysical Fluid Dynamics Laboratory.

Pacanowski, R. C., K. Dixon, and A. Rosati, 1991: *The GFDL Modular Ocean Model User Guide*. NOAA/Geophysical Fluid Dynamics Laboratory.

Pacanowski, R. C., and A. Gnanadesikan, 1998: Transient response in a z-level ocean model that resolves topography with partial-cells. *Monthly Weather Review*, 126, 3248–3270.

Pacanowski, R. C., and S. M. Griffies, 1999: *The MOM3 Manual*. NOAA/Geophysical Fluid Dynamics Laboratory.

Pacanowski, R. C., and G. Philander, 1981: Parametrization of vertical mixing in numerical models of the tropical ocean. *Journal of Physical Oceanography*, 11, 1442–1451.

Paulson, E. A., and J. J. Simpson, 1977: Irradiance measurements in the upper ocean. *Journal of Physical Oceanography*, 7, 952–956.

Pedlosky, J., 1987: *Geophysical Fluid Dynamics*. 2nd ed., Springer-Verlag.

Pickard, G. L., and W. J. Emery, 1990: *Descriptive Physical Oceanography*. 5th ed., Pergamon Press, 320 pp.

Press, W. H., S. A. Teukolsky, W. T. Vetterling, and B. P. Flannery, 1992: *Numerical Recipes in FORTRAN: The Art of Scientific Computing*. 2nd ed., Cambridge University Press.

Rahmstorf, S., 1993: A fast and complete convection scheme for ocean models. *Ocean Modelling*, 101, 9–11.

Ray, R. D., 1998: Ocean self-attraction and loading in numerical tidal models. *Marine Geodesy*, 21, 181–192.

Rosati, A., and K. Miyakoda, 1988: A general circulation model for upper ocean simulation. *Journal of Physical Oceanography*, 18, 1601–1626.

Semtner, A. J., 1974: An oceanic general circulation model with bottom topography. *Numerical Simulation of Weather and Climate*, Technical Report No. 9, UCLA Department of Meteorology.

Semtner, A. J., and Y. Mintz, 1977: Numerical simulation of the gulf stream and mid-ocean eddies. *Journal of Physical Oceanography*, 7, 208–230.

Smith, R. D., 1999: The primitive equations in the stochastic theory of adiabatic stratified turbulence. *Journal of Physical Oceanography*, 29, 1865–1880.

Smith, R. D., J. K. Dukowicz, and R. C. Malone, 1992: Parallel ocean general circulation modeling. *Physica D*, 60, 38–61.

Smith, R. D., and J. C. McWilliams, 2002: Anisotropic horizonal viscosity for ocean models. *Ocean Modelling*, 5, 129–156.

Thiele, G., and J. L. Sarmiento, 1990: Tracer dating and ocean ventilation. *Journal of Geophysical Research*, 95, 9377–9391.

Veronis, G., 1973: Large scale ocean circulation. *Advances in Applied Mechanics*, 13, 2–92.

Visbeck, M., J. C. Marshall, T. Haine, and M. Spall, 1997: Specification of eddy transfer coefficients in coarse resolution ocean circulation models. *Journal of Physical Oceanography*, 27, 381–402.

Wahr, J., 1998: Body tides on an elliptical, rotating, elastic and oceanless earth. *Geophysical Journal of the Royal Astronomical Society*, 64, 677–703.

Webb, D. J., A. C. Coward, B. A. de Cuevas, and C. S. Gwilliam, 1998: The first main run of the OCCAM global ocean model. *Southampton Oceanography Centre*, Internal Document No. 34.

Winters, K. B., and E. A. D'Asaro, 1995: Diascalar flux and the rate of fluid mixing. *Journal of Fluid Mechanics*, 317, 179–193.

Winters, K. B., P. N. Lombard, J. J. Riley, and E. A. D'Asaro, 1995: Available potential energy and mixing in density-stratified fluids. *Journal of Fluid Mechanics*, 289, 115–128.

Winton, M., R. W. Hallberg, and A. Gnanadesikan, 1998: Simulation of density-driven frictional downslope flow in z-coordinate ocean models. *Journal of Physical Oceanography*, 28, 2163–2174.

Wright, D. G., 1997: An equation of state for use in ocean models: Eckart's formula revisited. *Journal of Atmospheric and Oceanic Technology*, 14, 735–740.

INDEX